Instability and Strain Localization Analysis of Water-saturated Clay by Elasto-viscoplastic Constitutive Models

December 2003

Yosuke HIGO

Instability and Strain Localization Analysis of Water-saturated Clay by Elasto-viscoplastic Constitutive Models

December 2003

Yosuke HIGO

Abstract

Strain localization is an important geotechnical problem related to large deformations and the onset of failure such as slope failure. Therefore, it is necessary to clarify the mechanisms of strain localization of geomaterials in order to predict large deformations of the ground which induce serious disasters. The main purpose of this dissertation is to study the strain localization of water-saturated clay by experimental, theoretical, and numerical work. In addition, an elasto-viscoplastic constitutive model for clay is developed to accurately describe the time dependency, the dilatancy characteristics, and the material instability of clay.

A linear instability analysis, using a gradient-dependent elasto-viscoplastic constitutive model, is conducted to theoretically study the effects of permeability and strain gradients on material instability. It is found that the growth rate of the fluctuation is greatly affected by the permeability and that the strain gradient term acts as a stabilizer in the material system. The strain localization of water-saturated normally consolidated clay is numerically studied under plane strain conditions by a soil-water coupled finite element analysis based on the finite deformation theory. A weak form of the dynamic yield function is formulated in order to obtain a second order gradient for the viscoplastic strain. The effects of permeability and gradient parameters on the strain localization obtained from the numerical analysis are consistent with the theoretical considerations given by the instability analysis. In addition, the effects of partially drainage conditions and material heterogeneity on strain localization are studied.

Next, the elasto-viscoplastic model for normally consolidated clay is extended to overconsolidated clay. The proposed model can effectively reproduce the dilatancy characteristics of both normally consolidated clay and overconsolidated clay. The instability of the model under undrained triaxial creep conditions is analyzed in terms of the accelerating creep failure. Then, a finite element analysis of the deformation of water-saturated clay is presented with focus on the numerical results under plane strain conditions. From the numerical analysis, it is found that dilatancy, permeability, strain rates, and material instability prominently affect the strain localization behavior.

In order to grasp the strain localization behavior of clay under three-dimensional conditions, a series of undrained triaxial compression tests using rectangular clay specimens with different shapes and strain rates is conducted for normally consolidated and overconsolidated reconstituted clay samples. The shear strain distribution localized by compression is successfully observed with an image analysis of digital photographs showing two sides of the specimens. Bifurcation phenomena, e.g., the formation and the progress of various three-dimensional shear bands, failure with buckling, etc., are observed. It is seen that the shapes of the specimens, strain rates, and the dilatancy characteristics affect the shear band formations of clay.

Finally, the triaxial compression tests using rectangular clay specimen are numerically sim-

ulated with the finite element method using an elasto-viscoplastic model considering structural changes. The simulation can well reproduce the generation and the growing process of shear bands. The distributions of strain, stress, and pore water pressure inside the specimens are given in the simulation results. A comparison between experimental and simulation results offers new findings regarding the strain localization of clay under three-dimensional conditions.

Acknowledgments

The work for this dissertation was carried out over a period of six years at the Laboratory of Geomechanics in the Department of Civil and Earth Resource Engineering (in the former five years, at the Laboratory of Soil Mechanics in the Department of Civil Engineering) at Kyoto University, starting when I was an undergraduate student. The completion of this dissertation could not have been achieved without much support and encouragement from professors and colleagues, to whom I would like to express my gratitude.

First and foremost, I would like to express my sincerest appreciation and profound gratitude to my supervisor, Professor Fusao Oka, for encouraging me to pursue my studies toward a doctor's degree in engineering. Without his guidance and support, based on his deep insight and experience in the field, I could not have completed the present work. His invaluable advice and support always inspired me and significantly influenced the path I have chosen in my life. I am very grateful and proud to have been one of his students over the past six years.

I also wish to express my sincere gratitude to the members of Dissertation Committee, namely, Professor Takeshi Tamura and Professor Toshifumi Matsuoka, for their constructive suggestions and active discussions.

I would next like to express my special respect and gratitude to Associate Professor Takeshi Kodaka. His great support, based on his vast knowledge of experiments, made the experimental work of my dissertation possible. I have appreciated his constant guidance and heartful encouragement over the years.

I also extend my appreciation to Dr. Sayuri Kimoto, Research Associate, for her support and encouragement. Her research work on constitutive equations helped me successfully complete this thesis. In addition, I extend my appreciation to Dr. Shinichiro Nakashima, a former Research Associate, presently at the Public Works Research Institute, for his generous assistance.

Special thanks are especially extended to Mr. Tsutomu Takyu, a former student who is now in Japan Highway Public Corporation, Mr. Tomomitsu Satomura, a former student who is now in Nishimatsu Construction Co., Ltd., and Ms. Tomoko Ichinose, a master course student. Their valuable efforts with the experimental work made it possible for me to achieve this goal. Special thanks are also extended to Mr. Boonlert Siribumrungwong, a doctor course student, and Mr. Yuji Fujita, a master course student, for their meaningful contribution to promote the analysis method. I would also like to acknowledge past and present members of the Geomechanics Laboratory for their friendship and encouragement. I had a great time with them and will always cherish many wonderful memories.

Finally, I offer very special thanks to my parents, Katsumi and Kazuko, and my brother, Takeshi, for their love, support, and faith which continuously sustained throughout my studies.

December 2003
Yosuke HIGO

Table of Contents

List of Tables, Photos, and Figures

Chapter 1

Introduction

1.1 Background and Objectives

It has been widely recognized that the strain localization of granular media is an important problem since it is closely related to the onset of failure. The failure of slopes is a typical localization problem in which deformation occurs in a narrow zone. The problem of strain localization in such geomaterials as soil and rock has been studied in the context of experimental, theoretical, and numerical approaches over the last three decades. It has been found that the onset conditions for strain localization, such as shear banding, can be captured by a bifurcation analysis (e.g., Rudnicki and Rice 1975 and Rice 1976). As such, many researchers have tried to numerically simulate shear banding in various engineering materials, including metals and geological materials. Through these numerical studies, it has been realized that instability and ill-posedness are sometimes encountered when using a rate-independent elasto-plastic model in the numerical analysis.

In general, there are three methods which can be used to overcome the above-mentioned instability. One method is to introduce the rate dependency of the material through the use of an elasto-viscoplastic model or regularization in the numerical analysis (Cormeau 1975; Hughes and Taylor 1978; and Simo and Hughes 1997). The second method is to introduce higher order strain gradients into the constitutive model (Aifantis 1984, 1987; Mühlhaus and Aifantis 1991; Vardoulakis and Aifantis 1991; and Hutchinson 2001). The third approach is to incorporate a Darcy type of soil-fluid interaction which can alleviate the problem of instability by delaying the onset of material instability (Rice 1975, 1976; Loret and Prévost 1991; Oka et al. 1995; and Schrefler et al. 1996).

The present study deals with the behavior of clay in which the aspect of rate dependency comes naturally into the modeling. Constitutive models for clay used in this study are based on an elasto-viscoplasticity theory, which was originally proposed by Oka (1981) and Adachi and Oka (1982). In addition, since the transport of water must be considered in the behavior of water-saturated clay, the problem is formulated within the solid-fluid two-phase theory. Moreover, the

finite deformation theory is required since deformations in shear band are large (e.g., Yatomi et al. 1989). Furthermore, a second order strain gradient is introduced into the elasto-viscoplastic model in this study. It has been shown that the strain gradient-dependent model has several advantages, such as its ability to predict the thickness of shear bands, to retrieve the ill-posedness of boundary value problems with a local constitutive model, to consider the microstructure by introducing the characteristic length scale etc. (e.g., Mühlhaus and Vardoulakis 1987; Zbib and Aifantis 1989; Fleck and Hutchinson 1997; Oka et al. 2000a; Zhang and Schrefler 2000). However, the role of strain gradients and the quantitative estimation of gradient parameters still need to be determined.

Strain localization analysis using a soil-water coupled theory, based on the finite deformation theory, has been numerically and analytically conducted by many researchers with particular constitutive models, e.g., Yatomi et al. (1989), Oka et al. (1994, 1995), Asaoka et al. (1995), Schrefler et al. (1996), Iizuka et al. (1998). Oka et al. (1994, 1995, 2000a, and 2000b) studied strain localization problems pertinent to water-saturated clay using a viscoplastic model. In particular, it was found that strain localization in the shear bands of water-saturated clay could be simulated via a finite element analysis based on finite deformation theory using an elasto-viscoplastic model with viscoplastic softening (Oka et al. 1995). However, the model used in the analysis was limited to normally consolidated clay with negative dilatancy.

As for the experimental study, the strain localization of geomaterials has been discussed mainly under plane strain conditions (Han and Vardoulakis 1991; Yoshida et al. 1994; and Mokni and Desrues 1998). With respect to practical strain localization in the ground, shear band formation is a three-dimensional problem such as the failure surface of a landslide. Thus, it is necessary to deal with strain localization phenomena under three-dimensional conditions. Asaoka et al. (1997), Alshibli et al. (2000), etc. studied three-dimensional strain localization through triaxial tests using cylindrical specimens. However, some difficulties were encountered in simulating the triaxial test conditions with cylindrical specimens in the three-dimensional computation work, e.g., an axisymmetric assumption is needed. Kodaka et al. (2001) used rectangular clay specimens for the undrained triaxial compression tests, and studied three-dimensional strain localization with an image analysis of digital photographs taken during deformation. Using rectangular specimens, it is easy to set up the boundary conditions in a three-dimensional analysis. In addition, a quantitative comparison is possible through the distribution of shear strain obtained by the image analysis.

In the present study, the quasi-static strain localization of water-saturated clay is theoretically and numerically studied using an elasto-viscoplastic constitutive model. Theoretical consideration is given by a soil-water coupled instability analysis using a simplified gradient-dependent elasto-viscoplastic model in terms of the growth rate of the fluctuation. In the instability analysis, the effects of permeability and gradient parameters on the material instability are discussed. As for the numerical study, the strain localization analysis by a soil-water coupled

finite element method, based on finite deformation theory using an elasto-viscoplastic model for water-saturated clay, is conducted under plane strain conditions. The elasto-viscoplastic constitutive model is extended to describe the behavior of both normally consolidated clay and overconsolidated clay. The instability of the proposed model is demonstrated in terms of undrained triaxial creep conditions. The effects of dilatancy, the transport of water such as permeability and drainage conditions, the strain rates, the material instability, and the inherent material heterogeneity on strain localization are discussed. The role of strain gradients is numerically examined for normally consolidated clay.

Moreover, in order to investigate the strain localization behavior of geomaterials under three-dimensional conditions, undrained triaxial compression tests using rectangular specimens and their simulation by a finite element analysis using an elasto-viscoplastic model are conducted. In the experiments, both normally consolidated and overconsolidated clay samples are tested with different shaped specimens and different strain rates in the same manner as that by Kodaka et al. (2001). Using the distribution of shear strain obtained by the image analysis of digital photographs taken during deformation, the effects of the shapes of the specimens, the strain rates, and dilatancy on strain localization are studied in detail. The method of numerical simulation is a soil-water coupled finite element method which is based on the finite deformation theory, using an elasto-viscoplastic model for water-saturated clay considering structural changes, proposed by Kimoto (2002), Kimoto et al. (2004; to appear), and Kimoto and Oka (2003). The results of the simulation include not only the distribution of shear strain on the surfaces of the specimens, but also the distributions of strain, stress, and pore water pressure inside the specimens. Through a comparison of the experimental results and the simulation results, the mechanisms of strain localization are studied under three-dimensional conditions.

1.2 Scope and Organization

The present research is roughly divided into three parts, namely, a constitutive equation, experimental work, and the instability and strain localization analysis. The outline of each chapter is described below.

In **Chapter 2**, an elasto-viscoplastic constitutive model for normally consolidated clay, originally proposed by Adachi and Oka (1982), is derived. A second material function is introduced into the model in order to address the material instability of clay (Adachi et al. 1987). Furthermore, a strain gradient-dependent model is demonstrated by the introduction of a second order gradient of the viscoplastic volumetric strain into the static yield function (Oka et al. 1992).

In **Chapter 3**, a linear instability analysis is performed to explore the effects of permeability and gradient parameters on the instability conditions using a simplified gradient-dependent elasto-viscoplastic model in the context of a Biot type of mixture theory. Next, a finite element formulation of the gradient-dependent elasto-viscoplastic model is described. In the FEM anal-

ysis, a Biot type of two-phase mixture formulation and an updated Lagrangian scheme are used for the water-saturated material. Then, the effects of the transport of water, namely, permeability and partially drainage conditions, the strain gradient parameters, and the fluctuation of material properties on the strain localization of clay are numerically studied under plane strain conditions.

In **Chapter 4**, an extended elasto-viscoplastic model for both normally consolidated clay and overconsolidated clay is proposed using a Chaboche type of viscoplasticity (1983), an overconsolidation boundary (Oka 1982 etc.), and a stress history ratio (Adachi and Oka 1995, etc.). The model can address both the positive and the negative dilatancy characteristics of clay, which are important characteristics of soil.

In **Chapter 5**, the instability of the proposed model is examined under undrained triaxial creep conditions. The difference in material instability between normally consolidated clay and overconsolidated clay is discussed. A numerical simulation for both normally consolidated clay and overconsolidated clay under plane strain conditions is conducted to investigate the effects of dilatancy, permeability, the strain rates, and material instability on strain localization.

In **Chapter 6**, the three-dimensional strain localization behavior of clay is studied through undrained triaxial compression tests using rectangular reconstituted clay specimens. An image analysis of digital photographs taken during deformation provides the distribution of shear strain on the surfaces of the specimens. Three-dimensional shear band formations are estimated, and the effects of the shapes of the specimens, the strain rates, and dilatancy on strain localization are investigated.

In **Chapter 7**, a numerical simulation of the undrained triaxial compression tests using rectangular specimens are conducted by a soil-water coupled finite element method based on the finite deformation theory using an elasto-viscoplastic model for water-saturated clay considering structural changes proposed by Kimoto (2002) etc. The distributions of strain, stress, and pore water pressure obtained from the simulation results and a comparison between the test results and the simulation results clarify the mechanisms of the three-dimensional strain localization of clay.

In **Chapter 8**, the conclusion of this dissertation and recommendations for future work are given.

References

Adachi, T. and Oka, F. (1982), Constitutive equations for normally consolidated clay based on elasto-viscoplasticity, *Soils and Foundations*, **22**, 4, pp. 57-70.

Adachi, T., Oka, F. and Mimura, M. (1987), An elasto-viscoplastic theory for clay failure, *Proc. 8th Asian Regional Conference on Soil Mechanics and Foundation Engineering*, Kyoto, JSSMFE, **1**, pp. 5-8.

Adachi, T. and Oka, F. (1995), An elasto-plastic constitutive model for soft rock with strain softening, *Int. J. Numerical and Analytical Methods in Geomechanics*, **19**, pp. 233-247.

Aifantis, E.C. (1984), On the microstructural origin of certain inelastic models, ASME, *J. Engineering Materials and Technology*, **106**, pp. 326-330.

Aifantis, E.C. (1987), The physics of plastic deformation, *Int. J. Plasticity*, **3**, pp. 211- 247.

Alshibli, K.A., Sture, S., Costes, N.C., Frank, M.L. and Lankto, M.R. (2000), Assessment of localized deformations in sand using X-ray computed tomography, *Geotechnical Testing Journal*, **23**, 3, pp. 274-299.

Asaoka, A. and Noda, T. (1995), Imperfection-sensitive bifurcation of cam-clay under plane strain compression with undrained boundaries, *Soils and Foundations*, **35**, 1, pp. 83-100.

Asaoka, A., Nakano, M., Noda, T., Takaine, T. and Kaneda, K. (1997), Progressive failure of heavily overconsolidated clay under constant load application, an experiment and its simulation, *Deformation and Progressive Failure in Geomechanics*, Proc. Int. Symp., Nagoya, Pergamon, pp. 69-74.

Chaboche, J.L. and Rousselier, G. (1983), On the plastic and viscoplastic constitutive equations-Part I: Rules developed with internal variable concept, *J. Pressure Vessel Technology*, ASME, **105**, pp. 103-158.

Cormeau, I.C. (1975), Numerical stability in quasi-static elasto/viscoplasticity, *Int. J. Numerical Methods in Engineering*, **9**, pp. 109-127.

Fleck, A.N. and Hutchinson, J.W. (1997), Strain gradient plasticity, *Advances in Applied Mechanics*, Hutchinson, J.W., and Wu, T.Y. eds., Academic Press, **33**, pp. 296-361.

Han, C. and Vardoulakis, I. (1991), Plane-strain compression experiments on water-saturated fine-grained sand, *Géotechnique*, **41**, 1, pp. 49-78.

Hughes, T.J.R. and Taylor, R.J. (1978), Unconditionally stable algorithms for quasi-static elasto-viscoplastic finite element analysis, *Computers and Structures*, **8**, pp. 169-173.

Hutchinson, J.W. (2001), Strain gradient plasticity theory revisited, *Material Science for 21st Century*, Invited Papers, The Society of Material Science, Japan, May 2001, Vol. A, pp. 307-315.

Iizuka, A., Kobayashi, I., and Ohta, H. (1998), Dilatancy localization in clay specimen under shearing, *Proc. 4th Int. Workshop on Localization and Bifurcation Theory for Soils and Rocks*, Adachi, T., Oka, F., and Yashima, A. eds., Gifu, Balkema, pp. 345-353.

Kimoto, S. (2002), Constitutive models for geomaterials considering structural changes and anisotropy, Doctoral thesis, Kyoto University, Japan.

Kimoto, S., Oka, F. and Higo, Y. (2004), Strain localization analysis of elasto-viscoplastic soil considering structural degradation, *Computer Methods in Applied Mechanics & Engineering*, to appear.

Kimoto, S. and Oka, F. (2003), An elasto-viscoplastic model for clay considering destructuralization and prediction of compaction bands, *Proc. Int. Workshop on Prediction and Simulation Methods in Geomechanics*, TC34 of ISSMGE, Athens, Greece, Oka, F., Vardoulakis, I., Murakami, A., and Kodaka, T. eds., pp. 65-68.

Kodaka, T., Higo, Y. and Takyu, T. (2001), Deformation and failure characteristics of rectangular specimens under three-dimensional condition, *Proc. 15th ICSMGE*, Istanbul, Balkema, **1**, pp. 167-170.

Loret, B and Prévost, J.H. (1991), Dynamic strain localization in fluid-saturated porous media, *J. Engineering Mechanics*, ASCE, **117**, 4, pp. 907-922.

Mokni, M. and Desrues, J. (1998), Strain localization measurements in undrained plane-strain biaxial tests on Hostun RF sand, *Mechanics of Cohesive-Frictional Materials*, **4**, pp. 419-441.

Mühlhaus, H.-B. and Aifantis, E.C. (1991), A variational principle for gradient plasticity, *Int. J. of Solids and Structures*, **28**, 7, pp. 845-857.

Mühlhaus, H.-B. and Vardoulakis, I. (1987), The Thickness of Shear Bands in Granular Materials, *Géotechnique*, **37**, pp. 271-283.

Oka, F. (1981), Prediction of time-dependent behavior of clay, *Proc. 10th ICSMFE*, Stockholm, **1**, pp. 215-218.

Oka, F. (1982), Elasto-viscoplastic constitutive equation for overconsolidated clay, *Proc. 1st Int. Symp. on Numerical Models in Geomechanics*, Zurich, Dungar, R., Pande, G.N. and Studer, J.A. eds., Balkema, pp. 147-156.

Oka, F., Yashima, A., Adachi, T. and Aifantis, E.C. (1992), Instability of gradient dependent viscoplastic model for clay saturated with water and FEM analysis, *Applied Mechanics Reviews*, **45**, 3, pp. 140-148.

Oka, F., Adachi, T. and Yashima, A. (1994), Instability of an elasto-viscoplastic constitutive model for clay and strain localization, *Mechanics of Materials*, **18**, pp. 119-129.

Oka, F., Adachi, T. and Yashima, A. (1995), A strain localization analysis of clay using a strain softening viscoplastic model, *Int. J. Plasticity*, **11**, 5, pp. 523-545.

Oka, F., Yashima, A., Sawada, K. and Aifantis, E.C. (2000a), Instability of gradient-dependent elastoviscoplastic model for clay and strain localization, *Computer Methods in Applied Mechanics and Engineering*, **183**, pp. 67-86.

Oka, F., Higo, Y. and Jiang, M. (2000b), Effects of material inhomogeneity and transport of pore water on strain localization analysis of fluid-saturated strain gradient viscoplastic geomaterial, *Proc. 8th Int. Symp. on Plasticity and Current Applications*, Whistler, A.S. Khan, H. Zhang and Y. Yuan eds., Neat Press, pp. 306-308.

Rice, J. (1975), On the stability of dilatant hardening for saturated rock masses, *J. Geophysical Research*, **80**, 11, pp. 1531-1536.

Rice, J. (1976), The localization of plastic deformation, *Proc. 14th Int. Congress on Theoretical and Applied Mechanics*, North-Holland, Koiter, W.T. ed., pp. 207-220.

Rudnicki, J.W. and Rice, J.R. (1975), Condition for the localization of deformation in pressure-sensitive dilatant material, *J. Mechanics and Physics of Solids*, **23**, pp. 371-394.

Schrefler, B.A., Sanavia, L. and Majorana, C.E. (1996), A multiphase medium model for localisation and postlocalisation simulation in geomaterials, *Mechanics of Cohesive-Frictional Materials*, **1**, 1, pp. 95-114.

Simo, J.C. and Hughes, T.J.R. (1997), *Computational Inelasticity*, Springer-Verlag.

Vardoulakis, I. and Aifantis, E.C. (1991), A gradient flow theory of plasticity for granular materials, *Acta Mechanica* **87**, pp. 197-217.

Yatomi, C., Yashima, A., Iizuka, A. and Sano, I. (1989), General theory of shear bands formation by a non-coaxial Cam-clay model, *Soils and Foundations*, **29**, 3, pp. 41-53.

Yoshida, T., Tatsuoka, F., Siddiquee, M.S.A., Kamegai, Y. and Park, C.-S. (1994), Shear banding in sands observed in plane strain compression, *Proc. 3rd Int. Workshop on Localization and Bifurcation Theory for Soils and Rocks*, Grenoble, Chambon, R., Desrues, J. and Vardoulakis, I. eds., Balkema, pp. 165-179.

Zbib, M.H. and Aifantis, E.C. (1989), A gradient-dependent flow theory of plasticity: application to metal and soil instability, *Applied Mechanics Reviews*, **42**, pp. 295-304.

Zhang, H.W. and Schrefler, B.A. (2000), Gradient-dependent plasticity model and dynamic strain localization analysis of saturated and partially saturated porous media: one dimensional model, *European Journal of Mechanics A/Solids*, **19**, 3, pp. 503-524.

Chapter 2

Gradient-dependent Elasto-viscoplastic Constitutive Model for Normally Consolidated Clay

2.1 Introduction

It is generally known that clay shows such time-dependent behavior as strain rate sensitivity, creep, stress relaxation, and secondary compression. Taking into account these characteristics, Adachi and Oka (1982) proposed an elasto-viscoplastic model for water-saturated normally consolidated clay based on a Perzyna type of viscoplasticity theory (Perzyna 1963) and the Cam-clay model. In addition, Adachi et al. (1987, 1990) introduced a second material function into the viscoplastic flow rule in order to describe material instability such as acceleration creep and strain softening. In this chapter, an elasto-viscoplastic constitutive model for normally consolidated clay with a second material function proposed by Adachi and Oka (1982) and Adachi et al. (1987, 1990) is demonstrated.

In the present study, we introduce a second order gradient of viscoplastic volumetric strain into the present model. It has been shown that the strain gradient-dependent model has advantages, such as its ability to predict the thickness of shear band, to retrieve the ill-posedness of boundary value problems, to consider the microstructure by the introduction of a characteristic length scale and the scale effects of deformation, etc. (e.g., Mühlhaus and Vardoulakis 1987; Zbib and Aifantis 1989; Mühlhaus and Oka 1996; and Fleck and Hutchinson 1997). Gradient-dependent models with higher order strain gradients have been proposed and used in post-failure and/or strain localization analyses (e.g., Oka 1995 and Aifantis et al. 1999). Even now, however, the meaning of gradient parameters and the influence of strain gradients on shear band problems are still need to be determined. In order to investigate these problems in this section, we introduce a second order strain gradient into the elasto-viscoplastic model.

2.2 Elastic Strain Rate

In the following, Terzaghi's effective stress concept is used for water-saturated soil because the compressibility of the pore water is effectively small, i.e.,

$$\sigma_{ij} = \sigma'_{ij} + u_w \delta_{ij} \tag{2.1}$$

where σ_{ij} is the total stress tensor, σ'_{ij} is the effective stress tensor, u_w is the pore water pressure, and δ_{ij} is Kronecker's delta.

Furthermore, an additive decomposition of total strain rate tensor $\dot{\varepsilon}_{ij}$ into elastic strain rate tensor $\dot{\varepsilon}^e_{ij}$ and viscoplastic strain rate tensor $\dot{\varepsilon}^{vp}_{ij}$ is assumed such that

$$\dot{\varepsilon}_{ij} = \dot{\varepsilon}^e_{ij} + \dot{\varepsilon}^{vp}_{ij}. \tag{2.2}$$

Elastic strain rate tensor $\dot{\varepsilon}^e_{ij}$ is given by a generalized Hooke type of law, namely,

$$\dot{\varepsilon}^e_{ij} = \frac{1}{2G}\dot{S}_{ij} + \frac{\kappa}{3(1+e)\sigma'_m}\dot{\sigma}'_m \delta_{ij} \tag{2.3}$$

where S_{ij} is the deviatoric stress rate tensor, σ'_m is the mean effective stress, G is the elastic shear modulus, e is the void ratio, κ is the swelling index, and the superimposed dot denotes the time differentiation. Swelling index κ is determined by the slope of the volumetric loading-unloading curve in a natural logarithmic scale.

Elastic shear modulus G is assumed to be proportional to the square root of σ'_m as

$$G = G_0 \sqrt{\frac{\sigma'_m}{\sigma'_{m0}}} \tag{2.4}$$

where G_0 is the initial value of G.

2.3 Overstress Type of Viscoplastic Flow Rule

Adachi and Oka (1982) noted that clay never reaches its static equilibrium state at the end of the primary consolidation even in cases of isotropic consolidation. This means that the natural ground will continue to subside by its own weight at very small strain rates. Thus, the static equilibrium state is defined as a state at which the deviatoric strain rate and the volumetric strain rate become zero. According to this definition, any deformation process with a definite strain rate is regarded as a dynamic state.

Perzyna (1963) indicated that the difference between the behavior of clay in the static state and that in the dynamic state occurs from the material strain rate sensitivity; he defined this behavior as viscoplasticity. Then, he proposed viscoplastic strain rate tensor $\dot{\varepsilon}^{vp}_{ij}$ which can describe the rate dependent behavior based on the associated flow rule, as follows:

$$\dot{\varepsilon}^{vp}_{ij} = \gamma \langle \Phi_1(F) \rangle \frac{\partial f}{\partial \sigma'_{ij}} \tag{2.5}$$

$$F = \frac{f(\sigma_{ij}, \varepsilon^{vp}_{ij}) - \kappa_s}{\kappa_s} \tag{2.6}$$

where γ is a viscoplastic parameter, f is the dynamic yield function, and κ_s is the work-hardening parameter of the static yield function.

Φ_1 is a function showing strain rate sensitivity; it is determined by the experimental results. $\langle\ \rangle$ is a Macauley's bracket as defined by the following relations:

$$\langle \Phi_1(F) \rangle = \begin{cases} 0 & (F \leq 0) \\ \Phi_1(F) & (F > 0) \end{cases} \tag{2.7}$$

In **Equation** (2.7), $F = 0$ represents the static yield function. From **Equations** (2.5) and (2.6), the following relations can be obtained:

$$f(\sigma_{ij}, \varepsilon_{ij}^{vp}) - \kappa_s = \kappa_s \Phi_1^{-1}(I_2^{vp} \left(\frac{\partial f}{\partial \sigma'_{kl}} \frac{\partial f}{\partial \sigma'_{kl}} \right)^{-\frac{1}{2}}) \tag{2.8}$$

where $\Phi_1^{-1}(*)$ is an inverse function of $\Phi_1(*)$, and $I_2^{vp} = \sqrt{\dot{\varepsilon}_{ij}^{vp} \dot{\varepsilon}_{ij}^{vp}}$ is the second invariant of the viscoplastic strain rate tensor.

Equation (2.8) shows that the dynamic yield function is dependent on work-hardening parameter κ_s and the second invariant of viscoplastic strain rate tensor I_2^{vp}. Then, we denote dynamic yield function f as f_d. The dynamic yield function loses its rate sensitivity only when $F = 0$ (or $f = \kappa_s$). At this state, f will be denoted by f_s. Furthermore, based on the critical state theory proposed by Roscoe et al. (1963), static yield function f_s and dynamic yield function f_d are assumed to be as follows:

$$f_s = \bar{\eta}^{*(s)} + M_f^* \ln \frac{\sigma_m^{\prime(s)}}{\sigma'_{m0}} = \kappa_s \tag{2.9}$$

$$f_d = \bar{\eta}^{*(d)} + M_f^* \ln \frac{\sigma_m^{\prime(d)}}{\sigma'_{m0}} = \kappa_d \tag{2.10}$$

Superscript (s) indicates the static state, while (d) indicates the dynamic state. σ'_m is the mean effective stress and σ'_{m0} is the unit mean effective stress. In **Equations** (2.9) and (2.10), $\bar{\eta}^*$ is a relative stress ratio (Sekiguchi & Ohta 1977), which represents the stress ratio of anisotropic consolidated clay, namely,

$$\bar{\eta}^* = \left\{ \left(\eta_{ij}^* - \eta_{ij(0)}^* \right) \left(\eta_{ij}^* - \eta_{ij(0)}^* \right) \right\}^{\frac{1}{2}} \quad , \quad \eta_{ij}^* = \frac{S_{ij}}{\sigma'_m} \quad , \quad \eta_{ij(0)}^* = \frac{S_{ij(0)}}{\sigma'_{m(0)}} \tag{2.11}$$

in which η_{ij}^* is the stress ratio tensor, M_f^* is the value of $\eta^* = \sqrt{\eta_{ij}^* \eta_{ij}^*}$ at failure, and subscript $_{(0)}$ denotes the values of the parameters at the end of the primary consolidation.

κ_s and κ_d are the strain-hardening parameters and are defined respectively as

$$\kappa_s = \ln \frac{\sigma_{my}^{\prime(s)}}{\sigma'_{m0}} \tag{2.12}$$

$$\kappa_d = \ln \frac{\sigma_{my}^{\prime(d)}}{\sigma'_{m0}} \tag{2.13}$$

$\sigma'^{(s)}_{my}$ and $\sigma'^{(d)}_{my}$ are the hardening parameters, and hardening parameter $\sigma'^{(s)}_{my}$ is related to the incremental of inelastic volumetric strain dv^p through the following equation:

$$dv^p = \frac{\lambda - \kappa}{1+e} \cdot \frac{d\sigma'^{(s)}_{my}}{\sigma'^{(s)}_{my}} \tag{2.14}$$

where compression index λ is determined by the slope of the volumetric loading curve in a natural logarithmic scale. Integrating the previous equation under the initial conditions of $\sigma'^{(s)}_{my} = \sigma'^{(s)}_{myi}$ and $v^p = v^p_i$, we obtain

$$v^p - v^p_i = \frac{\lambda - \kappa}{1+e} \ln \frac{\sigma'^{(s)}_{my}}{\sigma'^{(s)}_{myi}} \tag{2.15}$$

in which, v^p_i indicates the initial value of the plastic volumetric strain and $\sigma'^{(s)}_{myi}$ indicates the initial value of the strain-hardening parameter. **Figure 2.1** shows the strain-hardening rule defined by **Equation** (2.14). Line-I is the infinite time consolidation line, and the hardening parameter will change with increases in the plastic volumetric strain according to this line.

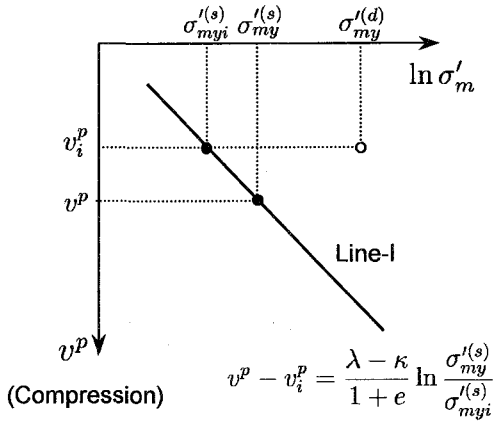

Figure 2.1 Relationship between the static-hardening parameter and viscoplastic volumetric strain

The form of function $\Phi_1(F)$ in **Equation** (2.5) is exponential in which the hardening parameters of the dynamic state and the static state are used based on experimental data from strain-rate constant triaxial tests (Adachi and Okano 1974), that is,

$$\gamma\Phi_1(F) = C_o M^*_f \sigma'_m \exp\left[m'\left(\ln\frac{\sigma'^{(d)}_{my}}{\sigma'_{m0}} - \ln\frac{\sigma'^{(s)}_{my}}{\sigma'_{m0}}\right)\right] \tag{2.16}$$

where C_o and m' are parameters of the time dependent behavior of clay and can be obtained from laboratory test results. For simplicity, superscript $^{(d)}$ will be disregarded in the following.

When v^p is defined as the increment in initial value v^p_i, **Equation** (2.15) will lead to

$$\ln\frac{\sigma'^{(s)}_{my}}{\sigma'_{m0}} = \ln\frac{\sigma'^{(s)}_{myi}}{\sigma'_{m0}} + \frac{1+e}{\lambda-\kappa}v^p \tag{2.17}$$

Substituting the dynamic yield function in **Equation** (2.10) and the static yield function **Equation** (2.17) into **Equation** (2.16) will yield

$$\gamma\Phi_1(F) = C_o M_f^* \sigma'_m \exp\left[m'\left(\frac{\bar{\eta}^*}{M_f^*} + \ln\frac{\sigma'_m}{\sigma'^{(s)}_{myi}} - \frac{1+e}{\lambda-\kappa}v^p\right)\right] \tag{2.18}$$

It is found that this function can be determined only if the value for $\sigma'^{(s)}_{myi}$ is given. However, it is practically impossible to determine this value since it takes an infinite amount of time to obtain Line-I. Therefore, **Equation** (2.18) yields the following:

$$\begin{aligned}
\gamma\Phi_1(F) &= C_o M_f^* \sigma'_m \exp\left[m'\left(\frac{\bar{\eta}^*}{M_f^*} + \ln\frac{\sigma'_m}{\sigma'_{me}} - \ln\frac{\sigma'^{(s)}_{myi}}{\sigma'_{me}} - \frac{1+e}{\lambda-\kappa}v^p\right)\right] \\
&= C_o M_f^* \sigma'_m \exp\left(-m'\ln\frac{\sigma'^{(s)}_{myi}}{\sigma'_{me}}\right)\exp\left[m'\left(\frac{\bar{\eta}^*}{M_f^*} + \ln\frac{\sigma'_m}{\sigma'_{me}} - \frac{1+e}{\lambda-\kappa}v^p\right)\right] \\
&= C M_f^* \sigma'_m \exp\left[m'\left(\frac{\bar{\eta}^*}{M_f^*} + \ln\frac{\sigma'_m}{\sigma'_{me}} - \frac{1+e}{\lambda-\kappa}v^p\right)\right]
\end{aligned} \tag{2.19}$$

$$C = C_o \exp\left(-m'\ln\frac{\sigma'^{(s)}_{myi}}{\sigma'_{me}}\right) \tag{2.20}$$

where σ'_{me} is the initial consolidation stress.

By defining parameter C, as shown in **Equation** (2.20), parameter C can be determined from laboratory tests; it is no longer necessary to acquire the initial value for hardening parameter $\sigma'^{(s)}_{myi}$.

2.4 Second Material Function

Granular materials, including clay, exhibit material instability due to microstructural changes such as creep failure and strain softening. However, this behavior cannot be expressed by the Perzyna type of constitutive model as has been previously pointed out (Adachi et al. 1987, 1990).

Overstress F is given by the following one-dimensional form:

$$F = \sigma - f(\varepsilon^{vp}) \tag{2.21}$$

Viscoplastic strain rate $\dot{\varepsilon}^{vp}$ can be obtained from the following equation as

$$\dot{\varepsilon}^{vp} = g(F) \tag{2.22}$$

By differentiating the viscoplastic strain rate with respect to time, the rate of viscoplastic strain rate with time will become

$$\dot{\varepsilon}^{vp} = \frac{\partial g}{\partial F}\frac{\partial F}{\partial t} \tag{2.23}$$

In cases where function g is monotonically increasing function corresponding to F, $\partial g/\partial F$ will always be positive. When considering viscoplastic strain hardening, therefore, the differential of f with respect to ε^{vp} will become

$$\frac{\partial f}{\partial \varepsilon^{vp}} \geq 0 \tag{2.24}$$

As a result, since stress σ will be constant during the creep process, this will yield

$$\frac{\partial F}{\partial t} = -\frac{\partial f}{\partial \varepsilon^{vp}} \dot{\varepsilon}^{vp} \leq 0 \tag{2.25}$$

which will lead to,

$$\dot{\varepsilon}^{vp} \leq 0 \tag{2.26}$$

This means that, during the creep process, the viscoplastic strain rate will monotonically decrease and the accelerating creep behavior cannot be represented. On the contrary, when considering viscoplastic strain softening, the differentiation will become

$$\frac{\partial f}{\partial \varepsilon^{vp}} < 0 \tag{2.27}$$

in which $\dot{\varepsilon}^{vp} > 0$ and the accelerating creep behavior can be represented. Since the Perzyna type of constitutive equation is a strain-hardening type of model, the model itself is not able to represent the softening behavior. This means that the model cannot give the accelerating creep behavior. As such, Adachi et al. (1987) extended and improved the model by introducing a second material function into the model. The flow rule for the viscoplastic strain rate tensor with a second material function, Φ_2, can be given by

$$\dot{\varepsilon}_{ij}^{vp} = \gamma \left\langle \Phi_1 \left(F \right) \right\rangle \Phi_2(\xi) \frac{\partial f}{\partial \sigma'_{ij}} \tag{2.28}$$

ξ is an internal state variable which controls the failure of the material structure, and the second material function was introduced to describe the failure state. At the critical state, it is known experimentally that the material does not show strain rate sensitivity behavior. This means that the failure conditions do not depend on the strain rate. The second material function was defined in consideration of such a point. The second material function is assumed to satisfy the following conditions.

- When ξ become infinity, Φ_2 will also become infinity
- ξ is positive

Similar to **Equation** (2.8), the dynamic yield function is defined as follows.

$$f(\sigma_{ij}, \varepsilon_{ij}^{vp}) - \kappa_s = \kappa_s \Phi_1^{-1} \left(\frac{I_2^{vp}}{\gamma \Phi_2(\xi)} \left(\frac{\partial f}{\partial \sigma'_{kl}} \frac{\partial f}{\partial \sigma'_{kl}} \right)^{-\frac{1}{2}} \right) \tag{2.29}$$

If Φ_2 become infinity, **Equation** (2.29) will become

$$f(\sigma_{ij}, \varepsilon_{ij}^{vp}) = \kappa_s \tag{2.30}$$

Herein, the term I_2^{vp} will disappear and the rate dependency of the yield function will vanish.

To express the accelerating creep behavior, the internal variable and the second material function are assumed as the following evolutional equations. For the isotropically consolidated clay, Φ_2 is given by

$$\dot{\xi} = \frac{M_f^{*2}}{G_2^*(M_f^* - \eta^*)}\dot{\eta}^* \quad , \quad \eta^* = \frac{\sqrt{2J_2}}{\sigma'_m} \tag{2.31}$$

in which $t = 0$, $\xi(0) = 0$, and $\eta^*(0) = 0$ at the initial state, and G_2^* is a softening parameter.

$$\Phi_2(\xi) = 1 + \xi \tag{2.32}$$

The second material function will increase as the critical state is approached. Until the state approaches failure, therefore, the material behavior can be expressed by $\Phi_1(F)$ which has already been described.

Under anisotropic consolidation conditions, by employing $\bar{\eta}^*$, where $\bar{\eta}^*$ is the relative stress ratio given by **Equation** (2.31), the integrated form of the evolutional equation of the internal state variable ξ is extended as

$$\xi = \frac{M_f^*\bar{\eta}^*}{G_2^*\left\{M_f^* - \dfrac{\eta_{mn}^*(\eta_{mn}^* - \eta_{mn(0)}^*)}{\bar{\eta}^*}\right\}} \tag{2.33}$$

Since $\partial f/\partial\sigma'_{ij}$ is calculated as

$$\frac{\partial f}{\partial \sigma'_{ij}} = \frac{1}{M_f^*\sigma'_m}\left[\frac{\eta_{ij}^* - \eta_{ij(0)}^*}{\bar{\eta}^*} + \left\{M_f^* - \frac{\eta_{kl}^*\left(\eta_{kl}^* - \eta_{kl(0)}^*\right)}{\bar{\eta}^*}\right\}\frac{1}{3}\delta_{ij}\right] \tag{2.34}$$

The derived constitutive model can express both strain rate dependency and accelerating creep behavior. Using **Equations** (2.28) and (2.34), deviatoric viscoplastic strain rate $\dot{e}_{ij}^{vp}$ and volumetric viscoplastic strain rate $\dot{\varepsilon}_{kk}^{vp}$ can be expressed as follows:

$$\dot{e}_{ij}^{vp} = C\exp\left[m'\left(\frac{\bar{\eta}^*}{M_f^*} + \ln\frac{\sigma'_m}{\sigma'_{me}} - \frac{1+e}{\lambda-\kappa}v^p\right)\right]\Phi_2(\xi)\frac{\left(\eta_{ij}^* - \eta_{ij(0)}^*\right)}{\bar{\eta}^*} \tag{2.35}$$

$$\dot{\varepsilon}_{kk}^{vp} = C\exp\left[m'\left(\frac{\bar{\eta}^*}{M_f^*} + \ln\frac{\sigma'_m}{\sigma'_{me}} - \frac{1+e}{\lambda-\kappa}v^p\right)\right]\Phi_2(\xi)\left\{M_f^* - \frac{\eta_{kl}^*\left(\eta_{kl}^* - \eta_{kl(0)}^*\right)}{\bar{\eta}^*}\right\} \tag{2.36}$$

2.5 Strain Gradient-dependent Elasto-viscoplastic Constitutive Model for Clay

It has been experimentally found that the shear strength and the deformation characteristics of clay depend on the volumetric strain. The volumetric plastic strain is used as a hardening parameter in the well-known Cam-clay model. The volumetric inelastic strain associated with

both consolidation and dilatancy is a measure of the deterioration of granular materials. On the other hand, Oka (1995), Mühlhaus and Oka (1995), Mühlhaus and Oka (1996), Oka et al. (1998) demonstrated that the higher order gradients may be attributed to the fact that the soil is discrete. Frantziskonis (1993) also showed that material inhomogeneity can be described by a constitutive model with higher order strain gradients. Thus, in the present paper, we have introduced the second order gradient of the volumetric viscoplastic strain into the constitutive model to describe more accurately and sufficiently the deformation of clay by considering the non-local and the viscoplastic effects of the material (Oka et al. 1992). In particular, the yield function, shown in **Equation** (2.10), includes the Laplacian of the viscoplastic volumetric strain and is proposed as follows:

$$f = \frac{\bar{\eta}^*}{M_f^*} + \ln \frac{\sigma'_m}{\sigma'_{my}} - a_3 \nabla^2 \varepsilon_v^{vp} = 0 \tag{2.37}$$

where f is dynamic yield function, σ'_{my} is the hardening parameter, ε_v^{vp} is the viscoplastic volumetric strain ($=\int \dot{\varepsilon}_{kk}^{vp} dt$), $a_3 \nabla^2 \varepsilon_v^{vp}$ is the gradient term with a_3 defined as a material constant, $\bar{\eta}^*$ is the relative stress ratio defined by **Equation** (2.11), M_f^* is the strain ratio invariant at failure, and σ'_m is the mean effective stress.

Using the strain gradient-dependent yield function, material function Φ_1 by which rate sensitivity is taken into account is given in the same manner as that in **Equation** (2.18), in other words,

$$\gamma \Phi_1(F) = C M_f^* \sigma'_m \exp\left[m' \left(\frac{\bar{\eta}^*}{M_f^*} + \ln \frac{\sigma'_m}{\sigma'_{me}} - \frac{1+e}{\lambda - \kappa} \varepsilon^{vp} - a_3 \nabla^2 \varepsilon_v^{vp} \right) \right] \tag{2.38}$$

$$C = C_o \exp\left(-m' \ln \frac{\sigma'^{(s)}_{myi}}{\sigma'_{me}} \right) \tag{2.39}$$

in which m' and C are viscoplastic parameters and gradient coefficient a_3 is assumed to be constant. σ'_{me} is the initial value of σ'_m, $\sigma'^{(s)}_{myi}$ is the initial value of the hardening parameter, λ is the consolidation index, κ is the swelling index, and e is the void ratio.

The viscoplastic flow rule, the second material function, and the elastic strain rates are given by **Equations** (2.28), (2.32) and (2.33), and (2.3), respectively.

2.6 Summary

In this chapter, we reviewed an elasto-viscoplastic model for normally consolidated clay, based on a Perzyna type of viscoplasticity and a Cam-clay type of yield function. This model can express rate sensitivity and such material instability as creep failure. In addition, we introduced a higher order strain gradient into the model for normally consolidated clay in order to investigate the effects of strain gradients on material instability and strain localization in next chapter.

References

Adachi, T. and Oka, F. (1982), Constitutive equations for normally consolidated clay based on elasto-viscoplasticity, *Soils and Foundations*, **22**, 4, pp. 57-70.

Adachi, T. and Okano, M. (1974), A constitutive equation for normally consolidated clay, *Soils and Foundations*, **14**, 4, pp. 55-73.

Adachi, T., Oka, F. and Mimura, M. (1987), An elasto-viscoplastic theory for clay failure, *Proc. 8th Asian Regional Conference on Soil Mechanics and Foundation Engineering*, Kyoto, JSSMFE, **1**, pp. 5-8.

Adachi, T., Oka, F. and Mimura, M. (1990), Elasto-viscoplastic constitutive equations and their application to consolidation analysis, *J. of Engineering Materials and Technology*, ASME, **112**, pp. 202-209.

Aifantis, E.C., Oka, F., Yashima, A. and Adachi, T. (1999), Instability of gradient dependent elasto-viscoplasticity for clay, *Int. J. Numerical and Analytical Methods in Geomechanics*, **23**, 10, pp. 973-994.

Fleck, A.N. and Hutchinson, J.W. (1997), Strain gradient plasticity, *Advances in Applied Mechanics*, Hutchinson, J.W., and Wu, T.Y. eds., Academic Press, **33**, pp. 296-361.

Frantziskonis, G. (1993), Crack pattern related universal constants, *Probabilities and Materials*, Tests, Models and Applications, Breysse, D. ed., Kulwer Academic Pub., pp. 361-376.

Mühlhaus, H.-B. and Oka, F. (1995), A continuum theory for random packings of elastic spheres, *Fracture of Brittle and Disordered Materials*, Proc. IUTAM Symp. on Fracture of Brittle and Disordered Materials, Concrete, Rocks and Ceramics, Brisbane, Australia, Baker, G. and Karihaloo, B.L., eds., E & FN Spon pp. 285-298.

Mühlhaus, H.-B. and Oka, F. (1996), Dispersion and wave propagation in discrete and continuous models for granular materials, *Int. J. Solids and Structures*, **33**, 19, pp. 2841-2858.

Mühlhaus, H.-B. and Vardoulakis, I. (1987), The thickness of shear bands in granular materials, *Géotechnique*, **37**, pp. 271-283.

Oka, F., Yashima, A., Adachi, T. and Aifantis, E.C. (1992), Instability of gradient dependent viscoplastic model for clay saturated with water and FEM analysis, *Applied Mechanics Reviews*, **45**, 3, pp. 140-148.

Oka, F. (1995), A gradient-dependent elastic model for granular materials and strain localization, *Continuum Models for Materials with Microstructure*, Mühlhaus, H.-B. ed., John Wiley & Sons, pp. 145-158.

Oka, F., Mühlhaus, H.B., Yashima, A. and Sawada, K. (1998), Quasi-static and dynamic characteristics of strain gradient dependent non-local constitutive models, *Material Instabilities in Solids*, de Bost, R. and Van der Giessen, E. eds., John Wiley & Sons, pp. 387-404.

Perzyna, P. (1963), The constitutive equations for work-hardening and rate sensitive plastic materials, *Proc. Vibrational Problems*, Warsaw, **4**, 3, pp. 281-290.

Roscoe, K.H, Schofield, A.N. and Thurairajah, A. (1963), Yielding of clays in states wetter than critical, *Géotechnique*, **13**, 3, pp. 211-240.

Sekiguchi, H. and Ohta, H. (1977), Induced anisotropy and time dependency in clays, *Proc. Speciality Session 9*, 9th ICSMFE, Tokyo, pp. 229-238.

Zbib, M.H. and Aifantis, E.C. (1989), A gradient-dependent flow theory of plasticity: application to metal and soil instability, *Applied Mechanics Reviews*, **42**, pp. 295-304.

Chapter 3

Instability and Strain Localization Analysis for Fluid-saturated Gradient-dependent Viscoplastic Geomaterials

3.1 Introduction

The effects of pore fluid on the localization problem have been analyzed by several researchers in the context of a two-phase mixture theory, such as Biot's theory (1956). Loret and Prévost (1991), Schrefler et al. (1995, 1996), and Ehlers and Volk (1998) numerically studied the localization problem of water-saturated geomaterials with the rate independent constitutive model. Oka et al. (1994) have been dealing with the localization problem of water-saturated clay through the use of viscoplastic constitutive equations because of the rate-dependent nature of cohesive soil. Zhang and Schrefler (2000) investigated the interaction between permeability and gradient-dependent parameters with a one-dimensional instability analysis and a numerical simulation in the context of dynamic strain localization of saturated and partially saturated porous media. As for the experimental study, Finno et al. (1998) discussed the effects of drained conditions on the strain localization in sand specimens.

In these studies, many points have been clarified such as the effect of dilatancy, permeability, strain rates etc., for particular constitutive models. Loret and Prévost (1991) and Schrefler et al. (1995) showed that strain localizes in a narrow zone in the case of higher permeability levels. On the other hand, Oka et al. (1995) reported different results in which deformation was more localized in the case of low permeability levels. Several problems remain which need to be studied. One of them is to clarify the roles of permeability and drainage conditions in the instability of the governing equations and the deformation patterning of non-local viscoplastic materials, such as the higher order strain gradient-dependent model. The other problem is to clarify the effects of the initial heterogeneity.

Before conducting the numerical analysis of a water-saturated viscoplastic material, the effects of permeability and the strain gradient term on the growth rate of the fluctuation were examined via the linear instability analysis. In the numerical analysis, the deformation behavior of clay specimens, modeled as a viscoplastic model with a second order strain gradient during shear, is analyzed by a soil-water coupled finite element method under both globally undrained and drained conditions. It was found that the strain localization pattern and the stress-strain curve greatly depend on the permeability and the initial non-homogeneous properties. In addition, the effects of the second order gradient on the consolidation problem were numerically studied.

3.2 Instability Analysis of a Fluid-saturated Viscoplastic Material by a Simplified Model

Loret and Prévost (1991) and Schrefler et al. (1995) studied the effects of permeability on the strain localization analysis. Loret and Prévost (1991) stated that in the case of low permeability levels, the instability may develop more slowly than in the case of high permeability levels. On the other hand, according to the numerical results by Oka et al. (1995), strain may easily localize in the case of a lower permeability coefficient. There seems to be a discrepancy between the two cases. It is worth noting that the model used by Loret and Prévost (1991) is a dilatant elasto-plastic material with softening in the context of a small strain dynamic analysis, while Oka et al. (1995) used an elasto-viscoplastic model with negative dilatancy in the quasi-static large strain analysis. It is likely that the different conclusions come from the different trends of dilatancy. Hence, the question of how permeability affects the strain localization remains unanswered. In order to more clearly discuss the effects of permeability on strain localization, an instability analysis was carried out under two-dimensional conditions in the context of a small strain theory for simplicity. An instability analysis has been conducted by Oka et al. (2001) in which a simplified linear rigid-viscoplastic model was used. In the present study, we used both a simplified linear elasto-viscoplastic model and a simplified linear rigid-viscoplastic model.

3.2.1 Perturbed Governing Equations

Constitutive Equations

A simplified elasto-viscoplastic model is used in this analysis. Strain rate tensor $\dot{\varepsilon}_{ij}$ is broken down into elastic strain rate tensor $\dot{\varepsilon}^e_{ij}$ and viscoplastic strain rate tensor $\dot{\varepsilon}^{vp}_{ij}$, namely,

$$\dot{\varepsilon}_{ij} = \dot{\varepsilon}^e_{ij} + \dot{\varepsilon}^{vp}_{ij} \tag{3.1}$$

The elastic strain rate is given based on the linear elasticity theory as

$$\dot{\sigma}'_{ij} = 2G\dot{\varepsilon}^e_{ij} + \frac{1}{2}\left(3K - 2G\right)\dot{\varepsilon}^e_{kk}\delta_{ij} \tag{3.2}$$

or

$$\dot{\varepsilon}_{ij}^{e} = \frac{1}{2G}\dot{\sigma}'_{ij} + \frac{1}{2}\left(\frac{1}{3K} - \frac{1}{2G}\right)\dot{\sigma}'_{kk}\delta_{ij} \tag{3.3}$$

where σ'_{ij} is Terzaghi's effective stress tensor, K is the elastic bulk modulus, G is the elastic shear modulus, and δ_{ij} $(i = 1, 2,\ j = 1, 2)$ is Kronecker's delta.

A simplified viscoplastic constitutive model is given as

$$\sigma'_{ij} = 2\mu\dot{\varepsilon}_{ij}^{vp} + \frac{1}{2}\dot{\varepsilon}_{mm}^{vp}\mu'_k\delta_{ij} + 2G''\varepsilon_{ij} + \frac{1}{2}\varepsilon_{mm}K'\delta_{ij} \tag{3.4}$$

or

$$\dot{\varepsilon}_{ij}^{vp} = \frac{1}{2\mu}\left[\sigma'_{ij} - \frac{1}{2}\mu''_k\sigma'_{kk}\delta_{ij} - 2G''\varepsilon_{ij} - \frac{1}{2}K''\varepsilon_{kk}\delta_{ij}\right] \tag{3.5}$$

where

$$\mu''_k = \frac{\mu'_k}{2\mu + \mu'_k} \tag{3.6}$$

$$K'' = \frac{2(\mu K' - \mu'_k G'')}{2\mu + \mu'_k} \tag{3.7}$$

in which μ and μ'_k are parameters of the viscosity, G'' and K' are viscoplastic hardening parameters, and the accumulated strain is defined by

$$\varepsilon_{ij}^{vp} = \int \dot{\varepsilon}_{ij}^{vp} dt. \tag{3.8}$$

When we introduce a second order gradient of the viscoplastic volumetric strain, **Equations** (3.4) and (3.5) become

$$\sigma'_{ij} = 2\mu\dot{\varepsilon}_{ij}^{vp} + \frac{1}{2}\dot{\varepsilon}_{mm}^{vp}\mu'_k\delta_{ij} + 2G''\varepsilon_{ij}^{vp} + \frac{1}{2}\varepsilon_{mm}^{vp}K'\delta_{ij} - \frac{1}{2}a_3\varepsilon_{mm,nn}^{vp}\delta_{ij} \tag{3.9}$$

or

$$\dot{\varepsilon}_{ij}^{vp} = \frac{1}{2\mu}\left[\sigma'_{ij} - \frac{1}{2}\mu''_k\sigma'_{kk}\delta_{ij} - 2G''\varepsilon_{ij} - \frac{1}{2}K''\varepsilon_{kk}\delta_{ij} + \frac{1}{2}a'_3\varepsilon_{mm,nn}^{vp}\delta_{ij}\right] \tag{3.10}$$

$$a'_3 = \frac{2\mu}{2\mu + \mu'_k}a_3 \tag{3.11}$$

where a_3 is the gradient parameter.

Equations of Equilibrium

Let us consider the equilibrium equations, namely, undrained conditions in a perturbed configuration. The equilibrium equations can be written as follows

$$\sigma_{ij,j} = \sigma'_{ij,j} + u_{w,j}\delta_{ij} = 0 \tag{3.12}$$

where σ_{ij} is the total stress tensor, u_w is the pore water pressure and, as usual, the commas denote differentiation with respect to spatial coordinates.

Pore Fluid Flow

From the solid-fluid two-phase mixture theory, the governing equation of the pore fluid is given by

$$\dot{\varepsilon}_{mm} = -\frac{k}{\gamma_w}\nabla^2 u_w \tag{3.13}$$

where k is the permeability coefficient and γ_w is the unit weight of the pore water.

Perturbed Governing Equation

The perturbations of pore water pressure u_w and velocities v_i are assumed to be of the periodic form in two-dimensional form as

$$\begin{bmatrix} \tilde{u}_w \\ \tilde{v}_i \\ \tilde{\sigma}'_{ij} \end{bmatrix} = \begin{bmatrix} u_w^* \\ v_i^* \\ \sigma_{ij}'^* \end{bmatrix} \exp[iq(n_k x_k) + \omega t], \tag{3.14}$$

where the perturbed variable is indicated by tilde, q is the wave number ($= 2\pi/l$, l: wave length), ω is the speed of the fluctuation growth, n_i is the component of the unit vector $\boldsymbol{n}$, which is normal to the shear band, and superscript * indicates the amplitude of each variable.

$$\boldsymbol{n} = (-\sin\theta,\ \cos\theta) = (n_1,\ n_2) \tag{3.15}$$

The perturbed equilibrium equations are

$$\tilde{\sigma}_{ij,j} = \tilde{\sigma}'_{ij,j} + \tilde{u}_{w,j}\delta_{ij} = 0, \tag{3.16}$$

the perturbed continuity equation is

$$\tilde{\dot{\varepsilon}}_{mm} = -\frac{k}{\gamma_w}\nabla^2 \tilde{u}_w, \tag{3.17}$$

and the perturbed constitutive equations are given by **Equations** (2.2), (3.3), and (3.5) as

$$\begin{aligned} \tilde{\dot{\varepsilon}}_{ij} &= \tilde{\dot{\varepsilon}}^e_{ij} + \tilde{\dot{\varepsilon}}^{vp}_{ij} \\ &= \frac{1}{2G}\tilde{\sigma}'_{ij} + \frac{1}{2}\left(\frac{1}{3K} - \frac{1}{2G}\right)\tilde{\sigma}'_{kk}\delta_{ij} \\ &+ \frac{1}{2\mu}\left[\tilde{\sigma}'_{ij} - \frac{1}{2}\mu''_k\tilde{\sigma}'_{kk}\delta_{ij} - 2G''\tilde{\varepsilon}_{ij} - \frac{1}{2}K''\tilde{\varepsilon}_{kk}\delta_{ij}\right]. \end{aligned} \tag{3.18}$$

Using the following relations,

$$\tilde{\dot{\varepsilon}}_{ij} = \frac{1}{2}\left(\tilde{v}_{i,j} + \tilde{v}_{j,i}\right) \tag{3.19}$$

we can rewrite the equations of equilibrium and pore fluid flow and the constitutive equations in a matrix form as

$$[A]\{y\}^T = \{0\} \tag{3.20}$$

in which

$$[A] = \begin{bmatrix} n_1 & 0 & n_2 & n_1 & 0 & 0 \\ 0 & n_2 & n_1 & n_2 & 0 & 0 \\ 0 & 0 & 0 & A_{34} & n_1 & n_2 \\ A_{41} & A_{42} & 0 & A_{44} & A_{45} & 0 \\ A_{51} & A_{52} & 0 & A_{54} & 0 & A_{56} \\ 0 & 0 & A_{63} & 0 & A_{65} & A_{66} \end{bmatrix} \tag{3.21}$$

$$\{y\} = \{\sigma_{11}'^*, \quad \sigma_{22}'^*, \quad \sigma_{12}'^*, \quad u_w^*, \quad v_1^*, \quad v_2^*\} \tag{3.22}$$

$$A_{34} = \frac{k}{\gamma_w} iq \tag{3.23}$$

$$A_{41} = A_{52} = \frac{i}{q}\left\{\frac{\omega}{G} + \omega\left(\frac{1}{3K} - \frac{1}{2G}\right) + \frac{1}{\mu}\left(1 - \frac{\mu_k''}{2}\right)\right\} \tag{3.24}$$

$$A_{42} = A_{51} = \frac{i}{q}\left\{\omega\left(\frac{1}{3K} - \frac{1}{2G}\right) - \frac{1}{\mu}\frac{\mu_k''}{2}\right\} \tag{3.25}$$

$$A_{44} = A_{54} = -\frac{K'' kiq}{2\mu\gamma_w\omega} \tag{3.26}$$

$$A_{45} = 2n_1\left(1 + \frac{G''}{\mu\omega}\right) \tag{3.27}$$

$$A_{56} = 2n_2\left(1 + \frac{G''}{\mu\omega}\right) \tag{3.28}$$

$$A_{63} = \frac{i}{q}\left(\frac{\omega}{G} + \frac{1}{\mu}\right) \tag{3.29}$$

$$A_{65} = n_2\left(1 + \frac{G''}{\mu\omega}\right) \tag{3.30}$$

$$A_{66} = n_1\left(1 + \frac{G''}{\mu\omega}\right) \tag{3.31}$$

The eigenvalue is obtained from the condition $\det[A] = 0$ (see Appendix A).

$$\left(\omega + \frac{G''}{\mu}\right)\left(\omega^3 + \alpha_1\omega^2 + \alpha_2\omega + \alpha_3\right) = 0 \tag{3.32}$$

where

$$\alpha_1 = \frac{1}{2\gamma_w\mu(2\mu + \mu_k')}\left[2\gamma_w\left\{3K\mu + G(2\mu + \mu_k')\right\} + kq^2\mu(2G + 3K)(2\mu + \mu_k')\right] \tag{3.33}$$

$$\alpha_2 = \frac{1}{2\gamma_w\mu(2\mu + \mu_k')}\Big[6\gamma_w GK + kq^2\Big\{3K\mu(2G'' + K') + G\Big(4\mu(G'' + 3K) + \mu_k'(2G'' + 3K)\Big)\Big\}\Big] \tag{3.34}$$

$$\alpha_3 = \frac{3GKkq^2}{2\gamma_w\mu(2\mu + \mu_k')}(4G'' + K') \tag{3.35}$$

3.2.2 Instability of the Material System

In the following, we discuss the instability of the material system. If the growth rate of perturbation ω, which is the root of **Equation** (3.32), is positive, the material system is stable. On the other hand, if ω is negative, the material system is unstable. In order to investigate whether ω is negative or positive, we adopt the Routh-Hurwitz criteria. The roots of **Equation** (3.32) have negative real parts when the coefficients of the characteristic polynomial satisfy

$$\alpha_1 > 0, \quad \alpha_2 > 0, \quad \alpha_3 > 0, \quad \alpha_1\alpha_2 - \alpha_3 > 0 \tag{3.36}$$

in which

$$\begin{aligned}\alpha_1\alpha_2 - \alpha_3 = \frac{1}{4\gamma_w^2\mu^2(2\mu+\mu_k')}\Big[&12\gamma_w^2 GK\Big\{3K\mu + G(2\mu+\mu_k')\Big\} \\ &+2\gamma_w kq^2\Big\{9K^2\mu^2(2G''+K') + 18GK^2\mu(3\mu+\mu_k') \\ &+G^2(2\mu+\mu_k')\Big(2\mu(2G''+9K)+\mu_k'(2G''+3K)\Big)\Big\} \\ &+k^2q^4(2G+3K)\mu(2\mu+\mu_k')\Big\{3(2G''+K')K\mu \\ &+G\Big(4\mu(G''+3K)+\mu_k'(2G''+3K)\Big)\Big\}\Big]\end{aligned} \tag{3.37}$$

Since elastic moduli G and K and the parameters of viscosity μ and μ_k' are positive, $\alpha_1 > 0$ is always satisfied. The other conditions, $\alpha_2 > 0$, $\alpha_3 > 0$, and $\alpha_1\alpha_2 - \alpha_3 > 0$, depend on viscoplastic hardening parameter G''.

Elasto-viscoplastic Model without a Gradient Term

Firstly, let us consider the model without a strain gradient term. In the case of $G'' > 0$, i.e., viscoplastic hardening, $\alpha_2 > 0$, $\alpha_3 > 0$, and $\alpha_1\alpha_2 - \alpha_3 > 0$ are satisfied, so that the material system is stable.

In the case of $G'' < 0$, i.e., viscoplastic softening, it is possible that α_2, α_3, and $\alpha_1\alpha_2 - \alpha_3$ are negative. Thus, the system can become unstable. In this case, when k is relatively larger, α_2, α_3, and $\alpha_1\alpha_2 - \alpha_3$ become negative more easily, namely, the possibility of instability is higher. On the other hand, when k is relatively smaller, it can be said that the material system is less unstable.

From the above results of the instability analysis using an elasto-viscoplastic model, it is seen that the material system is stable in the strain-hardening range, while the material system becomes unstable in the strain-softening regime. In addition, a material system with high permeability levels becomes more unstable compared with a material system with lower values of permeability.

Gradient-dependent Elasto-viscoplastic Model

Next, we will discuss the effects of the strain gradient on instability. The introduction of a second order strain gradient into the model (**Equation** (3.10)) transforms viscoplastic hardening

modulus K', namely,

$$K' \rightarrow (K' + a_3 q^2) \tag{3.38}$$

since μ, μ'_k, and K' are positive, K' increases if gradient parameter a_3 is positive. If a_3 is large enough, α_2, α_3, and $\alpha_1\alpha_2 - \alpha_3$ can become positive, even though $G'' < 0$. Hence, the strain gradient can make the material system less unstable or more stable even in the regime of viscoplastic softening.

Rigid-viscoplastic Model without a Gradient Term

To study the instability of the material system more simply, we assume a rigid-viscoplastic constitutive model that is achieved by

$$G \rightarrow \infty, \quad K \rightarrow \infty \tag{3.39}$$

This assumption and $\det[A] = 0$ yield (see Appendix A)

$$\omega = \frac{-(4G'' + K')}{2\gamma_w / kq^2 + (4\mu + \mu'_k)} \tag{3.40}$$

In the case of $G'' > 0$, the viscoplastic-hardening case, ω becomes negative. These results are the same as those of the elasto-viscoplastic model, but further discussion can be done as follows. When k is relatively smaller, $\mid \omega \mid$ becomes smaller. The system then becomes relatively less stable. When k is relatively larger, however, $\mid \omega \mid$ becomes larger and the system becomes relatively more stable.

In the case of viscoplastic softening, namely, $G'' < 0$, ω becomes positive. In this case, when k is relatively smaller, $\mid \omega \mid$ becomes smaller. The system then becomes relatively less unstable. When k is relatively larger, however, $\mid \omega \mid$ becomes larger, and the system becomes relatively more unstable. These results obtained in the viscoplastic softening region are consistent with those for the case of elasto-viscoplastic model.

An instability analysis using a rigid-viscoplastic model, disregarding the effects of elasticity on instability, provided an additional conclusion that lower permeability levels lead to relative instability in the strain-hardening range.

Gradient-dependent Rigid-viscoplastic Model

In the case of the gradient-dependent rigid-viscoplastic model, we have obtained a growth rate of fluctuation ω as

$$\omega = \frac{-(4G'' + K' + a_3 q^2)}{2\gamma_w / kq^2 + (4\mu + \mu'_k)} \tag{3.41}$$

A comparison between **Equations** (3.40) and (3.41) provides the same relation as in **Equation** (3.38). Even though $G'' < 0$, in the strain-softening regime, the numerator can be negative when $a_3 > 0$ is large enough and/or q is large, that is, the wave length is small enough. Namely, the material system can be stable even in the case of $G'' < 0$ if the gradient term is large enough. In any case, the gradient term can act as a stabilizer in the analysis as has been observed in many analyses (see Oka et al. 1994, 2000).

3.3 Finite Element Formulation for a Strain Localization Analysis of Water-saturated Clay

A finite element formulation for two-phase mixtures based on the finite deformation theory is shown in this chapter. Biot's (1956) two-phase mixture theory is adopted to give the governing equations of the soil-water coupling problem. For simplified and practical formulations, both the grain particles and the fluid are assumed to be incompressible.

Strain localization phenomenon is a geometrically nonlinear problem since deformation in shear band is large. In addition, constitutive equation of clay used in this study is nonlinear and defined as incremental form. In order to deal with such a nonlinear large deformation problem using an incremental constitutive model, an updated Lagrangian method with the objective Jaumann rate of Cauchy stress is used for the weak form of the rate type of equilibrium equations. As for the element type, an eight-node quadrilateral isoparametric element with a reduced Gaussian four points integration is used for the displacement in order to eliminate shear locking as well as to reduce the appearance of a spurious hourglass mode. The pore water pressure is defined by a four-node quadrilateral isoparametric element (see **Figure 3.1**).

In this section, direct notation is used for vectors and tensors, which are indicated by boldface letters. A dot denotes a contraction of inner indices, e.g., $a_i b_i \equiv \boldsymbol{a} \cdot \boldsymbol{b}$, so that $A_{ij} B_{ij} \equiv \boldsymbol{A} : \boldsymbol{B}$.

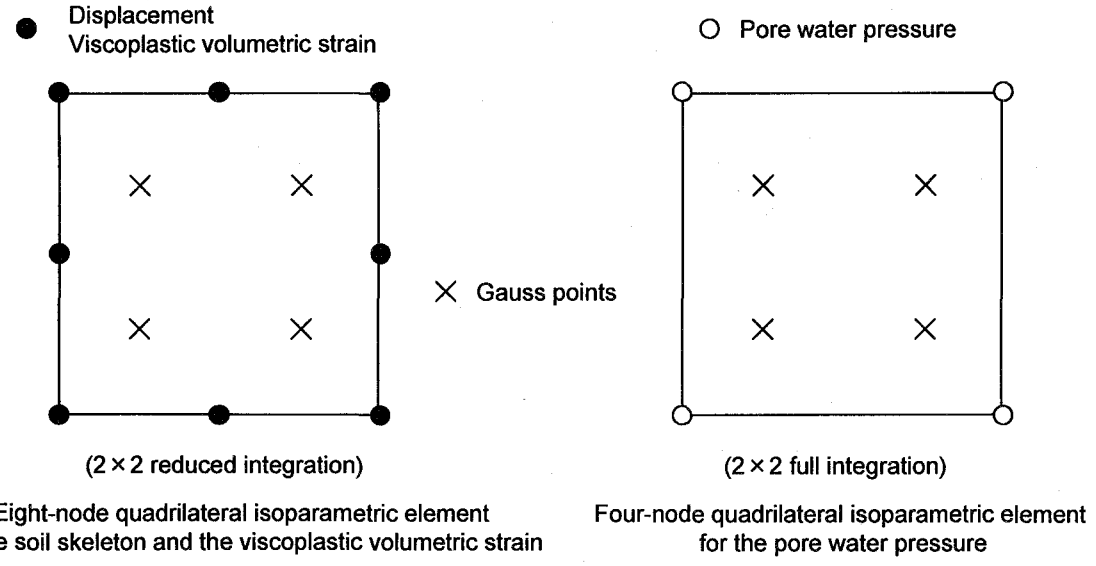

Figure 3.1 Isoparametric elements for the soil skeleton and the pore water pressure

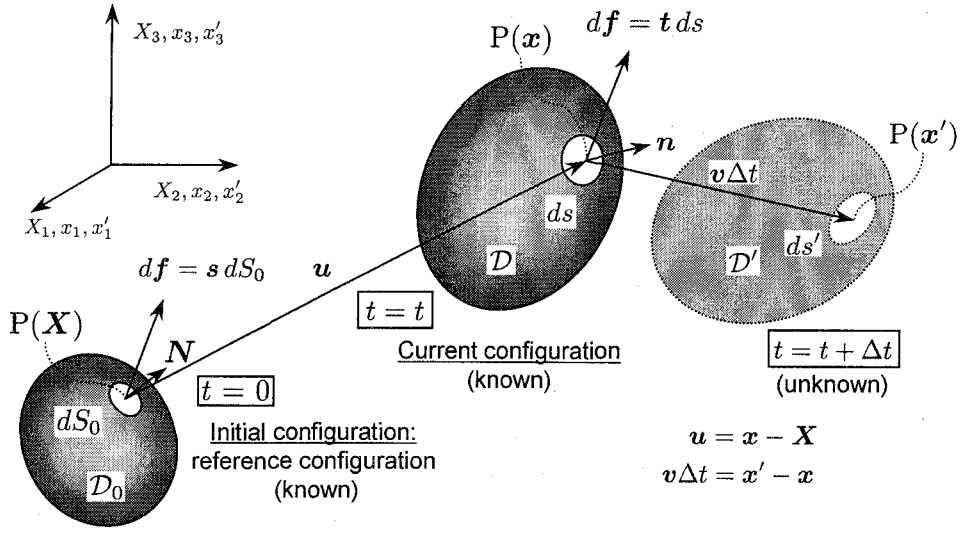

(a) Total Lagrangian formulation

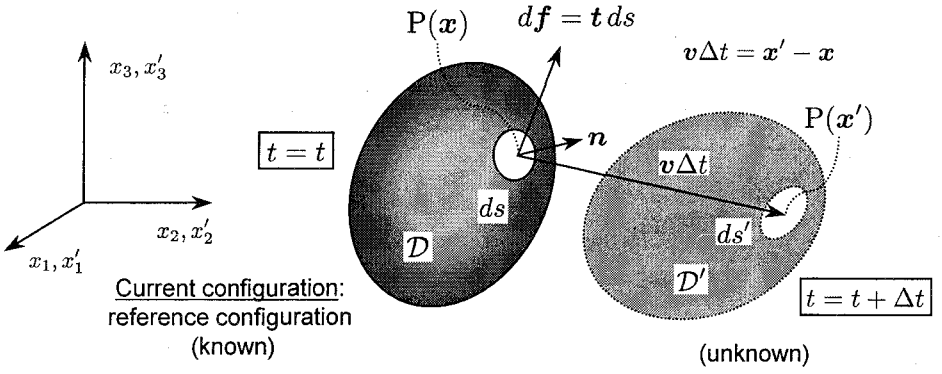

(b) Updated Lagrangian formulation

Figure 3.2 Motion of body in stationary Cartesian coordinate system

3.3.1 Updated Lagrangian Formulation

Figure 3.2 shows the motion of a general body in a stationary Cartesian coordinate system, in which $\boldsymbol{X} = X_i$, $\boldsymbol{x} = x_i$, and $\boldsymbol{x}' = x_i'$, $(i = 1, 2, 3)$, are coordinates of the point P at time $t = 0$, $t = t$, and $t = t + \Delta t$, respectively. The configuration at time $t = 0$ is the initial configuration, i.e., the body is not deformed yet; the configuration at time $t = t$ is the current configuration, i.e., the latest known configuration; and the configuration at time $t = t + \Delta t$ is unknown. In the present study, we deal with the incremental boundary value problem employing the rate type of the equilibrium equations for solid-fluid mixture with incremental constitutive equations and appropriate boundary conditions. Hence, the configuration at time $t + \Delta t$ is provided by solving the rate type of the equilibrium equations at the current configuration $(t = t)$ with a time increment Δt, i.e., linear approximation in terms of time. By iterating this procedure from

$t = 0$, to $\Delta t, 2\Delta t, \cdots$, approximate solutions of nonlinear equations can be obtained.

Finite element formulation used in this study is the updated Lagrangian method, which is effective for strongly nonlinear problem inducing large deformation and rotation since the reference configuration is always updated to the latest deformed configuration.

In the Lagrangian descriptions, the nodes, the elements, and the quadrature points move with the material, so that constitutive equations are always evaluated at the same material points, which is advantage for history-dependent materials such as soils. On the other hand, Eulerian descriptions have not been used much in solid mechanics. Since Eulerian elements do not deform with the material, they retain their original shape regardless of the magnitudes of the deformation; hence, Eulerian descriptions are useful in problems with very large deformation such as hydrodynamics (Belytschko et al. 2000).

Finite element discretizations with Lagrangian descriptions are commonly classified as updated Lagrangian formulations and total Lagrangian formulations. By comparing these two formulations, we can observe that they are quite analogous and that the only theoretical difference lies in the choice of different reference configurations (Tomita 1990; Jeremić 2002). The reference configuration of the total Lagrangian formulation is the initial configuration (**Figure 3.2**(a)), hence, the rate type of the equilibrium equations and its weak form employ integrals over the initial configuration. On the other hand, reference configuration of updated Lagrangian formulation is the current configuration (**Figure 3.2**(b)); the rate type of the equilibrium equations and its weak form involve integrals over the current configuration. In addition, since the reference configuration is updated at each iterative procedure, it is necessary for the updated Lagrangian formulation to use an objective stress rate, which is a frame-invariant rate.

3.3.2 Definition of the Effective Stress of the Fluid-solid Mixture Theory

Based on Terzaghi's concept of effective stress, the total stress tensor and the time rate of stress are given as

$$\boldsymbol{T} = \boldsymbol{T}' + u_w \boldsymbol{I} \tag{3.42}$$

$$\dot{\boldsymbol{T}} = \dot{\boldsymbol{T}}' + \dot{u}_w \boldsymbol{I} \tag{3.43}$$

in which $\boldsymbol{T}$ denotes the total Cauchy stress tensor, $\boldsymbol{T}'$ denotes the effective Cauchy stress tensor, u_w denotes the pore water pressure, $\boldsymbol{I}$ is the second order identity tensor, and the superimposed dots indicate a time differentiation.

3.3.3 Equilibrium Equations

Rate Type of the Equilibrium Equations

In the following, we will derive the rate type of the equilibrium equations by the material derivative of equilibrium equations in the current configuration. The following derivation procedure is based on Yatomi et al. (1989) and Tamura (2000). Then, the weak form of the rate type of the equilibrium equations is formulated.

When we consider an arbitrary domain $\mathcal{D}$ with boundary $\partial\mathcal{D}$ (see **Figure** 3.2), the conservation of linear momentum for the whole fluid-solid mixture in the current configuration is given by the following equation:

$$\frac{D}{Dt}\int_{\mathcal{D}} \rho \boldsymbol{v}\, dv = \int_{\partial\mathcal{D}} \boldsymbol{t}\, ds + \int_{\mathcal{D}} \rho \boldsymbol{b}\, dv \tag{3.44}$$

in which D/Dt is the material time derivative, ρ is the mass density, $\boldsymbol{v}$ is the velocity vector, $\boldsymbol{t}$ is the surface traction vector, and $\boldsymbol{b}$ is the body force vector.

In this study, we deal with static and small scale problems, so that the acceleration and body force can be assumed to be zero. Consequently, this assumption provides the equilibrium equations resulting from **Equation** (3.44):

$$\int_{\partial\mathcal{D}} \boldsymbol{t}\, ds = 0 \tag{3.45}$$

Thus, the rate type of the equilibrium equations is expressed as follows:

$$\frac{D}{Dt}\int_{\partial\mathcal{D}} \boldsymbol{t}\, ds = 0 \tag{3.46}$$

The relation between the surface traction vector $\boldsymbol{t}$ and the Cauchy stress tensor $\boldsymbol{T}$ is defined by Cauchy's stress theorem, namely,

$$\boldsymbol{t} = \boldsymbol{T}^{\mathrm{T}}\boldsymbol{n} \tag{3.47}$$

in which $\boldsymbol{n}$ is the unit normal vector to ds.

When the traction force $d\boldsymbol{f} = \boldsymbol{t}\, ds$ is shifted to the initial configuration, i.e., $d\boldsymbol{f} = \boldsymbol{s}\, dS_0$ (see **Figure 3.2**(a)), the nominal traction (Piola's traction) $\boldsymbol{s}$ is written as

$$\boldsymbol{s} = \boldsymbol{\Pi}^{\mathrm{T}}\boldsymbol{N} \tag{3.48}$$

where $\boldsymbol{\Pi}$ is the nominal stress (the first Piola-Kirchhoff stress) tensor and $\boldsymbol{N}$ is the unit normal vector to dS_0, that is, the surface area in the initial configuration. Note that the Cauchy stress $\boldsymbol{T}$ is a symmetric tensor, while the nominal stress $\boldsymbol{\Pi}$ is an asymmetric tensor.

Since **Equations** (3.47) and (3.48) provide following equation, i.e.,

$$\boldsymbol{T}^{\mathrm{T}}\boldsymbol{n}\, ds = \boldsymbol{\Pi}^{\mathrm{T}}\boldsymbol{N}\, dS_0\ , \quad (\boldsymbol{t}\, ds = \boldsymbol{s}\, dS_0) \tag{3.49}$$

we obtain the relation between the Cauchy stress $\boldsymbol{T}$ and the nominal stress $\boldsymbol{\Pi}$ as

$$\boldsymbol{\Pi}^{\mathrm{T}} = J\boldsymbol{T}^{\mathrm{T}}\boldsymbol{F}^{-\mathrm{T}} \tag{3.50}$$

in which we used Nanson's law:

$$\boldsymbol{n}\, ds = J\boldsymbol{F}^{-\mathrm{T}}\boldsymbol{N}\, dS_0 \tag{3.51}$$

where $\boldsymbol{F}$ is the deformation gradient tensor and J is the Jacobian determinant defined as $J = \det \boldsymbol{F}$.

Combining **Equations** (3.46)$\sim$(3.50) gives the rate type of the equilibrium equations in the initial configuration as

$$\frac{D}{Dt}\int_{\partial\mathcal{D}_0} \boldsymbol{s}\, dS_0 = \frac{D}{Dt}\int_{\partial\mathcal{D}_0} \boldsymbol{\Pi}^{\mathrm{T}}\boldsymbol{N}\, dS_0 = 0 \tag{3.52}$$

Since $\boldsymbol{N}$ and dS_0 are not dependent on time, **Equation** (3.52) yields

$$\int_{\partial \mathcal{D}_0} \dot{\boldsymbol{\Pi}}^{\mathrm{T}} \boldsymbol{N}\, dS_0 = 0 \tag{3.53}$$

where $\dot{\boldsymbol{\Pi}}$ is the material time derivative of the nominal stress, which is given by differentiating **Equation** (3.50) with respect to time (see Appendix B):

$$\dot{\boldsymbol{\Pi}}^{\mathrm{T}} = J(\dot{\boldsymbol{T}} + \boldsymbol{T}\mathrm{tr}\boldsymbol{L} - \boldsymbol{T}\boldsymbol{L}^{\mathrm{T}})\boldsymbol{F}^{-\mathrm{T}} \tag{3.54}$$

where $\boldsymbol{L}$ is the velocity gradient tensor defined as $\boldsymbol{L} = \dot{\boldsymbol{F}}\boldsymbol{F}^{-\mathrm{T}}$. Therefore, replacing **Equation** (3.53) by **Equation** (3.54) gives

$$\int_{\partial \mathcal{D}_0} J(\dot{\boldsymbol{T}} + \boldsymbol{T}\mathrm{tr}\boldsymbol{L} - \boldsymbol{T}\boldsymbol{L}^{\mathrm{T}})\boldsymbol{F}^{-\mathrm{T}}\boldsymbol{N}\, dS_0 = 0 \tag{3.55}$$

Adopting Nanson's law, **Equation** (3.51), and the Gauss theorem provides the rate form of the equilibrium equations in the current configuration as

$$\int_{\mathcal{D}} \mathrm{div}\dot{\boldsymbol{S}}_t\, dv = 0 \tag{3.56}$$

in which the total nominal stress rate tensor $\dot{\boldsymbol{S}}_t$ is defined as follows:

$$\dot{\boldsymbol{S}}_t \equiv \dot{\boldsymbol{T}} + \boldsymbol{T}\mathrm{tr}\boldsymbol{L} - \boldsymbol{T}\boldsymbol{L}^{\mathrm{T}} \tag{3.57}$$

Finally, we obtain the continuing equilibrium equations, namely,

$$\mathrm{div}\dot{\boldsymbol{S}}_t = 0 \tag{3.58}$$

The effective nominal stress rate tensor $\dot{\boldsymbol{S}}_t{}'$ is given by the following equations,

$$\dot{\boldsymbol{S}}_t{}' = \dot{\boldsymbol{T}}' + \boldsymbol{T}'\mathrm{tr}\boldsymbol{L} - \boldsymbol{T}'\boldsymbol{L}^{\mathrm{T}} \tag{3.59}$$

To obtain the relation between $\dot{\boldsymbol{S}}_t$ and $\dot{\boldsymbol{S}}_t{}'$, substituting the definition of the effective Cauchy stress and the effective Cauchy stress rate, **Equations** (3.42) and (3.43), respectively, into **Equation** (3.57) gives,

$$\dot{\boldsymbol{S}}_t = \dot{\boldsymbol{S}}_t{}' + \dot{u}_w\boldsymbol{I} + \mathrm{tr}\boldsymbol{L}u_w\boldsymbol{I} - u_w\boldsymbol{I}\boldsymbol{L}^{\mathrm{T}} \tag{3.60}$$

By letting $\boldsymbol{U} = \mathrm{tr}\boldsymbol{L}u_w\boldsymbol{I} - u_w\boldsymbol{I}\boldsymbol{L}^{\mathrm{T}}$, **Equation** (3.60) will become

$$\dot{\boldsymbol{S}}_t = \dot{\boldsymbol{S}}_t{}' + \dot{u}_w\boldsymbol{I} + \boldsymbol{U} \tag{3.61}$$

Weak Form of the Rate Type of the Equilibrium Equations

When we consider the closed domain $\mathcal{D}$ at current time $t = t$, the weak form of the rate type of the equilibrium equations is given as follows:

$$\int_{\mathcal{D}} \mathrm{div}\dot{\boldsymbol{S}}_t \cdot \delta\boldsymbol{v}\, dv = 0 \tag{3.62}$$

in which $\delta \boldsymbol{v}$ is the virtual velocity vector. The boundary conditions for the fluid-solid mixture are illustrated in **Figure 3.3**. A displacement boundary is denoted by $\partial \mathcal{D}_u$ if the displacement is prescribed; $\partial \mathcal{D}_t$ denotes a traction boundary if the traction is prescribed.

$$\boldsymbol{v} = \bar{\boldsymbol{v}} \quad \text{on} \quad \partial \mathcal{D}_u \tag{3.63}$$

$$\dot{\boldsymbol{S}}_t \boldsymbol{n} = \bar{\dot{\boldsymbol{s}}}_t \quad \text{on} \quad \partial \mathcal{D}_t \tag{3.64}$$

in which $\boldsymbol{v}$ is the velocity vector, $\boldsymbol{n}$ indicates the unit normal to the body, $\dot{\boldsymbol{s}}_t$ is the nominal traction rate vector (see Appendix B), and the specified values are designated by a superposed bar. The traction and the displacement cannot be prescribed at the same point; one of them must be prescribed at each boundary point. This is indicated by

$$\partial \mathcal{D}_u \cap \partial \mathcal{D}_t = 0 \qquad \partial \mathcal{D}_u \cup \partial \mathcal{D}_t = \partial \mathcal{D} \tag{3.65}$$

where $\partial \mathcal{D}$ denotes the whole boundary (Belytschko et al. 2000).

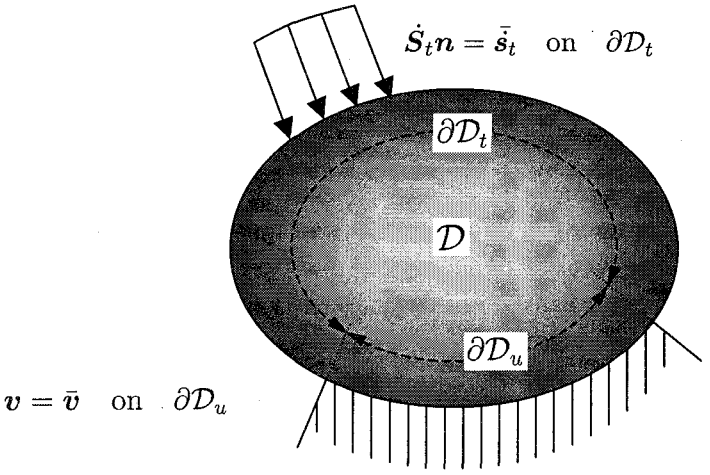

Figure 3.3 Boundary conditions for the whole fluid-solid mixture

Substituting relation

$$\operatorname{div}(\dot{\boldsymbol{S}}_t \delta \boldsymbol{v}) = \operatorname{div} \dot{\boldsymbol{S}}_t \cdot \delta \boldsymbol{v} + \dot{\boldsymbol{S}}_t : \operatorname{grad}(\delta \boldsymbol{v}) \tag{3.66}$$

into **Equation** (3.62) yields

$$\int_{\mathcal{D}} \operatorname{div}(\dot{\boldsymbol{S}}_t \delta \boldsymbol{v})\, dv - \int_{\mathcal{D}} \dot{\boldsymbol{S}}_t : \operatorname{grad}(\delta \boldsymbol{v})\, dv = 0 \tag{3.67}$$

By taking the Gauss theorem and the compatibility condition, i.e., $\operatorname{grad}(\delta \boldsymbol{v}) = \delta \boldsymbol{L}$, **Equation** (3.67) can be written as

$$\int_{\partial \mathcal{D}} (\dot{\boldsymbol{S}}_t \delta \boldsymbol{v}) \cdot \boldsymbol{n}\, ds - \int_{\mathcal{D}} \dot{\boldsymbol{S}}_t : \delta \boldsymbol{L}\, dv = 0 \tag{3.68}$$

Substituting **Equation** (3.61) into the second term of **Equation** (3.68) and transform of the first term by the following relations (see Appendix B), namely,

$$\dot{\boldsymbol{s}}_t = \dot{\boldsymbol{S}}_t \boldsymbol{n} \tag{3.69}$$

and yields

$$\int_{\mathcal{D}} \dot{\boldsymbol{S}}_t' : \delta \boldsymbol{L}\, dv + \int_{\mathcal{D}} \dot{u}_w \mathrm{tr}\delta \boldsymbol{L}\, dv + \int_{\mathcal{D}} \boldsymbol{U} : \delta \boldsymbol{L}\, dv - \int_{\partial \mathcal{D}_t} \dot{\boldsymbol{s}}_t \cdot \delta \boldsymbol{v}\, ds = 0 \tag{3.70}$$

Since the stretching tensor $\boldsymbol{D}$ is defined as

$$\boldsymbol{D} = \frac{1}{2}(\boldsymbol{L} + \boldsymbol{L}^{\mathrm{T}}) \ , \tag{3.71}$$

the following relation is obtained:

$$\mathrm{tr}\delta \boldsymbol{L} = \mathrm{tr}\delta \boldsymbol{D} \tag{3.72}$$

Substituting **Equations** (3.72) and (3.59), the effective nominal stress rate, into **Equation** (3.70) gives

$$\int_{\mathcal{D}} \dot{\boldsymbol{T}}' : \delta \boldsymbol{L}\, dv + \int_{\mathcal{D}} (\boldsymbol{T}' \mathrm{tr}\boldsymbol{D}) : \delta \boldsymbol{L}\, dv - \int_{\mathcal{D}} (\boldsymbol{T}' \boldsymbol{L}^{\mathrm{T}}) : \delta \boldsymbol{L}\, dv + \int_{\mathcal{D}} \dot{u}_w \mathrm{tr}\delta \boldsymbol{D}\, dv + \int_{\mathcal{D}} \boldsymbol{U} : \delta \boldsymbol{L}\, dv - \int_{\partial \mathcal{D}_t} \dot{\boldsymbol{s}}_t \cdot \delta \boldsymbol{v}\, ds = 0 \tag{3.73}$$

From the symmetry of the effective Cauchy stress tensor,

$$\dot{\boldsymbol{T}}' : \delta \boldsymbol{L} = \frac{1}{2}\dot{\boldsymbol{T}}' : (\delta \boldsymbol{L} + \delta \boldsymbol{L}^{\mathrm{T}}) = \dot{\boldsymbol{T}}' : \delta \boldsymbol{D} \tag{3.74}$$

is obtained.

For the discretization of the weak form of the equilibrium equation, the following relations are defined:

$$\boldsymbol{v} = [N]\{v^*\} \ , \quad \delta \boldsymbol{v} = [N]\{\delta v^*\} \tag{3.75}$$

in which $\{v\}$ is the velocity vector in an element, $\{v^*\}$ is the nodal velocity vector, and $[N]$ is a shape function of the eight-node quadrilateral element.

$$\boldsymbol{D} = \{D\} = [B]\{v^*\} \ , \quad \delta \boldsymbol{D} = \{\delta D\} = [B]\{\delta v^*\} \tag{3.76}$$

in which $[B]$ is the matrix which transforms the nodal velocity vector to the vector form of stretching tensor $\{D\}$.

$$\boldsymbol{L} = \{L\} = [B_M]\{v^*\} \ , \quad \delta \boldsymbol{L} = \{\delta L\} = [B_M]\{\delta v^*\} \tag{3.77}$$

where $[B_M]$ is the matrix which transforms the nodal velocity vector to the vector form of velocity gradient vector $\{L\}$.

$$\mathrm{tr}\boldsymbol{D} = \{B_v\}^{\mathrm{T}}\{v^*\} \ , \quad \mathrm{tr}\delta \boldsymbol{D} = \{B_v\}^{\mathrm{T}}\{\delta v^*\} \tag{3.78}$$

where $\{B_v\}$ is the vector which transform the nodal velocity into the trace of $\boldsymbol{D}$.

$$\dot{u}_w = \{N_h\}\{\dot{u}_w^*\} \tag{3.79}$$

in which $\{\dot{u}_w\}$ represents the pore pressure rate, $\{\dot{u}_w^*\}$ represents the nodal pore pressure rate vector, and $\{N_h\}$ represents the four-node quadrilateral element shape function.

Finally, by substituting **Equation** (3.74) into **Equation** (3.73), a weak form of the equilibrium equation can be obtained, as shown in the following equation:

$$\int_{\mathcal{D}} \delta \boldsymbol{D}^{\mathrm{T}} : \dot{\boldsymbol{T}}' \, dv + \int_{\mathcal{D}} \delta \boldsymbol{L}^{\mathrm{T}} : \boldsymbol{T}' \mathrm{tr}\boldsymbol{D} \, dv - \int_{\mathcal{D}} \delta \boldsymbol{L}^{\mathrm{T}} : (\boldsymbol{T}' \boldsymbol{L}^{\mathrm{T}}) \, dv + \int_{\mathcal{D}} \mathrm{tr}\delta \boldsymbol{D} \dot{u}_w \, dv + \int_{\mathcal{D}} \delta \boldsymbol{L}^{\mathrm{T}} : \boldsymbol{U} \, dv - \int_{\partial \mathcal{D}_t} \delta \boldsymbol{v}^{\mathrm{T}} \cdot \dot{\boldsymbol{s}}_t \, ds = 0 \tag{3.80}$$

In this formulation, the finite deformation theory is used; thus, the Jaumann rate of effective Cauchy stress tensor $\hat{\boldsymbol{T}}'$ is adopted for the constitutive model. The Jaumann rate of effective Cauchy stress tensor $\hat{\boldsymbol{T}}'$ is the objective tensor and is defined as

$$\hat{\boldsymbol{T}}' = \dot{\boldsymbol{T}}' - \boldsymbol{W}\boldsymbol{T}' + \boldsymbol{T}'\boldsymbol{W} \tag{3.81}$$

where $\boldsymbol{W}$ is the spin tensor, namely,

$$\boldsymbol{W} = \frac{1}{2}(\boldsymbol{L} - \boldsymbol{L}^{\mathrm{T}}). \tag{3.82}$$

The stretching tensor $\boldsymbol{D}$ is assumed to be a composition of elastic stretching tensor $\boldsymbol{D}^e$ and viscoplastic stretching tensor $\boldsymbol{D}^{vp}$, that is,

$$\boldsymbol{D} = \boldsymbol{D}^e + \boldsymbol{D}^{vp} \tag{3.83}$$

The relation between elastic stretching tensor $\boldsymbol{D}^e$ and the Jaumann rate of Cauchy stress tensor $\hat{\boldsymbol{T}}'$ can be obtained as

$$\hat{\boldsymbol{T}}' = \boldsymbol{C}^e : \boldsymbol{D}^e \ , \quad \hat{T}'_{ij} = C^e_{ijkl} D^e_{kl} \tag{3.84}$$

where $\boldsymbol{C}^e$ is the elastic tangential stiffness of the forth order tensor. **Equations** (3.83) and (3.84) lead to the relation

$$\hat{\boldsymbol{T}}' = \boldsymbol{C}^e : (\boldsymbol{D} - \boldsymbol{D}^{vp}) \ , \quad \hat{T}'_{ij} = C^e_{ijkl}(D_{kl} - D^{vp}_{kl}) \tag{3.85}$$

From the flow rule in the last chapter, viscoplastic stretching tensor $\boldsymbol{D}^{vp}$ can be obtained as

$$\boldsymbol{D}^{vp} = \gamma \langle \Phi_1 (F) \rangle \Phi_2(\xi) \frac{\partial f_p}{\partial \boldsymbol{T}'} \ , \quad D^{vp}_{ij} = \gamma \langle \Phi_1 (F) \rangle \Phi_2(\xi) \frac{\partial f_p}{\partial T'_{ij}} \tag{3.86}$$

where γ is a viscoplastic parameter.

Herein, the tangent modulus method (Peirce et al. 1984) is adopted in order to evaluate viscoplastic stretching tensor D^{vp}_{ij} (see Oka et al. 1992a and Higo 2001). Next, the relation between the rate of effective stress and the stretching tensor can be written in matrix form, as shown in the following equation:

$$\{\hat{T}'\} = [C]\{D\} - \{Q\} \tag{3.87}$$

Substituting **Equation** (3.81) into **Equation** (3.87) yields

$$\{\dot{T}'\} = [C]\{D\} - \{Q\} + \{W^*\} \tag{3.88}$$

where $[C]$ is the tangential stiffness matrix, $\{Q\}$ is the relaxation stress vector, and $\{W^*\} = \boldsymbol{W}\boldsymbol{T}' - \boldsymbol{T}'\boldsymbol{W}$ is the vector related to the spin tensor.

By all the matrix and vector relations obtained previously, and based on the theory of virtual displacement, dividing **Equation** (3.80) by $\{\delta v^*\}^T$ produces

$$[K]\{v^*\} - \int_{\mathcal{D}}[B]^{\mathrm{T}}\{Q\}\,dv + \int_{\mathcal{D}}[B]^{\mathrm{T}}\{W^*\}\,dv + [K_L]\{v^*\} + [K_v]\{\dot{u}_w^*\} = \{\dot{F}\} \tag{3.89}$$

in which

$$[K] = \int_{\mathcal{D}}[B]^{\mathrm{T}}[C][B]\,dv \tag{3.90}$$

$$[K_L] = \int_{\mathcal{D}}[B_M]^{\mathrm{T}}[D_s'][B_M]\,dv + \int_{\mathcal{D}}[B_M]^{\mathrm{T}}[U][B_M]\,dv + \int_{\mathcal{D}}[B_M]^{\mathrm{T}}\{T'\}\{B_v\}^{\mathrm{T}}\,dv \tag{3.91}$$

$$[K_v] = \int_{\mathcal{D}}\{B_v\}\{N_h\}\,dv \tag{3.92}$$

$$\{\dot{F}\} = \int_{\partial\mathcal{D}_t}[N]^{\mathrm{T}}\{\hat{s}\}\,ds \tag{3.93}$$

In the above equations, the matrix form of $(-\boldsymbol{T}'\boldsymbol{L}^{\mathrm{T}})$ and $\boldsymbol{U}$ are denoted as

$$-\boldsymbol{T}'\boldsymbol{L}^{\mathrm{T}} = [D_s'][B_M]\{v^*\} \tag{3.94}$$

$$\boldsymbol{U} = u_w\boldsymbol{I}\,(\mathrm{tr}\boldsymbol{L}) - u_w\boldsymbol{I}\boldsymbol{L}^{\mathrm{T}} = [U][B_M]\{v^*\} \tag{3.95}$$

The relation between nodal velocity vector $\{v^*\}$ and nodal displacement increment vector $\{\Delta u^*\}$ can be obtained by using Euler's approximation as

$$\{v^*\} = \frac{\{\Delta u^*\}}{\Delta t} \tag{3.96}$$

Similarly, the pore water pressure can be obtained as

$$\{\dot{u}_w^*\} = \frac{\{u_w^*\}_{t+\Delta t} - \{u_w^*\}_t}{\Delta t} \tag{3.97}$$

Substituting **Equations** (3.96) and (3.97) into **Equation** (3.89), the weak form of the equilibrium equations is obtained, that is,

$$\begin{aligned}\Big[[K] + [K_L]\Big]\{\Delta u^*\} + [K_v]\{u_w^*\}_{t+\Delta t} &= \Delta t\{\dot{F}\} + [K_v]\{u_w^*\}_t \\ &+\Delta t\int_{\mathcal{D}}[B]^{\mathrm{T}}\{Q\}\,dv - \Delta t\int_{\mathcal{D}}[B]^{\mathrm{T}}\{W^*\}\,dv\end{aligned} \tag{3.98}$$

3.3.4 Continuity Equation

For describing the motion of pore water, a Biot's type of two-phase mixture theory (Biot 1956) is used in the analysis with a $\boldsymbol{v}$(velocity)$-u_w$(pore pressure) formulation. The Darcy law and the conservation of mass for the mixture give the continuity equation as

$$\frac{k}{\gamma_w}\nabla^2 u_w + \mathrm{tr}\boldsymbol{D} = 0 \tag{3.99}$$

where k is the coefficient of permeability, γ_w is the unit weight of the pore water, and $\boldsymbol{D}$ is the stretching tensor.

Considering the test function of $\hat{u}_w$, we can obtain the weak form of the continuity equation as

$$\frac{k}{\gamma_w}\int_{\mathcal{D}} \nabla^2 u_w \hat{u}_w \, dv + \int_{\mathcal{D}} \mathrm{tr}\boldsymbol{D}\, \hat{u}_w \, dv = 0 \tag{3.100}$$

As shown in **Figure 3.4**, $\mathcal{D}$ demonstrates a closed domain. In a similar manner to that of the boundary for the fluid-solid mixture, the boundary surface can be broken down into two parts, namely,

$$\partial\mathcal{D}_p \cap \partial\mathcal{D}_v = 0 \qquad \partial\mathcal{D}_p \cup \partial\mathcal{D}_v = \partial\mathcal{D} \tag{3.101}$$

in which $\partial\mathcal{D}_p$ is the boundary where the pore pressure is specified and $\partial\mathcal{D}_v$ is the boundary where the flow of water is specified.

$$u_w = \bar{u}_w \quad \text{on} \quad \partial\mathcal{D}_p \tag{3.102}$$

$$\frac{k}{\gamma_w}\nabla u_w = \bar{\boldsymbol{v}} \quad \text{on} \quad \partial\mathcal{D}_v \tag{3.103}$$

in which the specified values are designated by a superposed bar, and $\boldsymbol{v}$ is the velocity of the pore water through the boundary surface.

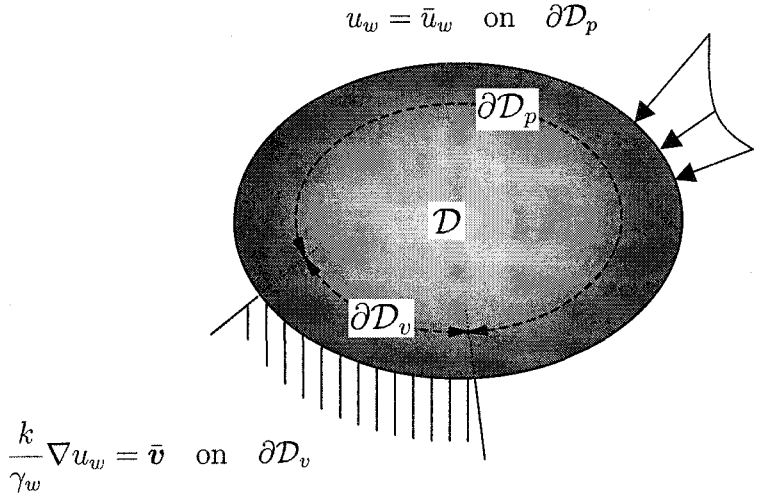

Figure 3.4 Boundary conditions for the fluid phase

From the relation

$$\nabla^2 u_w \hat{u}_w = \nabla\cdot(\nabla u_w \hat{u}_w) - \nabla u_w \cdot \nabla \hat{u}_w \tag{3.104}$$

Equation (3.100) can be rewritten as

$$\frac{k}{\gamma_w}\int_{\mathcal{D}} \nabla\cdot(\nabla u_w \hat{u}_w)\, dv - \frac{k}{\gamma_w}\int_{\mathcal{D}} \nabla u_w \cdot \nabla \hat{u}_w \, dv + \int_{\mathcal{D}} \hat{u}_w \mathrm{tr}\boldsymbol{D}\, dv = 0 \tag{3.105}$$

By applying the Gauss theorem to the previous equation and substituting **Equation** (3.103) into **Equation** (3.105), the following equation can be obtained:

$$\int_{\partial\mathcal{D}_v} \bar{\boldsymbol{v}}\cdot\boldsymbol{n}\, ds - \frac{k}{\gamma_w}\int_{\mathcal{D}} \nabla\hat{u}_w \cdot \nabla u_w \, dv + \int_{\mathcal{D}} \hat{u}_w \mathrm{tr}\boldsymbol{D}\, dv = 0 \tag{3.106}$$

in which $\boldsymbol{n}$ is the unit normal vector of the body.

For the discretization, the following vectors and matrixes are used:

$$u_w = \{N_h\}\{u_w^*\} \ , \quad \hat{u}_w = \{N_h\}\{\hat{u}_w^*\} \tag{3.107}$$

where $\{u_w^*\}$ is the nodal pore pressure vector and $\{N_h\}$ is the shape function of the four-node quadrilateral element.

$$\nabla u_w = \nabla\{N_h\}\{u_w^*\} = [B_h]\{u_w^*\} \tag{3.108}$$

in which $[B_h]$ is the matrix which transforms the nodal pore pressure into the spatial derivative of the pore pressure.

$$\mathrm{tr}\boldsymbol{D} = \{B_v\}^{\mathrm{T}}\{v^*\} \tag{3.109}$$

where $\{B_v\}$ is the vector which transforms the nodal velocity vector $\{v^*\}$ into the trace of the stretching tensor.

Substituting **Equations** (3.107), (3.108), and (3.109) into **Equation** (3.106) yields

$$\int_{\partial\mathcal{D}_v}\{\hat{u}_w^*\}^{\mathrm{T}}\{N_h\}^{\mathrm{T}}\{\bar{v}\}^{\mathrm{T}}\{n\}\,ds - \frac{k}{\gamma_w}\int_{\mathcal{D}}\{\hat{u}_w^*\}^{\mathrm{T}}[B_h]^{\mathrm{T}}[B_h]\{u_w^*\}\,dv + \int_{\mathcal{D}}\{\hat{u}_w^*\}^{\mathrm{T}}\{N_h\}^{\mathrm{T}}\{B_v\}^{\mathrm{T}}\{v^*\}\,dv = 0 \tag{3.110}$$

By taking the arbitration of the test function, dividing both sides of the previous equation by $\{\hat{u}_w^*\}^T$ gives

$$\int_{\partial\mathcal{D}_v}[N_h]^{\mathrm{T}}\{\bar{v}\}^{\mathrm{T}}\{n\}\,ds - \frac{k}{\gamma_w}\int_{\mathcal{D}}[B_h]^{\mathrm{T}}[B_h]\,dv\,\{u_w^*\} + \int_{\mathcal{D}}[N_h]^{\mathrm{T}}[B_v]^{\mathrm{T}}dv\,\{v^*\} = 0 \tag{3.111}$$

Using the same approximation of **Equation** (3.96), the discretization of the continuity equation is obtained as follows:

$$[K_v]^{\mathrm{T}}\{v^*\} - \Delta t\,[K_h]\{u_w^*\}_{t+\Delta t} = \Delta t\,[V] \tag{3.112}$$

where

$$[K_h] = \frac{k}{\gamma_w}\int_{\mathcal{D}}[B_h]^{\mathrm{T}}[B_h]\,dv \tag{3.113}$$

$$[K_v]^{\mathrm{T}} = \int_{\mathcal{D}}[N_h]^{\mathrm{T}}[B_v]^{\mathrm{T}}dv \tag{3.114}$$

$$[V] = -\int_{\partial\mathcal{D}_v}[N_h]^{\mathrm{T}}\{\bar{v}\}^{\mathrm{T}}\{n\}\,ds \tag{3.115}$$

3.4 Finite Element Formulation of the Gradient-dependent Elasto-viscoplastic Model

Higher order gradient terms have been introduced into the constitutive equations to simulate localization problems. In the present study, a second order gradient of viscoplastic volumetric

strain v^p is used in the constitutive equation. Hence, the discretization of v^p as an independent variable by the eight-node quadrilateral element is needed (see **Figure 3.1**). In this section, we assume the weak form of the dynamic yield function and define viscoplastic volumetric strain v^p at each node in a similar manner to that by Aifantis et al. (1999).

However, there are still difficult questions to be solved when we use a constitutive equation with higher order gradient terms in relation to boundary value problems defined in the finite domain. Mühlhaus and Aifantis (1991) and Vardoulakis and Aifantis (1991) pointed out the importance of this and proposed variational principles to exact appropriate boundary conditions. In the present study, we assume the related boundary conditions for the first gradient of viscoplastic strain. For the first gradient of v^p, we assume the following relation between the flux $\tilde{\boldsymbol{Q}}$ associated with the internal structure change including the ∇v^p or $\nabla \dot{v}^p$:

$$\tilde{\boldsymbol{Q}} = \nabla v^p \quad \text{or} \quad \nabla \dot{v}^p \tag{3.116}$$

To obtain the weak form of the dynamic yield function, we assume the simplified viscoplastic model as follows (Oka et al. 1992b):

$$\dot{\varepsilon}^{vp} = -a_1 \varepsilon^{vp} + f - a_3 \nabla^2 \varepsilon^{vp} \tag{3.117}$$

where ε^{vp} is the viscoplastic strain, a_1 is the hardening parameter, f is the dynamic yield function, and a_3 is a gradient parameter.

The weak form of the dynamic yield function with boundary conditions can be written as

$$\int_{\mathcal{D}} \left(f - a_1 v^p - a_3 \nabla^2 v^p - g(\dot{v}^p) \right) \delta v^p dv + \lambda \int_{\partial \mathcal{D}} \left(\tilde{\boldsymbol{Q}} - \nabla_n v^p \right) \delta v^p \cdot \boldsymbol{n} \, ds = 0 \tag{3.118}$$

in which $\mathcal{D}$ is a closed domain, $\partial \mathcal{D}$ is the boundary surface, v^p is the viscoplastic volumetric strain, ∇_n is the normal gradient to the boundary, δv^p is the virtual viscoplastic volumetric strain associated with virtual displacement during the deformation process and λ is an arbitrary scalar. In the present study, the viscoplastic strain rate is assumed to always occur.

When $g(\cdot)$ is linear with respect to v^p, it is easy to employ the weak form of **Equation** (3.118). However, if $g(\cdot)$ is non-linear with respect to v^p, a problem arises. In such a case, we need an iterative procedure to solve **Equation** (3.118). It is worth noting that a serious difficulty is encountered in numerically solving it by the finite element method because of the non-linearity of the field equation. In the case of the proposed constitutive model, function $g(\cdot)$ is non-linear. In this case, we adopt a Taylor series expansion around the current state and consider the first term to obtain the weak form. We can rewrite the dynamic yield function as

$$\dot{v}^p = G(\sigma_{ij}, v^p, \nabla^2 v^p) \tag{3.119}$$

In the following, the stress tensor σ_{ij} denotes the effective stress tensor without notice for simplicity.

Expanding the viscoplastic volumetric strain rate in a Taylor series and disregarding the second- and higher-order terms, we obtain a linearized dynamic yield function of the form

$$\dot{v}^p = \dot{v}_0^p + \left([G_\sigma][\dot{\sigma}] + G_{v^p} \dot{v}^p + G_\beta (\nabla^2 \dot{v}^p) \right) \tag{3.120}$$

where

$$G_\sigma = \frac{\partial G}{\partial \sigma_{ij}}\ , \quad G_{v^p} = \frac{\partial G}{\partial v^p}\ , \quad G_\beta = \frac{\partial G}{\partial(\nabla^2 v^p)}\ , \tag{3.121}$$

$\dot{v}_0^p$ denotes the value of the volumetric strain rate at the current state. Using a Taylor series expansion and truncating the first order term, we obtain the following expression for the total strain rate tensor:

$$[\dot{\varepsilon}] = [L^*]^{-1}[\dot{\sigma}] + [\dot{\varepsilon}_0^p] + [A]\dot{v}^p + [A^*][\dot{\sigma}] + [A^{**}]\nabla^2\dot{v}^p \tag{3.122}$$

where $[L^*]^{-1}$ denotes the inversion of the elastic compliance tensor and

$$A = \frac{\partial \dot{\varepsilon}_{ij}^{vp}}{\partial v^p}\ , \quad A^* = \frac{\partial \dot{\varepsilon}_{ij}^{vp}}{\partial \sigma_{kl}}\ , \quad A^{**} = \frac{\partial \dot{\varepsilon}_{ij}^{vp}}{\partial(\nabla^2 v^p)}\ , \tag{3.123}$$

where $[\dot{\varepsilon}]$ is the total strain rate tensor, $[\dot{\varepsilon}_0^p]$ is the viscoplastic strain rate tensor at the current state and $\dot{\varepsilon}_{ij}^{vp}$ is the viscoplastic strain rate tensor.

From **Equation** (3.122), stress rate tensor $[\dot{\sigma}]$ is obtained as

$$[\dot{\sigma}] = [L][\dot{\varepsilon}] - [L][\dot{\varepsilon}_0^p] - [L][A]\dot{v}^p - [L][A^{**}]\nabla^2\dot{v}^p \tag{3.124}$$

$$[L]^{-1} = [L^*]^{-1} + [A^*] \tag{3.125}$$

Substituting **Equation** (3.124) into **Equation** (3.120) yield

$$H\dot{v}^p = \dot{J}_0^p + [G_\sigma][L][\dot{\varepsilon}] + R\nabla^2\dot{v}^p \tag{3.126}$$

where

$$H = 1 - G_{v^p} + [G_\sigma][L][A] \tag{3.127}$$

$$\dot{J}_0^p = \dot{v}_0^p - [G_\sigma][L][\dot{\varepsilon}_0^p] \tag{3.128}$$

$$R = G_\beta - [G_\sigma][L][A^{**}] \tag{3.129}$$

The weak form of **Equation** (3.120) with boundary conditions is given by

$$\int_{\mathcal{D}} \left(R\nabla^2\dot{v}^p - H\dot{v}^p + \dot{J}_0^p + [G_\sigma][L][\dot{\varepsilon}]\right)\delta\dot{v}^p dv + \lambda\int_{\partial\mathcal{D}} \left(\tilde{\boldsymbol{Q}} - \nabla\dot{v}^p\right)\delta\dot{v}^p \cdot \boldsymbol{n}\, ds = 0 \tag{3.130}$$

where λ is an arbitrary scalar and $\delta\dot{v}^p$ is the virtual viscoplastic volumetric strain rate.

Since

$$\delta\dot{v}^p\nabla^2\dot{v}^p = \nabla\cdot(\delta\dot{v}^p\nabla\dot{v}^p) - \nabla\delta\dot{v}^p\cdot\nabla\dot{v}^p \tag{3.131}$$

Equation (3.130) becomes

$$\int_{\mathcal{D}} R\Big(\nabla\cdot(\delta\dot{v}^p\nabla\dot{v}^p) - \nabla\delta\dot{v}^p\cdot\nabla\dot{v}^p\Big)\,dv + \int_{\mathcal{D}} \delta\dot{v}^p\left(-H\dot{v}^p + \dot{J}_0^p + [G_\sigma][L][\dot{\varepsilon}]\right)\,dv$$
$$+\lambda\int_{\partial\mathcal{D}} \delta\dot{v}^p\tilde{\boldsymbol{Q}}\cdot\boldsymbol{n}\,ds - \lambda\int_{\partial\mathcal{D}} \delta\dot{v}^p\nabla\dot{v}^p\cdot\boldsymbol{n}\,ds = 0 \tag{3.132}$$

Using the divergence theorem for **Equation** (3.132), we have

$$\int_{\mathcal{D}} R\nabla\delta\dot{v}^p \cdot \nabla\dot{v}^p dv - \int_{\mathcal{D}} \delta\dot{v}^p \left(-H\dot{v}^p + j_0^p + [G_\sigma][L][\dot{\varepsilon}]\right) dv - \lambda \int_{\partial\mathcal{D}} \delta\dot{v}^p \tilde{\boldsymbol{Q}} \cdot \boldsymbol{n}\, ds$$
$$+(-R+\lambda)\int_{\partial\mathcal{D}} \delta\dot{v}^p \nabla\dot{v}^p \cdot \boldsymbol{n}\, ds = 0 \tag{3.133}$$

In order for parameter λ to be arbitrary, we set $\lambda = R$.

Introducing the shape function, we can discretize the viscoplastic strain rate, and the corresponding strain tensor by using the expression

$$\dot{v}^p = [N^*]\{\dot{v}^{p*}\} \ , \quad \delta\dot{v}^p = [N^*]\{\delta\dot{v}^{p*}\} \tag{3.134}$$

where $\{\dot{v}^{p*}\}$ denotes the vector of the rate of the viscoplastic volumetric strain rates at the nodal points and $[N^*]$ is a shape function of the eight-node quadrilateral element.

$$\nabla\dot{v}^p = [N^*]'\{\dot{v}^{p*}\} \tag{3.135}$$

$$[\dot{\varepsilon}] = [B]\{\dot{u}^*\} \tag{3.136}$$

where $\{\dot{u}^*\}$ is the velocity vector at the nodal points, $[B]$ is the strain rate-velocity matrix and $[N^*]' = \nabla[N^*]$.

Upon the substitution of the shape function into **Equation** (3.133), we get the following equation since $\{\delta\dot{v}^{p*}\}$ is arbitrary:

$$\int_{\mathcal{D}} R[N^*]'^{\mathrm{T}}[N^*]' dv\,\{\dot{v}^{p*}\} + \int_{\mathcal{D}} H[N^*]^{\mathrm{T}}[N^*]\, dv\,\{\dot{v}^{p*}\} - \int_{\mathcal{D}} [N^*]^{\mathrm{T}}[G_\sigma][L][B]\, dv\,\{\dot{u}^*\}$$
$$-\int_{\mathcal{D}} [N^*]^{\mathrm{T}} j_0^p\, dv - R\int_{\partial\mathcal{D}} [N^*]^{\mathrm{T}}\{\tilde{Q}\}^{\mathrm{T}}\{n\}\, ds = 0 \tag{3.137}$$

which can be written as

$$[K_1]\{\dot{v}^{p*}\} + [K_2]\{\dot{u}^*\} = \{F_1\} \tag{3.138}$$

where

$$[K_1] = \int_{\mathcal{D}} \left(R[N^*]'^{\mathrm{T}}[N^*]' + H[N^*]^{\mathrm{T}}[N^*]\right) dv \tag{3.139}$$

$$[K_2] = -\int_{\mathcal{D}} [N^*]^{\mathrm{T}}[G_\sigma][L][B]\, dv \tag{3.140}$$

$$\{F_1\} = \int_{\mathcal{D}} [N^*]^{\mathrm{T}} j_0^p\, dv + R\int_{\partial\mathcal{D}} [N^*]^{\mathrm{T}}\{\tilde{Q}\}^{\mathrm{T}}\{n\}\, ds \tag{3.141}$$

In addition, using the following Euler approximation and **Equation** (3.96):

$$\{\dot{v}^{p*}\} = \frac{\{\Delta v^{p*}\}}{\Delta t}, \tag{3.142}$$

Equation (3.138) becomes

$$[K_1]\{\Delta v^{p*}\} + [K_2]\{\Delta u^*\} = \Delta t\{F_1\} \tag{3.143}$$

It should be pointed out that, when we implement the proposed model into the FEM code, we should specify the boundary of $\tilde{Q}$, which describes microstructure change flux $\tilde{Q}$ at the boundary, namely,

$$\tilde{Q} = \nabla \dot{v}^p \tag{3.144}$$

In this respect, we postulate that flux $\tilde{Q}$ is zero at the boundary between the rigid or the elastic material and the viscoplastic material. From a physical point of view, we could say that flux $\tilde{Q}$ never flows from the rigid or the elastic material, which will never deform plastically, and also that flux $\tilde{Q}$ never flows out from the viscoplastic material into the rigid or the elastic material. At the boundary where the stress levels are specified like a free surface of the ground, flux $\tilde{Q}$ also assumed to be zero.

Finally, from **Equations** (3.98), (3.112), and (3.138), we can obtain the governing equations used in the finite element analysis as follows:

$$\begin{bmatrix} [K]+[K_L] & [K_v]^{\mathrm{T}} & [0] \\ [K_v] & -\Delta t\,[K_h] & [0] \\ [K_2] & [0] & [K_1] \end{bmatrix} \begin{bmatrix} \{\Delta u^*\} \\ \{u_w^*\}_{t+\Delta t} \\ \{\Delta v^{p*}\} \end{bmatrix} \tag{3.145}$$

$$= \begin{bmatrix} \Delta t\{\dot{F}\} + [K_v]^{\mathrm{T}}\{u_w^*\}_t + \Delta t\int_{\mathcal{D}} [B]^{\mathrm{T}}\{Q\}\,dv - \Delta t\int_{\mathcal{D}} [B]^{\mathrm{T}}\{W^*\}\,dv \\ \Delta t\{V\} \\ \Delta t\{F_1\} \end{bmatrix} \tag{3.146}$$

3.5 Effects of Permeability on the Strain Localization Analysis

In **Figure 3.5**, the boundary conditions are shown for the plane strain problem used in the numerical analysis, while the parameters used in the computation are shown in **Table 3.1**. The gradient parameter, in principle, can be determined by the width of shear band, namely, the wavelength of the localized pattern. The strain rate of compression is 1.0%/min. The horizontal displacement of the top and the bottom of the specimen was fixed as a trigger of localization. All of the boundaries are assumed to be impermeable, while the pore fluid is allowed to flow in the specimen.

The average vertical stress vs. strain relations with different coefficients of permeability are shown in **Figure 3.6**. In the early stage of loading, i.e., in the hardening range, little difference can be seen among these three cases. On the other hand, in the strain-softening range, the material with a low permeability level of 1.54×10^{-12}(m/s) is less unstable because the average stress is larger than those with higher permeability level of 1.54×10^{-6}(m/s) and 10^{-8}(m/s). This behavior is consistent with the theoretical consideration mentioned in **Section 3.2**. After an axial strain of 5%, however, the case of $k = 1.54 \times 10^{-8}$(m/s) is smaller than the case of $k = 1.54 \times 10^{-6}$(m/s). These results do not agree with those of the instability analysis.

The calculations with coefficients of permeability $k = 1.54 \times 10^{-8}$(m/s) and 10^{-12}(m/s) diverged around 8% of the axial strain. The calculations with $k = 1.54 \times 10^{-6}$(m/s) also

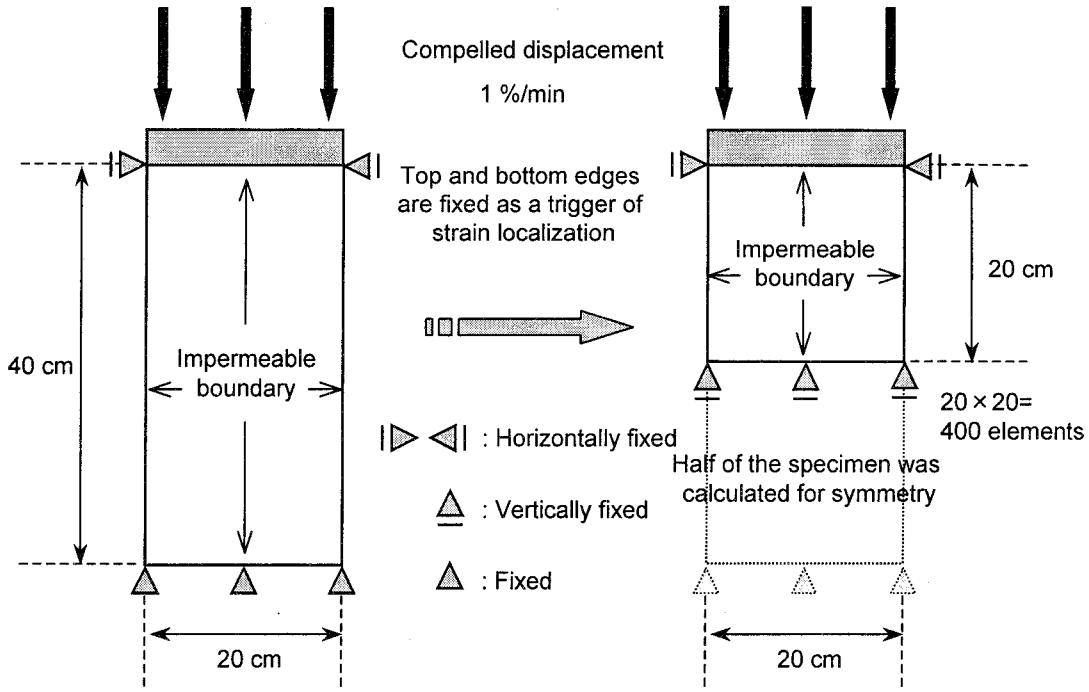

Figure 3.5 Boundary conditions and the size of the specimen (undrained plane strain condition)

Table 3.1 Material parameters for the strain localization analysis with different permeability coefficients

Compression index	λ	0.172
Swelling index	κ	0.054
Initial void ratio	e_0	1.28
Initial mean effective stress	σ'_{me}	200 (kPa)
Coefficient of earth pressure at rest	K_0	1.0
Viscoplastic parameter	m'	21.5
Viscoplastic parameter	C	4.5×10^{-8} (1/s)
Stress ratio at failure	M_f^*	1.05
Elastic shear modulus	G	5500 (kPa)
Softening parameter	G_2^*	100
Gradient parameter	a_3	0.0, 5.0, 30.0 ($\times10^{-4}$ m^2)
Coefficient of permeability	k_x=k_y	1.54×10^{-6} (m/s) 1.54×10^{-8} (m/s) 1.54×10^{-12} (m/s)

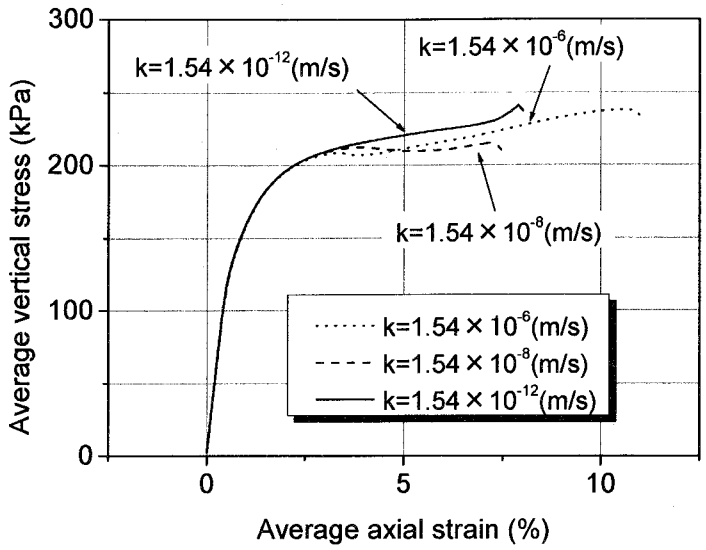

Figure 3.6 Average vertical stress-strain relations with different coefficients of permeability

diverged around 11% of the axial strain. This is because the constraint conditions, i.e., no lateral displacements at either the top or the bottom plates, induce numerical instability near the top and the bottom of the specimen.

Figure 3.7 shows the deformed mesh at an average axial strain of 7% with different coefficients of permeability k. It is shown that the pore fluid has an apparent influence on the formation of shear bands. It is found that a symmetrical deformation can be seen in all cases, in particular, a clear shear band formed in the case of $k = 1.54 \times 10^{-6}$(m/s).

In **Figure 3.8**, velocity vectors are shown in half of the specimen at an average axial strain of 7% with different coefficients of permeability k. Discontinuous distributions of velocity fields are found in all cases due to the formation of shear bands. The patterns of distributions of the velocity vectors are consistent with the deformed mesh.

Figure 3.9 shows the distributions of accumulated viscoplastic shear strain γ^p at an average axial strain of 3% and that of 7% with different coefficients of permeability k. γ^p is defined as follows:

$$\gamma^p = \int d\gamma^p \ , \quad d\gamma^p = (de^p_{ij} de^p_{ij})^{1/2} \tag{3.147}$$

where de^p_{ij} is the viscoplastic deviatoric strain-increment tensor. The localized patterns of the figures for 3% are very similar to each other, but the maximum value for γ^p is larger as the coefficient of permeability k decreases. On the other hand, at an average axial strain of 7%, the maximum value for γ^p is larger in the case of higher coefficients of permeability than that of lower coefficients of permeability. It can be said that materials with larger accumulated shear strain are more unstable than those with smaller shear strain. Following this point of view, when the average axial strain is small, i.e., in the viscoplastic-hardening area, materials with lower permeability levels are rather unstable. On the other hand, when the average axial strain becomes large, i.e., in the viscoplastic-softening area, materials with higher permeability levels

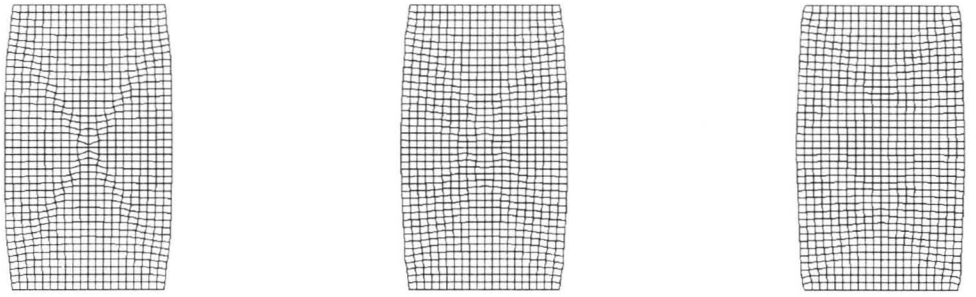

$k = 1.54 \times 10^{-6}$ m/s $\quad$ $k = 1.54 \times 10^{-8}$ m/s $\quad$ $k = 1.54 \times 10^{-12}$ m/s

Figure 3.7 Deformed mesh at an average axial strain of 7%

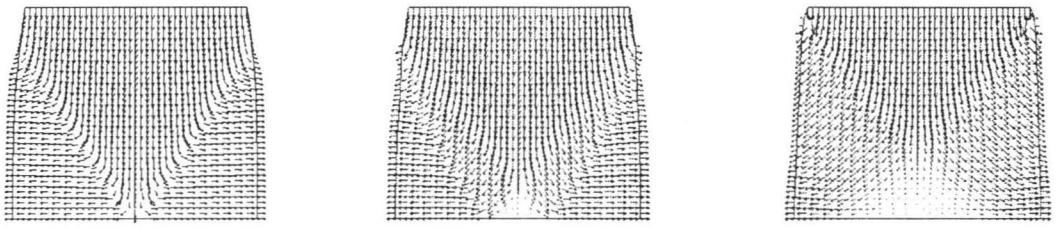

$k = 1.54 \times 10^{-6}$ m/s $\quad$ $k = 1.54 \times 10^{-8}$ m/s $\quad$ $k = 1.54 \times 10^{-12}$ m/s

Figure 3.8 Distributions of the velocity vector at an average axial strain of 7%

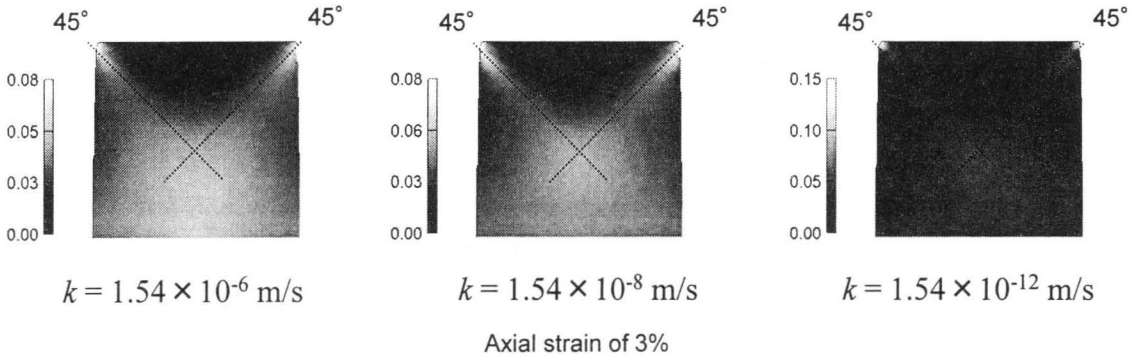

$k = 1.54 \times 10^{-6}$ m/s $\quad$ $k = 1.54 \times 10^{-8}$ m/s $\quad$ $k = 1.54 \times 10^{-12}$ m/s

Axial strain of 3%

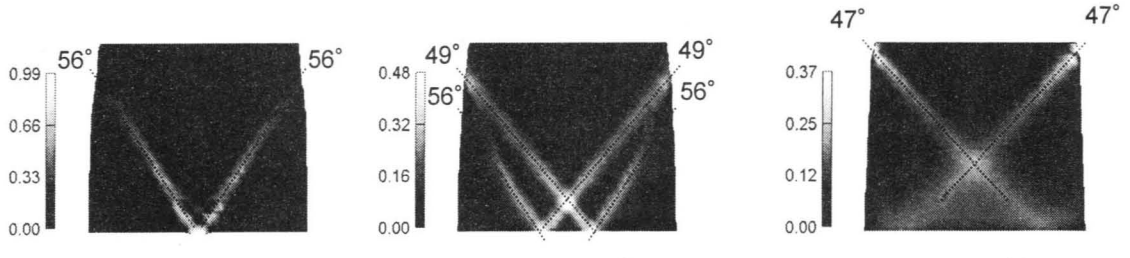

$k = 1.54 \times 10^{-6}$ m/s $\quad$ $k = 1.54 \times 10^{-8}$ m/s $\quad$ $k = 1.54 \times 10^{-12}$ m/s

Axial strain of 7%

Figure 3.9 Distribution of γ^p at average axial strains of 3% and 7%

are relatively unstable. This tendency is also consistent with the results obtained in **Section 3.2**. In addition, a larger difference between the maximum and the minimum values for γ^p is also seen in the case of higher permeability levels. This suggests that the strain localizes prominently when materials have high permeability levels. It is interesting, however, that two shear bands appear in the case of $k = 1.54 \times 10^{-6}$(m/s), while the other cases have four shear bands and the distance between two shear bands is larger in the case of small permeability compared with the case of larger permeability.

Inclination angles of shear bands for all cases are 45 degrees at small axial strain of 3%. When the axial strain becomes 7%, angles of shear bands with higher permeability become larger than those of lower permeability. Oka et al. (1995) demonstrated that the preferred orientation of shear bands is 45 degrees under plane strain locally undrained condition, i.e., $k = 0$, for the Adachi and Oka viscoplastic model introduced in **Chapter 2**. The reason why the angles of shear bands with lower strain is proximate to 45 degrees that materials with lower permeability levels are similar to those under locally undrained conditions.

In **Figure 3.10**, the distributions of pore water pressure are shown with different coefficients of permeability k. When permeability k is smaller, the pore water pressure is more localized. In **Figures 3.11**, **3.12**, and **3.13** the distributions of mean effective stress, the second invariant of deviatoric stress, and volumetric viscoplastic strain at an average axial strain of 7% are shown with different coefficients of permeability k. They are all affected by the formation of shear bands and are inhomogeneous. The mean effective stress inside the shear band becomes smaller than that outside the shear band. The maximum values for the deviatoric stress and the volumetric viscoplastic strain become larger with higher permeability levels.

Loret and Prévost (1991) showed that materials with higher permeability levels are more unstable in the post-localization regime. The results obtained in this section and the last section for the instability analysis are consistent with Loret and Prévost (1991) in the softening area. Note that the numerical simulations done by Loret and Prévost (1991) are based on the infinitesimal strain theory using a dilatant elasto-plastic model, while calculations in this study are based on the finite deformation theory using a contractant elasto-viscoplastic model. Oka et al. (1995), using basically the same analysis method, concluded that materials with higher permeability levels are stable because the distribution of pore water pressure is rather moderate. In this study, however, materials with higher permeability levels which show a relatively moderate distribution of pore water pressure are more unstable because γ^p is more localized.

3.6 Effects of the Strain Gradient Parameter on the Strain Localization Analysis

Strain gradients, in principle, can describe the thickness of shear bands. In addition, it is found in the instability analysis of **Section 3.2** that strain gradients act as stabilizers. In this section, the effects of the strain gradient parameter on the strain localization analysis are investigated. The boundary conditions and the material parameters are the same as in the last section.

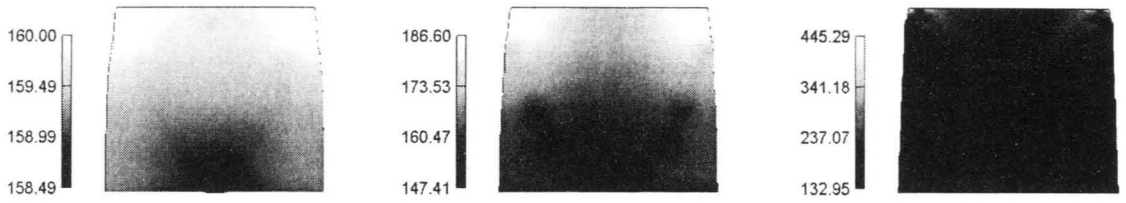

Figure 3.10 Distributions of pore water pressure at an average axial strain of 7% (Unit: kPa)

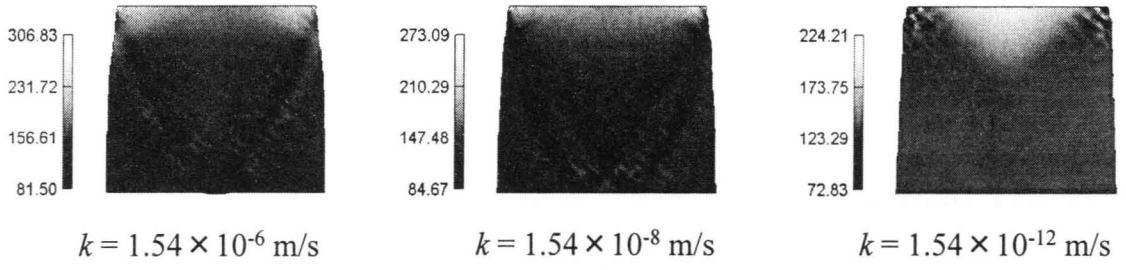

Figure 3.11 Distributions of mean effective stress at an average axial strain of 7% (Unit: kPa)

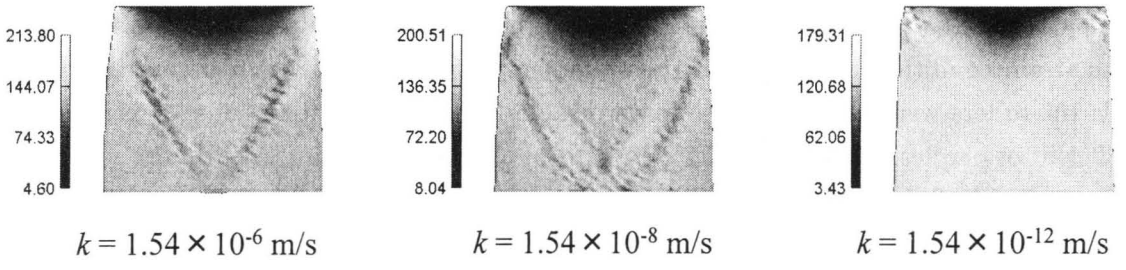

Figure 3.12 Distributions of the second invariant of deviatoric stress at an average axial strain of 7% (Unit: kPa)

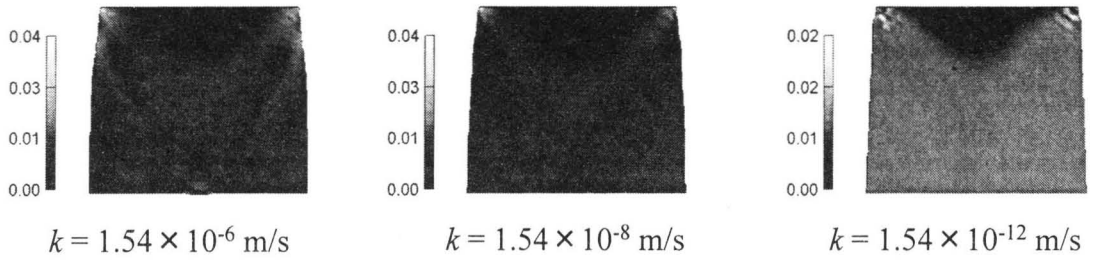

Figure 3.13 Distributions of volumetric viscoplastic strain at an average axial strain of 7%

Figure 3.14 depicts the distributions of accumulated viscoplastic shear strain γ^p at an average axial strain of 7% with different gradient parameters. In this case, $k = 1.54 \times 10^{-10}$(m/s). It can be found from the figure that the thickness, the spacing of the shear bands, and the extent of the strain localization also depend on gradient parameter a_3. The accumulated strain is more localized when gradient parameter a_3 is rather small. This suggests that the gradient term makes the system more stable. The distance between shear bands will decrease with gradient parameter a_3, while the angles of shear bands are consistently 48 degrees.

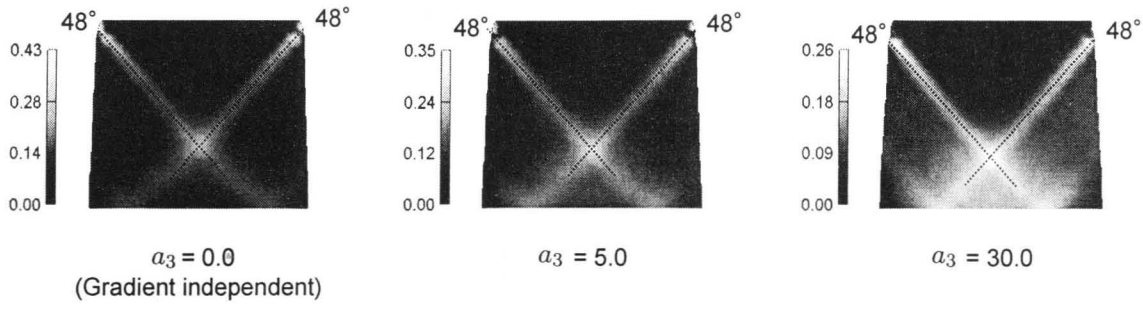

a_3 = 0.0
(Gradient independent)

a_3 = 5.0

a_3 = 30.0

Figure 3.14 Distributions of γ^p at an average axial strain of 7% ($k = 1.54 \times 10^{-10}$ m/s)

3.7 Effects of Partially Drained Conditions on the Strain Localization Analysis

In this section, we will discuss the effects of partially drained conditions on strain localization. **Figure 3.15** shows the boundary conditions for the numerical analysis under partially drained plane strain conditions. The top of the specimen was assumed to be a permeable boundary, while the others were assumed to be impermeable. The gradient parameter a_3 is zero and the coefficient of permeability is $k = 1.54 \times 10^{-8}$(m/s). The other parameters are the same as those shown in **Table 3.1**. A numerical analysis was performed with the displacement rate controlled method using overall strain rates of 0.01%/min, 0.1%/min, 1%/min and 10%/min. As for the end conditions, friction coefficient μ_f between the specimen and the end plate is assumed to be $\mu_f = 0.025$ to trigger the localization.

The relations between the average vertical stress and the strain with different strain rates are shown in **Figure 3.16**. We can see that average stress-strain relations are strongly affected by the strain rate associated with the consolidation of the specimen. In the case of a low strain rate, the clay becomes stronger due to the increase in mean effective stress by consolidation. **Figures 3.17** and **3.18** show the deformed mesh and velocity the vector field at an overall axial strain of 10%, respectively. It is easily seen that the deformation and the displacement vector, at an average axial strain of 10%, are localized in the case of higher strain rates. In contrast, specimens with low strain rates deformed homogeneously. The trend for cases with high strain rates is similar to that for cases with low permeability levels because of the slow dissipation of pore water pressure.

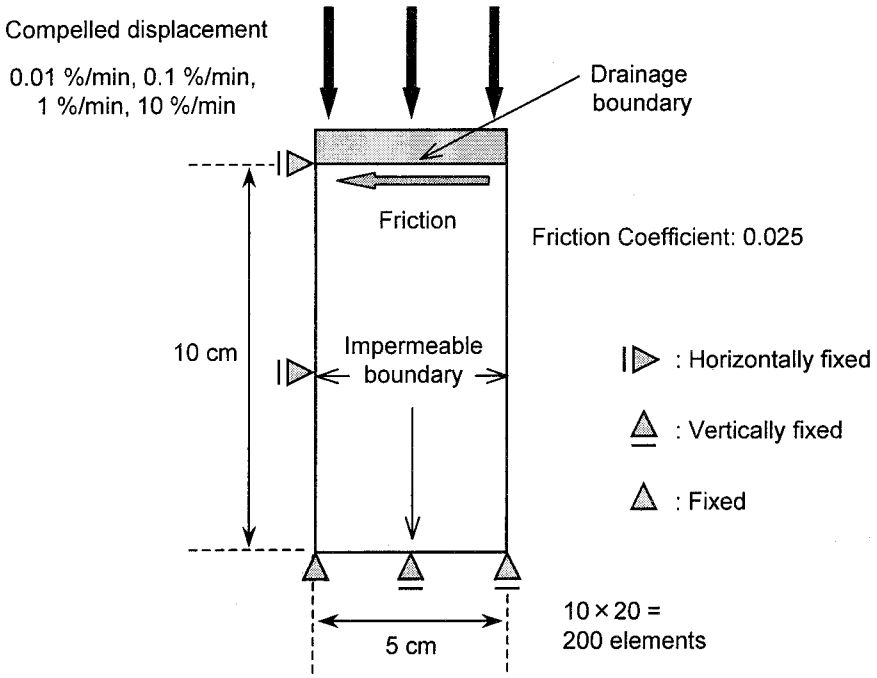

Figure 3.15 Boundary and partially drainage conditions (frictional boundary at the top edge, plane strain condition)

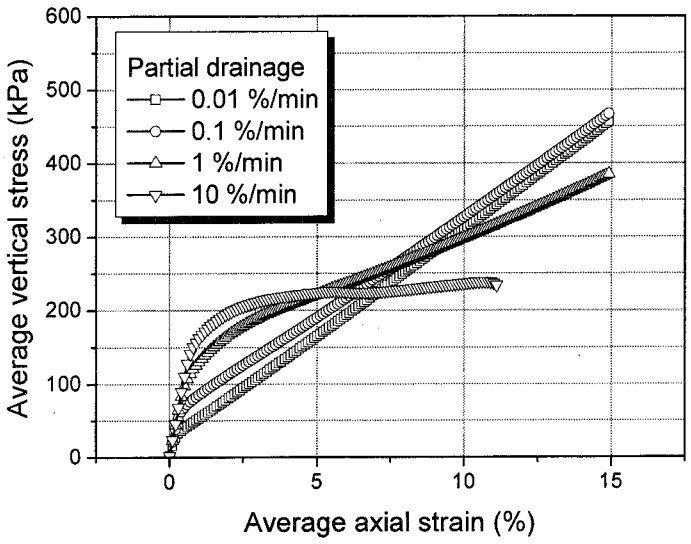

Figure 3.16 Stress-strain relations with different strain rates (partially drained and frictional boundary)

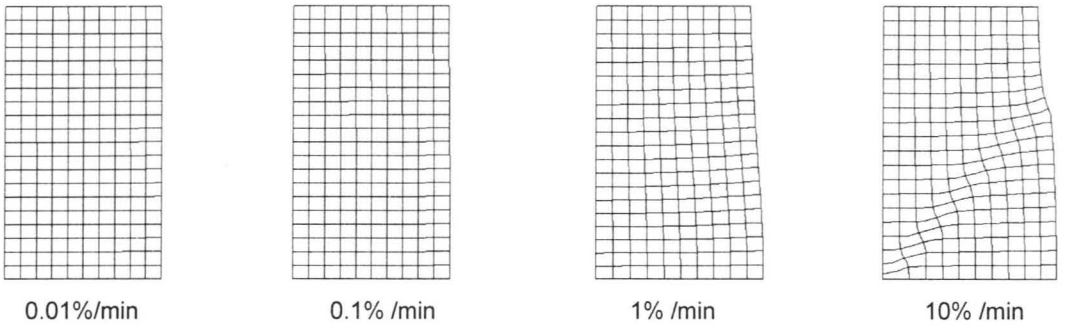

Figure 3.17 Deformed mesh with different strain rates at an average axial strain of 10% (partially drained and frictional boundary)

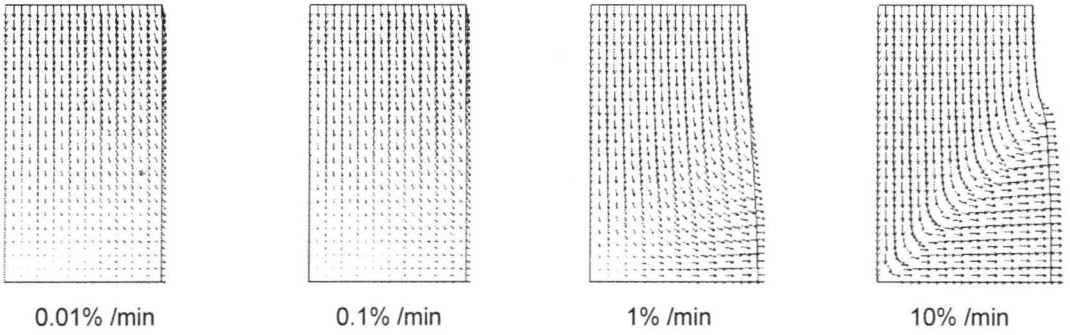

Figure 3.18 Displacement vector with different strain rates at an average axial strain of 10% (partially drained and frictional boundary)

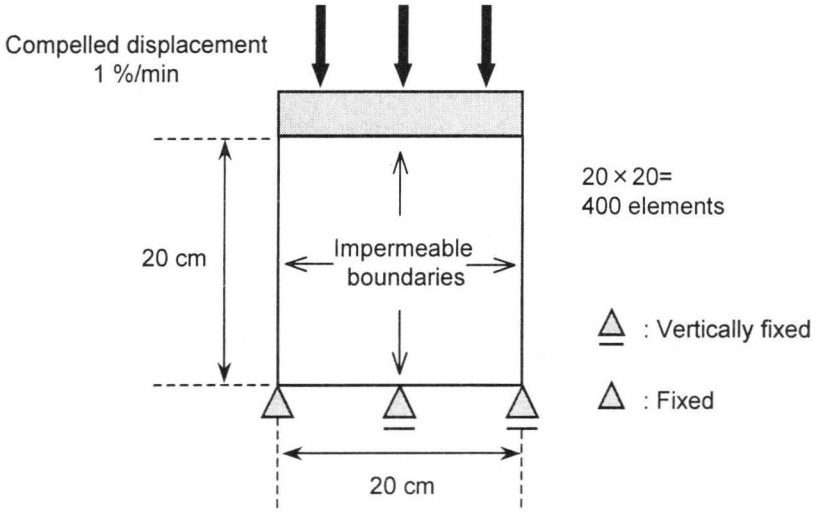

Figure 3.19 Boundary conditions and the size of the specimen (undrained plane strain condition)

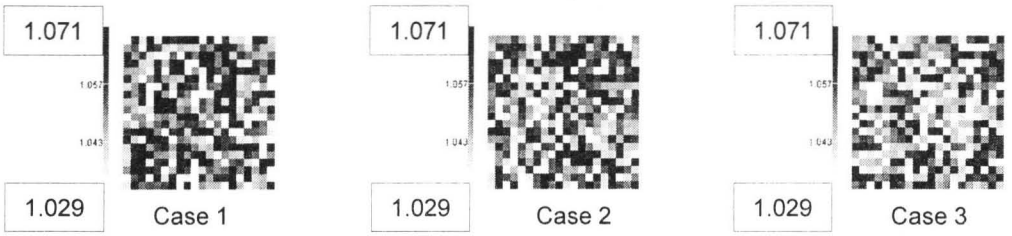

Figure 3.20 Initial distributions of M_f^* ($R = 2.0\%$)

3.8 Effects of Material Heterogeneity on the Strain Localization Analysis

The boundary conditions are shown in **Figure 3.19**, while **Table 3.2** shows material parameters used in the analysis of this section. We assumed three cases of distribution for the stress ratio at failure, M_f^*, as shown in **Figure 3.20**. The perturbation of M_f^* was obtained using a pseudo-random number by the linear congruential method. In **Figure 3.21**, the stress-strain relations for Cases 1 and 3 are obtained by the different ranges in perturbation of M_f^*, R; $R = 0\%$, 0.5%, 1.0%, and 3.0%. $R = 0$ means a homogeneous clay sample. The applied strain rate is 1.0%/min.

Table 3.2 Material parameters for the strain localization analysis of homogeneous and heterogeneous types of clay

Compression index	λ	0.372
Swelling index	κ	0.054
Initial void ratio	e_0	1.28
Initial mean effective stress	σ'_{me}	600 (kPa)
Coefficient of earth pressure at rest	K_0	1.0
Viscoplastic parameter	m'	21.5
Viscoplastic parameter	C	4.5×10^{-8} (1/s)
Stress ratio at failure	M_f^*	1.05
Elastic shear modulus	G	13210 (kPa)
Softening parameter	G_2^*	100
Gradient parameter	a_3	0.0 (m^2)
Coefficient of permeability	k_x=k_y	1.16×10^{-14} (m/s)

The effects of heterogeneity on the stress-strain relations are dependent on the initial distribution of M_f^*. It can be seen in Case 1 that the average vertical stress of the non-homogeneous clay is a little larger than that of the homogeneous clay, but that it becomes smaller at the failure state. On the other hand, the heterogeneous clay in Case 3 shows softening behavior and their average stress is smaller than that of the homogeneous clay. The axial strain at the failure state is consistently smaller as the range of perturbation R is larger. **Figure 3.22** shows the deformed mesh and the distributions of γ^p for homogeneous one and for Case1 with different R at an average axial strain of 10%. Regarding the homogeneous case, deformation and distribution of γ^p are uniform in the specimen. On the contrary, localized deformations are seen in the non-homogeneous clay and the shear band of $R = 3\%$ is clearer than the others. We can also observe in **Figure 3.23** that different modes of deformation appear which are dependent on the initial distribution of M_f^*. Similar results have been obtained by Ehlers and Volk (1998). They showed that a random distribution of the Lamé constant within local deviations of $\pm0.5\%$ provide apparent shear bands under plane strain conditions, although the homogeneous specimens do not.

Next, we consider the frictional boundary as a trigger of the localized deformation shown in **Figure 3.24**. Coefficient of friction μ_f is equal to 0.01. **Figure 3.25** depicts distributions of

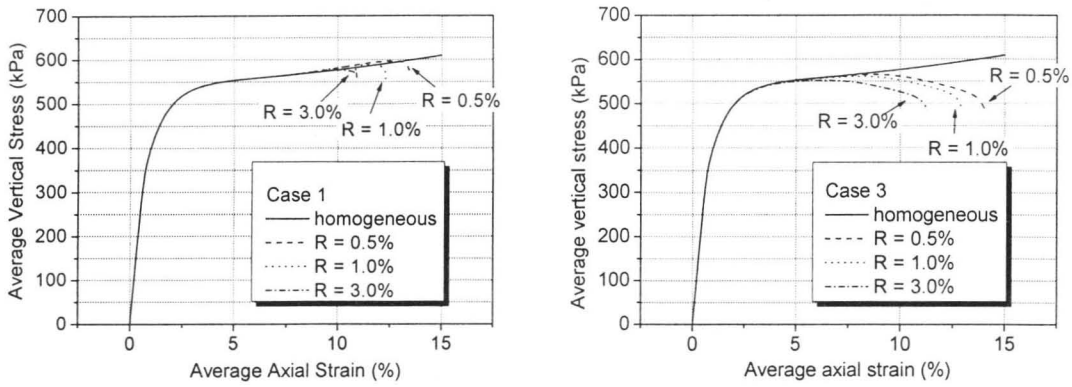

Figure 3.21 Stress-strain curves for Cases 1 and 3 obtained by different R

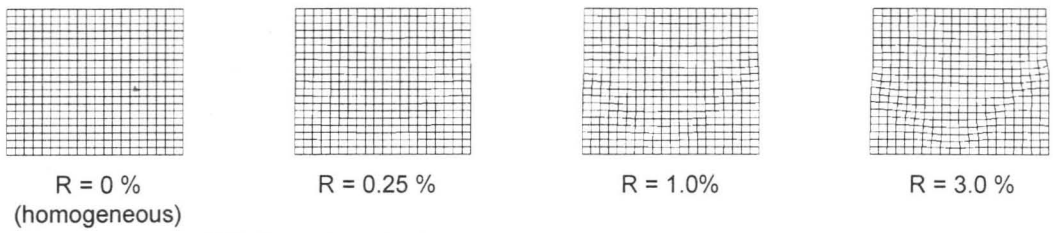

(i)Deformed mesh at an average axial strain of 10%

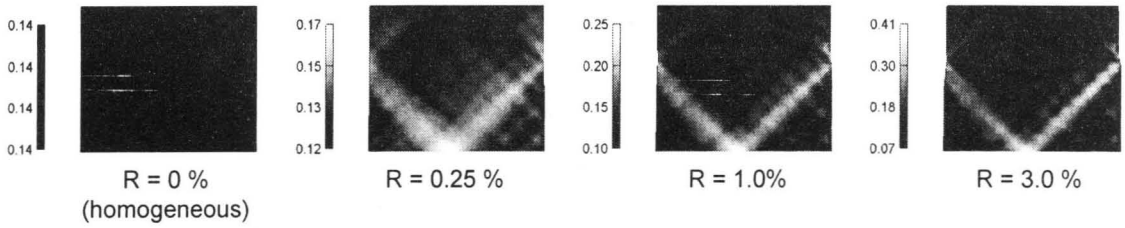

(ii) Distributions of γ^p at an average axial strain of 10%

Figure 3.22 Deformed mesh and the distributions of γ^p for a homogeneous one and for Case 1 with different R

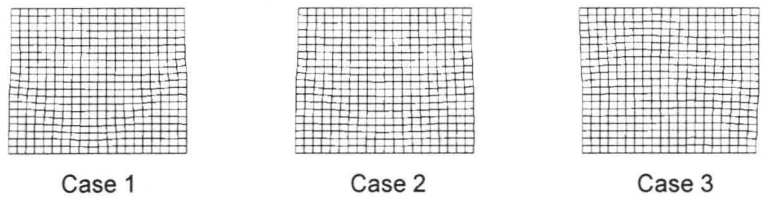

(i) Deformed mesh at an average axial strain of 10%

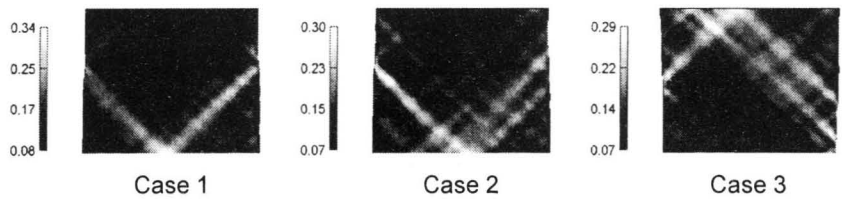

(ii) Distributions of γ^p at an average axial strain of 10%

Figure 3.23 Deformed mesh and the distributions of γ^p for Cases 1, 2, and 3 ($R = 2.0$ %)

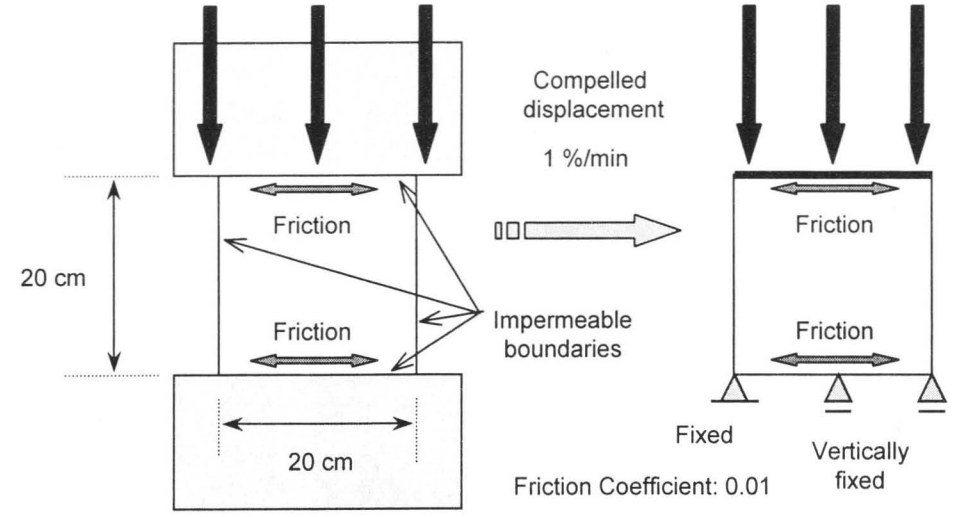

Figure 3.24 Frictional boundary conditions (undrained plane strain conditions, permeable between each element)

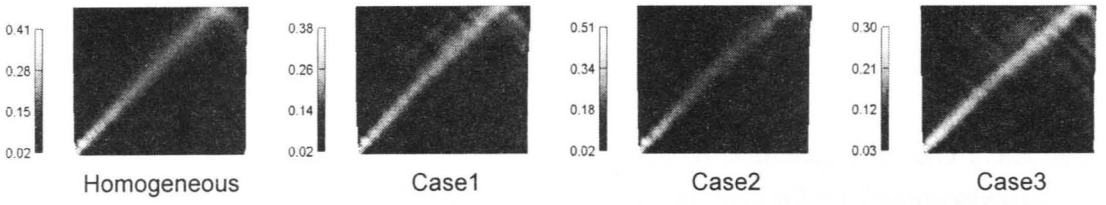

Figure 3.25 Distributions of γ^p for homogeneous and heterogeneous types of clay (frictional boundary, $R = 2.0\%$, axial strain: 8%)

γ^p for homogeneous clay and for three cases of heterogeneous clay with 2.0% of R at an average axial strain of 8%. In the case of the homogeneous clay, the localized deformation from the bottom left-hand side, where the displacement is fixed, can be observed due to the friction force acting on the top and the bottom of the specimen. This type of localized pattern also appears in the heterogeneous clay, in the distribution of γ^p of Case 1 and Case 3. However, it displays rather extensively localized deformation compared with the homogeneous case.

3.9 Summary

In order to study the effects of permeability on the instability of the material system, a soil-water coupled instability analysis is conducted with a simplified gradient-dependent elasto-viscoplastic model. In the hardening range, the growth rate of the perturbation is negative, namely, the material system is stable. In contrast, the material system may become unstable in the softening regime. It was confirmed that materials with higher permeability levels are more unstable than those with lower permeability levels. An instability analysis using a rigid-viscoplastic model gave an additional conclusion that the system is less stable in the hardening regime, when the coefficient of permeability is rather small. In addition, the strain gradient term makes the system

stable if gradient parameter a_3 is large enough.

From the numerical study, it was found that in the range of small strain, i.e., in the viscoplastic strain-hardening range, the viscoplastic material system with low permeability levels is less stable. On the other hand, in the large strain, i.e., in the strain-softening range, the material system is less unstable. These trends are consistent with the theoretical results by the instability analysis. As for the deformation pattern, permeability, namely, pore water transport, has a great influence on the formation of shear bands. When gradient term a_3 is large, the accumulated shear strain is less localized. It was confirmed that the gradient term acts as a stabilizer under globally undrained conditions. Under partially drained conditions, the materials with lower strain rates show consolidation, while the materials with higher strain rates show localized deformation. Material heterogeneity causes strain localization, although the deformation of homogeneous clay becomes uniform. The initial distribution of material parameters affects the deformation pattern.

References

Aifantis, E.C., Oka, F., Yashima, A. and Adachi, T. (1999), Instability of gradient dependent elasto-viscoplasticity for clay, *Int. J. Numerical and Analytical Methods in Geomechanics*, **23**, pp. 973-994.

Belytschko, T., Liu, W.K. and Moran, B. (2000), *Nonlinear Finite Elements for Continua and Structures*, John Wiley & Sons, New York.

Biot, M.A. (1956), Theory of propagation of elastic waves in a fluid-saturated porous solid, *J. Acoustic Society of America*, **28**, 2, pp. 168-178.

Ehlers, W. and Volk, W. (1998), On the theoretical and numerical methods in the theory of porous media based on polar and non-polar elasto-plastic solid materials, *Int. J. Solids and Structures*, **35**, 34-35, pp. 4597-4617.

Finno, R.J., Viggiani, G., Harris, W.W., and Mooney, M.A. (1998), Localization of strains in plane strain compression of sand, *Proc. 4th Int. Workshop on Localization and Bifurcation Theory for Soils and Rocks*, Adachi, T., Oka, F., and Yashima, A. eds., Gifu, Balkema, pp. 249-258.

Higo, Y. (2001), Strain localization analysis of water-saturated clay using an elasto-viscoplastic model, Master's thesis, Kyoto University, Japan, in Japanese.

Jeremić, B. (2002), Draft lecture notes for inelastic finite elements part I, http://sokocalo.engr.ucdavis.edu/~jeremic/CG/LectureNotes01_2up.pdf.

Loret, B. and Prévost, J.H. (1991), Dynamic strain localization in fluid-saturated porous media, *J. Engineering Mechanics*, ASCE, **11**, pp. 177-190.

Mühlhaus, H.-B. and Vardoulakis, I. (1987), The Thickness of Shear Bands in Granular Materials, *Géotechnique*, **37**, pp. 271-283.

Mühlhaus, H.-B. and Aifantis, E.C. (1991), A variational principle for gradient plasticity, *Int. J. Solids and Structures*, **23**, pp. 239-264.

Mühlhaus, H.-B. and Oka, F. (1996), Dispersion and wave propagation in discrete and continuous models for granular materials, *Int. J. Solids and Structures*, **33**, 19, pp. 2841-2858.

Oka, F., Yashima, A. and Kohara, I. (1992a), A finite element analysis of clay foundation based on finite elasto-viscoplasticity, *Proc. 4th Int. Symposium on Numerical Models in Geomechanics*, Swansea, Pande, G.N. and Pietruszczak, S. eds., **2**, Balkema, pp. 915-922.

Oka, F., Yashima, A., Adachi, T. and Aifantis, E.C. (1992b), Instability of gradient dependent viscoplastic model for clay saturated with water and FEM analysis, *Applied Mechanics Reviews*, **45**, 3, pp. 140-148.

Oka, F., Adachi, T. and Yashima, A. (1994), Instability of an elasto-viscoplastic constitutive model for clay and strain localization, *Mechanics of Materials*, **18**, pp. 119-129.

Oka, F., Adachi, T. and Yashima, A. (1995), A strain localization analysis using a viscoplastic softening model for clay, *Int. J. of Plasticity*, **11**, 5, pp. 523-545.

Oka, F., Yashima, A., Sawada, K. and Aifantis, E.C. (2000), Instability of gradient-dependent elastoviscoplastic model for clay and strain localization, *Computer Methods in Applied Mechanics and Engineering*, **183**, pp. 67-86.

Oka, F., Jiang, M. and Higo, Y. (2001), Effect of transport of water on strain localization analysis of fluid-saturated strain gradient dependent viscoplastic geomaterial, *Bifurcation and Localization Theory in Geomechanics*, Proc. 5th IWBL, Perth, 1999, Mühlhaus, H.-B., Dyskin, A.V. and Pasternak, E. eds., Balkema, pp.77-83.

Peirce, D., Shih, C. and Needleman, A. (1984), A tangent modulus method for rate dependent solids, *Computers and Structures*, **18**, 5, pp. 845-887.

Rice, J.R. (1975), On the stability of dilatant hardening for saturated rock masses, *J. Geophysical Research*, **80**, 11, pp. 1531-1536.

Rudnicki, J.W. and Rice, J.R. (1975), Condition for the localization of deformation in pressure-sensitive dilatant material, *J. Mechanics and Physics of Solids*, **23**, pp. 371-394.

Schrefler, B.A., Majorana, C.E. and Sanavia, L. (1995), Shear band localization in saturated porous media, *Achieves of Mechanics*, **47**, 3, pp. 577-599.

Schrefler, B.A., Sanavia, L. and Majorana, C.E. (1996), A multiphase medium model for localization and postlocalization simulation in geomaterials, *Mechanics of Cohesive-Frictional Materials*, **1**, pp. 95-114.

Tamura, T. (2000), *Introduction of continuum mechanics*, Asakura, pp. 137-142, in Japanese.

Tomita, Y. (1990), *Numerical elasto-plastic mechanics*, Yokendo, pp. 106-201, in Japanese.

Vardoulakis, I. and Aifantis, E.C. (1991), A gradient flow theory of plasticity for granular materials, *Acta Mechanica*, **87**, pp. 197-217.

Yatomi, C., Yashima, A., Iizuka, A. and Sano, I. (1989), General theory of shear bands formation by a non-coaxial Cam-clay model, *Soils and Foundations*, **29**, 3, pp. 41-53.

Zhang, H.W. and Schrefler, B.A. (2000), Gradient-dependent plasticity model and dynamic strain localization analysis of saturated and partially saturated porous media: one dimensional model, *European Journal of Mechanics*, A/Solids, **19**, 3, pp. 503-524.

Chapter 4

Elasto-viscoplastic Constitutive Model for both Normally Consolidated Clay and Overconsolidated Clay

4.1 Introduction

It is well known that geomaterials such as soil show changes in volume during shear deformation, called dilatancy. Dilatancy is a typical property of granular materials such as soil and is strongly related to changes in the microstructure. Normally consolidated clay exhibits negative dilatancy or contractancy, namely, decreases in volume during shearing. On the other hand, overconsolidated clay shows positive dilatancy, namely, increases in volume during shearing. **Figure 4.1** shows undrained triaxial compression test results for normally consolidated (NC) and overconsolidated (OC) clay samples by Yashima et al. (1999). As shown in **Figure 4.1**(b), the mean effective stress of normally consolidated clay decreases monotonically due to negative

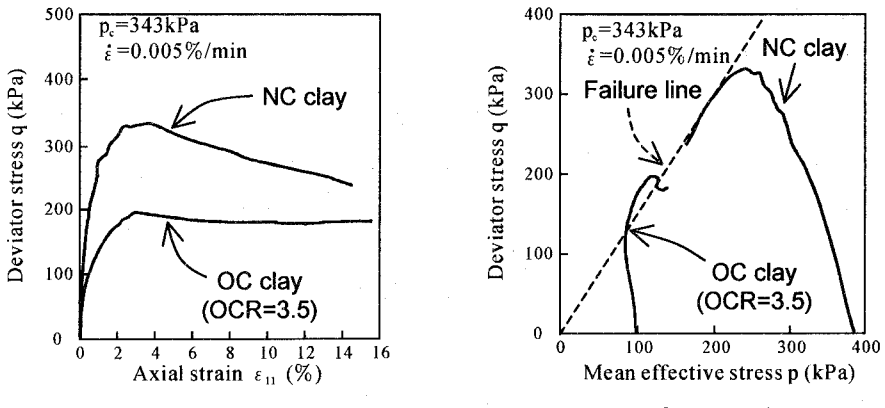

(a)Stress-strain relations (b)Stress paths

Figure 4.1 Stress-strain relations and stress paths of undrained triaxial tests on Osaka Pleistocene clay (Yashima et al. 1999)

dilatancy. On the other hand, the mean effective stress of heavily overconsolidated clay of OCR = 3.5 increases due to positive dilatancy. Another characteristic of clay can be seen in the stress paths (**Figure 4.1**(b)). The stress ratio of normally consolidated clay is always less than that at the failure state. In contrast, the stress path of overconsolidated clay reaches a point over the failure line, and then the stress ratio decreases toward the failure state. These two characteristics should be taken into account in order to develop a constitutive model for overconsolidated clay. In addition, strain-softening behavior can be seen in the stress-strain relations of NC clay and OC clay (**Figure 4.1**(a)).

As for a constitutive model for overconsolidated clay, Adachi and Oka (1984) formulated an elasto-plastic model in a similar manner to that of an elasto-plastic model for sand. An elasto-viscoplastic model for OC clay was proposed by Oka (1982) based on Perzyna's theory. These models successfully describe successfully the dilatancy characteristics of OC clay by assuming a boundary surface between the NC region and the OC region. The former model, however, cannot address the time-dependent behavior, and neither of them consider the material instability, such as the second material function introduced in **Section 2.4**.

In the present study, an elasto-viscoplastic model for both normally consolidated clay and overconsolidated clay with material instability is developed. The model can be seen as an extension of the viscoplastic model for NC clay proposed by Adachi and Oka (1982). In order to address the dilatancy characteristics of OC clay, the following extensions are adopted in the NC model.

1. Non-linear kinematic hardening and a Chaboche type of viscoplasticity theory (Chaboche and Rousselier 1983) is newly adopted. Two hardening parameters are used in the yield function, namely, one depends on the deviatoric strain and the other depends on the volumetric strain. This hardening rule achieves a double hardening model.

2. An overconsolidation boundary surface (Oka 1982) is introduced. The OC boundary surface defines the boundary between the OC and the NC regions and controls the shape of the plastic potential function. Even the plastic yielding inside the boundary surface, i.e., the clay is overconsolidated, is addressed.

3. The second material function is extended using a stress-history ratio (Oka 1985; Adachi and Oka 1995). The second material function defined by the stress ratio is available only in the region where the stress ratio is less than that of the critical state. In general, the stress ratio of OC clay becomes larger than that of the critical state (see **Figure 4.1**(b)). Thus, a new definition for the second material function using a stress-history ratio is adopted.

4.2 Overconsolidation Boundary Surface

In the model, it is assumed that there is an overconsolidation (OC) boundary surface that delineates the overconsolidation region ($f_b < 0$) from the normal consolidation region ($f_b \geq 0$)

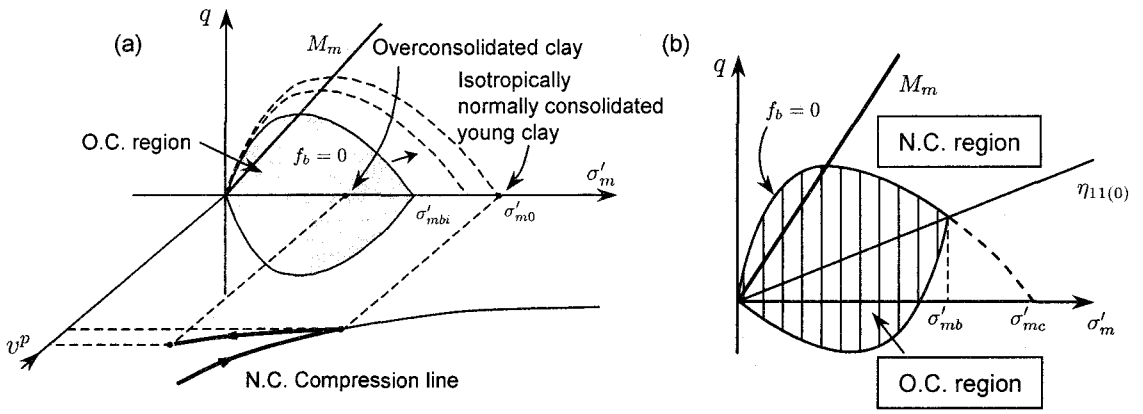

Figure 4.2 Schematic view of the overconsolidation boundary surface under triaxial conditions (a) OC boundary surface for isotropic consolidation, i.e., $\eta_{ij(0)} = 0$, $\sigma'_{mc} = \sigma'_{mb}$, and the relationship between the OC boundary surface, and the compression and the swelling line (b) Anisotropic consolidation

(see **Figure 4.2**). In previous papers (Adachi & Oka 1984; Oka 1992; and Oka et al. 1999), a similar OC boundary surface was used in an elasto-plastic model for sand and overconsolidated clay. The overconsolidation boundary surface was introduced to control the shape of the plastic potential function.

In order to describe the volumetric relaxation and/or the secondary compression under isotropic stress conditions, it is assumed that the stress state of normally consolidated clay is generally outside of the OC boundary surface and defined as

$$f_b = \bar{\eta}^* + M_m^* \ln \frac{\sigma'_m}{\sigma'_{mb}} = 0 \tag{4.1}$$

where $\bar{\eta}^*$ is the relative stress ratio which is the same as that is **Equation** (2.11), η^*_{ij} is the stress ratio tensor, M^*_m is the value of $\eta^* = \sqrt{\eta^*_{ij}\eta^*_{ij}}$ at maximum compression, and σ'_m is the mean effective stress. (0) denotes the state at the end of consolidation, in other words, the initial state before deformation occurs.

σ'_{mb} controls the size of the surface and σ'_{mbi} is the initial value of σ'_{mb}, which is defined as the isotropic consolidation yield stress.

$$\sigma'_{mb} = \sigma'_{mbi} \exp\left(\frac{1+e}{\lambda-\kappa}\,\varepsilon^{vp}_{kk}\right) \tag{4.2}$$

where λ is the compression index, e is the void ratio, and ε^{vp}_{kk} is the viscoplastic volumetric strain.

$$\sigma'_{mc} = \sigma'_{mb} \exp\left(\frac{\eta^*_{(0)}}{M^*_m}\right) = \sigma'_{mbi} \exp\left(\frac{1+e}{\lambda-\kappa}\varepsilon^{vp}_{kk}\right) \exp\left(\frac{\eta^*_{(0)}}{M^*_m}\right) \tag{4.3}$$

in which σ'_{mc} denotes the mean effective stress at the intersection of the overconsolidation boundary surface and the σ'_m axis. In **Figure 4.2**(b), $\eta_{11(0)} (= \sqrt{3/2}\eta^*_{11(0)})$ stands for the anisotropic consolidation history.

4.3 Yield Function

Yield function f_y with two nonlinear kinematic hardening parameters, namely, x^*_{ij} and y^*_m, is given by

$$f_y = \bar{\eta}^*_x + \tilde{M}^* \left(\ln \frac{\sigma'_m}{\sigma'_{ma}} - y^*_m \right) = 0 \tag{4.4}$$

$$\bar{\eta}^*_x = \left\{ \left(\eta^*_{ij} - x^*_{ij} \right) \left(\eta^*_{ij} - x^*_{ij} \right) \right\}^{\frac{1}{2}} \quad , \quad \eta^*_{ij} = \frac{S_{ij}}{\sigma'_m} \tag{4.5}$$

where σ'_{ma} is taken as the initial value of the mean effective stress and $\tilde{M}^*$ is a coefficient of dilatancy given by **Equations** (4.13) and (4.14).

Herein, two strain-hardening parameters are used in the model, namely, x^*_{ij}, which depends on the viscoplastic shear strain rate, and y^*_m, which is related to volumetric viscoplastic strain ε^{vp}_{kk}. The nonlinear evolutional equations for x^*_{ij} and y^*_m are given by

$$dx^*_{ij} = B^*_1 \left(A^*_1 de^{vp}_{ij} - x^*_{ij} d\gamma^p \right) \tag{4.6}$$

$$de^{vp}_{ij} = d\varepsilon^{vp}_{ij} - \frac{1}{3} d\varepsilon^{vp}_{kk} \delta_{ij} \quad , \quad d\gamma^p = \sqrt{de^{vp}_{ij} de^{vp}_{ij}} \tag{4.7}$$

$$dy^*_m = dy^*_{m1} + dy^*_{m2} \tag{4.8}$$

$$dy^*_{m1} = B^*_2 \left(A^*_2 d\varepsilon^{vp}_{kk} - y^*_{m1} |d\varepsilon^{vp}_{kk}| \right) \tag{4.9}$$

$$dy^*_{m2} = \frac{1+e}{\lambda - \kappa} d\varepsilon^{vp}_{kk} \tag{4.10}$$

where A^*_1, A^*_2, B^*_1, and B^*_2 are material parameters and $A^*_1 (= M^*_f)$ is the value of η^* at the failure state.

In the case of this hardening model, we cannot define a scalar hardening parameter such as in **Equations** (2.12) and (2.13). Hence, static yield function f_y and dynamic yield function f_d cannot be formulated respectively. f_y plays the role of overstress, i.e., $f_d - f_s$, and $f_y = 0$ demonstrates a static yield function.

4.4 Plastic Potential Function

The plastic potential is given by the following equation, which is similar to the yield function given in **Equation** (4.4):

$$f_p = \bar{\eta}^*_x + \tilde{M}^* \left(\ln \frac{\sigma'_m}{\sigma'_{mp}} - y^*_m \right) = 0 \tag{4.11}$$

$$\bar{\eta}^*_x = \left\{ \left(\eta^*_{ij} - x^*_{ij} \right) \left(\eta^*_{ij} - x^*_{ij} \right) \right\}^{\frac{1}{2}} \quad , \quad \eta^*_{ij} = \frac{S_{ij}}{\sigma'_m} \tag{4.12}$$

where σ'_{mp} is a material parameter, herein taken to be equal to the initial value of σ'_m. $\tilde{M}^*$ depends on the overconsolidation boundary surface given by **Equation** (4.1). In the OC region, $f_b < 0$; in the NC region, $f_b \geq 0$ and $\tilde{M}^*$ is defined as follows:

$$f_b < 0 \quad \text{(OC region)}; \quad \tilde{M}^* = -\frac{\bar{\eta}^*}{\ln\left(\sigma'_m/\sigma'_{mc}\right)} \tag{4.13}$$

$$f_b \geq 0 \quad \text{(NC region)}; \quad \tilde{M}^* = M_m^* \tag{4.14}$$

in which σ'_{mc} is the mean effective stress at the intersection of the overconsolidation boundary surface and the σ'_m axis given by **Equation** (4.3).

4.5 Second Material Function Based on a Stress-history Ratio

A second material function, Φ_2, which is dependent on the internal state variables, is chosen to control the failure state. In the same way as in the model for NC clay, it is assumed that Φ_2 becomes infinite at failure, i.e.,

$$\Phi_2(\xi) = 1 + \xi \tag{4.15}$$

in which ξ is an internal variable.

In general, ξ follows an evolutional equation whose integrated form, satisfying the above-mentioned failure requirement for the internal variable, is given by

$$\xi = \frac{M_f^* \bar{\eta}_{x(0)}^{**}}{G_2^* \left\{ M_f^* - \dfrac{\eta_{mn}^{**}(\eta_{mn}^{**} - x_{mn}^*)}{\bar{\eta}_x^{**}} \right\}} \tag{4.16}$$

where G_2^* is a parameter for the second material function and M_f^* is the value of the stress invariant ratio at failure and

$$\bar{\eta}_x^{**} = \left\{ \left(\eta_{ij}^{**} - x_{ij}^*\right)\left(\eta_{ij}^{**} - x_{ij}^*\right) \right\}^{\frac{1}{2}}, \quad \eta_{ij}^{**} = \frac{S_{ij}^*}{\sigma_m^*} \tag{4.17}$$

$$\bar{\eta}_{x(0)}^{**} = \left\{ \left(\eta_{ij}^{**} - x_{ij(0)}^*\right)\left(\eta_{ij}^{**} - x_{ij(0)}^*\right) \right\}^{\frac{1}{2}} \tag{4.18}$$

where η_{ij}^{**} is the stress-history ratio tensor, S_{ij}^* and σ_m^* are the deviatoric and the mean components of stress-history tensor σ_{ij}^*, respectively, and $x_{ij(0)}^*$ denotes the initial value of x_{ij}^*.

Furthermore, stress-history tensor σ_{ij}^* is defined as

$$\sigma_{ij}^* = \frac{1}{\tau}\int_0^z \exp\left(-(z - z')/\tau\right)\sigma_{ij}(z')dz', \qquad 0 \leq z' < z \tag{4.19}$$

$$z = \int_0^t dz', \qquad dz' = \sqrt{de_{ij}de_{ij}} \tag{4.20}$$

where t is time, de_{ij} is the increment in deviatoric total strain, and τ is a material parameter.

The stress-history tensor was advocated by Oka (1985) and Adachi and Oka (1995). In their theory, both the yield and the hardening functions depend on the stress history rather than on the real stress in order to describe the strain-softening behavior of geomaterials.

In the case of compressive shear deformation, that is, the stress ratio increases and is positive, the stress-history ratio is always less than the stress ratio, so that when the stress history approaches the critical state, the stress ratio will become larger than the stress ratio at failure. Additionally, **Equations** (4.15) and (4.16) provide that Φ_2 becomes infinity when the stress-history ratio is close to the stress ratio at failure. From the assumption that the second material function, Φ_2, is a function of stress-history ratio tensor η_{ij}^{**}, it becomes possible to describe the material behavior in which the stress path can reach a point over the failure line. This type of behavior is dominant for overconsolidated clay as was revealed in the experiments (see, for example, **Figure 4.1**(b)).

4.6 Viscoplastic Flow Rule

A viscoplastic flow rule is given by

$$\dot{\varepsilon}_{ij}^{vp} = C_{ijkl} \langle \Phi_1 (f_y) \rangle \Phi_2(\xi) \frac{\partial f_p}{\partial \sigma'_{kl}} \tag{4.21}$$

$$C_{ijkl} = a\delta_{ij}\delta_{kl} + b(\delta_{ik}\delta_{jl} + \delta_{il}\delta_{jk}), \qquad C_{o1} = 2b,\ C_{o2} = 3a + 2b \tag{4.22}$$

in which <> is the Macauley's bracket defined in **Equation** (2.7), C_{o1} and C_{o2} are viscoplastic parameters, $C_{ijkl} \langle \Phi_1 (f_y) \rangle$ denotes a function for strain rate sensitivity, f_y is the yield function, f_p is the plastic potential function, and Φ_2 controls the failure state where deviatoric strain becomes infinite.

In a similar manner to the model for NC clay (see **Equation** (2.16)), Φ_1 is defined based on the experimental results of the strain-rate constant triaxial tests, namely,

$$\Phi_1(f_y) = \sigma'_m \exp(m' f_y), \tag{4.23}$$

where m' is the viscoplastic parameter for a given degree of rate sensitivity.

Using the flow rule and the plastic potential function, we obtain the deviatoric viscoplastic strain rates $\dot{e}_{ij}^{vp}$ and the volumetric viscoplastic strain rate $\dot{\varepsilon}_{kk}^{vp}$ as

$$\dot{e}_{ij}^{vp} = C_{o1} \exp\left[m' \left\{ \bar{\eta}_x^* + \tilde{M}^* \left(\ln \frac{\sigma'_m}{\sigma'_{ma0}} - y_m^* \right) \right\} \right] \Phi_2(\xi) \frac{\left(\eta_{ij}^* - x_{ij}^* \right)}{\bar{\eta}_x^*} \tag{4.24}$$

$$\dot{\varepsilon}_{kk}^{vp} = C_{o2} \exp\left[m' \left\{ \bar{\eta}_x^* + \tilde{M}^* \left(\ln \frac{\sigma'_m}{\sigma'_{ma0}} - y_m^* \right) \right\} \right] \Phi_2(\xi) \left\{ \tilde{M}^* - \frac{\eta_{mn}^* (\eta_{mn}^* - x_{mn}^*)}{\bar{\eta}_x^*} \right\} \tag{4.25}$$

From **Equation** (4.25), it is seen that the sign for the volumetric inelastic strain rate depends on the stress state even inside the overconsolidation boundary surface. This is because the volumetric strain depends on the value of $\tilde{M}^*$ given by **Equations** (4.13) and (4.14), and inside the overconsolidation boundary surface, $\tilde{M}^*$ is a function of σ'_{mc} defined by **Equation** (4.3), which is related to the shape of the overconsolidation boundary surface shown in **Figure 4.2**.

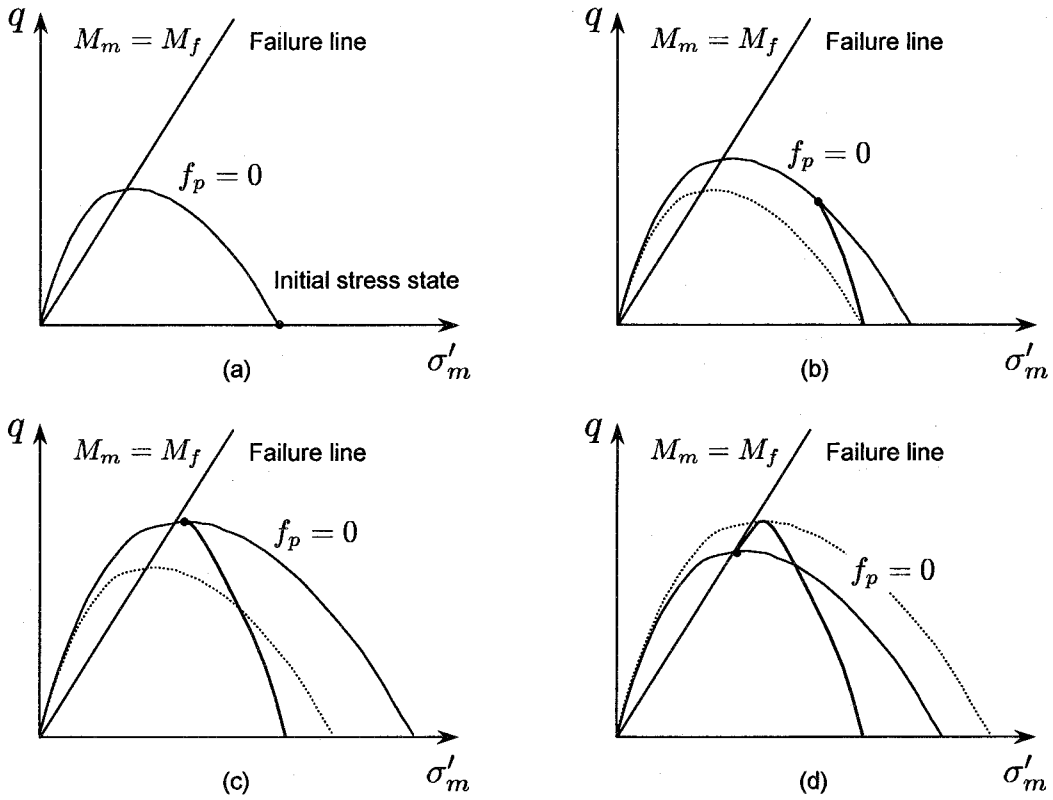

Figure 4.3 Schematic figures of undrained triaxial test for NC clay

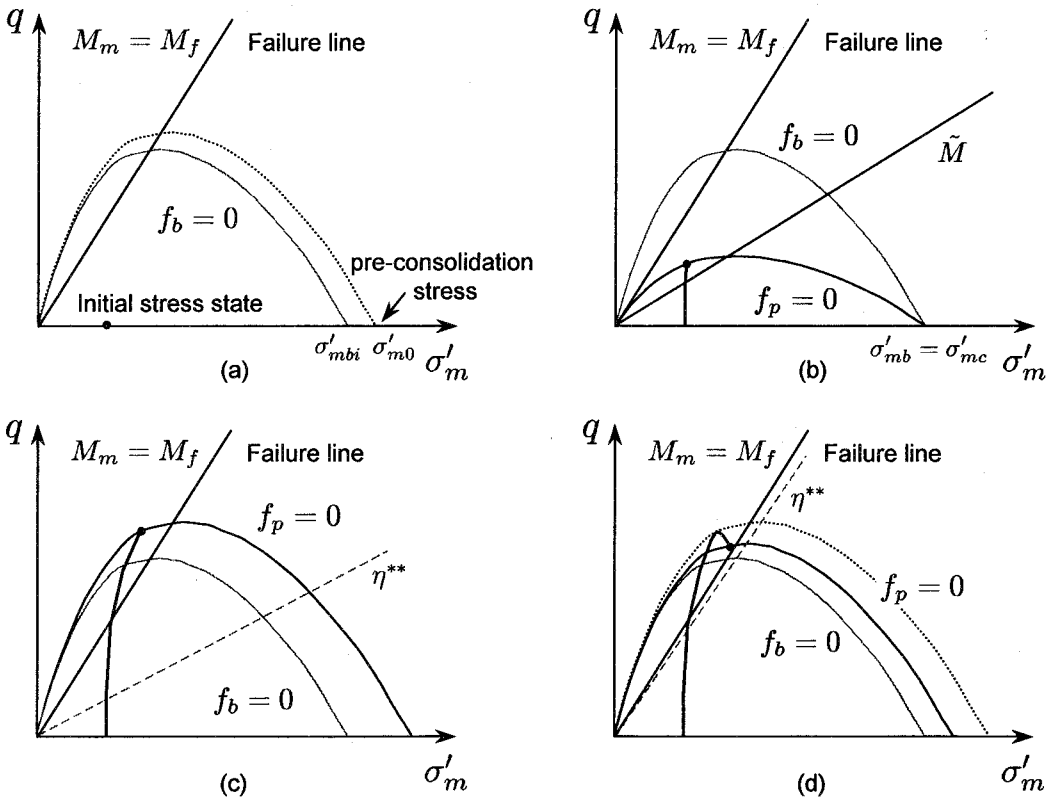

Figure 4.4 Schematic figures of undrained triaxial test for OC clay

The elastic strain rate tensor is the same as that introduced in **Equation** (2.3), and an additive decomposition of the total strain rate into the elastic strain rate and the viscoplastic strain rate is assumed.

Figures 4.3 and **4.4** schematically illustrate the stress paths of NC clay and OC clay, the overconsolidation boundary surface $f_b = 0$, and the plastic potential $f_p = 0$ under undrained triaxial compression test conditions. No kinematic hardening, i.e., $x^*_{ij} = 0$, isotropic consolidation, i.e., $\eta^*_{ij(0)} = 0$ and $M^*_m = M^*_f$ are assumed. q is the deviator stress, σ'_m is the mean effective stress, $\tilde{M} = \sqrt{3/2}\tilde{M}^*$, $M_m = \sqrt{3/2}M^*_m$, and $M_f = \sqrt{3/2}M^*_f$. In the case of NC clay, the stress ratio increases monotonically from the initial value of zero with isotropic hardening (**Figures 4.3**(a) and (b)). When the stress ratio approaches M_f (c), second material function Φ_2 becomes large, and then strain softening occurs (d).

Table 4.1 Material parameters used in the calculations

Parameter		N.C. clay	O.C. clay
Compression index	λ	0.172	0.172
Swelling index	κ	0.054	0.054
Initial void ratio	e_0	0.72	0.72
Initial mean effective stress	σ'_{me}	392 (kPa)	100 (kPa)
Parameter of O.C. boundary surface	σ'_{mbi}	392 (kPa)	392 (kPa)
Viscoplastic parameter	m'	21.5	21.5
Viscoplastic parameter	C_{o1}	4.5×10^{-8} (1/s)	4.5×10^{-8} (1/s)
Viscoplastic parameter	C_{o2}	4.5×10^{-8} (1/s)	4.5×10^{-8} (1/s)
Stress ratio ($\sqrt{2J_2}/\sigma'_m$) at failure	M^*_f	1.05	1.05
Stress ratio ($\sqrt{2J_2}/\sigma'_m$) at maximum compression	M^*_m	1.05	1.05
Elastic shear modulus	G	5500 (kPa)	5500 (kPa)
Softening parameter	G^*_2	100	1
Kinematic hardening parameter	B^*_1	0.0	0.5
Kinematic hardening parameter†	A^*_2	0.0	0.0
Kinematic hardening parameter†	B^*_2	0.0	0.0
Retardation parameter	τ	1.0×10^{-3}	0.2

†A^*_2 and B^*_2 were not used in the present analysis.

In the case of OC clay, the initial stress state is inside the OC boundary surface, which is pre-consolidated and unloaded isotropically. σ'_{mbi} is the initial value for σ_{mb}, namely, the consolidation yield stress is less than pre-consolidation stress σ'_{m0} (**Figure 4.4**(a)). As shown in **Figure 4.4**(b), plastic potential f_p is rather flat when stress state is in the OC region. Thus, the deviatoric component of the viscoplastic strain increment is dominant due to the flow rule. On the other hand, the volumetric component is smaller than the deviatoric one. Hence, changes in the mean effective stress are small and the stress path goes on rather vertically. The shape of f_p becomes close to the OC boundary surface as the stress ratio becomes larger. Once the stress state goes out of the OC boundary (**Figure 4.4**(c)), i.e., the NC region, $\tilde{M}$ becomes a constant value for M_m so that f_p is isotropically hardened with a similar shape to that of f_b. The stress ratio can become larger than M_f, unless stress-history ratio η^{**}, always less than stress ratio,

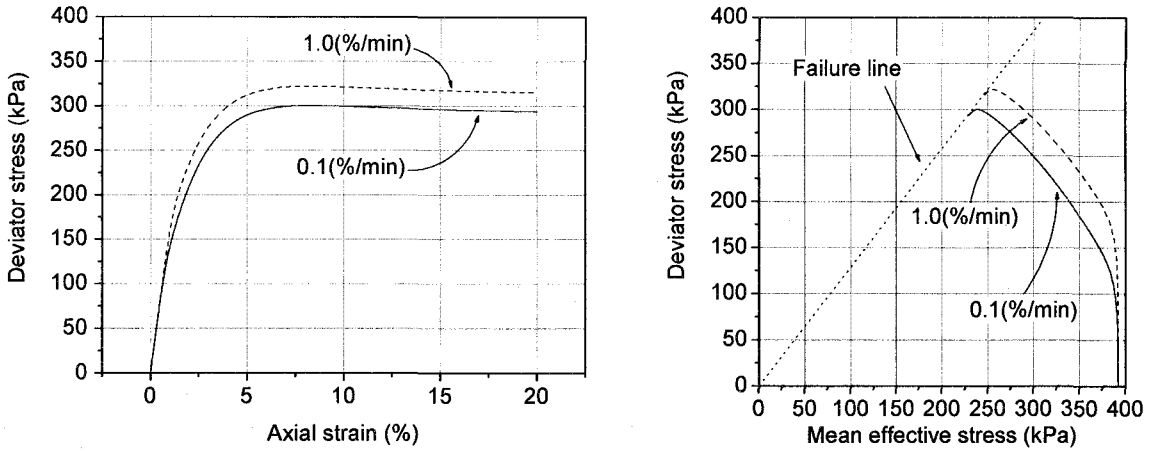

(a) Stress-strain relations (N.C. clay) (b) Stress paths (N.C. clay)

Figure 4.5 Stress-strain relations and stress paths of N.C. clay (Oka et al. 2002)

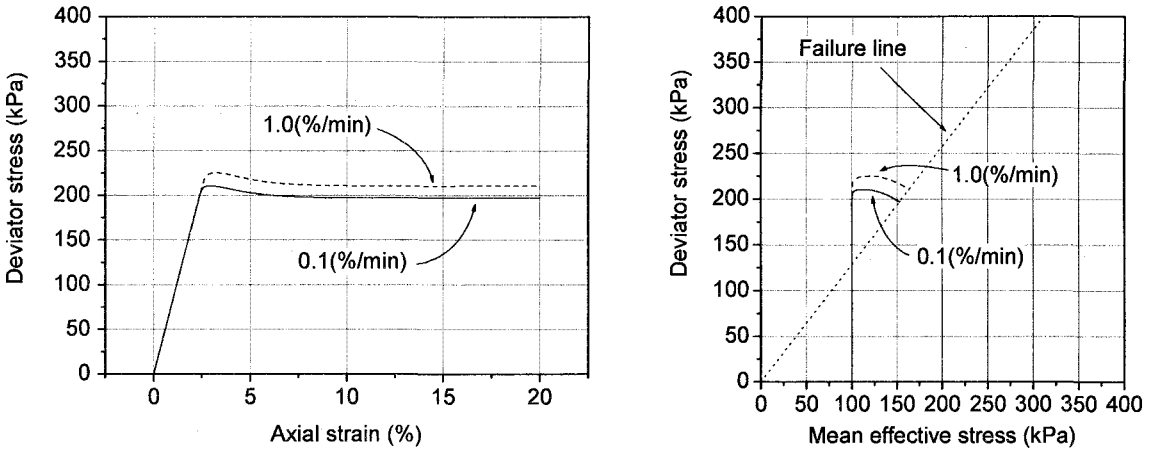

(a) Stress-strain relations (O.C. clay) (b) Stress paths (O.C. clay)

Figure 4.6 Stress-strain relations and stress paths of O.C. clay (Oka et al. 2002)

becomes larger than M_f. When η^{**} approaches M_f, as shown in **Figure 4.4**(d), the value of the second material function becomes large and strain softening occurs.

Figures 4.5 and **4.6** show the stress-strain relations and the stress paths under undrained triaxial compression conditions. **Table 4.1** lists the sixteen material parameters, including two parameters of the initial conditions, that were used in the analysis in which a linear kinematic hardening equation is assumed for changes in the mean effective stress. Three parameters are different for the overconsolidated clay and the normally consolidated clay. This means that the magnitude of strain softening and kinematic hardening depends on the magnitude of overconsolidation. Following the tradition of soil mechanics, compression is denoted as being positive in the table and in the figures. Both the strain rate effect and the strain-softening behavior are observed in **Figures 4.5** and **4.6**. From the stress paths, it is seen that the mean

effective stress increases due to positive dilatancy for overconsolidated clay, while the mean effective stress decreases due to negative dilatancy for normally consolidated clay.

4.7 Summary

In this chapter, an elasto-viscoplastic constitutive model for both normally consolidated clay and overconsolidated clay was derived by extending the elasto-viscoplastic model for normally consolidated clay introduced in **Chapter 2**. The newly-developed model is based on a Chaboche type of viscoplasticity theory, uses the overconsolidation boundary, and includes the second material function, which describes the material instability defined by stress-history ratio. The material instability of this model will be discussed in the next chapter. The proposed model can very well reproduce both positive and negative dilatancy characteristics, which are important characteristics of soil, as well as the time-dependent behavior of clay.

References

Adachi, T. and Oka, F. (1982), Constitutive equations for normally consolidated clay based on elasto-viscoplasticity, *Soils and Foundations*, **22**, 4, pp. 57-70.

Adachi, T. and Oka, F. (1984), Constitutive equations for sands and overconsolidated clays and assigned works for sand, *Proc. Int. Workshop on Constitutive Relations for Soils*, Grenoble, 1982, Gudehus, G. and Darve, F. eds., Balkema, pp. 141-157.

Adachi, T. and Oka, F. (1995), An elasto-plastic constitutive model for soft rock with strain softening, *Int. J. Numerical and Analytical Methods in Geomechanics*, **19**, pp. 233-247.

Chaboche, J.L. and Rousselier, G. (1983), On the plastic and viscoplastic constitutive equations-Part I: Rules developed with internal variable concept, *J. Pressure Vessel Technology*, ASME, **105**, pp. 103-158.

Oka, F. (1982), Elasto-viscoplastic constitutive equation for overconsolidated clay, *Proc. 1st Int. Symp. on Numerical Models in Geomechanics*, Zurich, Dungar, R., Pande, G.N. and Studer, J.A. eds., Balkema, pp. 147-156.

Oka, F. (1985), Elasto/viscoplastic constitutive equations with memory and internal variables, *Computers and Geotechnics*, **1**, pp. 59-69.

Oka, F. (1992), A cyclic elasto-viscoplastic constitutive model for clay based on the non-linear-hardening rule, *Proc. 4th Int. Symp. on Numerical Models in Geomechanics*, Swansea, Pande, G.N. and Pietruszczak, S. eds., 1, Balkema, pp. 105-114.

Oka, F., Yashima, A., Tateishi, A., Taguchi, Y. and Yamashita, S. (1999), A cyclic elasto-plastic constitutive model for sand considering a plastic-strain dependence of the shear modulus, *Géotechnique*, **49**, 5, pp. 661-680.

Oka, F., Higo, Y. and Kimoto, S. (2002), Effect of dilatancy on the strain localization of water-saturated elasto-viscoplastic soil, *Int. J. Solids and Structures*, **39**, pp. 3625-3647.

Yashima, A., Shigematsu, H., Oka, F. and Nagaya, J. (1999), Mechanical behavior and microstructure of Osaka upper-most Pleistocene marine clay, *J. Geotechnical Engineering*, JSCE, 624, III-47, pp. 217-229 (in Japanese).

Chapter 5

Effect of Dilatancy on the Strain Localization of Water-saturated Elasto-viscoplastic Soil

5.1 Introduction

It is well known that geomaterials with a particulate microstructure, such as soil, show increases in volume during shearing deformation; this is called dilatancy. Normally consolidated clay exhibits decreases in volume, i.e., negative dilatancy or contractancy. Overconsolidated clay shows increases in volume, i.e., positive dilatancy. Clay is referred to as "normally consolidated clay", in the classical sense, if the present effective stress is the maximum stress it has ever experienced in its entire history. The clay is called "overconsolidated clay" if it has been subjected to an effective stress greater than the present one. Improvements to the classical definitions are such that the present stress of overconsolidated clay is less than the consolidation yield stress, while the present stress of normally consolidated clay is equal to the consolidation yield stress.

The above discussion prompts the following question. How do both positive and negative dilatancies affect strain localization phenomena? The answer lies in a detailed study that must include comprehensive comparisons between numerical predictions and experimental results. For this purpose, an elasto-viscoplastic model for water-saturated clay has been proposed in the last chapter based on a Chaboche type of viscoplastic theory (Chaboche 1983) and the kinematic hardening rule with viscoplastic softening. The developed model can describe both negative and positive dilatancy characteristics.

The strain localization problem was numerically studied for water-saturated normally consolidated clay by Oka et al. (1994, 1995). They found that strain localization is closely linked to material instability, and can be simulated with a viscoplastic softening model. In previous studies, a model which can reproduce only negative dilatancy, such as in the case of normally consolidated clays, was used. In this study, the effects of dilatancy and permeability on strain

localization are numerically studied using the newly developed elasto-viscoplastic model which can be applied to both normally consolidated clay and overconsolidated clay. Numerical solutions for the plane strain compression problems of water-saturated clay are obtained via the finite element method in a similar manner to that in **Section 3.3**. In this chapter, firstly, the instability of the model under undrained triaxial conditions is discussed. Secondly, a discussion on the numerical results of the clay behavior under plane strain conditions, which highlights the effect of dilatancy on strain localization, follows.

5.2 Instability of the Constitutive Model

Oka et al. (1995) studied the instability of the viscoplastic model in terms of undrained creep failure for normally consolidated clay. An instability analysis for both normally consolidated clay and overconsolidated clay, considering structural changes has been conducted by Kimoto (2002) in which undrained triaxial creep conditions were adopted. Furthermore, Kimoto et al. (2004; to appear) have investigated strain localization problems using the structure change model.

In order to discuss the instability of the proposed viscoplastic model, we herein consider the response of the model under conventional triaxial undrained creep conditions (see **Figure 5.1**) using the method by Oka et al. (1995) and Kimoto (2002). Under undrained creep conditions, a constant deviatoric stress is maintained, although the mean effective stress may change due to the undrained conditions that require a total of zero for the volumetric strain rate.

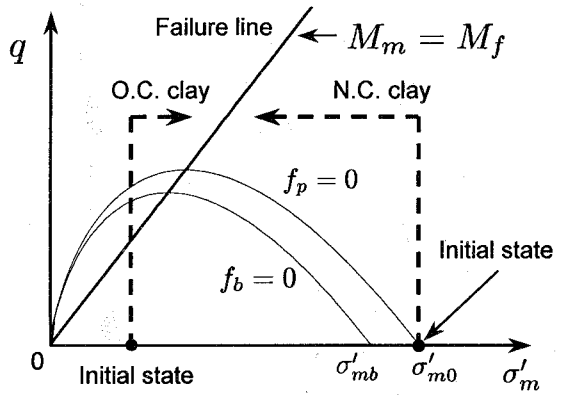

Figure 5.1 Stress paths of undrained creep for N.C. and O.C. clay samples under triaxial conditions

Under the axisymmetric triaxial testing conditions ($\sigma'_{11} > \sigma'_{22} = \sigma'_{33}$, $\sigma'_{ij} = 0$ $(i \neq j)$), the deviator stress is expressed by q which is defined as

$$q = \sigma'_{11} - \sigma'_{22} \tag{5.1}$$

Since the total volumetric strain is zero, the following relation is obtained after integration, that is:

$$\varepsilon^{vp}_{kk} = -\varepsilon^{e}_{kk} = -\frac{\kappa}{(1+e)} \ln \frac{\sigma'_m}{\sigma'_{me}} \tag{5.2}$$

where σ'_{me} is the initial value of the mean effective stress.

Herein, the following variables are used under the triaxial conditions:

$$\eta = \sqrt{3/2}\,\eta^*_{11} = q/\sigma'_m\ , \quad x_{11} = \sqrt{3/2}\,x^*_{11} \tag{5.3}$$

For simplicity, we assume that $M_f = M_m = M$ ($M_f = \sqrt{3/2}\,M^*_f$ and $M_m = \sqrt{3/2}\,M^*_m$).

Under undrained triaxial conditions, and disregarding the deviatoric elastic strain rate, viscoplastic axial strain rate $\dot{\varepsilon}^{vp}_{11}$ becomes

$$\dot{\varepsilon}^{vp}_{11} = C\Phi_2 \exp\left[m'\left(\frac{1}{M}(\eta - x_{11}) + \ln \sigma_m/\sigma'_{me} - y_m\right)\right] \tag{5.4}$$

Finally, the evolutional equations for the two hardening parameters, x_{11} and y_m, are given by

$$\dot{x}_{11} = B(A - x_{11})\dot{\varepsilon}^{vp}_{11} \tag{5.5}$$

$$\dot{y}_m = y_{m2} = A_3\dot{\varepsilon}^{vp}_{kk} \tag{5.6}$$

where $B = \sqrt{3/2}\,B^*$, $A = \sqrt{3/2}\,A^* = M_f$, $y_{m1} = 0$, and A_3 is the volumetric hardening parameter given by

$$A_3 = \frac{1+e}{\lambda - \kappa}. \tag{5.7}$$

Let us calculate a rate of strain rate denoted by $\ddot{\varepsilon}^{vp}_{11}$. By examining the sign for the rate of strain rate $\ddot{\varepsilon}^{vp}_{11}$, we can estimate the stability of the material system. For example, if the rate of strain rate is positive, the material undergoes a creep failure.

Upon time differentiation of a viscoplastic strain rate without a second material function, the rate of strain rate is obtained as

$$\ddot{\varepsilon}^{vp}_{11} = -m'a(\dot{\varepsilon}^{vp}_{11})^2 \tag{5.8}$$

$$a = \left[\frac{1+e}{M\kappa}(\eta - M)(\eta - \frac{\lambda}{\lambda - \kappa}M) + \frac{B}{M}(A - x_{11})\right] \tag{5.9}$$

In the above derivation, the stress dilatancy relation

$$\frac{\dot{\varepsilon}^{vp}_{kk}}{\dot{\varepsilon}^{vp}_{11}} = M - \eta \tag{5.10}$$

and the undrained conditions

$$\dot{\varepsilon}^{vp}_{kk} = -\frac{\kappa}{1+e}\frac{\dot{\sigma}'_m}{\sigma'_m} \tag{5.11}$$

are introduced.

We will discuss the instability of the model using **Equations** (5.8) and (5.9) and the assumption that the last term is small, since $A - x_{11} \approx 0$ near the failure state. Firstly, we consider

the case of undrained creep for normally consolidated clay in which $\eta < M$. In this case, the following conditions prevail:

$$M - \eta > 0 \ , \quad \frac{\lambda}{\lambda - \kappa} M - \eta > 0 \ , \quad \text{and} \quad A - x_{11} > 0 \ . \tag{5.12}$$

Since $a > 0$, the rate of strain rate is negative, which leads to the conclusion that the material system is structurally stable in terms of Liapunov.

Next, we will consider the second material function for normally consolidated clay. The second material function is simplified with the assumption that the initial value of $x_{11(0)}$ is zero; i.e., $x_{11} = 0$. Thus,

$$\Phi_2 = 1 + \frac{M\eta}{G_2(M - \eta)} = \frac{G_2(M - \eta) + M\eta}{G_2(M - \eta)} \tag{5.13}$$

in which $G_2 = \sqrt{2/3} G_2^*$.

$$\dot{\varepsilon}_{11}^{vp} = -m' a (\dot{\varepsilon}_{11}^{vp})^2 \tag{5.14}$$

$$a = -\frac{(1+e)M^2\eta}{m'\kappa\Big(G_2(M-\eta) + M\eta\Big)} + \frac{1+e}{M\kappa}(\eta - M)(\eta - \frac{\lambda}{\lambda - \kappa}M) + \frac{B}{M}(A_3 - x_{11}) \tag{5.15}$$

In contrast to cases without a second material function, it is found that when a second material function is included, the rate of strain rate $\dot{\varepsilon}_{11}^{vp}$ may become positive before η reaches M, since the first term of **Equation** (5.15) increases with a negative sign. Hence, the introduction of a second material function is inevitable for describing the creep failure of normally consolidated clay in the case of a monotonically increasing hardening function (see **Figure 5.2**). This is consistent with previous results of tests on the instability of normally consolidated clay obtained by Adachi et al. (1990) and Oka et al. (1995).

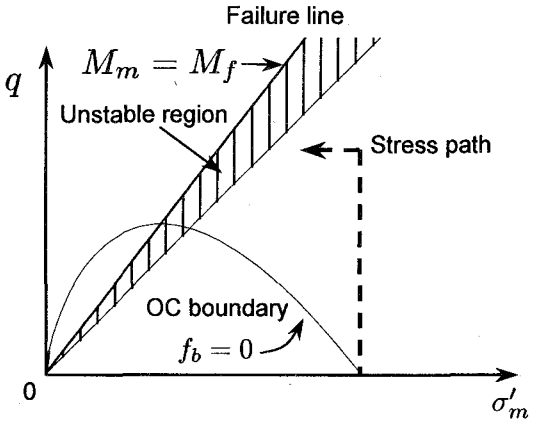

Figure 5.2 Unstable region of N.C. clay under undrained triaxial conditions (Undrained creep for N.C. clay with $\Phi_2(\xi)$)

Next, we will discuss the stability of the model in the region where $\eta > M$. This condition corresponds to the undrained creep tests which can be achieved by applying deviator stress q

with a small initial mean effective stress located in the overconsolidated region. When there is no second material function, term a becomes positive in region $M < \eta < \lambda M/(\lambda - \kappa)$, as shown in **Figure 5.3**. In this region, the material becomes unstable due to the fact that $\dot{\varepsilon}_{11}^{vp} > 0$. On the other hand, when second material function Φ_2 is introduced, the stability cannot be evaluated with **Equation** (5.15) in the region where $\eta > M$. This is because $\xi(= (M\eta)/[G_2(M - \eta)])$ becomes negative due to a simplification which involves the replacement of η_{ij}^{**}, defined by the stress-history tensor, with η_{ij}^{*} based on the stress tensor.

From the above considerations, it becomes evident that the model can simulate the instability associated with "undrained creep failure" in the specific stress regions. It is worth noting that in the region where $\eta > M$, the model can be unstable even if a second material function is not included.

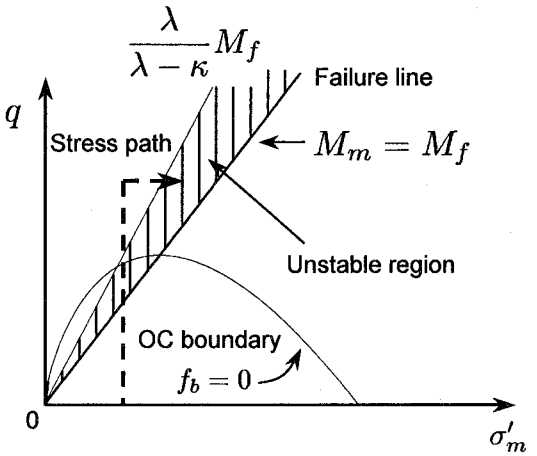

Figure 5.3 Unstable region of O.C. clay under undrained triaxial conditions without a second material function (Undrained creep for O.C. clay without $\Phi_2(\xi)$)

Using an isotropic hardening viscoplastic model, Oka et al. (1994) found that the material model developed by Adachi and Oka (1982) is always stable without a second material function, i.e., $\Phi_2 = 1.$, in the normally consolidated region. From the above consideration, however, it becomes evident that overconsolidated clay becomes unstable in region ($\eta > M$) even for models without a second material function.

5.3 Finite Element Analysis of Strain Localization by an Elasto-viscoplastic Model

In this chapter, the same finite element formulation as in **Chapter 3** is used. An eight-node quadrilateral element with a reduced Gaussian (2×2) integration (see **Figure 3.1**) is used to eliminate shear locking and to reduce the appearance of a spurious hourglass mode. On the other hand, the pore water pressure is defined at four corner nodes. A weak form of the continuity equation is integrated with a (2×2) full integration (see **Figure 3.1**).

Figure 5.4 shows the size of the specimen and the associated boundary conditions. As a trigger for strain localization, horizontal displacements on both top and bottom surface edges are

Table 5.1 Material parameters used in the calculations

Parameter		N.C. clay	O.C. clay
Compression index	λ	0.172	0.172
Swelling index	κ	0.054	0.054
Initial void ratio	e_0	0.72	0.72
Initial mean effective stress	σ'_{me}	392 (kPa)	100 (kPa)
Parameter of O.C. boundary surface	σ'_{mbi}	392 (kPa)	392 (kPa)
Coefficient of earth pressure at rest	K_0	1.0	1.0
Viscoplastic parameter	m'	21.5	21.5
Viscoplastic parameter	C_{o1}	4.5×10^{-8} (1/s)	4.5×10^{-8} (1/s)
Viscoplastic parameter	C_{o2}	4.5×10^{-8} (1/s)	4.5×10^{-8} (1/s)
Stress ratio at failure	M_f^*	1.05	1.05
Stress ratio ($\sqrt{2J_2}/\sigma'_m$) at maximum compression	M_m^*	1.05	1.05
Elastic shear modulus	G	5500 (kPa)	5500 (kPa)
Softening parameter	G_2^*	100	1
Kinematic hardening parameter	B_1^*	0.0	0.5
Retardation parameter	τ	1.0×10^{-3}	0.2
Coefficient of permeability	k	1.54×10^{-6} (m/s) 1.54×10^{-8} (m/s) 1.54×10^{-10} (m/s)	1.54×10^{-6} (m/s) 1.54×10^{-8} (m/s) 1.54×10^{-10} (m/s)

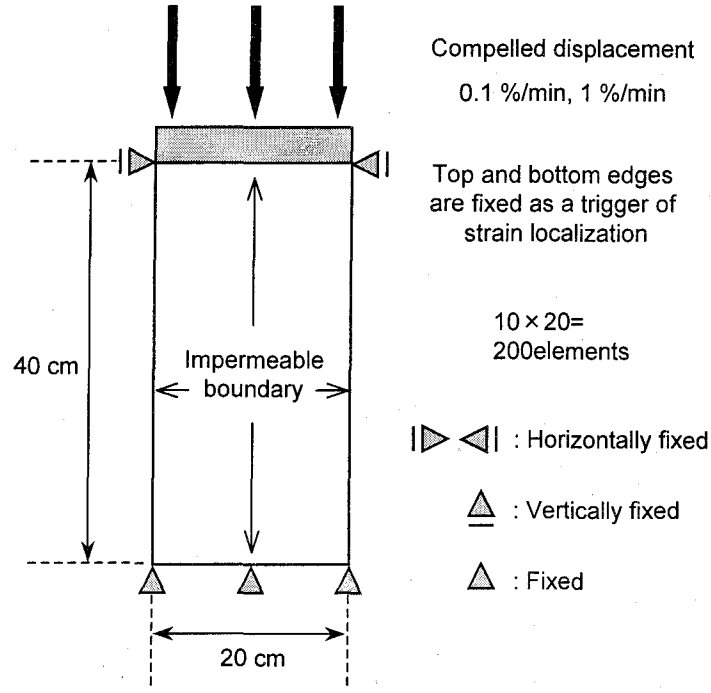

Figure 5.4 Size of the specimen and the boundary conditions (undrained plane strain condition)

constrained. The relaxation of this constraint through the introduction of a frictional boundary will be discussed later. The material parameters used in the analysis are listed in **Table 5.1** with the coefficient of permeability and the K_0 values. In the analysis, the time increment is determined by the increment of average strain $\Delta\varepsilon_{11} = 0.01\%$.

5.3.1 Effects of Dilatancy on the Strain Localization Analysis

The compression of a clay specimen is simulated under globally undrained plane strain conditions. The compression is performed under displacement control with average strain rates of 0.1%/min and 1%/min. **Figure 5.5** shows the average stress-strain relations; it is clearly seen that the strain rate influences the associated stress-strain responses. **Figure 5.6** shows the simulated results for normally consolidated clay and overconsolidated clay with a permeability coefficient of 1.54×10^{-8}(m/s).

It can be seen from **Figure 5.6** that the deformed meshes of normally and overconsolidated clay specimens display a localization of the deformation at an average axial strain of 8% and 6%, respectively. The appearance of a shear band at a larger strain levels in the N.C. clay is consistent with the stress-strain curves with gradual softening. The occurrence of localization at an early stage of deformation in the case of overconsolidated clay is consistent with the average stress-strain relations shown in **Figure 5.5**. This tendency has been observed in the experiments (e.g., Hicher et al. 1994).

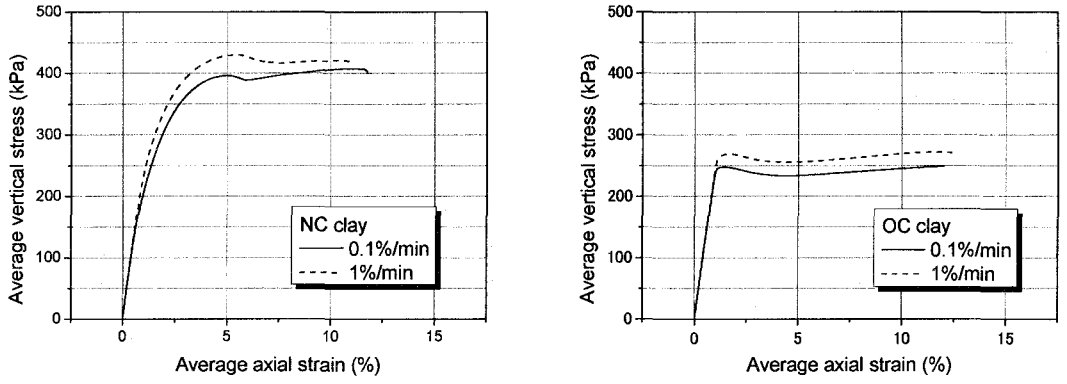

Figure 5.5 Average stress-strain relations ($k = 1.54 \times 10^{-8}$ m/s)

Figure 5.7 shows accumulated viscoplastic shear strain γ^p, namely,

$$\gamma^p = \int d\gamma^p \ , \quad d\gamma^p = (de_{ij}^{vp} de_{ij}^{vp})^{1/2} \tag{5.16}$$

in which de_{ij}^{vp} is the viscoplastic deviatoric strain increment tensor. In the case of overconsolidated clay, strain localization starts near the edges of the top and the bottom plates, and finally, four shear bands appear. In contrast to the case of overconsolidated clay, only two shear bands are seen for normally consolidated clay, with shear bands clearly developing just beneath the edges of the top and the bottom plates. As for the distribution of viscoplastic volumetric strain magnitude, it is seen from **Figure 5.8** that a decrease in viscoplastic volumetric strain (viscoplastic volume expansion) occurs along the shear bands for overconsolidated clay, while only

viscoplastic compression is seen in the case of normally consolidated clay. The tendency of the distribution of viscoplastic volumetric strain is, in fact, related to the changes in mean effective stress since calculations are carried out under globally undrained conditions. **Figure 5.9** shows the distribution of mean effective stress with the progress of the average axial strain. In the case of overconsolidated clay, the mean effective stress generally increases in the specimen from its initial value, i.e., 100(kPa). Along the shear bands, however, mean effective stress levels are lower than those in the other regions of the specimen. In the case of normally consolidated clay, the mean effective stress decreases from its initial value of 392(kPa) due to negative dilatancy. The extent of the decrease in mean effective stress is larger in shear bands. On the other hand, increases in mean effective stress due to consolidation can also be observed at the top and the bottom of the specimen.

In general the distribution of mean effective stress is related to pore fluid motion. Hence, it is necessary to evaluate the effects of the permeability coefficient in order to examine the distribution of mean effective stress. **Figure 5.10** shows the distributions of mean effective stress and viscoplastic volumetric strain for overconsolidated clay with a permeability coefficient as low as 1.54×10^{-10}(m/s). In this case, the mean effective stress along the shear bands is relatively higher than that in the regions between them. This tendency is in contrast to that found in the numerical results obtained for the high permeability case shown in **Figure 5.9**. The reason for this difference is that pore water can easily move within a material with high permeability. Hence, an increase in mean effective stress due to positive dilatancy can be cancelled by the inflow of pore water toward the shear bands. **Figure 5.11** displays the distribution of pore water pressure. Comparing the distributions of mean effective stress and plastic shear strain, it is seen that the distribution of pore water pressure is rather homogeneous for both normally consolidated clay and overconsolidated clay. However, higher levels of pore water pressure develop for normally consolidated clay. The relatively homogeneous distribution of pore water pressure within the specimen is considered to be due to the migration of pore water.

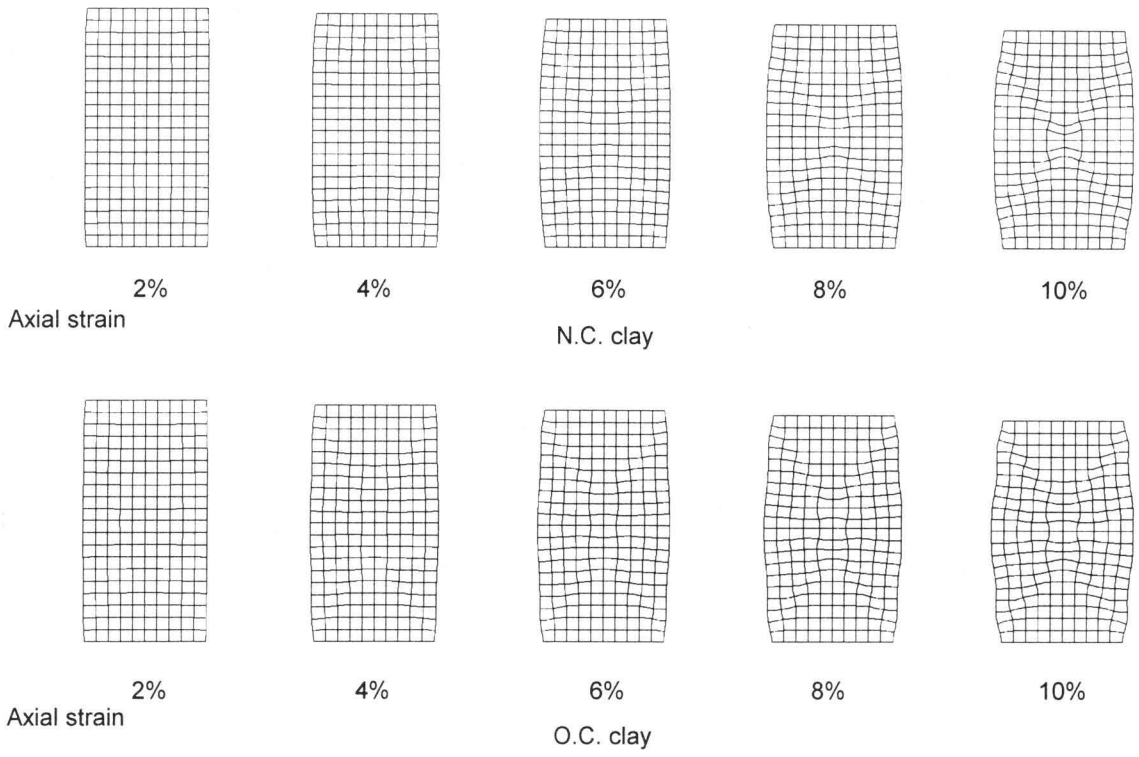

Figure 5.6 Deformed meshes of N.C. and O.C. clay samples (0.1%/min, 1.54×10^{-8}(m/s))

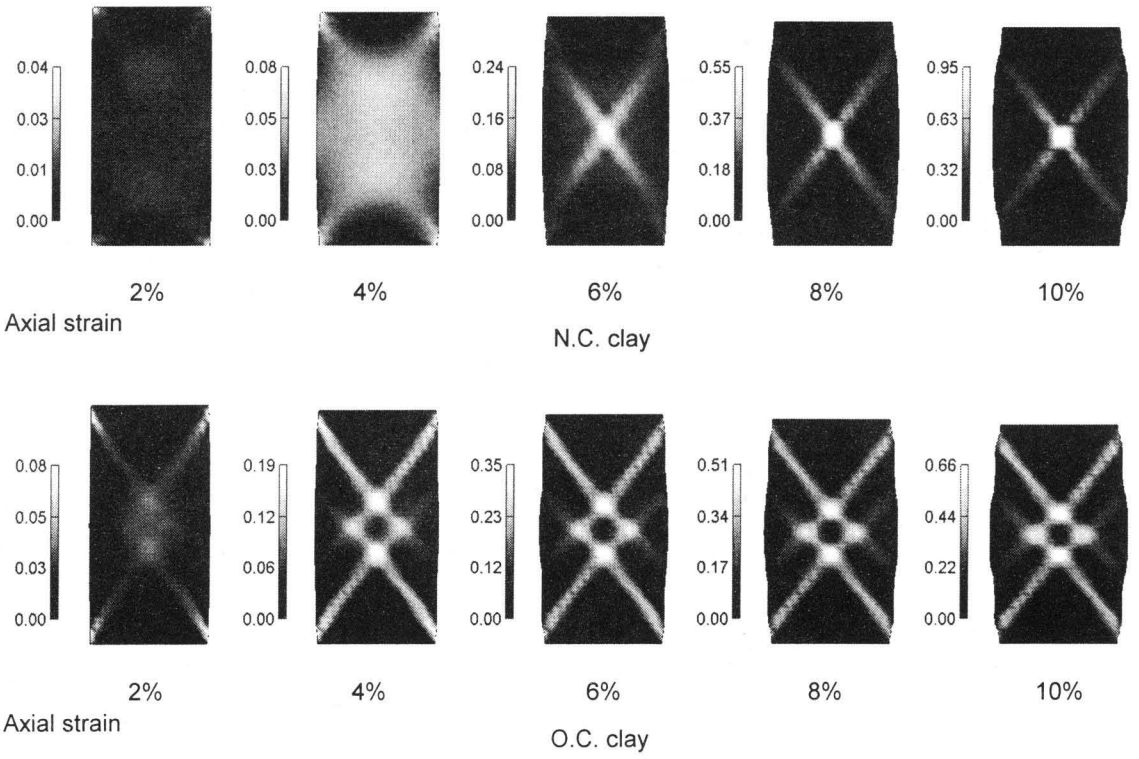

Figure 5.7 Distribution of γ^p for N.C. and O.C. clay samples (0.1%/min, 1.54×10^{-8}(m/s))

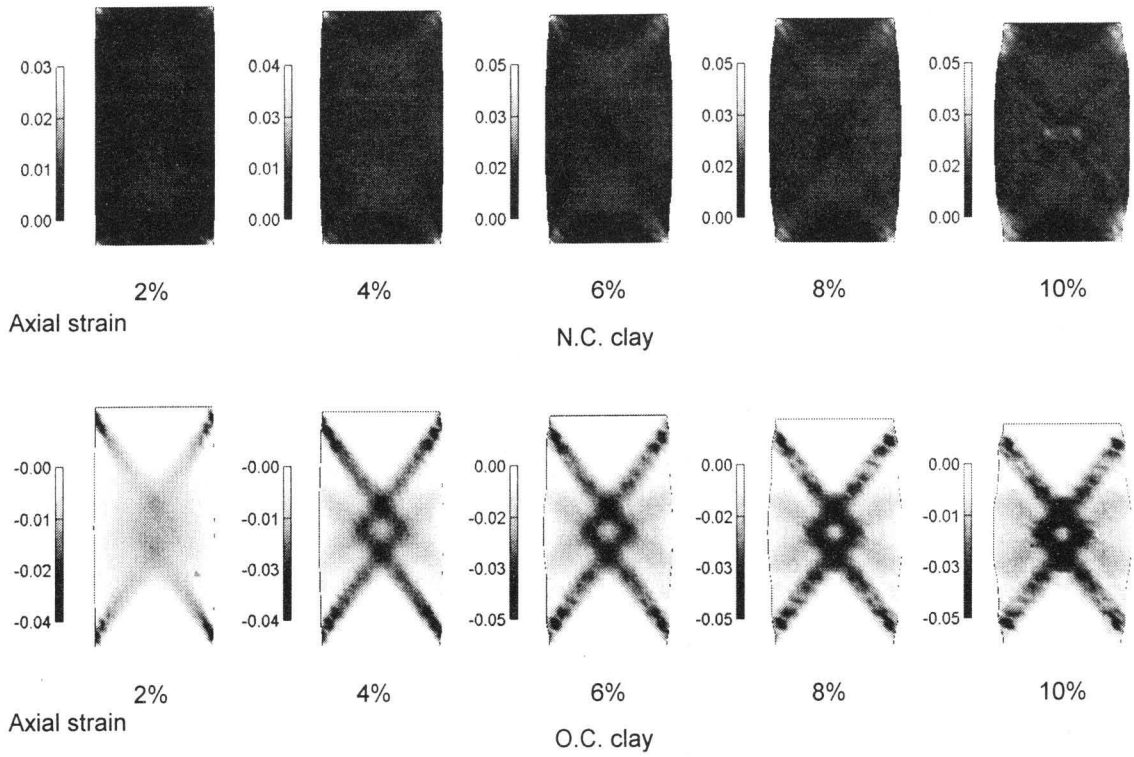

Figure 5.8 Distribution of accumulated viscoplastic volumetric strain for N.C. and O.C. clay samples (0.1%/min, 1.54×10^{-8}(m/s))

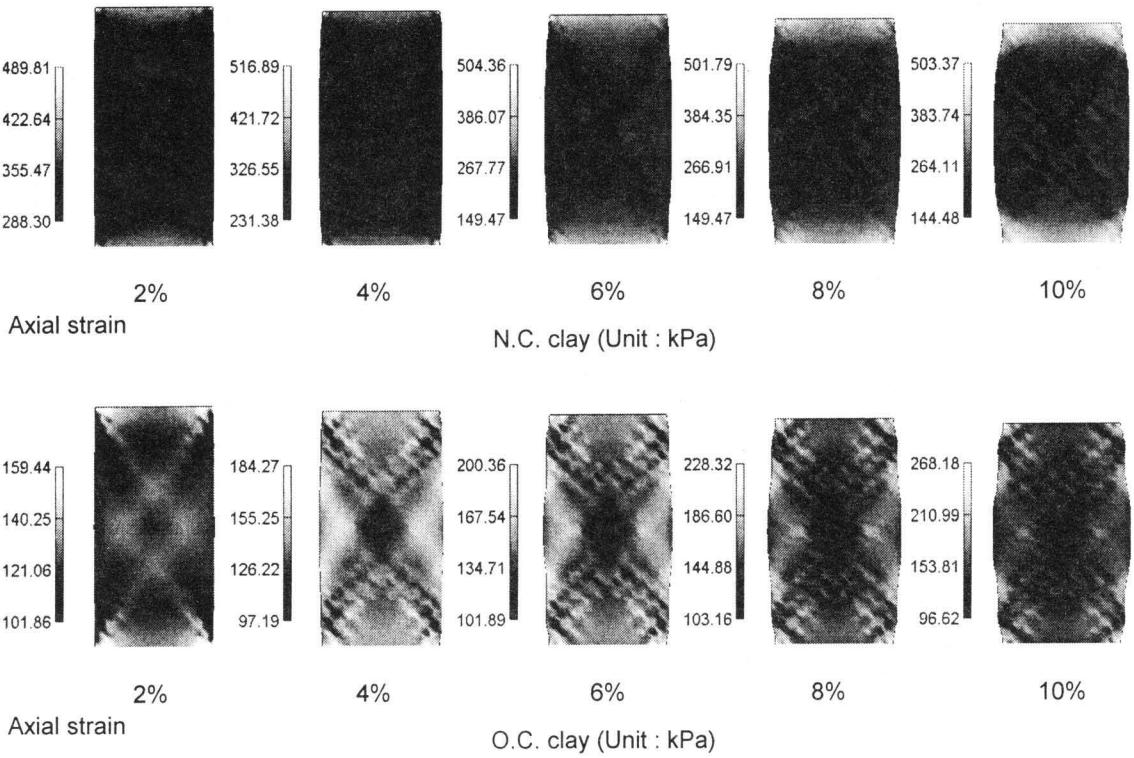

Figure 5.9 Distribution of mean effective stress for N.C. and O.C. clay samples (0.1%/min, 1.54×10^{-8}(m/s))

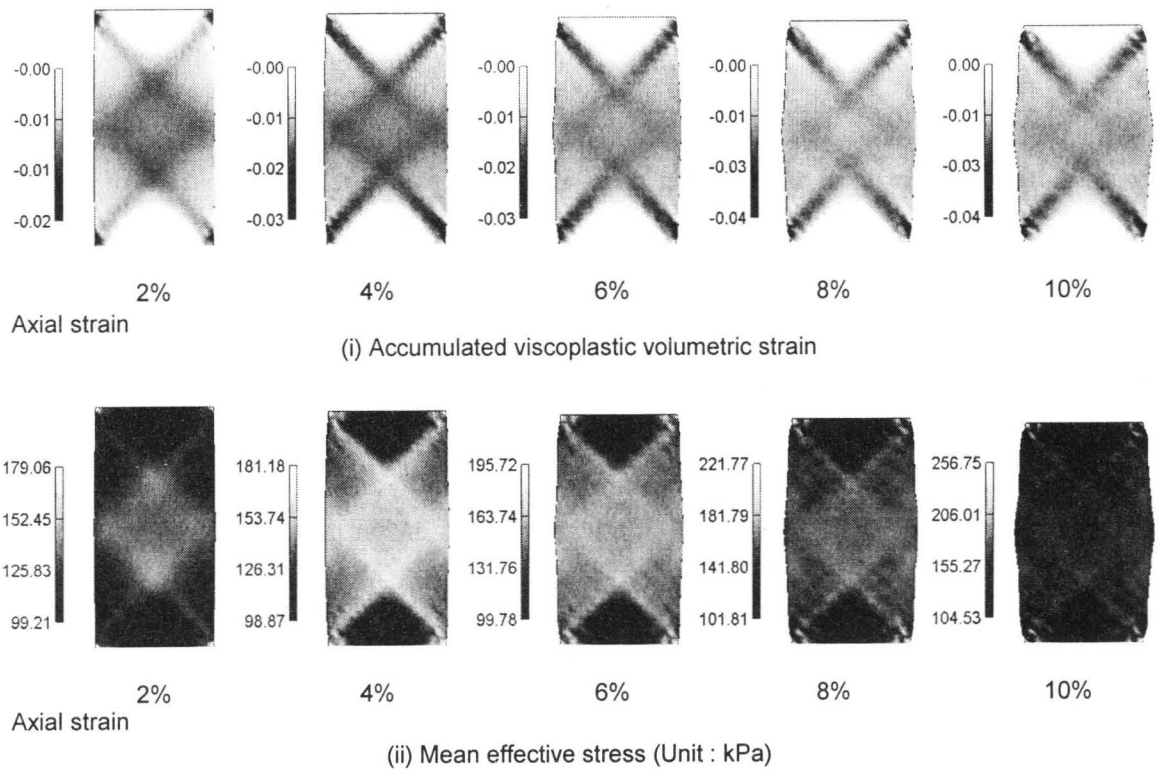

Figure 5.10 Distribution of accumulated viscoplastic volumetric strain and mean effective stress for O.C. clay (0.1%/min, 1.54×10^{-10}(m/s))

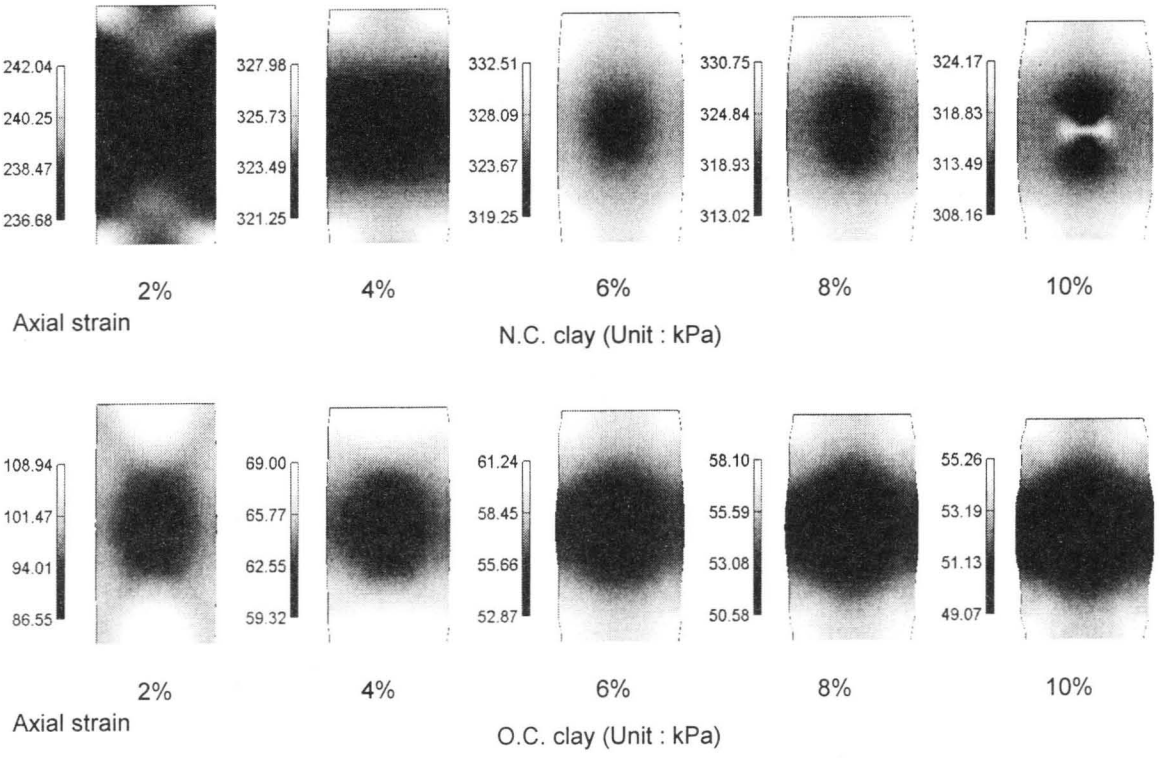

Figure 5.11 Distribution of pore water pressure for N.C. and O.C. clay samples (0.1%/min, 1.54×10^{-8}(m/s))

5.3.2 Effects of Permeability on the Strain Localization Analysis

Figure 5.12 displays the stress-strain relations and the distribution of accumulated viscoplastic shear strain γ^p with different permeability coefficients. The average vertical stress with lower permeability is larger than that with higher permeability in the both cases of both normally consolidated clay and overconsolidated clay. It can be seen in the distribution of γ^p that the appearance of four shear bands is clear for the cases of lower permeability levels. In addition, the figure shows that the distance between the shear bands is wider than that in the cases of higher permeability levels. A possible reason for the larger number of shear bands in the overconsolidated clay than in the normally consolidated clay is that the strain softening associated with dilation may cause a reduction in the mean effective stress. Consequently, the adjacent regions can easily deform so as to lead to the occurrence of a larger number of shear bands. The average stress is higher for cases with lower permeability levels ($k = 1.54 \times 10^{-10}$m/sec). As pointed out by Loret and Prévost (1991), materials with low permeability levels are more stable than those with high permeability levels. This tendency of the stress-strain response is similar to the effect of the strain rate. Inclination angles of shear bands with lower permeability levels are smaller than those with higher permeability levels in the case of normally consolidated clay and in small axial strain range of overconsolidated clay.

As mentioned above, the effects of permeability on strain localization and the stress-strain response of normally consolidated clay are consistent with the results obtained in **Section 3.5** with different material parameters.

5.3.3 Effects of the Strain Rates on the Strain Localization Analysis

Stress-strain relations and the distribution of γ^p for different average strain rates (0.1%/min and 1%/min) are shown in **Figure 5.13**; the strain rate sensitivities are clearly seen in the stress-strain curves. It is seen that normally consolidated clay and overconsolidated clay are both more stable with higher strain rates, since the average vertical stress is larger and the accumulated shear strain is smaller. Two apparent shear bands are seen for the cases of normally consolidated clay, while the appearance of four shear bands is clearly seen for the cases of overconsolidated clay. In addition, the figure shows that the distance between the shear bands is wider than that in the case of lower strain rate. The effect of strain rate on inclination angles of shear bands for normally consolidated is very small, while those for overconsolidated clay with lower strain rate is larger than that in the cases with higher strain rates.

5.3.4 Effects of Material Instability on the Strain Localization Analysis

Material instability has already been discussed by an instability analysis in **Section 5.2**. It is found that second material function $\Phi_2(\xi)$ expresses material instability for normally consolidated clay. On the other hand, overconsolidated clay exhibits material instability even without $\Phi_2(\xi)$. In this section, a strain localization analysis without $\Phi_2(\xi)$ is conducted in order to numerically investigate the material instability.

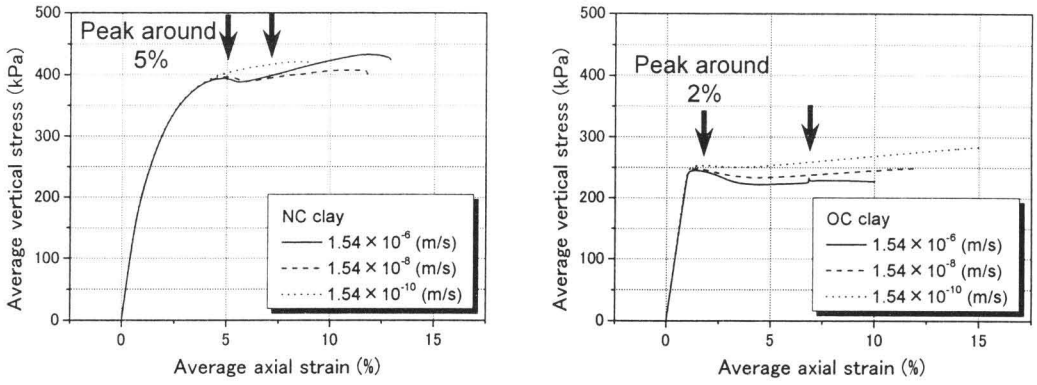

(i) Stress-strain relations with different permeability coefficients (strain rate : 0.1%/min)

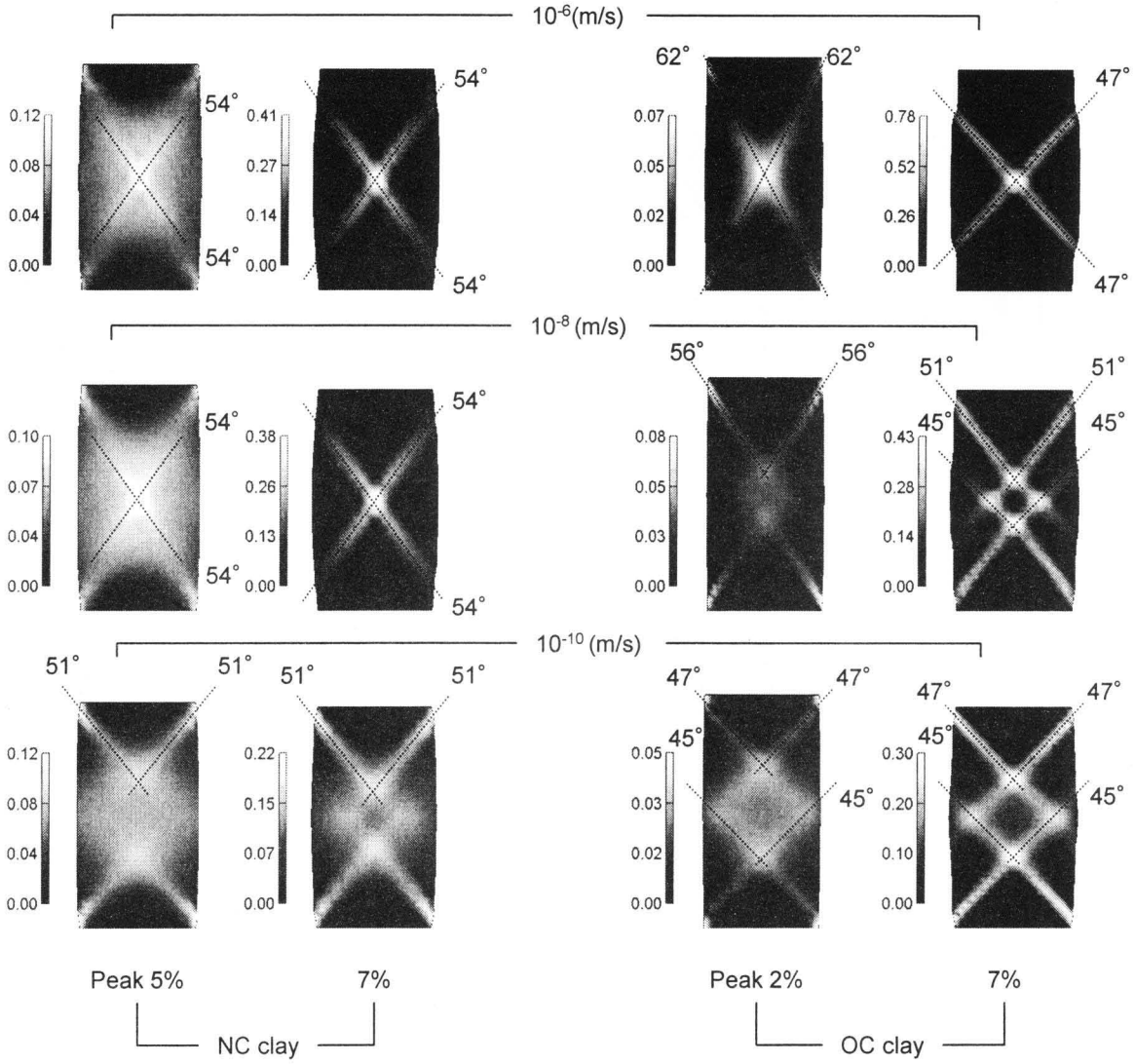

(ii) Distribution of accumulated viscoplastic shear strain (strain rate : 0.1%/min)

Figure 5.12 Stress-strain relations and distribution of accumulated viscoplastic shear strain γ^p with different permeability coefficients

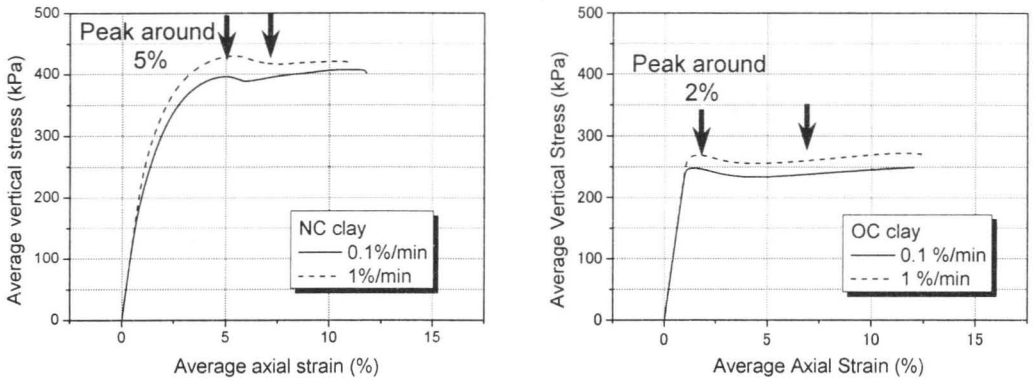

(i) Stress-strain relations with different strain rate (k = 1.54×10^{-8} m/s)

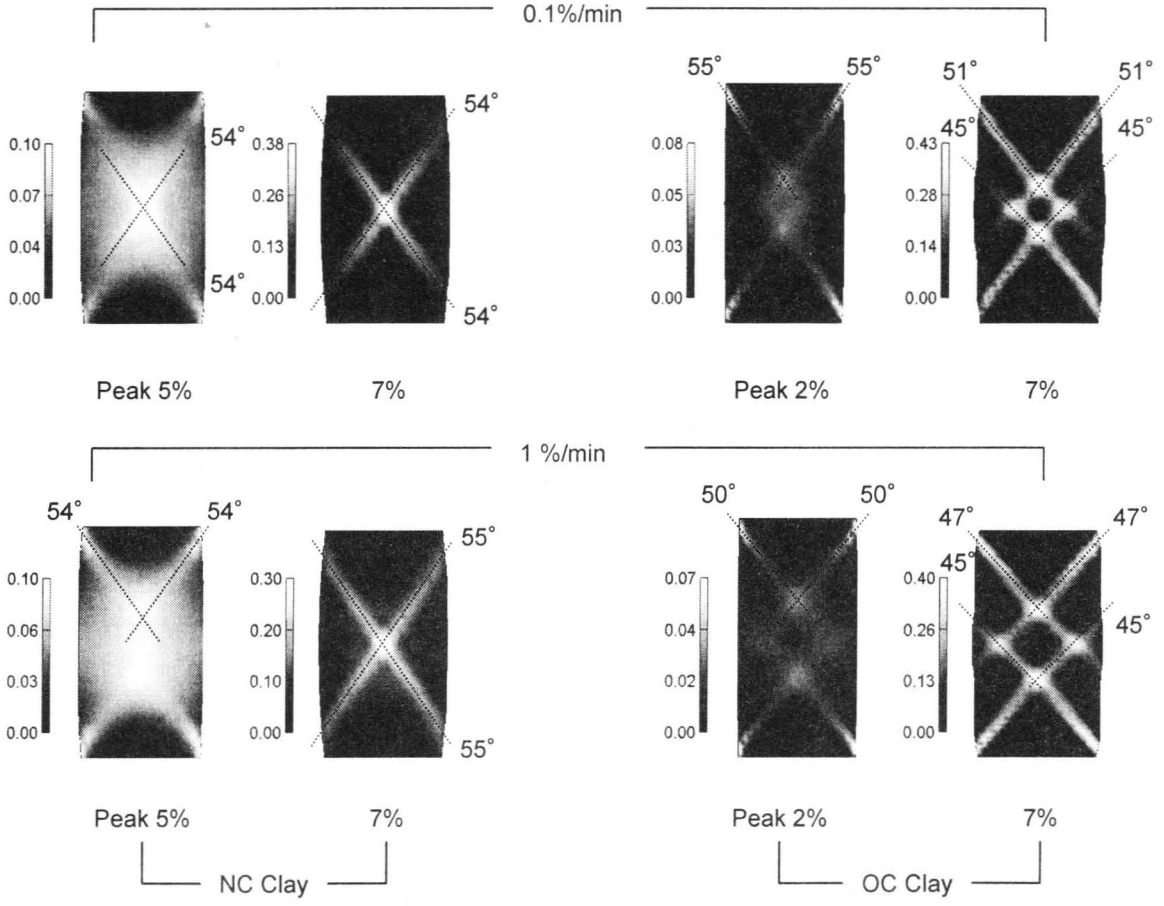

(ii) Distribution of accumulated viscoplastic shear strain (k = 1.54×10^{-8} m/s)

Figure 5.13 Stress-strain relations and distribution of accumulated viscoplastic shear strain γ^p with different strain rates ($k = 1.54 \times 10^{-8}$m/s)

Figure 5.14 shows a deformed mesh and the distribution of γ^p at an axial strain of 10%, and stress-strain relations are depicted in **Figure 5.15**. In this case, the strain rate is 0.1%/min and permeability coefficient $k = 1.54\times10^{-8}$m/s. Normally consolidated clay without $\Phi_2(\xi)$ deforms homogeneously, while the deformation with $\Phi_2(\xi)$ localized. We cannot see any softening behavior in the stress-strain relation in the case without $\Phi_2(\xi)$. On the other hand, four shear bands can be clearly seen in the figures for OC clay even if material function $\Phi_2(\xi)$ is not used. In addition, the stress-strain relations both with and without $\Phi_2(\xi)$ in **Figure 5.15** display strain-softening behavior. These findings suggest that the material system of normally consolidated clay is stable unless the constitutive equation with $\Phi_2(\xi)$ is used. In contrast, overconsolidated clay is unstable even if the constitutive equation does not include $\Phi_2(\xi)$. These results are consistent with the results of the instability analysis.

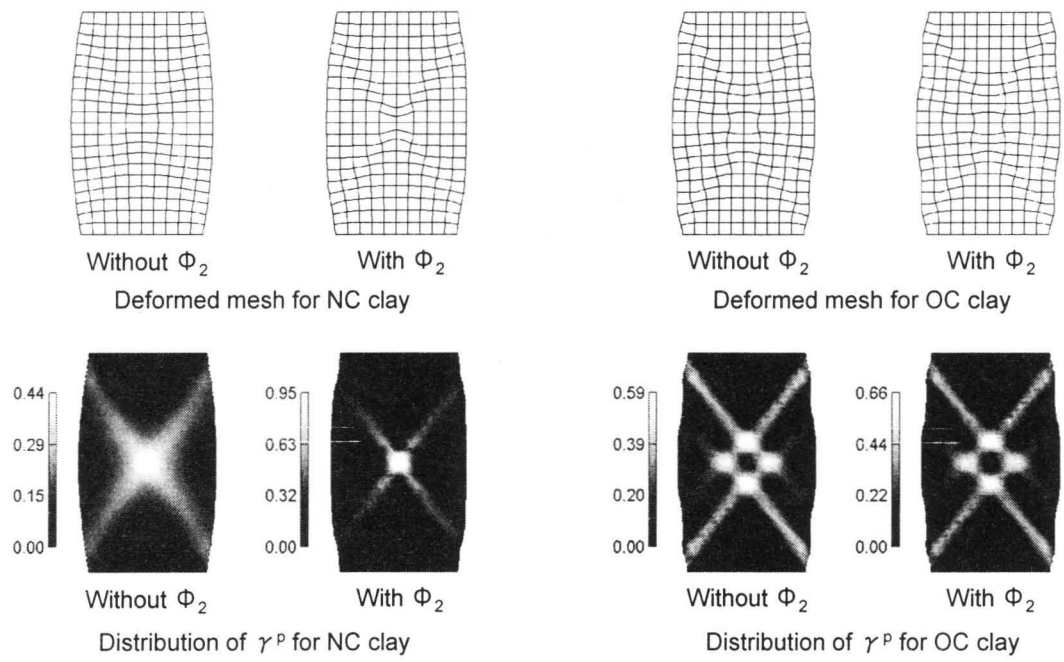

Figure 5.14 Deformed mesh and distribution of γ^p with and without $\Phi_2(\xi)$ (axial strain: 10%, strain rate: 0.1%/min, $k = 1.54 \times 10^{-8}$m/s)

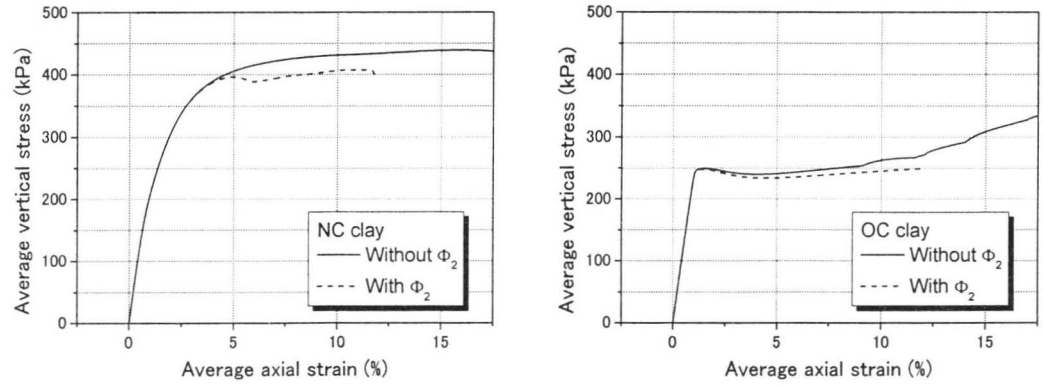

Figure 5.15 Stress-strain relations with and without $\Phi_2(\xi)$ (strain rate: 0.1%/min, $k = 1.54 \times 10^{-8}$m/s)

5.3.5 Mesh-size Dependency

In order to check the mesh-size dependency of the numerical results, simulations are performed using various mesh sizes. Some numerical calculations with smaller elements (800 elements) diverged after the peak stress since the top and the bottom of the specimen deformed extremely due to the end constraints. In order to examine the effects of the end constraints, the "no lateral displacements at top and bottom plates" was relaxed by instead using a frictional boundary with a frictional coefficient μ_f of 0.01. The frictional boundary conditions are shown in **Figure 5.16**. **Figure 5.17** shows the deformed meshes and the distribution of γ^p for different numbers of elements. Since no noticeable mesh-size dependency is observed in **Figure 5.17**, the occurrence of any numerical instability can only be the result of the imposition of strong constraints. The mesh size has little influence on the stress-strain responses, as seen in **Figure 5.18**.

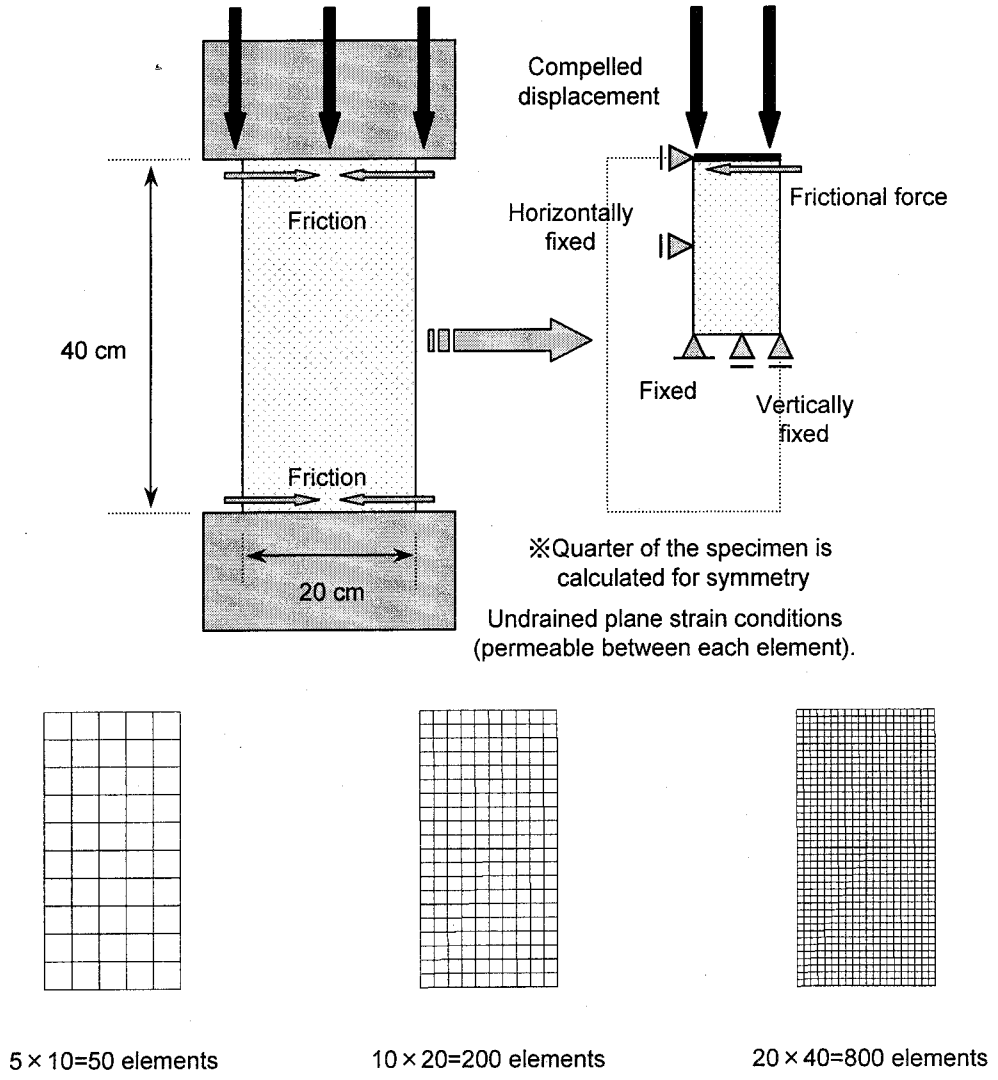

Figure 5.16 Frictional boundary conditions and the size of the meshes

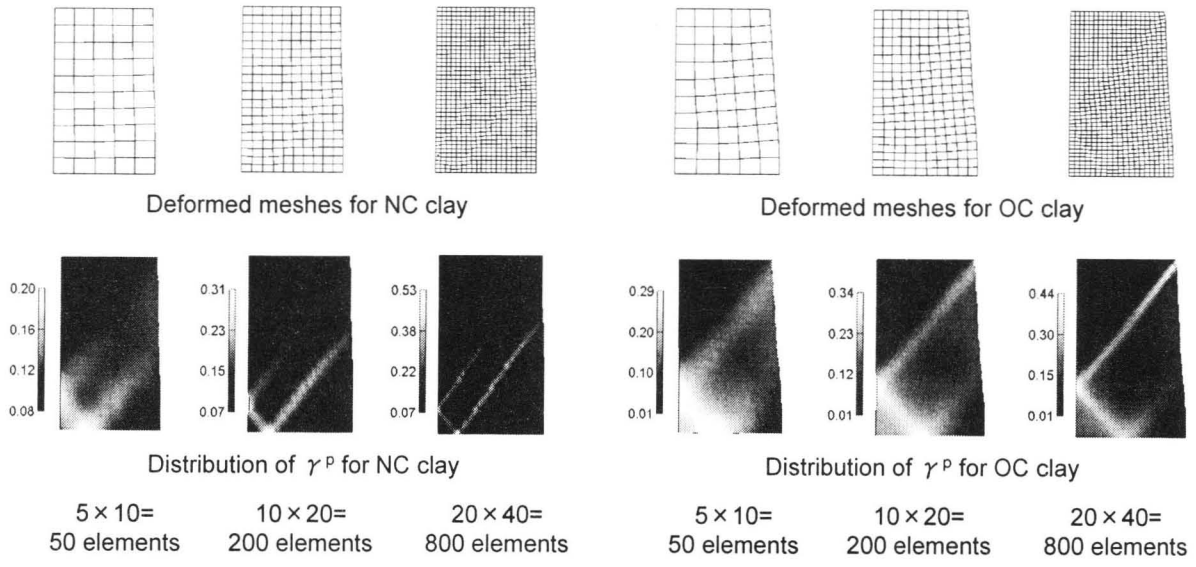

Figure 5.17 Deformation and distribution of γ^p with different numbers of elements (axial strain: 9%, strain rate: 0.1%/min, $k = 1.54 \times 10^{-8}$m/s, coefficient of friction: 0.01)

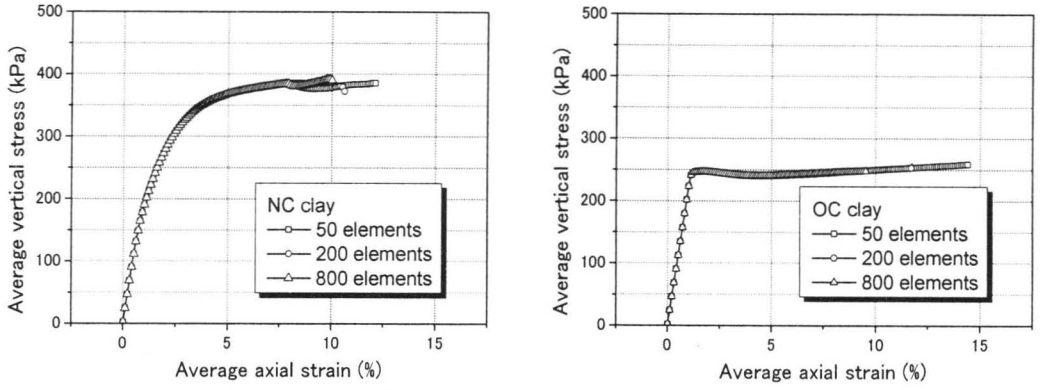

Figure 5.18 Stress-strain relations with different numbers of elements (strain rate: 0.1%/min, $k = 1.54 \times 10^{-8}$m/s, coefficient of friction: 0.01)

5.4 Summary

The obtained conclusions from this chapter are as follows. The instability of the model was studied under undrained triaxial creep conditions. It was seen that the model with positive dilatancy was more unstable than the model with negative dilatancy in terms of creep failure. Even when a second material function was not included in the formulation, the model became unstable with positive dilatancy. On the other hand, the model with negative dilatancy became unstable only when a second material function was introduced. As for the numerical simulation of the shear band development, using the elasto-viscoplastic model, it was found that the strain localization pattern was strongly affected by dilatancy characteristics as well as by the permeability and the strain rate. In addition, the effects of material instability on strain localization are consistent with the results obtained from the instability analysis.

References

Adachi, T. and Oka, F. (1982), Constitutive equations for normally consolidated clay based on elasto-viscoplasticity, *Soils and Foundations*, **22**, 4, pp. 57-70.

Adachi, T., Oka, F. and Mimura, M. (1990), Elasto-viscoplastic constitutive equations and their application to consolidation analysis, *J. Engineering Materials and Technology*, ASME, **112**, pp. 202-209.

Chaboche, J.L. and Rousselier, G. (1983), On the plastic and viscoplastic constitutive equations-Part I: Rules developed with internal variable concept, *J. Pressure Vessel Technology*, ASME, **105**, pp. 103-158.

Hicher, P.Y., Wahyudi, H. and Tessier, D. (1994), Microstructural analysis of strain localisation in clay, *Computers and Geotechnics*, **16**, pp. 205-222.

Kimoto, S. (2002), Constitutive models for geomaterials considering structural changes and anisotropy, Doctoral thesis, Kyoto University, Japan.

Kimoto, S., Oka, F. and Higo, Y. (2004), Strain localization analysis of elasto-viscoplastic soil considering structural degradation, *Computer Methods in Applied Mechanics & Engineering*, to appear.

Loret, B and Prévost, J.H. (1991), Dynamic strain localization in fluid-saturated porous media, *J. Engineering Mechanics*, ASCE, **117**, 4, pp. 907-922.

Oka, F., Adachi, T. and Yashima, A. (1994), Instability of an elasto-viscoplastic constitutive model for clay and strain localization, *Mechanics of Materials*, **18**, pp. 119-129.

Oka, F., Adachi, T. and Yashima, A. (1995), A strain localization analysis of clay using a strain softening viscoplastic model, *Int. J. Plasticity*, **11**, 5, pp. 523-545.

Chapter 6

Experimental Study on the Three-dimensional Strain Localization of Rectangular Clay Specimens

6.1 Introduction

In the natural ground, such strain localization phenomena as land slides involve three-dimensional shear bands. In the case of triaxial compression tests using cylindrical soil specimens, we can observe specific three-dimensional shear bands. In this way, the strain localization of geomaterials should be treated as a three-dimensional problem. However, it is mainly strain localization problems under plane strain conditions that have been discussed. Investigations into strain localization in plane strain compression tests for sand using some measurements of local displacements have been done by Han and Vardoulakis (1991), Han and Drescher (1993), Rechenmacher and Finno (2003), etc. Many visualization methods for strain localization have been developed by various researchers. Yoshida et al. (1994) studied the shear band generation of sand specimens under plane strain conditions by calculating the displacements of lattice points printed on a membrane. Similar observations using a printed membrane have been done by Liang et al. (1997), Hayano et al. (1999), and Kodaka et al. (2001). In order to observe strain localization inside specimens, X-Rays or X-Ray CTs have been used by many researchers, e.g., Han and Vardoulakis (1991), Oda and Kazama (1998), Otani et al. (2000), and Alshibli et al. (2000). Michalowski and Shi (2003) calculated the displacements of grains of sand using an image analysis of sequential photographs by which the development of strain localization has been investigated. The stereophotogrammetric method is an efficient method for analyzing the development of shear bands used by Harris et al. (1995), Mokni and Desrues (1998), Rechenmacher and Medina-Cetina (2003), etc. Some researchers have tried to observe strain localization under triaxial conditions (Burland 1990, Rampello 1991, etc.), and Asaoka et al. (1998) experimentally and numerically investigated the three-dimensional deformation behavior

of rectangular clay specimens. To the author's knowledge, however, the three-dimensional observation of shear bands has not been sufficient. As for the numerical studies of strain localization, most have been conducted under plane strain conditions using a particular constitutive equation (Loret and Prévost 1991; Schrefler et al. 1996; Oka et al. 1994; Zhang et al. 1999; Nüvel and Gudehus 2001; Oka et al. 2002; etc.).

Kodaka et al. (2001) have conducted triaxial compression tests using rectangular clay specimens to quantitatively observe the strain localization behavior through an image analysis of digital photographs. In the present study, triaxial compression tests using rectangular clay specimens and a detailed observation of the shear banding process by an image analysis were conducted, in the same manner as that by Kodaka et al. (2001), in order to investigate the three-dimensional strain localization behavior of geomaterials. It is easy to observe strain localization with rectangular specimens, since the transverse section of the specimens does not have many axes of symmetry compared to cylindrical specimens. In the case of cylindrical specimens, we cannot accurately predict where the deformation will localize. On the other hand, the localized deformation of rectangular specimens can be observed with certainty as long as focus is placed on two of the surfaces. An image analysis of the digital photographs showing the two surfaces of the rectangular specimens during shear deformation provides the distributions of shear strain. Using the strain distributions of the two surfaces during the tests, the generation of three-dimensional shear bands in the specimens can be very well observed. In addition, the set up of boundary conditions for the numerical simulations of rectangular specimens is easier than that of cylindrical specimens, so that we can conduct the simulations under the same conditions as the triaxial test conditions for rectangular specimens. We have numerically simulated the triaxial compression tests rectangular specimens by FEM using the elasto-viscoplastic constitutive equation that will be introduced in **Chapter 7**.

Takyu (2000) has studied the strain localization of reconstituted rectangular clay specimens, and Satomura (2001) has discussed the strain localization behavior of reconstituted normally consolidated Fukakusa clay. In addition, Satomura (2003) and Ichinose (2003) have studied the strain localization of both normally consolidated and overconsolidated Fukakusa clays. In the present study, the three-dimensional strain localization behavior has been studied in a series of triaxial tests on rectangular specimens with different shapes and strain rates for the reconstituted normally consolidated and overconsolidated Fukakusa clays by Satomura (2003) and Ichinose (2003). In particular, focus has been placed on the effects of the shapes of the specimens, dilatancy, and the strain rates.

6.2 Undrained Triaxial Compression Tests for Clay Using Rectangular Specimens

6.2.1 Clay Samples

The clay used in the experiment is Fukakusa clay which is Pleistocene marine clay produced in the southeastern part of the Kyoto Basin. Liquid limit $w_L = 62\%$, plasticity index $I_p = 33$, and the density of soil solid $\rho_s = 2.69$ g/cm^3. Dried and powdered Fukakusa clay is used as the building material, e.g., plaster. Reconstituted clay samples were prepared by remolding them in slurry and then pre-consolidating them. The specimens were consolidated one-dimensionally at a pre-consolidation pressure of 98 kPa. The pre-consolidated specimens were covered with paraffin and not to be disturbed.

The clay specimens used in the triaxial tests were trimmed to rectangular shapes. Their sizes are listed in **Table 6.1** and they are illustrated in **Figure 6.1**.

Table 6.1 Sizes of the specimens

No.	Size of the transverse section (cm)	Height (cm)
A	4×4	12
B	4×4	8
C	4×2	8
D	4×4	4

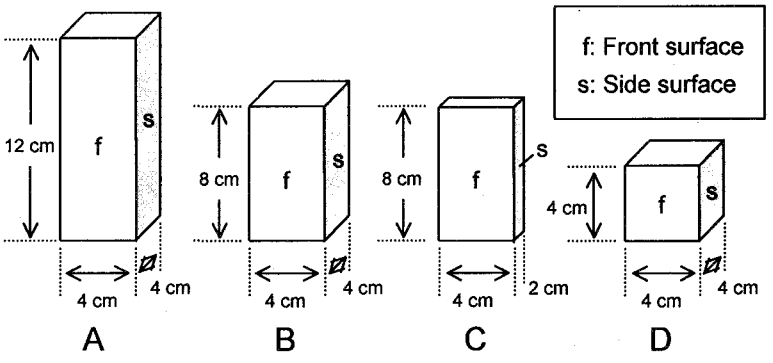

Figure 6.1 Sizes of the specimens

6.2.2 Testing Program

The photograph and the schematic figure of the triaxial test apparatus used in this study are shown in **Photo 6.1** and **Figure 6.2**, respectively. We used a lucid acrylic cell, so that the behavior of each specimen during shear deformation could be observed from the outside of the triaxial cell. The vertical load of the soil specimens was measured by the inner load cell set between the loading rod and the top cap in the triaxial cell. The cell pressure was measured by a

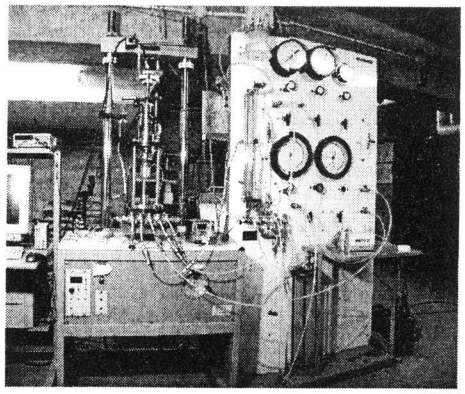

Photo 6.1 Triaxial test apparatus

pressure gauge installed in the triaxial cell, and the excess pore water pressure was simultaneously measured from the top and the bottom of each specimen. The axial displacement was measured by a proximity transducer for the range of low level axial strain (0.1% of axial strain) and by an LVDT for the range of medium to high level strain. The volume changes in pore water were measured by a differential pressure transducer.

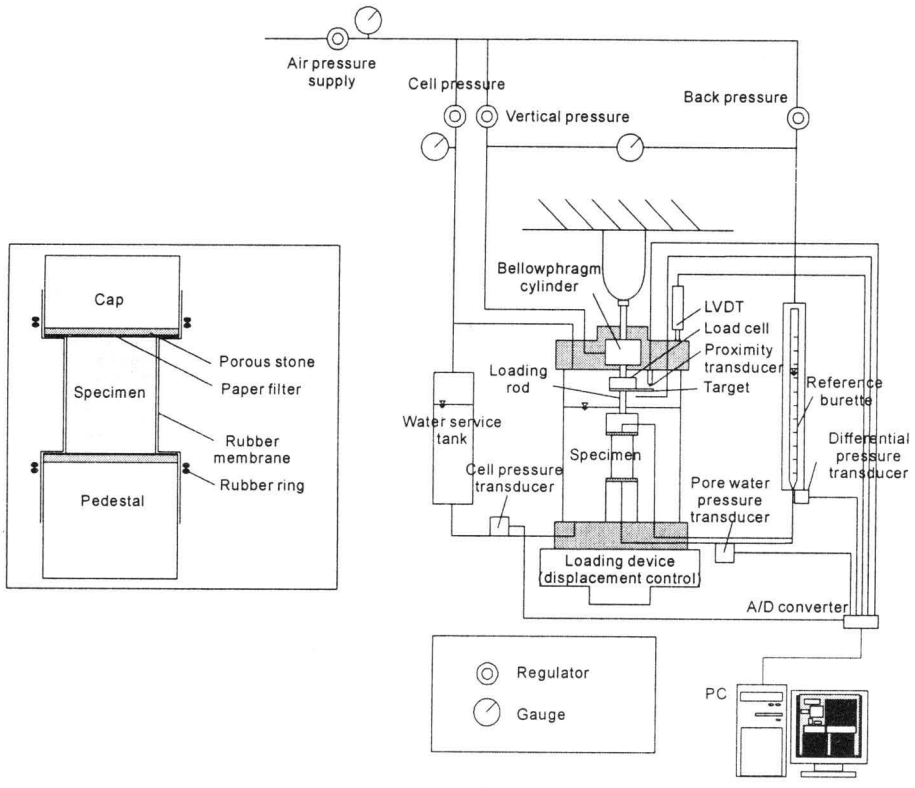

Figure 6.2 Schematic figure of the triaxial test apparatus

The test cases are listed in **Table 6.2**. All specimens used in the present study were saturated by the double vacuum method and were acted upon by 200 kPa of back pressure. The normally consolidated clay specimens were isotropically consolidated to 200 kPa. The over-consolidated clay specimens were isotropically consolidated to 300 kPa, and then isotropically

swelled to 50 kPa. Therefore, the overconsolidation ratio (OCR) is 6. The duration times for both consolidation and swelling are listed in **Table 6.3**. They are determined for each specimen height through a check by the 3-t method.

After the consolidation or the swelling procedure, axial pressure was applied under undrained conditions by an axial loading device with an axial strain or displacement control system. The three axial strain rates monotonically applied in the tests were 1%/min, 0.1%/min, and 0.01%/min. The tests were stopped at an axial strain of 20%.

Table 6.2 Test cases

Normally consolidated clay				**Overconsolidated clay**			
σ'_{m0} = 200 kPa (Consolidation pressure)				σ'_{mc} = 300 kPa (Pre-consolidation pressure), σ'_{m0} = 50 kPa (Swelling pressure), OCR=6			
No.†	Sizes (cm)	Strain rate (%/min)	Initial void ratio e_0‡	No.†	Sizes (cm)	Strain rate (%/min)	Initial void ratio e_0‡
A_N-1	4×4×12	1	1.14	A_O-1	4×4×12	1	1.14
A_N-2	4×4×12	0.1	1.14	A_O-2	4×4×12	0.1	1.07
A_N-3	4×4×12	0.01	1.13	A_O-3	4×4×12	0.01	1.15
B_N-1	4×4×8	1	1.06	B_O-1	4×4×8	1	1.07
B_N-2	4×4×8	0.1	1.04	B_O-2	4×4×8	0.1	1.12
B_N-3	4×4×8	0.01	1.09	B_O-3	4×4×8	0.01	1.14
C_N-1	4×2×8	1	1.18	C_O-1	4×2×8	1	1.02
C_N-2	4×2×8	0.1	1.02	C_O-2	4×2×8	0.1	0.95
C_N-3	4×2×8	0.01	0.95	C_O-3	4×2×8	0.01	1.09
D_N-1	4×4×4	1	1.16	D_O-1	4×4×4	1	1.07
D_N-2	4×4×4	0.1	1.08	D_O-2	4×4×4	0.1	1.13
D_N-3	4×4×4	0.01	1.17	D_O-3	4×4×4	0.01	1.08

† Subscripts N and O denote normally consolidated clay and overconsolidated clay, respectively.
‡ Initial void ratio before the undrained triaxial compression tests.

Table 6.3 The duration times for consolidation and swelling

Height (cm)	Consolidation (hour)	Swelling (hour)
12 (A)	28	25
8 (B, C)	12.5	6.5
4 (D)	3	2

6.2.3 Image Analysis

We drew 2 mm square meshes on the rubber membranes covering the specimen. A digital camera was used to take photographs of two surfaces of the specimens during the tests. **Photo 6.2** and **Figure 6.3** show a sample of the digital photographs taken through the triaxial cell and a schematic figure of the photography, respectively. We took pictures from the front and the side angles that were horizontally extended due to the refraction of the acrylic cell about

1.21348 times. After correcting the effects of the refraction, we digitized the nodal coordinates of the meshes. Using the coordinates at the initial state, i.e., before the undrained loading, and those of each axial strain level, the nodal displacements were calculated. Adopting the B matrix for the four-node isoparametric finite elements provides the strain of each element (see **Figure 6.4**).

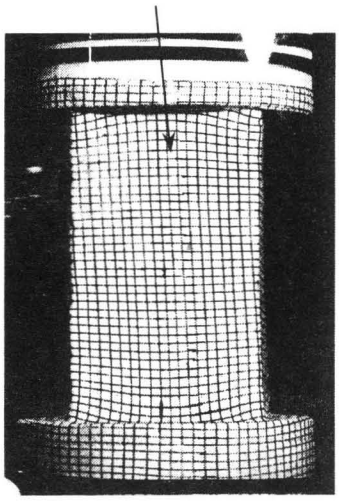

Photo 6.2 An example of the photographs taken through the acrylic cell

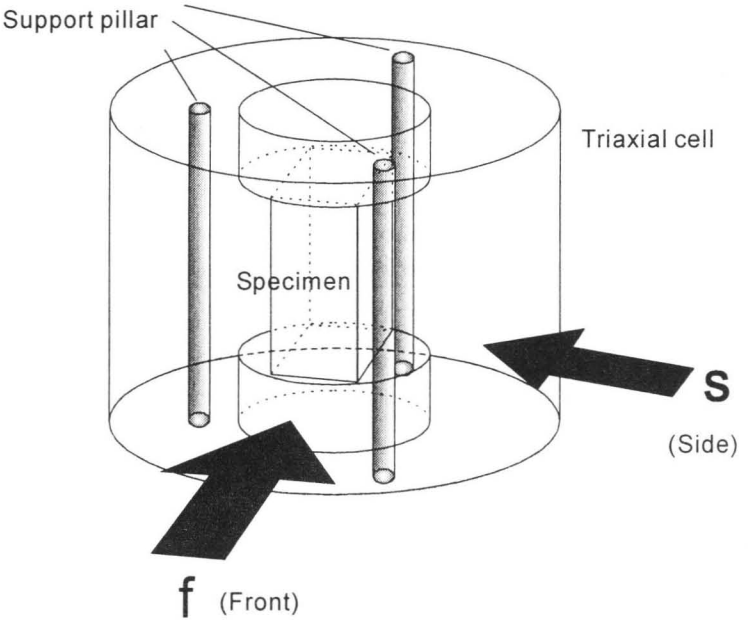

Figure 6.3 Schematic figure of the photography

$$\{\varepsilon\} = [B]\{u\} \tag{6.1}$$

in which

$$\{\varepsilon\}^{\mathrm{T}} = \{\varepsilon_x, \varepsilon_y, 2\varepsilon_{xy}\} \quad , \qquad \{u\}^{\mathrm{T}} = \{u_x^1, u_y^1, u_x^2, u_y^2, u_x^3, u_y^3, u_x^4, u_y^4\} \tag{6.2}$$

where ε is the strain, u is the displacement, subscripts $_x$ and $_y$ denote horizontal and vertical directions, and ε_{xy} is the shear strain. The superscripted numbers (1 to 4) indicate the nodal numbers of the isoparametric elements. The deviatoric strain is given as

$$\{e\}^{\mathrm{T}} = \{e_x, e_y, e_{xy}\} = \{\varepsilon_x - \varepsilon_v/2, \varepsilon_y - \varepsilon_v/2, \varepsilon_{xy}\} \tag{6.3}$$

where $\varepsilon_v (= \varepsilon_x + \varepsilon_y)$ is the volumetric strain in a two-dimensional form.

Finally, we obtain the second invariant of deviatoric strain γ as follows:

$$\gamma = \sqrt{e_x^2 + e_y^2 + 2e_{xy}^2} \tag{6.4}$$

The contours of γ were drawn for each axial strain, and then we discussed the strain localization during deformation. In the following, 'shear strain' indicates the second invariant of deviatoric strain γ.

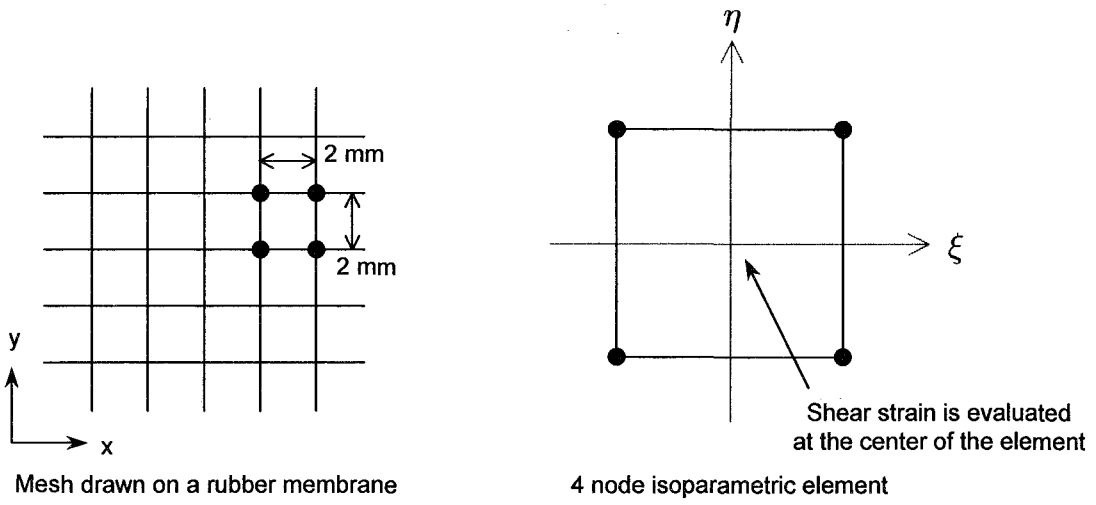

Figure 6.4 The four-node isoparametric element using in an image analysis

6.3 Experimental Results

Undrained triaxial compression tests for normally consolidated clay and overconsolidated clay with different shaped specimens were performed for different strain rates. **Figures 6.5~6.12** show the stress-strain relations, the effective stress paths, the distributions of the second invariants of shear strain γ, and photographs taken after the tests for all of the cases (see **Table 6.2**), respectively.

The stress-strain relations and the effective stress paths are shown in (a) and (b) of **Figures 6.5~6.12**, respectively, with three different strain rates for each case. We can see that they are affected by the strain rates and the shapes of the specimens. It is seen in the effective stress paths that the effective stress of normally consolidated clay decreases from the initial value. On the other hand, that of overconsolidated clay increases from its initial value. Namely, normally consolidated clay and overconsolidated clay exhibit negative and positive dilatancy characteristics, respectively.

The distributions of shear strain are shown in **Figures 6.5**(c)~**6.12**(c). In these figures, 's' and 'f' indicate the 'side surface' and the 'front surface' of the specimens, respectively (see **Figures 6.1** and **6.3**). On the whole, strain localization starts at an axial strain of 8% and shear bands are clearly seen at an axial strain of 12%. In addition, shear bands develop from the edges of the top and the bottom of the specimens since the friction force generating between the specimen and the top cap or the pedestal acts as a trigger of strain localization. As the axial strain becomes large, apparent shear bands appear on the side surface of the front surface, and develop with increases in the thickness of the shear bands. We can typically see this behavior in the case of B_O-1. On both two surfaces, the formation of four shear bands can be seen at an axial strain of 12%. Then, on the front surface, incorporating two shear bands from the top and the bottom, two shear bands develop which finally intercross each other. On the other hand, four shear bands develop less clearly on the side surface than on the front surface.

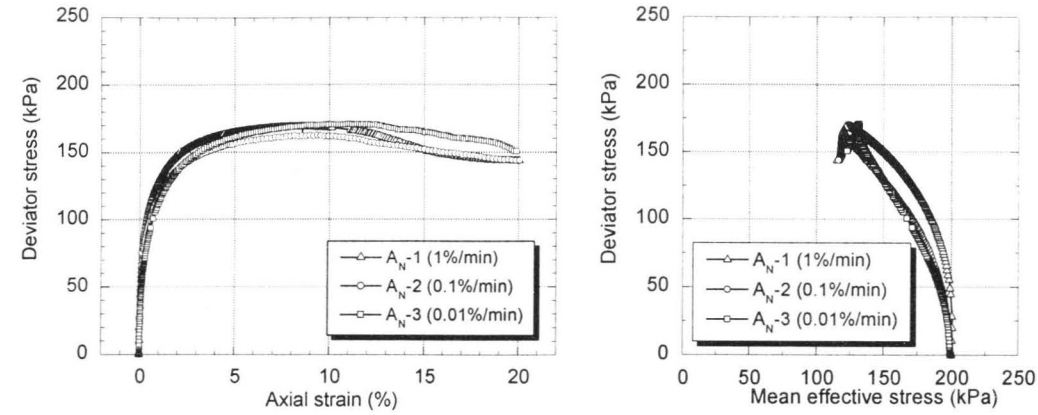

(a) Stress-strain relationships

(b) Effective stress paths

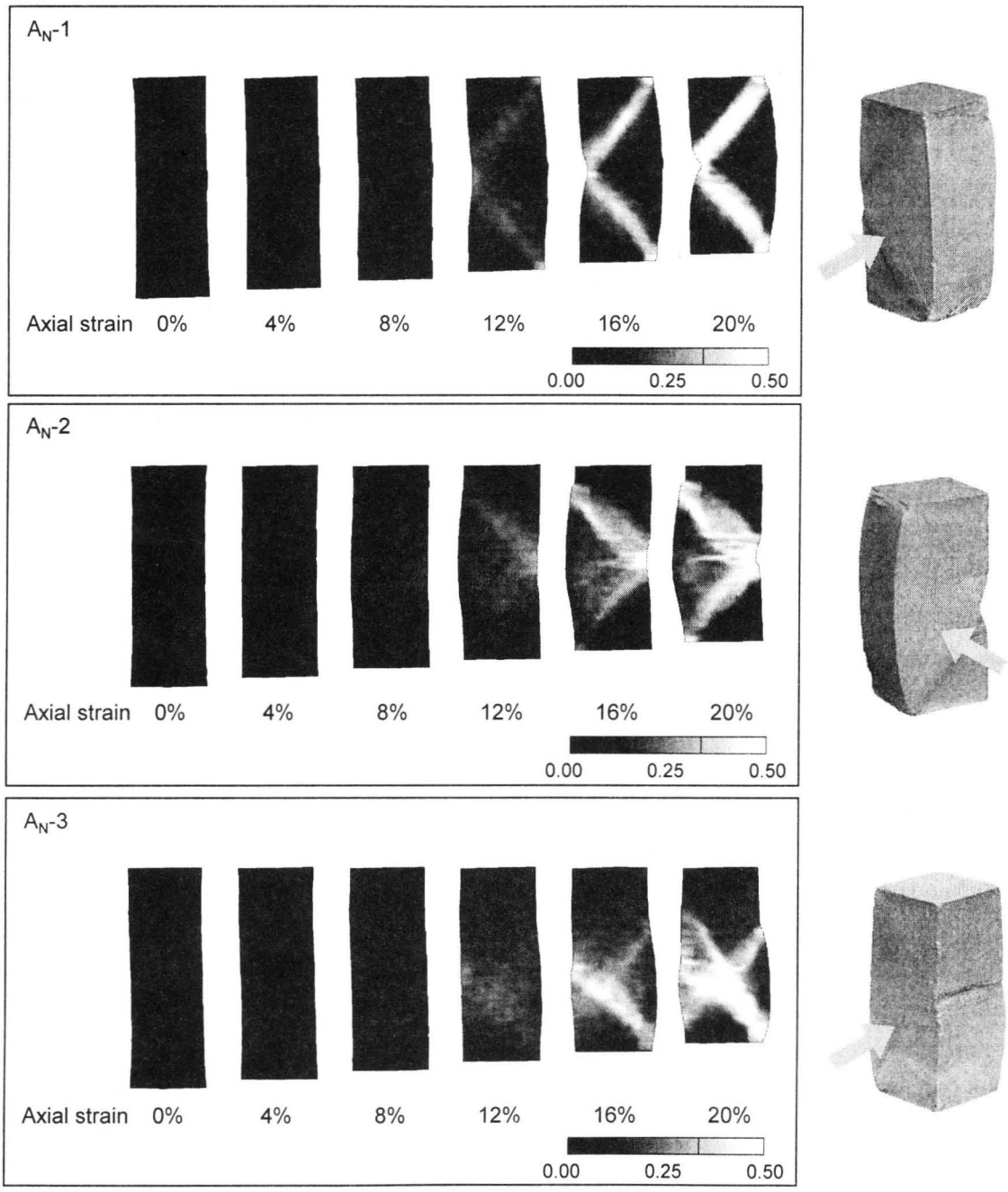

(c) Distributions of shear strain and photographs after the tests

Figure 6.5 Experimental results for the cases of A_N (Normally consolidated clay, 4×4×12 (cm))

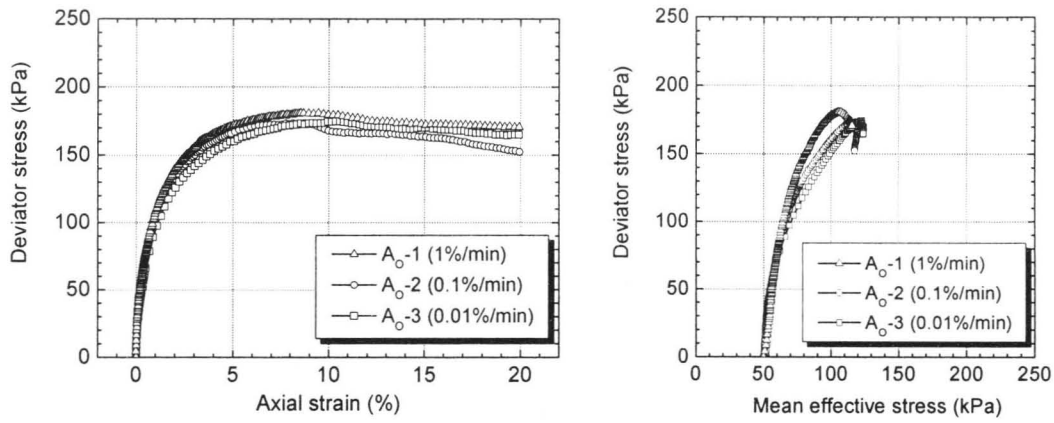

(a) Stress-strain relationships

(b) Effective stress paths

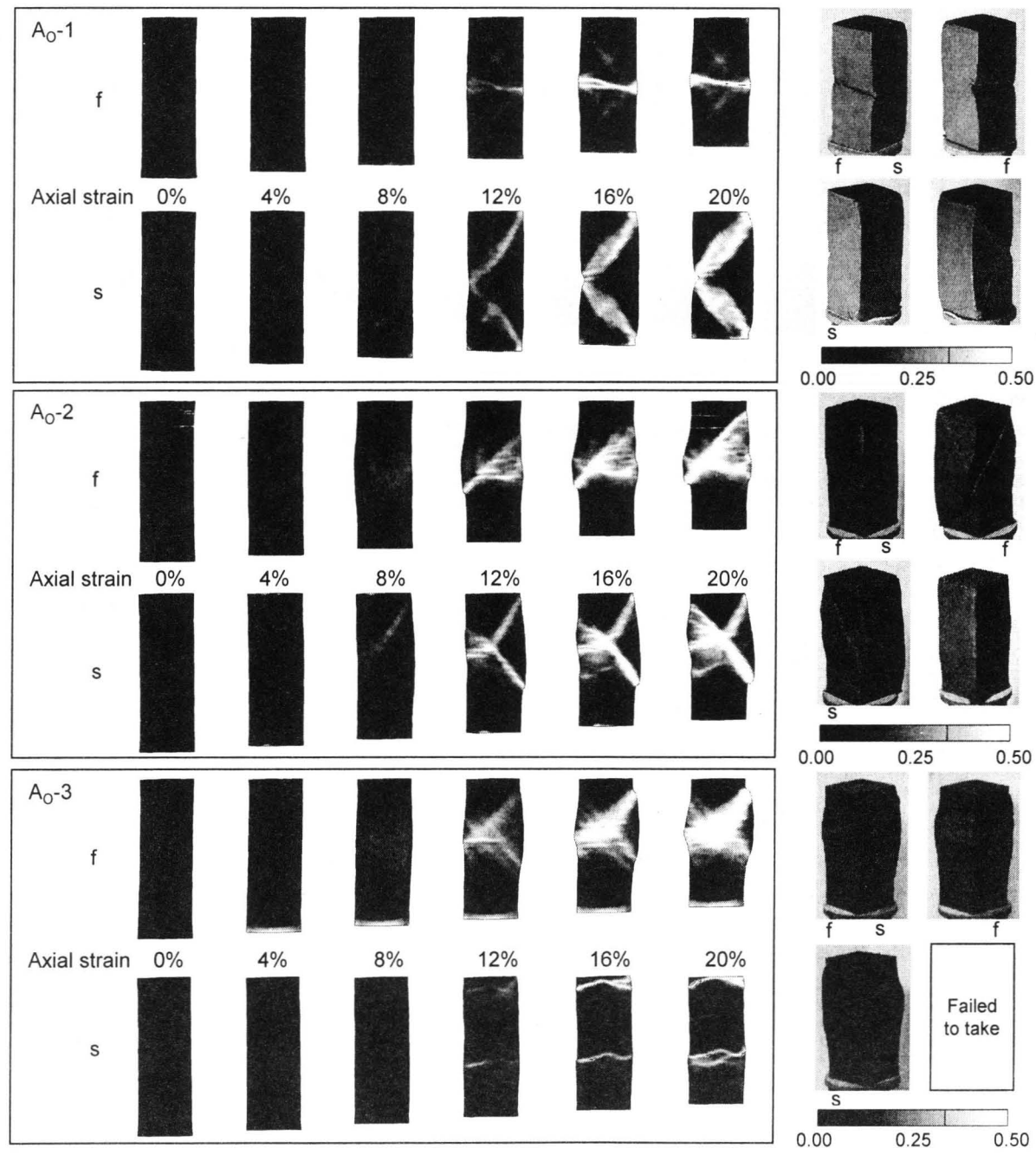

(c) Distributions of shear strain and photographs after the tests

Figure 6.6 Experimental results for the cases of A_O (Overconsolidated clay, 4×4×12 (cm))

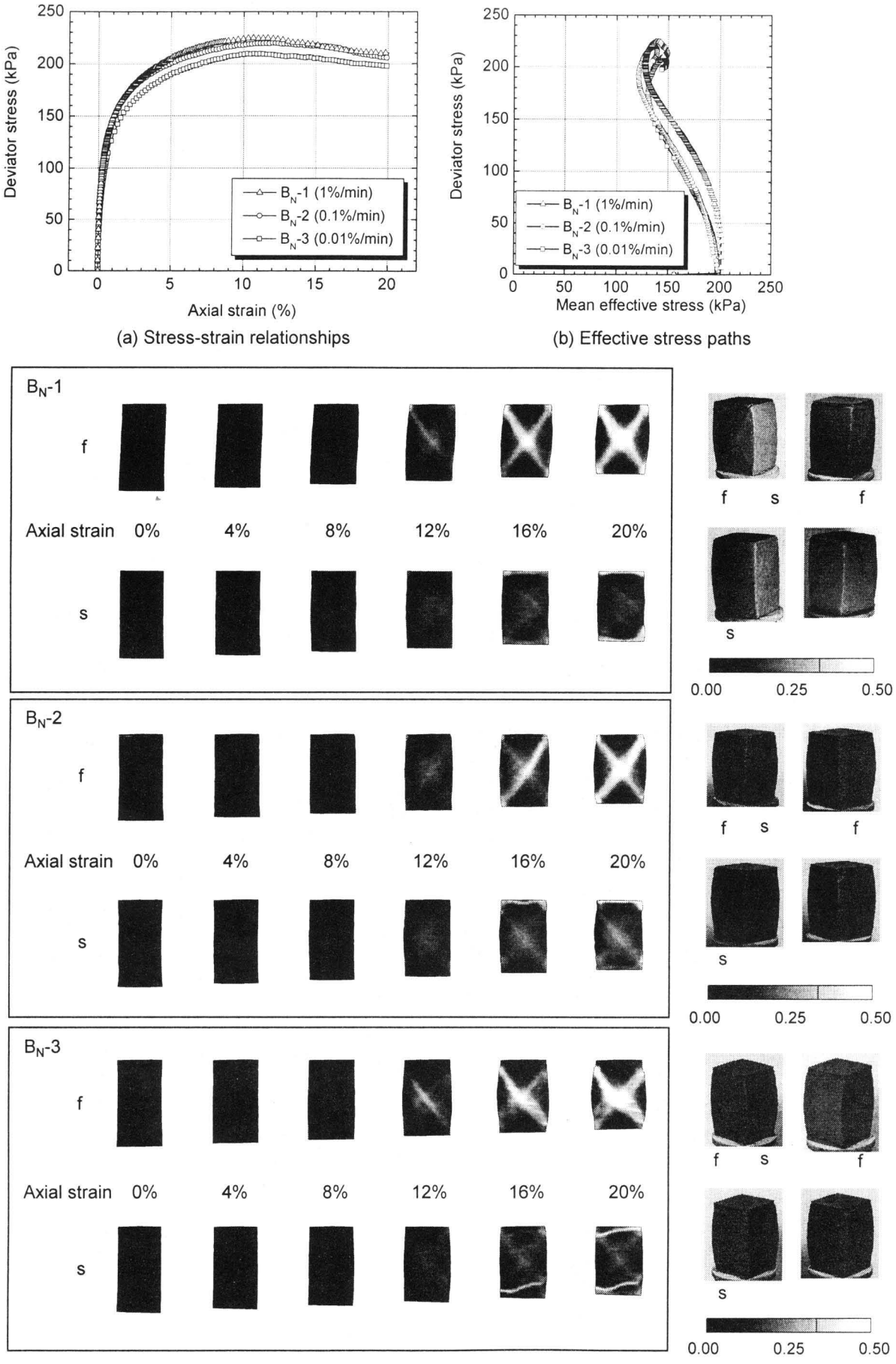

(a) Stress-strain relationships

(b) Effective stress paths

(c) Distributions of shear strain and photographs after the tests

Figure 6.7 Experimental results for the cases of B_N (Normally consolidated clay, 4×4×8 (cm))

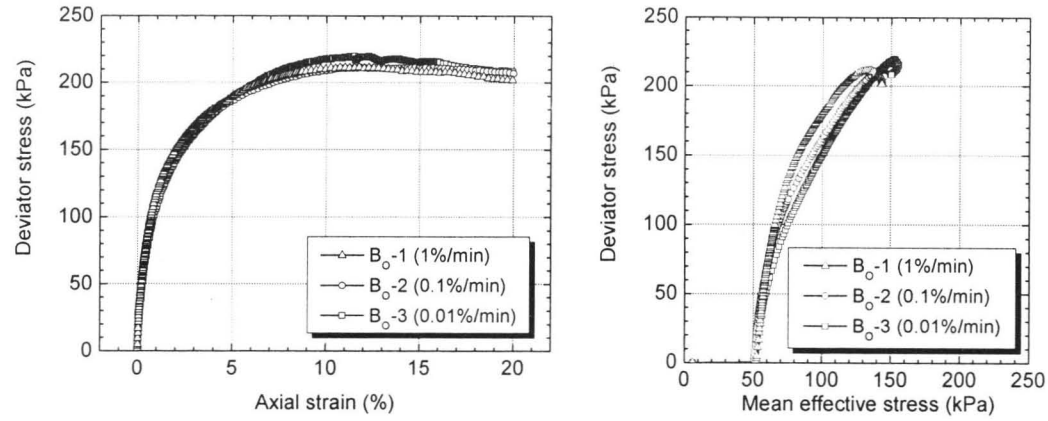

(a) Stress-strain relationships

(b) Effective stress paths

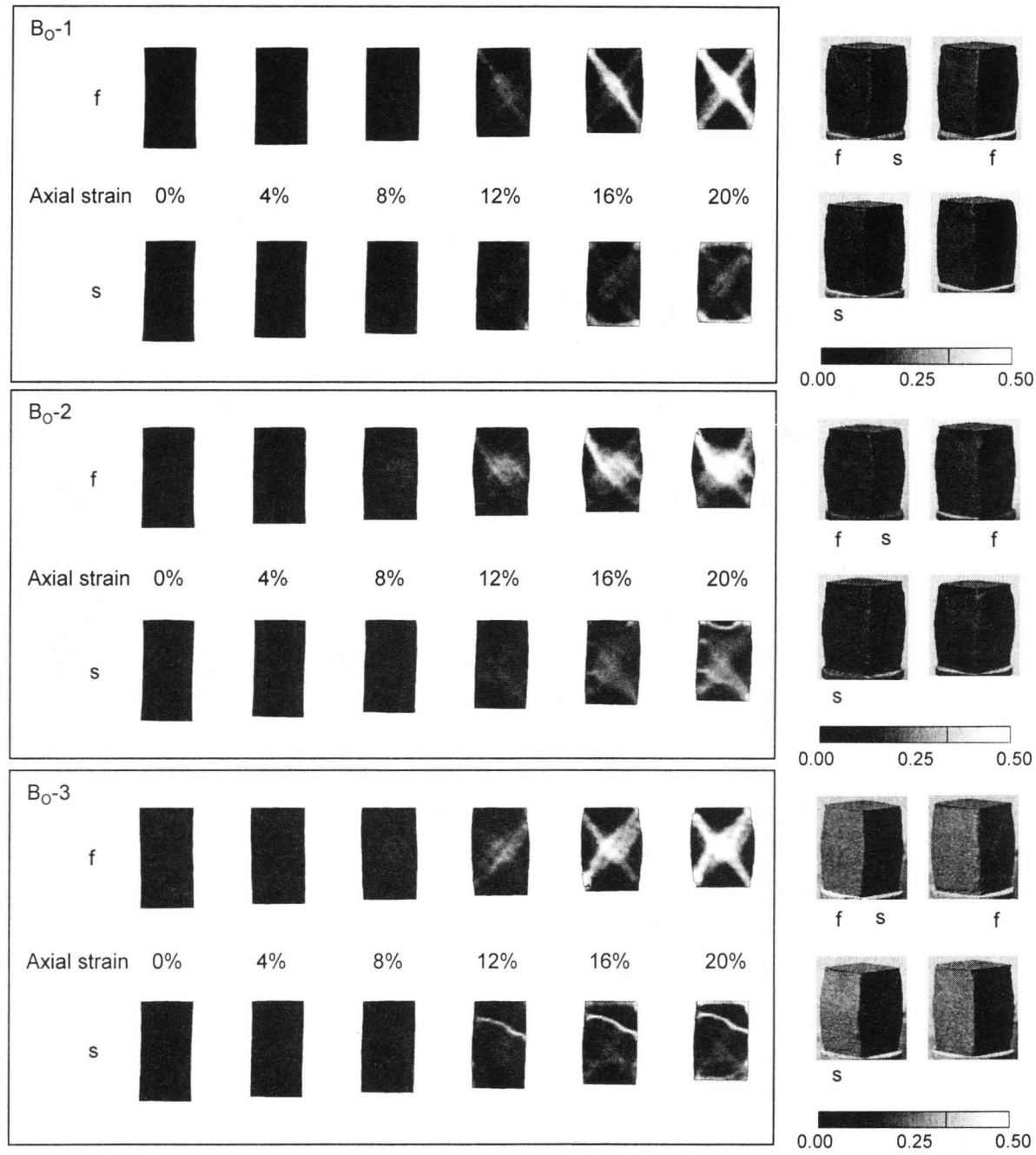

(c) Distributions of shear strain and photographs after the tests

Figure 6.8 Experimental results for the cases of B_O (Overconsolidated clay, 4×4×8 (cm))

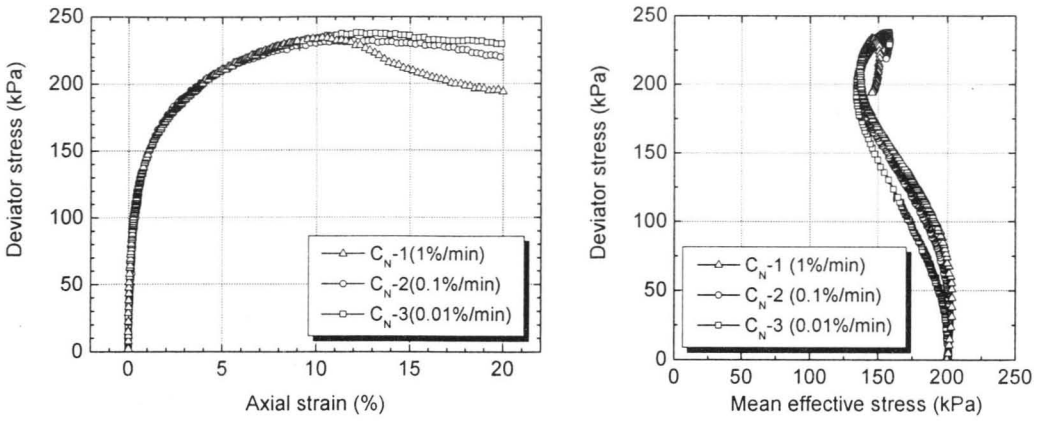

(a) Stress-strain relationships (b) Effective stress paths

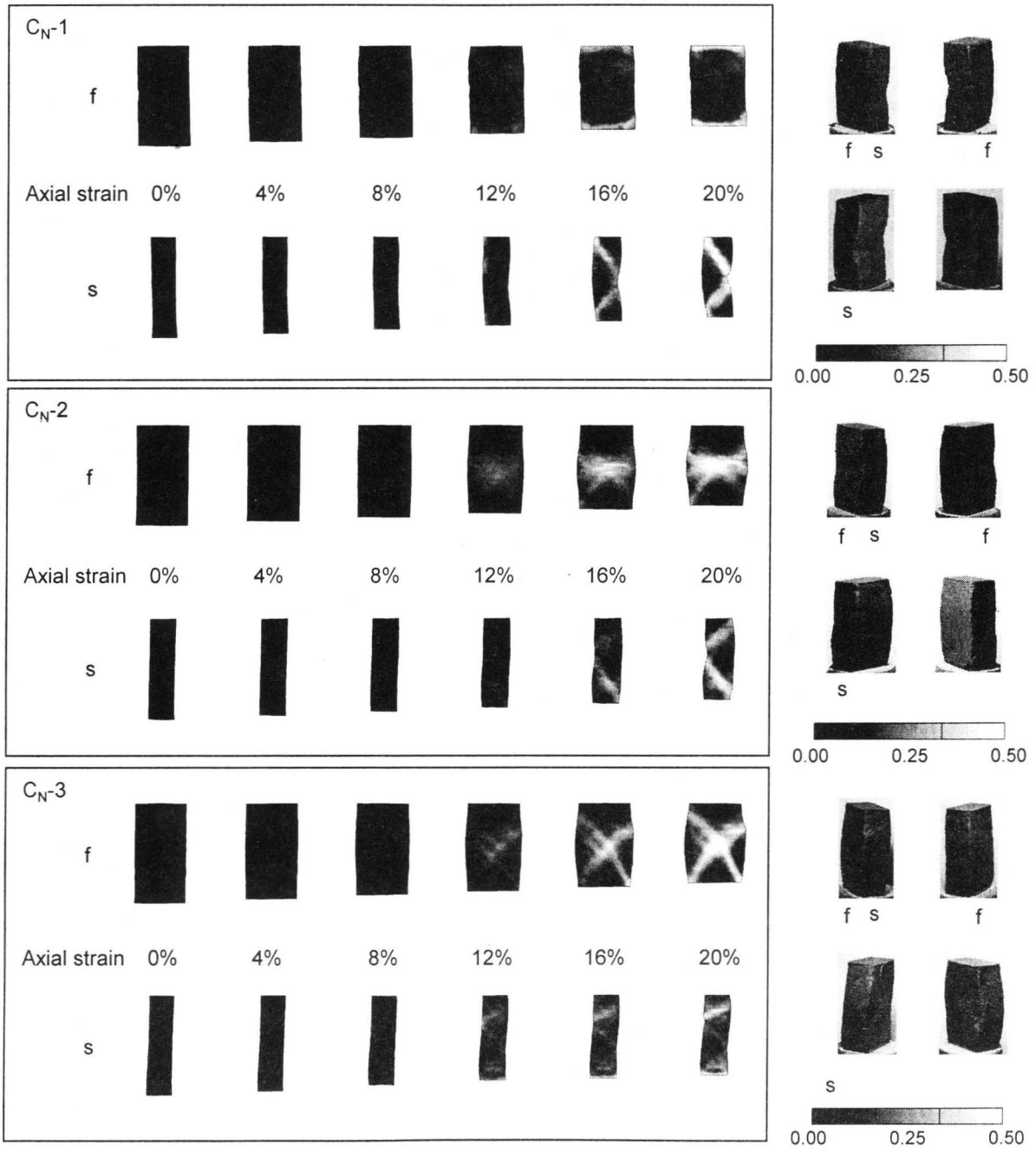

(c) Distributions of shear strain and photographs after the tests

Figure 6.9 Experimental results for the cases of C_N (Normally consolidated clay, 4×2×8 (cm))

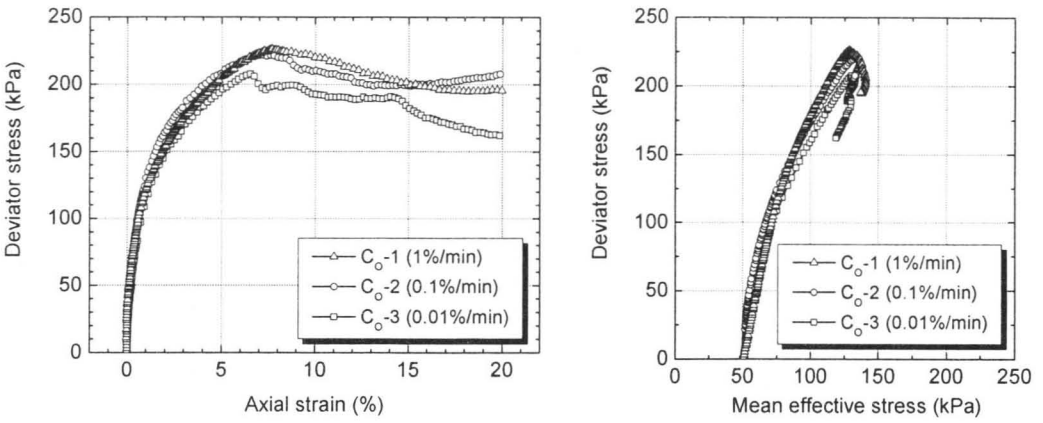

(a) Stress-strain relationships (b) Effective stress paths

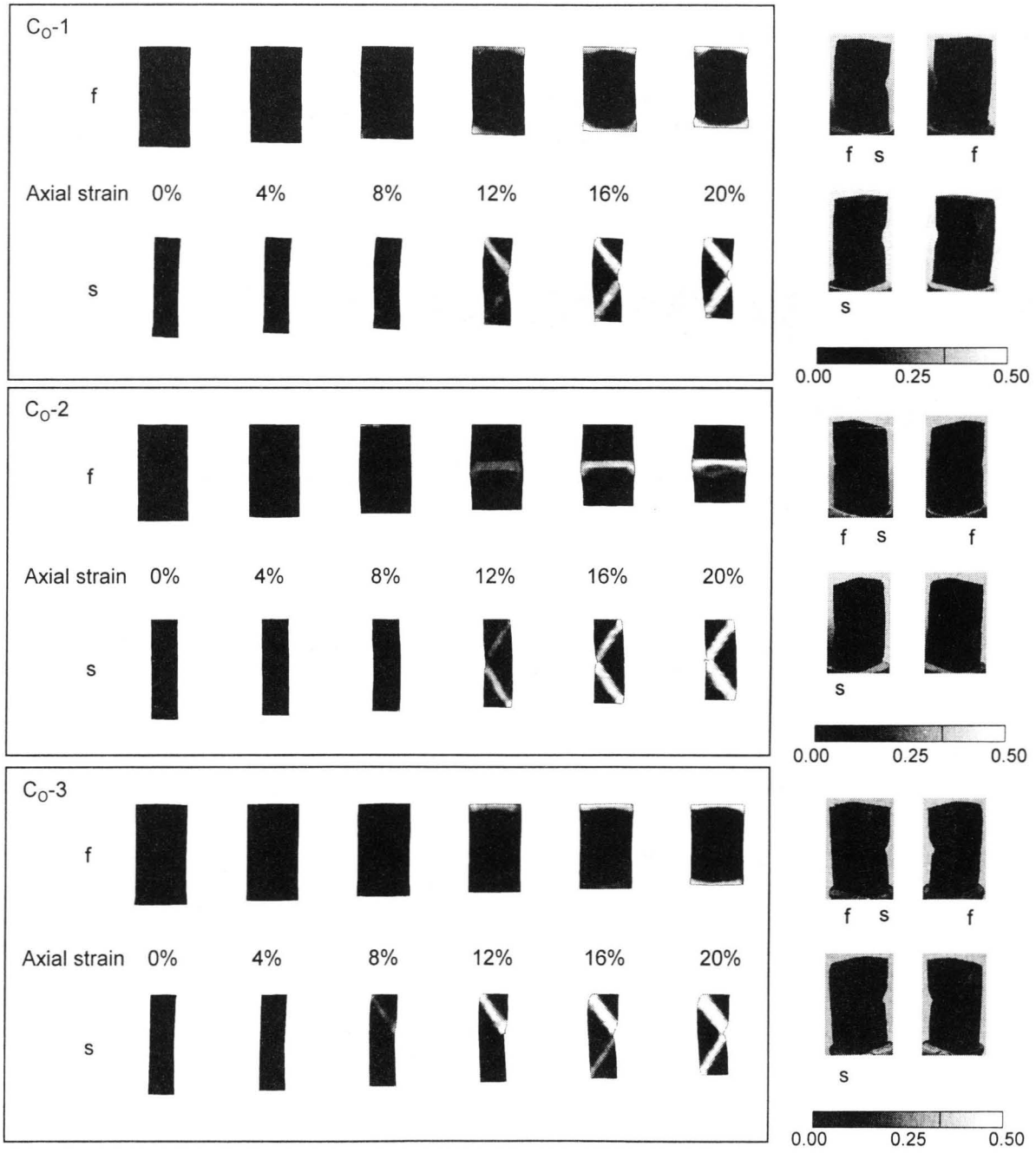

(c) Distributions of shear strain and photographs after the tests

Figure 6.10 Experimental results for the cases of C_O (Overconsolidated clay, 4×2×8 (cm))

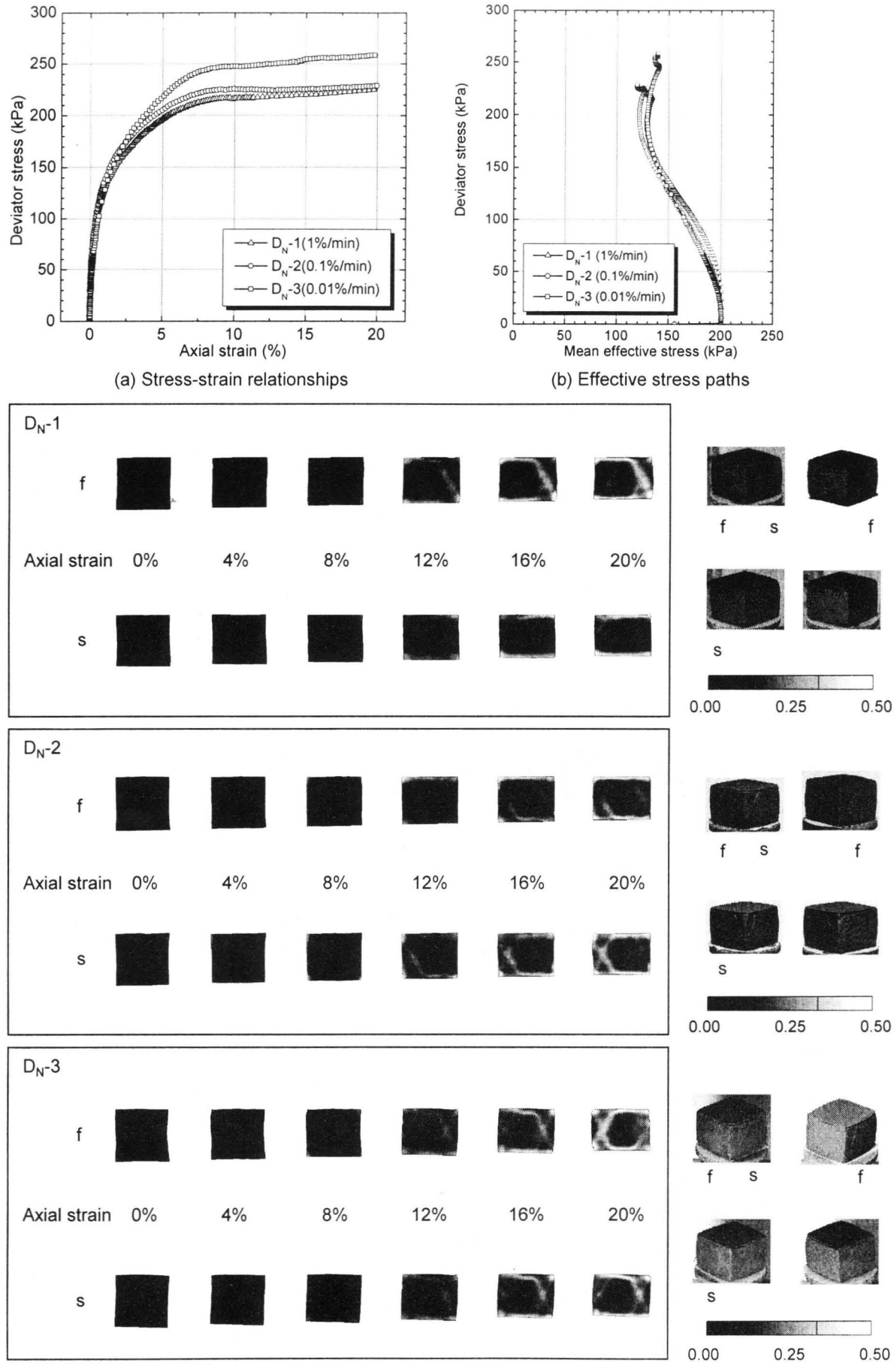

Figure 6.11 Experimental results for the cases of D_N (Normally consolidated clay, 4×4×4 (cm))

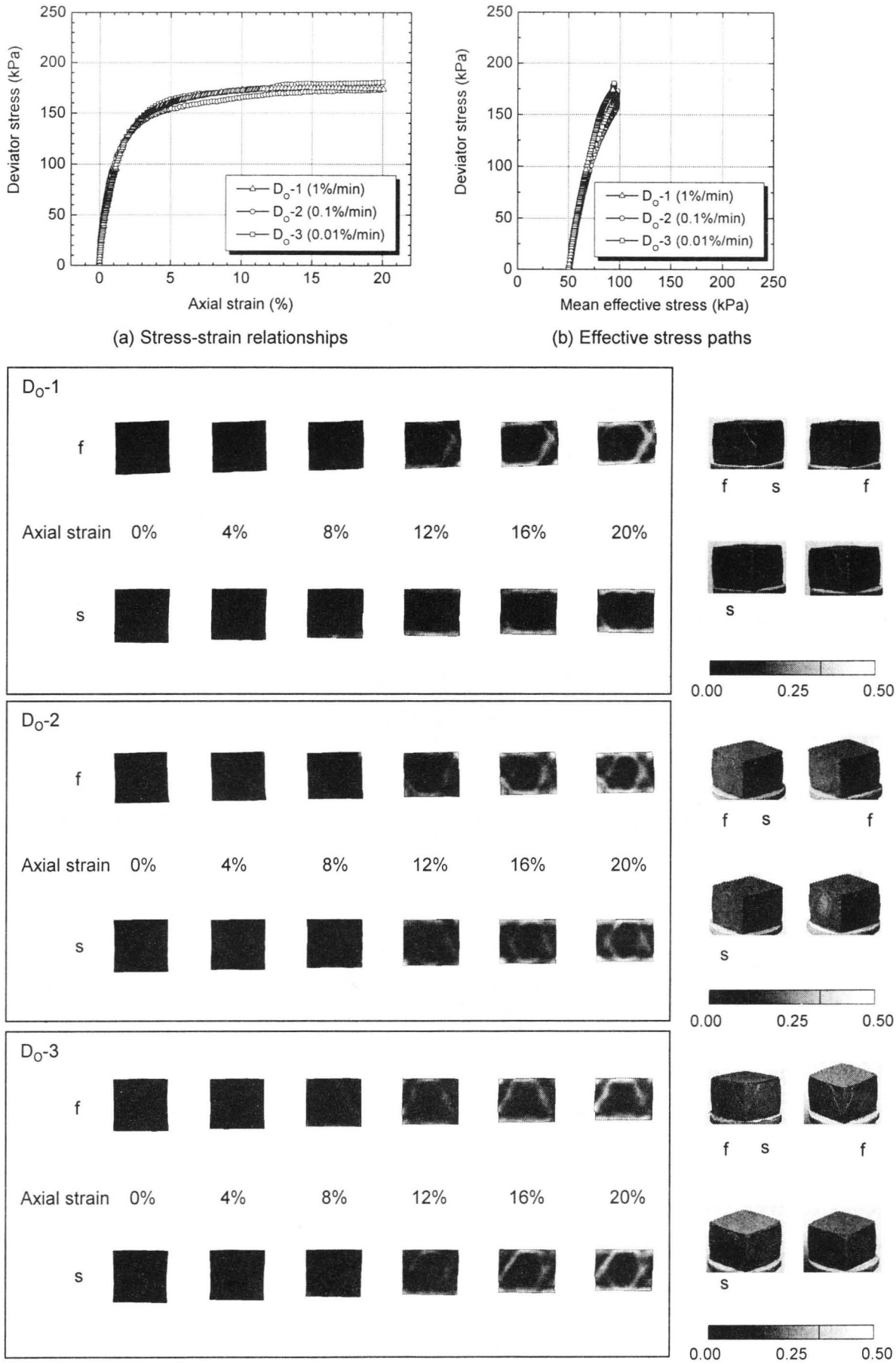

Figure 6.12 Experimental results for the cases of D_O (Overconsolidated clay, 4×4×4 (cm))

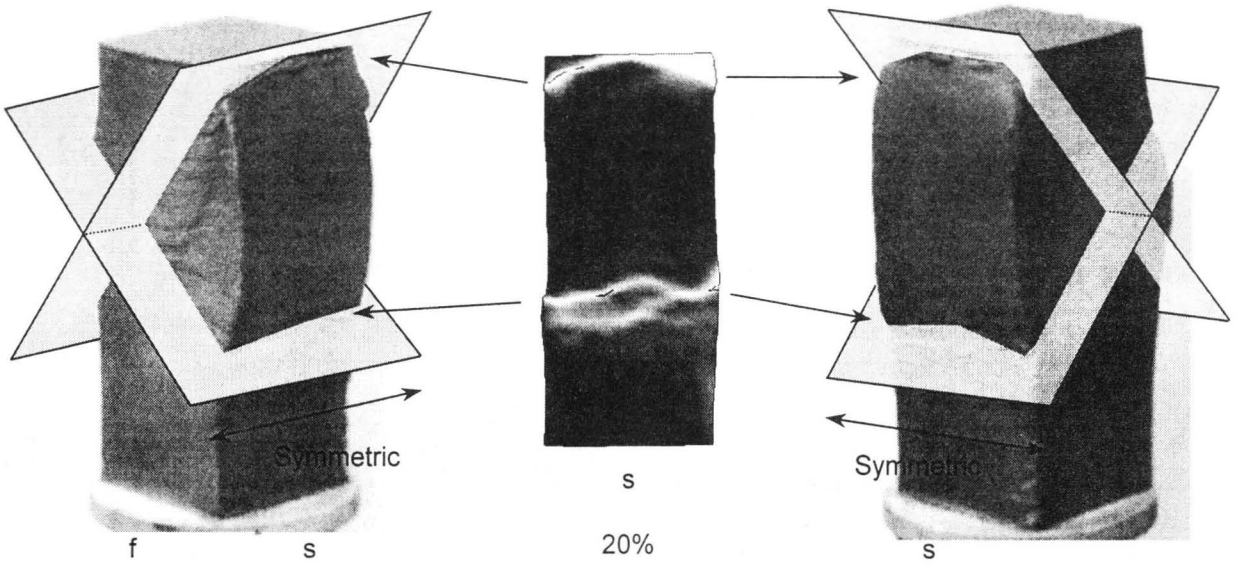

Figure 6.13 Estimated shear bands and strain localization developing on the side surface (A_O-3, photographs after the tests)

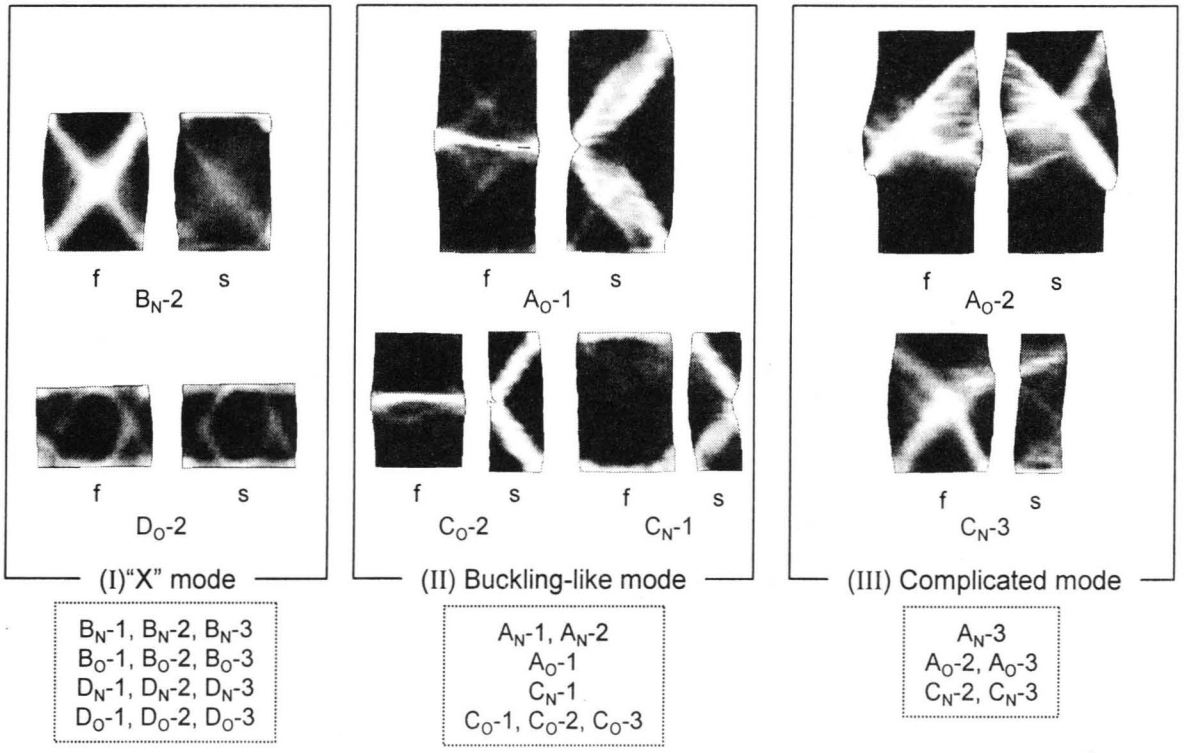

Figure 6.14 Three deformation modes (distributions of shear strain, axial strain: 20%) (I) "X" mode, (II) Buckling-like mode, and (III) Complicated mode

In the case of A_O-1, shown in **Figure 6.6**(c), four shear bands can be seen at an axial strain of 8% on both surfaces. However, only two shear bands on the side surface grow and their thickness becomes large. We can see on the front surface that the intersection of the shear bands appears at an axial strain of 12%. In general, these are not identified as shear bands. Rather, this is a kind of strain localization due to the deformation mode, just like the buckling of a column, as can be seen in the photographs. The same type of behavior can be seen on the front surface of C_O-2. On the side surface of A_O-3, B_N-3, and B_O-3, we can see shear bands, which are very sharp strain localization developing horizontally and are related to the shear bands being generated on the other surfaces. In these cases, shear surfaces are formed in the specimens just like shear bands under plane strain conditions. As shown in **Figure 6.13**, the edges of the shear bands are developing symmetrically in the direction indicated by the arrows which appear on the side surface.

6.3.1 Classification of the Strain Localization Patterns

We can classify deformation patterns into three types, as shown in **Figure 6.14**. The first one is a deformation pattern in which two or four shear bands develop from the edges of the top and the bottom of the specimens, as seen in all cases of specimen B and specimen D with the rather small aspect ratios of 2 and 1, respectively. This mode is due to the material instability induced by the frictional boundary conditions between the clay specimens and the top caps and the pedestals. The two shear bands intercrossing each other are just like an "X", thus, we call it the "X" mode. **Figure 6.15** shows the schematics of the estimated process generating the "X" mode. The four shear bands generated in the case of specimen B finally develop two clear and thick shear bands.

The second deformation pattern can be seen in cases A_N-1, A_N-2, A_O-1, C_N-1, C_N-2, and all cases of C_O, in which two vertically symmetric shear bands appear on one of the surfaces, while the deformations of the other surfaces are rather homogeneous, e.g., the front surface of case C_N-1, or show the intersection of shear bands as seen for case C_O-2. These types of behavior are similar to compressive buckling. This type of strain localization pattern is called "the buckling-like mode". **Figure 6.16** shows the schematic process of the shear band formation of the buckling-like mode. The buckling-like mode is often seen in the case of A and C, and is probably due to larger aspect ratios of 3 and 4, respectively. The geometric instability of the specimens induces the buckling, in addition to the localized deformation from both edges due to the frictional force. Shear bands then develop from the point where the buckling occurs to the top and the bottom of each specimen with increased thickness which is attributed to material instability. We can see on another surface, e.g., the front surface of case A_O-1, that the intersection of the shear bands appears.

The last pattern is the complicated mode which includes the cases of specimen A and specimen C which are not classified into the buckling-like mode, namely, A_N-3, A_O-2, A_O-3, and C_N-3. **Figure 6.17** shows the schematics of the estimated process of the complicated mode. In the cases of A_N-3, A_O-2, and A_O-3, a few shear bands form intricately. The shear bands of case A_N-3 are seen in the lower part of the specimen. On the other hand, the shear bands of cases

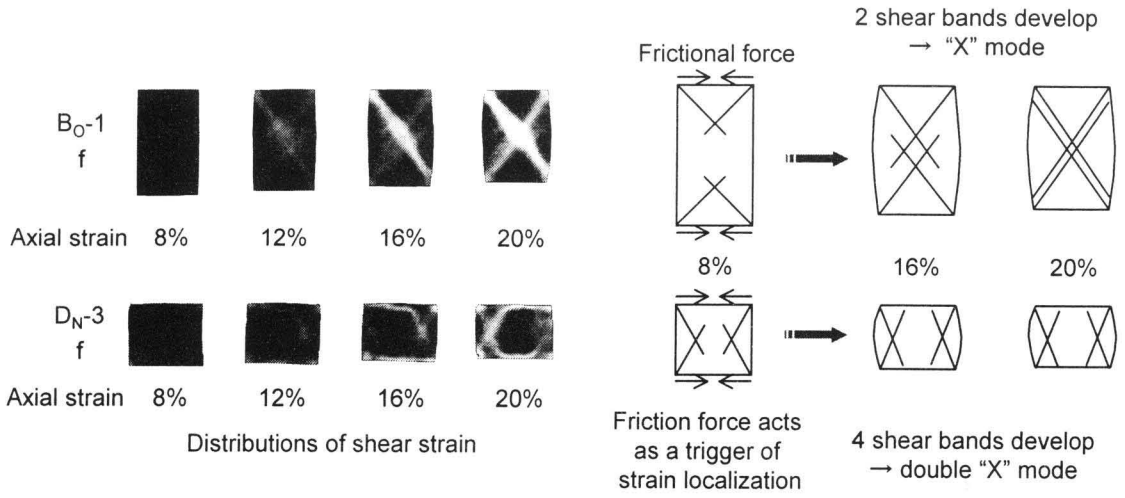

Figure 6.15 Schematics of the estimated process of the "X" mode (Cases B_O-1 and D_N-3)

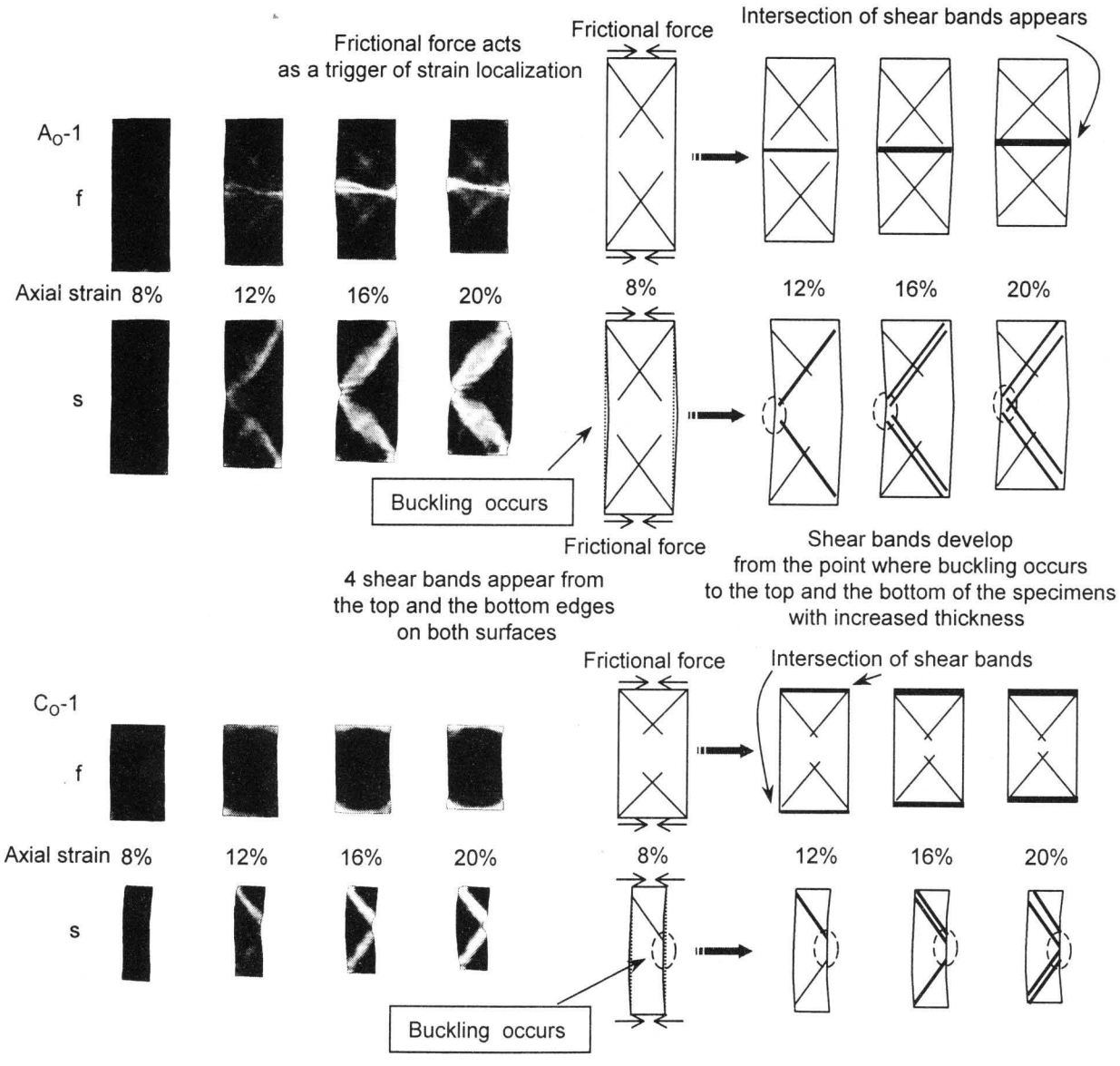

Figure 6.16 Schematics of the estimated process of the buckling-like mode (Cases A_O-1 and C_O-1)

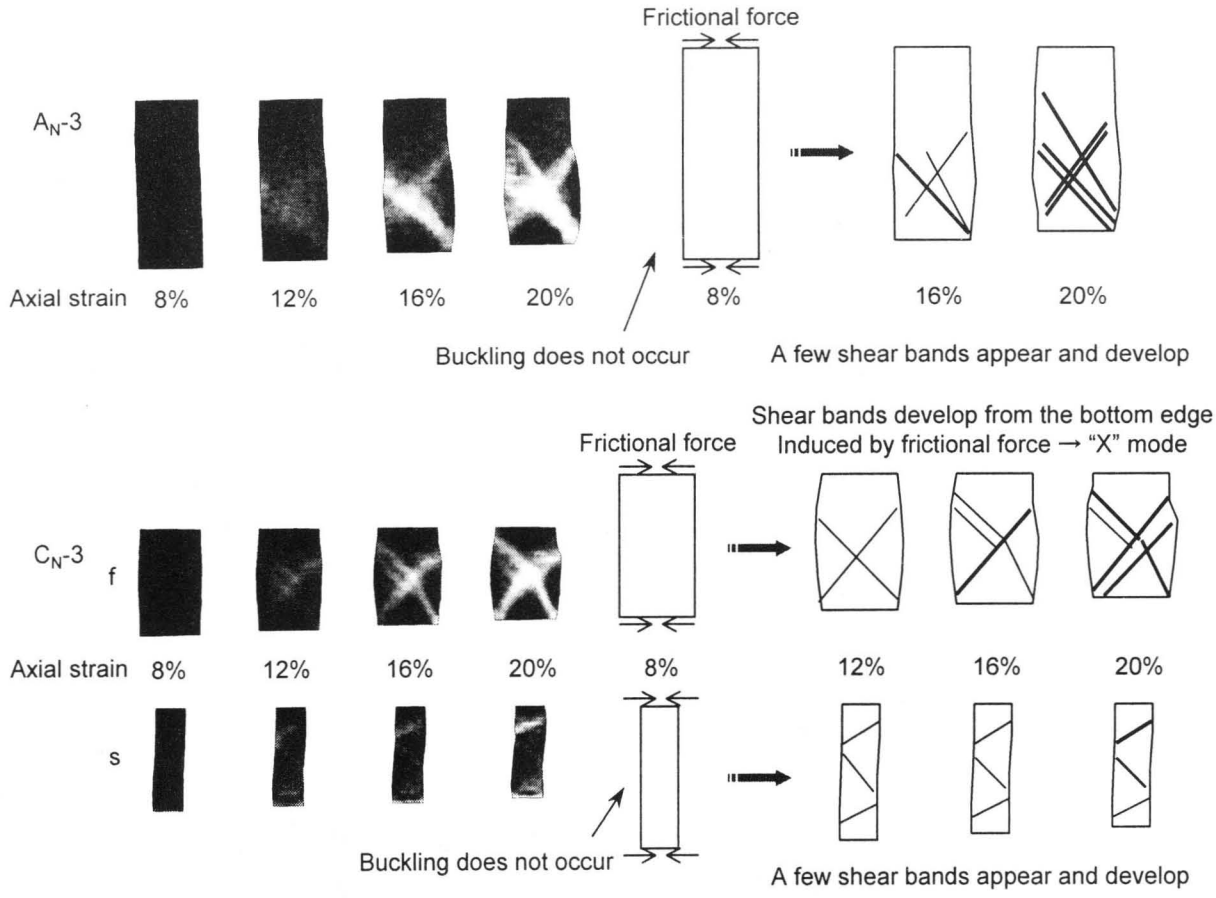

Figure 6.17 Schematics of the estimated process of the complicated mode (Cases A_N-3 and C_N-3)

A_O-2 and A_O-3 appear in the upper part of the specimen. One possible reason for this behavior is that after the "X" type of strain localization has occurred, a very small level of strain, which is difficult to see, generates in both the upper and the lower parts of the specimen, like in case A_O-1, and the upper or lower one becomes apparent. In the case of C_N-3, we can see on the front surface that two shear bands develop which intercross each other, namely, the "X" mode. On the side surface, however, a few shear bands appear.

6.3.2 Three-dimensional Shear Bands

From the distributions of shear strain on the two surfaces, we estimated three-dimensional shear bands in the same manner as that in **Figure 6.13** for case A_O-3. **Figure 6.18** displays the estimated shear bands for the "X" mode of cases B_N-3 and D_O-2. The shear bands of case B_N-3 intersect each other. It is possible that similar shear bands also exist perpendicular to the surfaces depicted in the figure, however, those are not apparent since the strain localization on the side surface is more moderate than the other. The shear surfaces in case D_O-2 also intersect each other and exist at four corners. However, it is not clear that the shear bands of specimen D penetrate the specimen, namely, the shear bands possibly appear only on the surfaces.

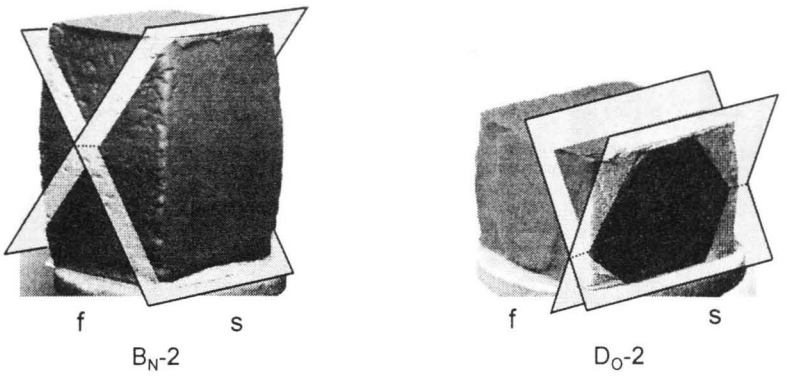

Figure 6.18 Estimated shear bands for the "X" mode for B_N-2 and D_O-2

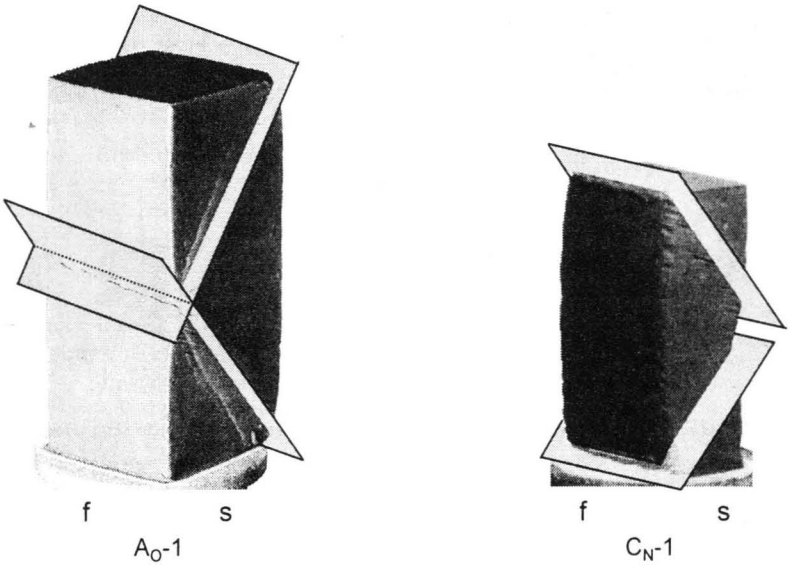

Figure 6.19 Estimated shear bands for the buckling-like mode for A_O-1 and C_N-1

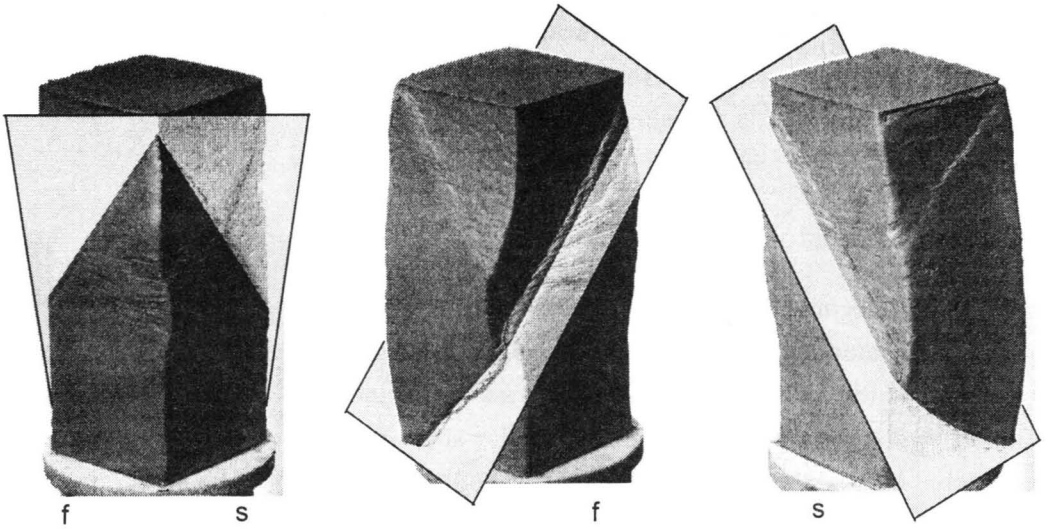

Figure 6.20 Estimated shear bands for the complicated mode for A_O-2

Figure 6.19 shows the estimated shear bands for cases A_O-1 and C_N-1, namely, the buckling-like mode. In this mode, it is easy to estimate that only two bands exist, as shown in the figure. On the other hand, we cannot easily estimate the shear bands of the complicated mode. For example, it is apparent that shear bands of C_N-2 are the same as for the buckling-like mode. It is seen on the front surface, however, that the shear bands from the bottom edge do not penetrate through the specimen. We cannot define an apparent shear band in such a case. **Figure 6.20** shows the estimated shear bands for A_O-2 for which we can identify an apparent shear band.

6.3.3 Effects of the Shapes of the Specimens

Strain Localization Pattern

Let us focus on the differences in the strain localization patterns among the four shapes of specimens listed in **Table 6.1**. It is seen in **Figures 6.7** and **6.8** that the deformation patterns of specimen B are similar. The deformations are homogeneous until the axial strain reaches 4% of the axial strain, however, strain localization starts at 8% and shear bands are clearly seen at 12%. At an axial strain of 20%, two shear bands finally appear from the edge of the top and the bottom of the specimen, and shear bands are more clearly seen on one of the surfaces than the other. The deformation patterns of specimen D have the same tendency as those of specimen B. The distribution of shear strain becomes non-homogeneous from an axial strain of 8%, and then, four shear bands develop near the edge of the top and the bottom of the specimen. On the other hand, the deformation patterns of specimen A and specimen C are different from those of specimen B and specimen D. We can see the buckling-like mode in the cases of A_N-1, A_N-2, A_O-1, C_N-1, C_N-2, and all cases of C_O. The other cases of specimens A and C, i.e., A_N-3, A_O-2, A_O-3, and C_N-3, show the relatively complicated mode.

Consequently, all cases of specimens B and D show the "X" mode due to the rather small aspect ratios of 2 and 1, respectively. On the other hand, specimens A and C are likely to show the buckling-like mode induced by their large aspect ratios of 4 and 3, respectively. Some cases of specimens A and C, however, show the other type of strain localization pattern with the complicated formation of shear bands.

Stress-strain Relations

Figures 6.5(a)~**6.6**(a) show the stress-strain relations of cases A_N and A_O, respectively. The specimens for all cases exhibit gradual strain softening, and each peak stress corresponds to the generation of shear bands. **Figure 6.21** shows the stress-strain relations and the distributions of shear strain for cases A_N-1 and A_O-2. The deformation of A_N-1 starts to localize at an axial strain of 8% and the shear bands of the buckling-like mode appear at 12%, corresponding to the beginning of the softening behavior. On the other hand, the deviator stress continues to increase, although strain localization for A_O-2 is clearly seen at 8% and 9%. This is probably because the dilatancy of overconsolidated clay increases the deviator stress much more than the softening induced by the shear band on the side surface. When the strain softening behavior starts, the second shear band generates from 10% and intersects the first one. Finally, the second

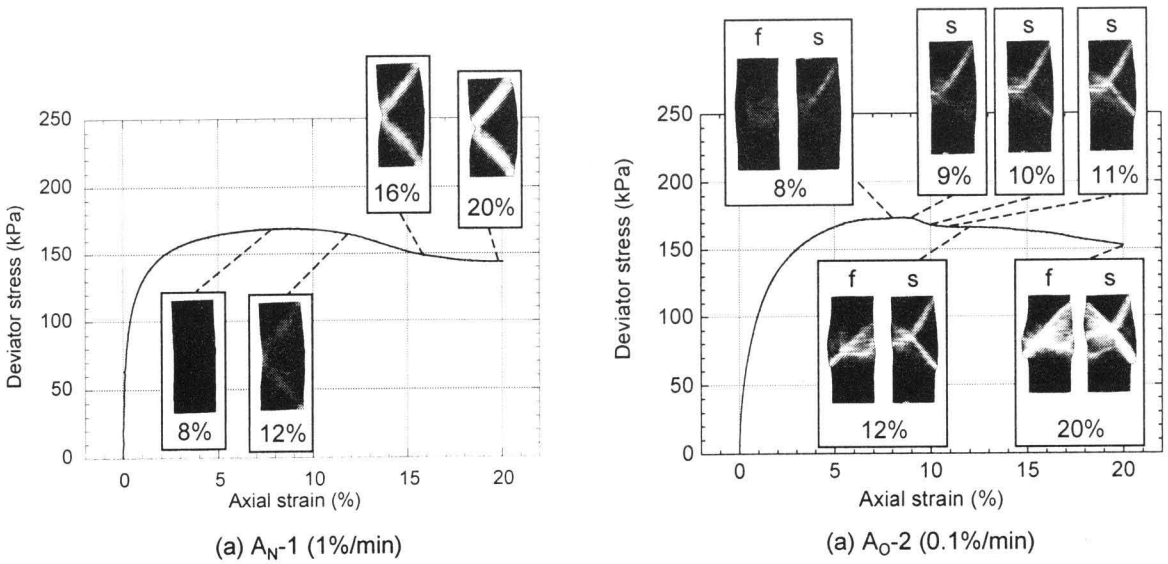

Figure 6.21 Stress-strain relations and the distributions of shear strain for (a)A_N-1 (1%/min) and (b)A_O-2 (0.1%/min)

shear band becomes apparent and the softening behavior continues up to 20%. In this way, the stress-strain relations of the cases of specimen A show strain softening corresponding to the beginning of the buckling-like mode or to the generation of apparent shear bands. However, the decrements in deviator stress do not have a clear tendency.

The stress-strain relations of the cases of specimen C are similar to those of specimen A. In addition, there is a specific relation between the localization mode and the softening behavior. The deviator stress in those cases, which show the buckling-like mode, decreases much more than the others. **Figure 6.22** shows the stress-strain relations and the distributions of shear strain for cases C_N-1 and C_N-3. The buckling-like mode of case C_N-1 appears at an axial strain of 12% just after the deviator stress begins to decrease. On the other hand, the stress-strain relations of case C_N-3 show gradual strain-softening behavior, although the "X" mode of the shear bands is clearly seen on the front surface. The stress-strain curve of case C_O-3 explicitly shows the softening behavior corresponding to the generation of shear bands, as shown in **Figure 6.23**. When the strain-softening behavior starts at an axial strain of 6%, the first shear band appears in the upper part of the specimen. The specimen shows strongly unstable behavior as the first shear band grows, and then, further decrease start around 14%. During the drastic decrease in deviator stress, the second shear band can be seen in the lower part at an axial strain of 16%.

The stress-strain relations of specimen B show rather moderate strain softening behavior just at the appearance of shear bands. The shear bands for all cases of specimen B are generated and the deviator stress levels of specimen B begin to decrease between axial strain levels of 8% and 12%. Contrary to these three cases for specimen A, specimen B, and specimen C, the stress-strain relations of specimen D show continuous hardening behavior, although shear bands appear in all cases. This is probably because the extremely small aspect ratio for the shape of specimen D induces geometric stability.

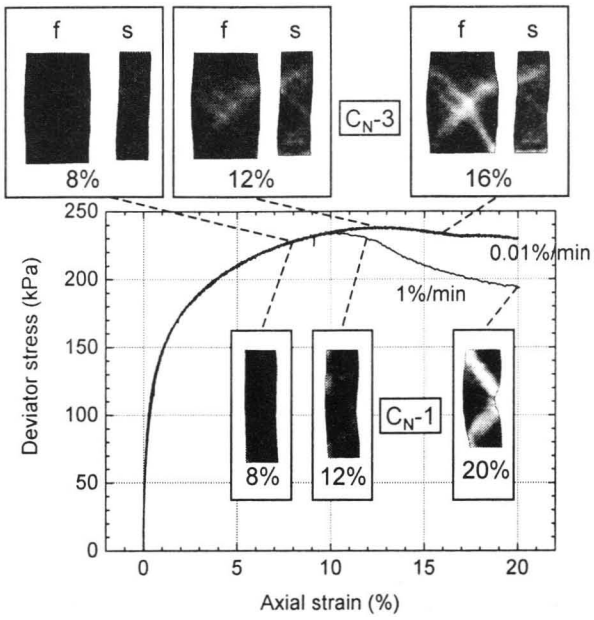

Figure 6.22 Stress-strain relations and the distributions of shear strain for C_N-1 (1%/min) and C_N-3 (0.01%/min)

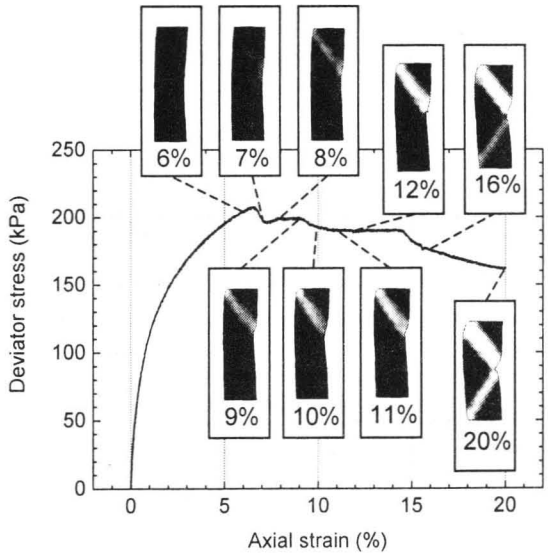

Figure 6.23 Stress-strain relations and the distributions of shear strain for C_O-3 (0.01%/min)

6.3.4 Effects of the Strain Rate

Strain Rate Sensitivity

It is well known that clay exhibits strain rate sensitivity. Oka et al. (2003) reported the strain rate sensitivity of Fukakusa clay under undrained triaxial compression conditions. As shown in **Figures 6.5**(a) to **6.12**(a), however, we can clearly see rate sensitivity only in case B_N. On the contrary, the other cases do not show apparent strain rate sensitivity. The reason for this is that the deviator stress is more greatly dependent on the deformation mode than the material characteristics of rate sensitivity. Since triaxial tests are a boundary value problem, non-homogeneous deformations are naturally induced and strain localization leads to a local decrease in stiffness by which the clay exhibits strain-softening behavior. **Figure 6.24** shows the stress-strain relations in the range of the small axial strain of 0.1%. The deviator stress obtained from the tests with higher strain rates is larger than that from tests with lower strain rates, except for case C_N. This tendency shows the typical strain rate sensitivity of clay.

Strain Localization Pattern

As mentioned in **Section 6.3.1**, strain localization patterns are classified into three types. The strain localization pattern for specimen B is the "X" mode, which is composed of two shear bands developing from the edges of the top and the bottom of the specimen. **Figure 6.25** shows distributions of shear strain for specimen B with different strain rates at an axial strain of 20% and inclination angles of the shear bands. Shear bands on the front surface are clearer than those on the side surface. In the case of the fastest strain rate of 1 %/min, shear bands develop from the top edge. On the other hand, in the case of the lowest strain rate of 0.01 %/min, shear bands develop beneath the top edge. There are black areas, namely, areas where the shear strain is very small, near the top and the bottom ends. Shear band formation that is seen in the case of a middle strain rate of 0.1 %/min starts from a relatively lower part than the top edge. Due to this tendency, the inclinations of the shear band with a strain rate of 0.01 %/min are lower than those with higher strain rates. In addition, the thickness of shear bands with lower strain rates is larger than that of bands with higher strain rates. On the side surface, it is worth mentioning that four shear bands formed in the case of the highest strain rate of 1.0 %/min.

Figure 6.26 shows the distributions of shear strain for specimen D with different strain rates at an axial strain of 20% and inclinations of shear bands. All shear bands develop from the top and the bottom edges and form two "X" modes. However, the number of shear bands decreases as the strain rate becomes larger. In particular, we can see relatively homogeneous deformations on the side surface for cases D_N-1 and D_O-1, while three or four shear bands are clearly seen on both surfaces for cases D_N-3 and D_O-3. There is no specific tendency of angles for the shear bands that are 46 to 68 degrees.

In the case of specimen A, shown in **Figure 6.27**, the specimens compressed with higher strain rates tend to show the buckling-like mode. Cases A_N-3, A_O-2, and A_O-3 show an apparent shear band and a rather extensive distribution of shear strain along the shear band. The shear

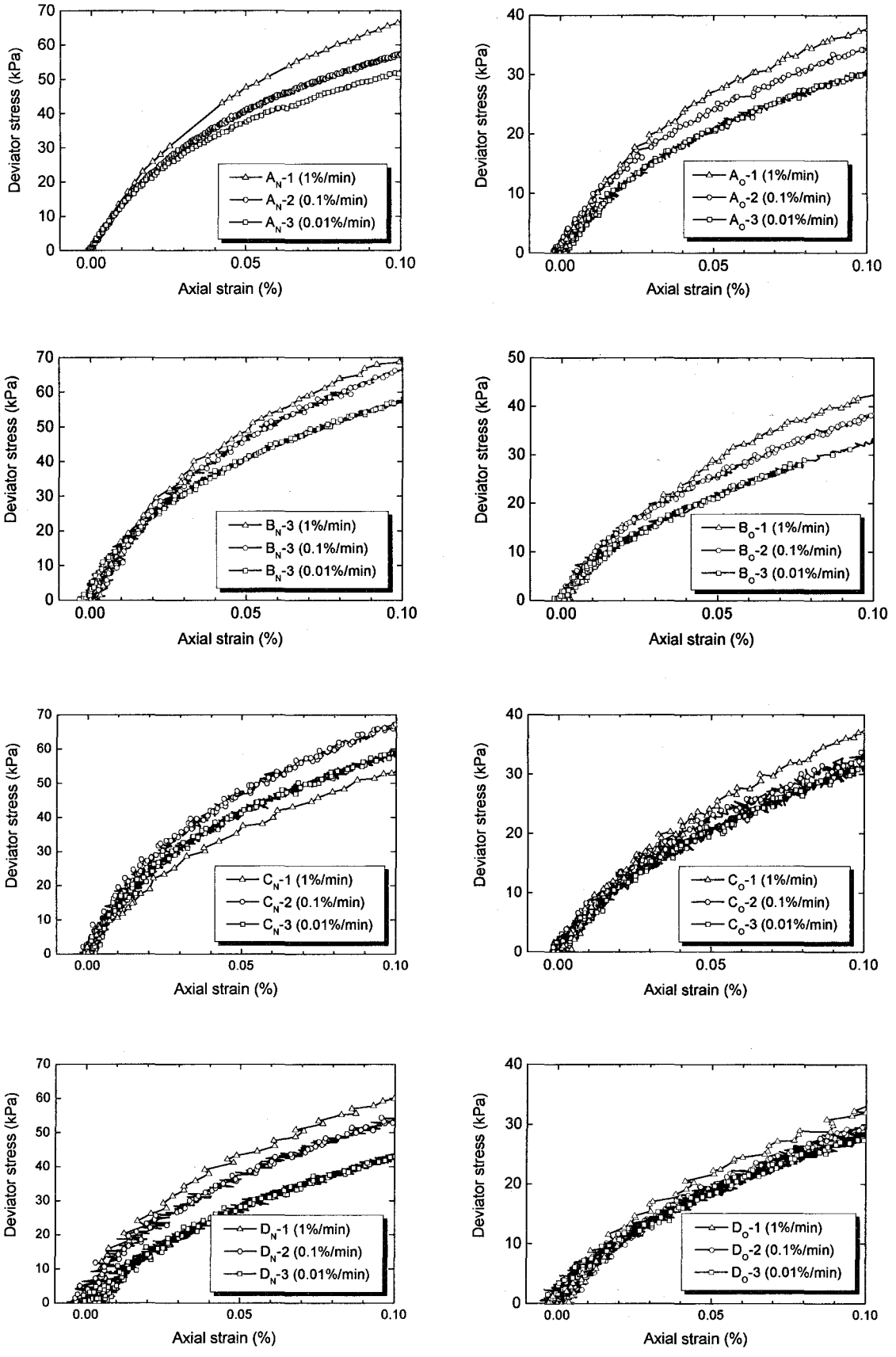

Figure 6.24 Stress-strain relations in a small axial strain range

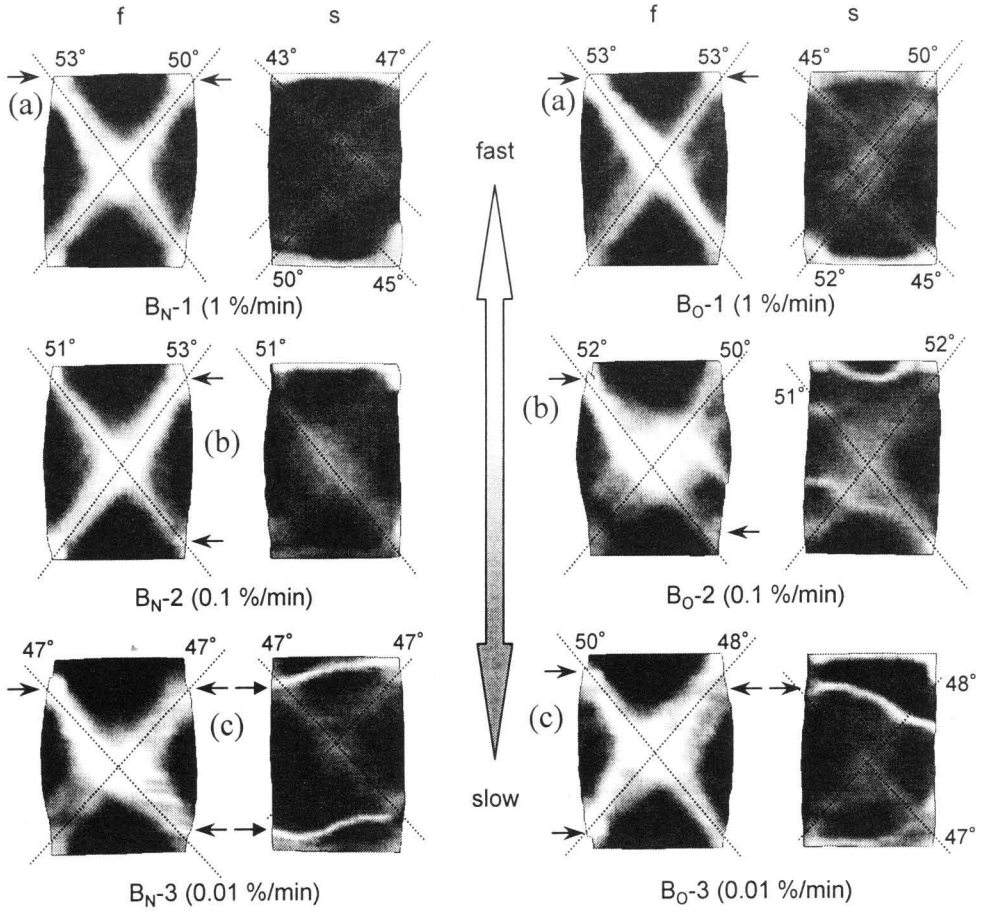

Figure 6.25 Distributions of shear strain for specimen B with different strain rates at an axial strain of 20% and inclinations of the shear bands: (a) shear bands develop from the top edge, (b) shear bands develop just beneath the top edge, and (c) shear bands develop beneath the top edge.

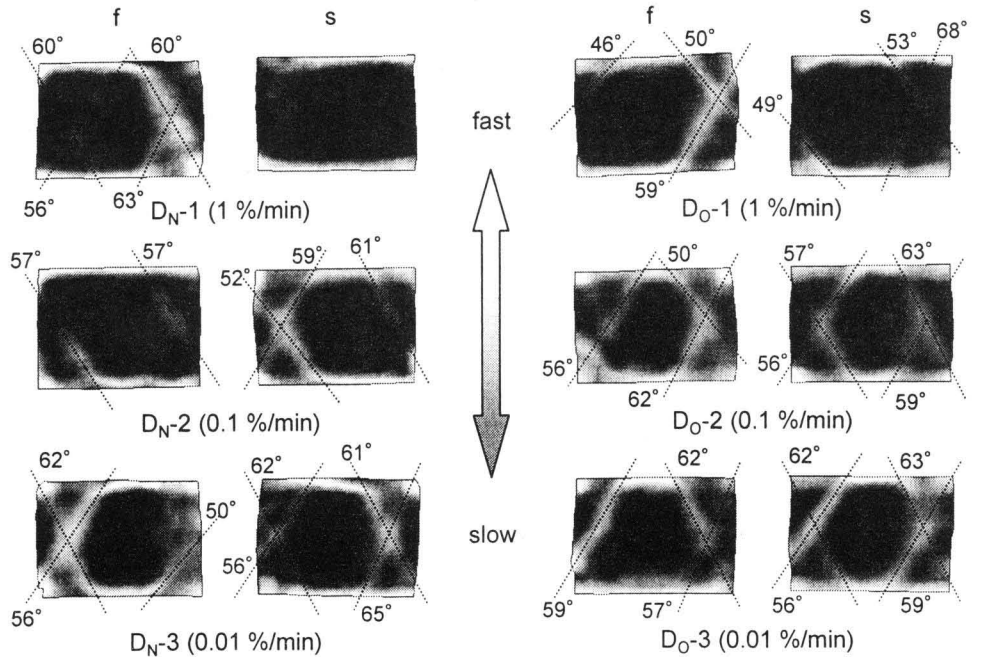

Figure 6.26 Distributions of shear strain for specimen D with different strain rates at an axial strain of 20% and inclinations of the shear bands

band inclination of the buckling-like mode is smaller than that of the complicated mode. The inclination angles of shear bands for case A_N-1, with a strain rate of 1 %/min, are larger than those of case A_N-2, with a strain rate of 0.1 %/min. In addition, the shear bands of case A_N-1 develop from the edges of the top and the bottom of the specimen, while those of case A_N-2 start beneath the edges. This tendency is consistent with the case of specimen B.

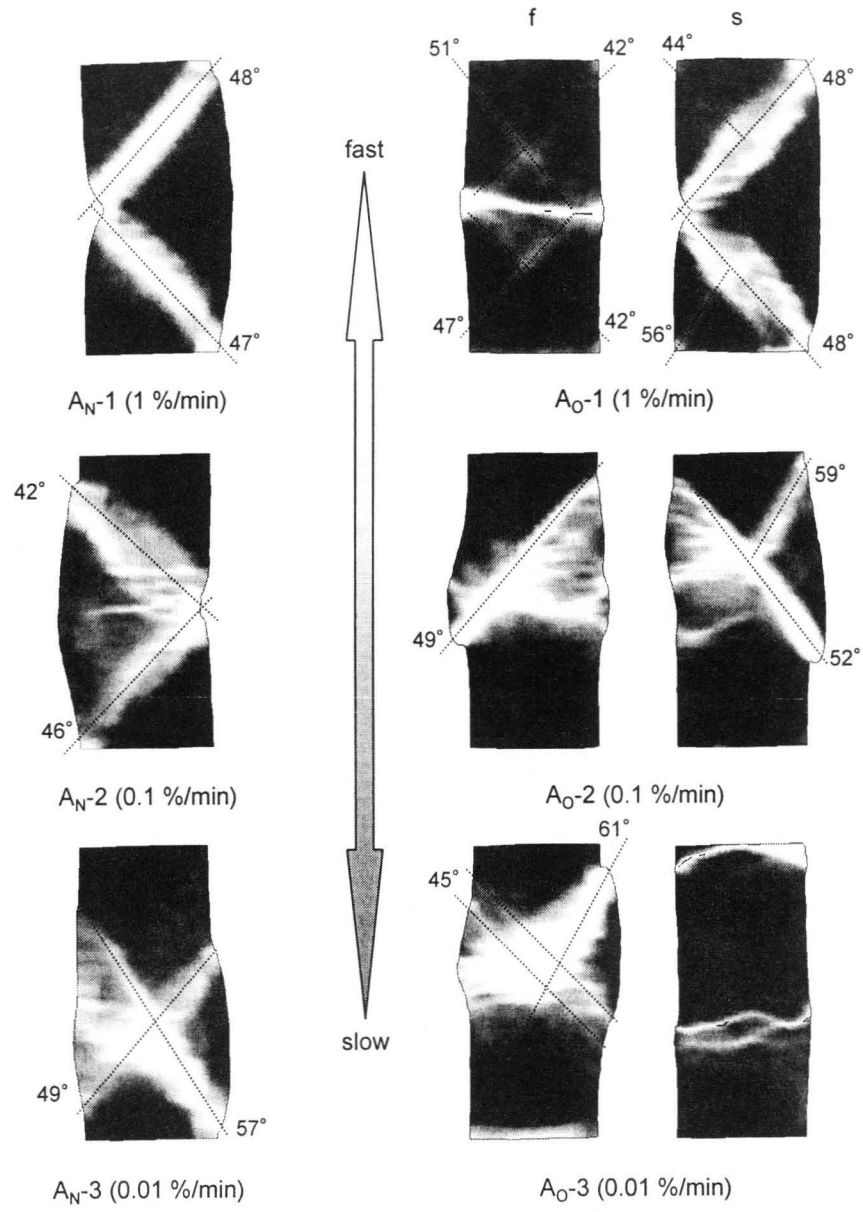

Figure 6.27 Distributions of shear strain for specimen A with different strain rates at an axial strain of 20% and inclinations of the shear bands

The effects of the strain rates on the strain localization pattern are prominently seen in the case of C_N. **Figure 6.28** shows the distributions of shear strain for specimen C with different strain rates at an axial strain of 20% and inclination angles of shear bands. All of the deformation modes for the C_O cases are the buckling-like mode, however, those of the C_N cases are greatly affected by the strain rate. The deformation pattern of case C_N-1, with the highest strain rate

of 1 %/min, shows the typical buckling-like mode. On the other hand, the deformation pattern of case C_N-3, with the lowest strain rate of 0.01%/min, is the "X" mode which is often seen in the case of specimen B. It is worth noting that case C_N-2, with a medium strain rate of 0.1%, shows both the buckling-like mode on the side surface and the "X" mode on the front surface. In the C_N cases we can conclude that the buckling-like mode tends to appear in the cases of higher strain rates. This tendency is consistent with the cases of specimen A.

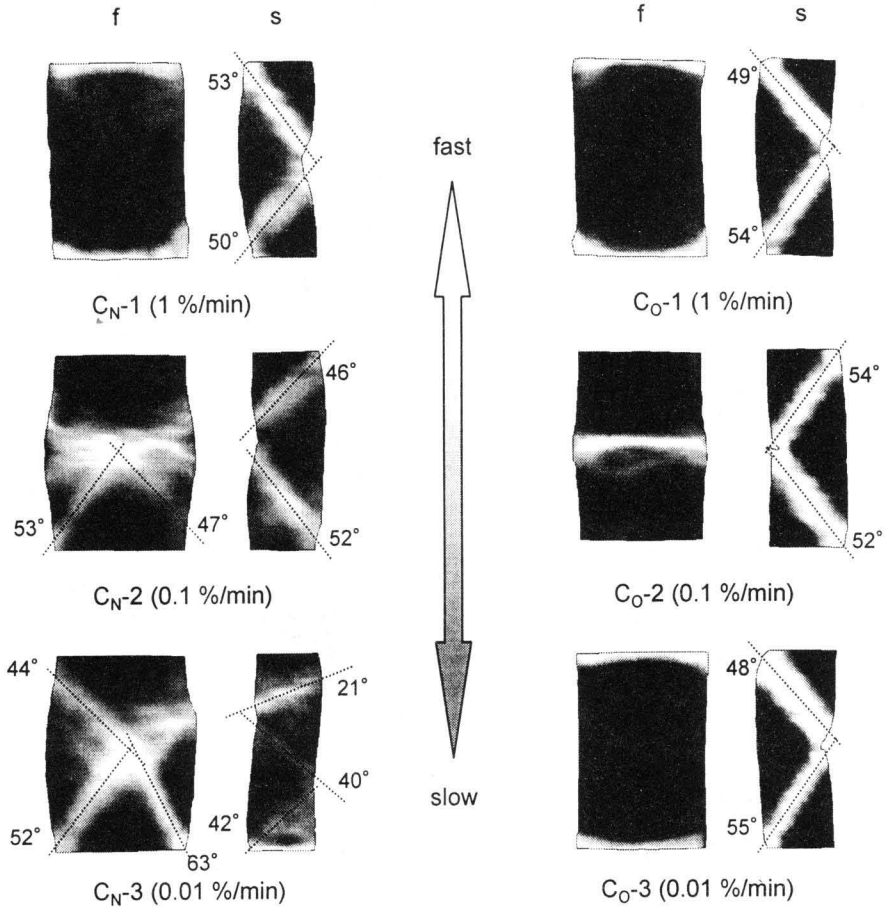

Figure 6.28 Distributions of shear strain for specimen C with different strain rates at an axial strain of 20% and inclinations of the shear bands

6.3.5 Effects of Dilatancy

As mentioned above, the deformation behavior is greatly dependent on the shapes of the specimens or the strain rates. We can conclude that overconsolidated clay is more brittle than normally consolidated clay. This tendency can be typically seen in the cases of specimen C. **Figures 6.29** and **6.30** shows the stress-strain relations and the distributions of shear strain at an axial strain of 12% for the C_N cases and the C_O cases, respectively. It is clearly seen in the stress-strain relations that the axial strain levels of the peak stress for the C_O cases are smaller than those for the C_N cases. This suggests that overconsolidated clay reaches the failure state earlier than normally consolidated clay. Shear bands are clearly observed in the distributions

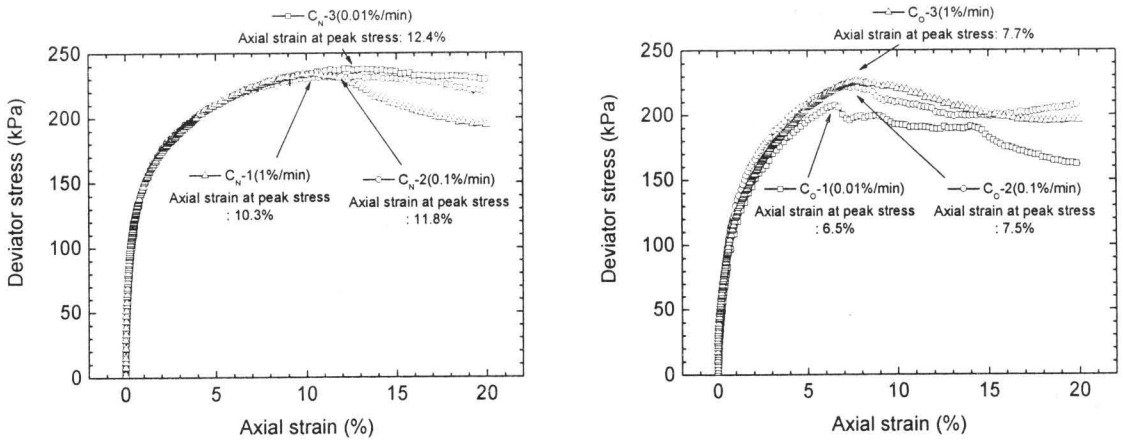

Figure 6.29 Stress-strain relations and axial strain levels at the peak stress for normally consolidated clay and overconsolidated clay of specimen C

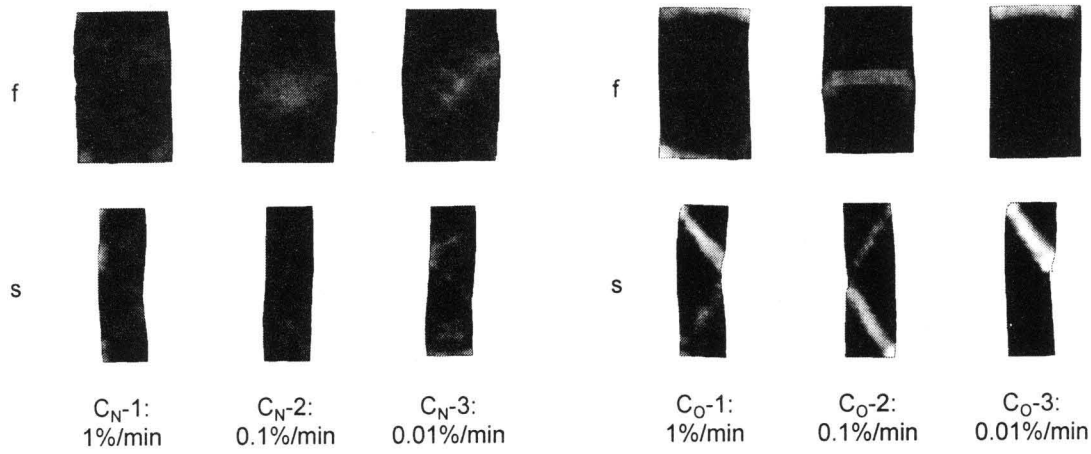

Figure 6.30 Distributions of shear strain at an axial strain of 12% for normally consolidated clay and overconsolidated clay of specimen C

of shear strain for overconsolidated clay at an axial strain of 12%, while apparent strain localization cannot be seen in those of normally consolidated clay. In addition, all of the cases for overconsolidated clay show the buckling-like mode and extensive strain softening. On the other hand, the strain softening in cases C_N-2 and C_N-3 is moderate and the buckling-like mode is not seen in these two cases, even though the geometric instability of specimen C, caused by the higher aspect ratio, may cause the buckling-like mode. In the case of specimens A, B and D, however, we cannot see a clear difference between the normally consolidated clay and the overconsolidated clay. Consequently, in the case of specimen C, we can conclude that normally consolidated clay is relatively ductile and that overconsolidated clay is relatively brittle.

6.4 Summary

Triaxial compression tests using rectangular specimens for normally consolidated clay and overconsolidated clay with different strain rates have been conducted. We have obtained the dis-

tributions of shear strain by an image analysis of photographs of the specimens taken during deformation. Using the distributions of shear strain, the strain localization behavior of clay has been investigated in detail.

In all cases, strain started to localize from the edges of the top and the bottom of the specimens, and then, the localized deformations lead to apparent shear bands. Corresponding to the generation of shear bands, strain-softening behavior was observed. Specimen D, however, showed monotonically hardening behavior. Three types of deformation modes were seen and three-dimensional shear bands were estimated from the distributions of shear strain. The deformation mode was greatly dependent on the shapes of the specimens and the strain rates. The deformation modes of specimens B and D were consistently the "X" mode, however, the formations of shear bands were affected by the strain rates. Specimens A and C, whose aspect ratio is large, with higher strain rates are likely to show the buckling-like mode and extensive softening behavior. On the other hand, specimens A and C, with lower strain rates, show the complicated mode that includes both the "X" mode and the buckling-like mode. In addition, it is found that overconsolidated clay is more brittle than normally consolidated clay.

References

Alshibli, K.A., Sture, S., Costes, N.C., Frank, M.L. and Lankto, M.R. (2000), Assessment of localized deformations in sand using X-ray computed tomography, *Geotechnical Testing Journal*, **23**, 3, pp. 274-299.

Asaoka, A., Nakano, M., Noda, T., Kaneda, K., and Akiyama, Y. (1998), Triaxial compression test of normally consolidated clay specimens having rectangular cross-section and its 3-D simulation, *Proc. 33rd JGS Symposium*, Yamaguchi, pp. 645-646 (in Japanese).

Burland, J.B. (1990), On the compressibility and shear strength of natural clays, *Géotechnique*, **40**, 3, pp. 329-378.

Han, C. and Vardoulakis, I. (1991), Plane-strain compression experiments on water-saturated fine-grained sand, *Géotechnique*, **41**, 1, pp. 49-78.

Han, C. and Drescher, A. (1993), Shear bands in biaxial tests on dry coarse sand, *Soils and Foundations*, **33**, 1, pp. 118-132.

Harris, W.W., Viggiani, G, Mooney, M.A., and Finno, R.J. (1995), Use of stereophotogrammetry to analyze the development of shear bands in sand, *Geotechnical Testing Journal*, **18**, 4, pp. 405-420.

Hayano, K., Maeshiro, T., Tatsuoka, F., Sato, L., Wang, L. and Kodaka, T. (1999), Shear banding in a sedimentary soft mudstone subjected to plane strain compression, *Geotechnical Testing Journal*, **22**, 1, pp. 67-79.

Ichinose, T. (2003), Experimental study on strain localization of clay using reconstituted rectangular specimens, Graduation thesis, Kyoto University, Japan, in Japanese.

Kodaka, T., Higo, Y. and Takyu, T. (2001), Deformation and failure characteristics of rectangular specimens under three-dimensional condition, *Proc. 15th ICSMGE*, Istanbul, Balkema, **1**, pp. 167-170.

Liang, L., Saada, A., Figueroa, J.L. and Cope, C.T. (1997), The use of digital image processing in monitoring shear band development, *Geotechnical Testing Journal*, **20**, 3, pp. 324-339.

Loret, B. and Prévost, J.H. (1991), Dynamic strain localization in fluid-saturated porous media, *J. Engineering Mechanics*, ASCE, **11**, pp. 177-190.

Michalowski, R.L. and Shi, L. (2003), Deformation patterns of reinforced foundation sand at failure, *J. Geotechnical and Geoenvironmental Engineering*, **29**, 6, pp. 439-449.

Mokni, M. and Desrues, J. (1998), Strain localization measurements in undrained plane-strain biaxial tests on Hostun RF sand, *Mechanics of Cohesive-Frictional Materials*, **4**, pp. 419-441.

Nüvel, K. and Gudehus, G. (2001), Numerical evolution of localized dilated shear zones, *Bifurcation and Localization Theory in Geomechanics*, Proceedings of the 5th IWBL, November 29-December 2, 1999, Perth, Australia, Mühlhaus, H.-B., Dyskin, A.V. and Pasternak, E. eds., Balkema, pp. 69-75.

Oda, M. and Kazama, H. (1998), Microstructure of shear bands and its relation to the mechanisms of dilatancy and of dense granular soils, *Géotechnique*, **48**, 4, pp. 465-481.

Oka, F., Adachi, T. and Yashima, A. (1994), Instability of an elasto-viscoplastic constitutive model for clay and strain localization, *Mechanics of Materials*, **18**, pp. 119-129.

Oka, F., Higo, Y. and Kimoto, S. (2002), Effect of dilatancy on the strain localization of water-saturated elasto-viscoplastic soil, *Int. J. Solids and Structures*, **39**, pp. 3625-3647.

Otani, J., Mukunoki, T. and Obara, Y. (2000), Application of X-ray CT method for characterization of failure in soils, *Soils and Foundations*, **40**, 2, pp. 111-118.

Rampello, S. (1991), Some remarks on the mechanical behaviour of stiff clays: the example of Todi clay, *Experimental characterization and modeling soils and soft rocks*, A workshop in Napoli, 29-31 October 1991, pp. 131-190.

Rechenmacher, A.L. and Finno, R.J. (2003), Shear band displacements and void ratio evolution to critical state in dilative sands, *Bifurcation and Instability in Geomechanics*, Proc. Int. Workshop on Bifurcation and Instabilities in Geomechanics, June 2-5, 2002, Minneapolis, MN, Labuz, J. and Drescher, A. eds., Balkema, pp. 193-206.

Rechenmacher, A.L. and Medina-Cetina, Z. (2003), Digital-imaging based measurement of deformed shapes of axisymmetric soil specimens, *Proc. 16th ASCE Engineering Mechanics Conference*, Seattle, WA, CD-ROM.

Satomura, T. (2003), Study on strain localization of normally consolidated and overconsolidated clay using reconstituted rectangular specimens, Master's thesis, Kyoto University, Japan, in Japanese.

Schrefler, B.A., Sanavia, L. and Majorana, C.E. (1996), A multiphase medium model for localization and postlocalization simulation in geomaterials, *Mechanics of Cohesive-Frictional Materials*, **1**, pp. 95-114.

Takyu, T. (2000), Observations of deformation and failure behaviors of clay by triaxial tests using rectangular specimens, Graduation thesis, Kyoto University, Japan, in Japanese.

Yoshida, T., Tatsuoka, F., Siddiquee, M.S.A., Kamegai, Y. and Park, C.-S. (1994), Shear banding in sands observed in plane strain compression, *Proc. 3rd Int. Workshop on Localization and Bifurcation Theory for Soils and Rocks*, Grenoble, Chambon, R., Desrues, J. and Vardoulakis, I. eds., Balkema, pp. 165-179.

Zhang, H.W., Sanavia, L. and Schrefler, B.A. (1999), An internal length scale in dynamic strain localization of multiphase porous media, *Mechanics of Cohesive-Frictional Materials*, **4**, 5, pp. 443-460.

Chapter 7

Numerical Simulation of Triaxial Tests for Rectangular Specimens

7.1 Introduction

A series of triaxial compression tests for the rectangular clay specimens reported in the last chapter have been numerically simulated in this chapter by the finite element method using an elasto-viscoplastic constitutive equation. As mentioned before, the same boundary conditions as those used in the undrained triaxial compression tests for rectangular specimens can be set up when simulating the tests by the finite element method. If we simulate the triaxial tests for cylindrical specimens by the finite element method, an assumption that the specimens are polygon poles or under axisymmetrical conditions is needed. On the other hand, no special assumptions are required to set up the boundary conditions for rectangular specimens.

The analysis method is a soil-water coupled finite element method based on the finite deformation theory. The code for the finite element method used in **Chapters 3** and **5** is extended to a three-dimensional one. The constitutive model used in this chapter is the elasto-viscoplastic model for clay considering the structural changes proposed by Kimoto (2002), Kimoto and Oka (2003), and Kimoto et al. (2004; to appear). This model can reproduce the behavior of both normally consolidated clay and overconsolidated clay, and can address the material instability induced by structural changes in the clay. In addition, there are fewer material parameters than in the model introduced in **Chapter 4**.

The simulation results yield much information on the inside of the specimens, e.g., the distributions of strain, the stress levels, and pore water pressure, which are not obtained from the experiment. All of the test cases with different shapes and strain rates have been simulated. Then, comparing the results of the experiment and the simulation, we have discussed the mechanism of strain localization.

7.2 Elasto-viscoplastic Constitutive Model Considering Structural Changes

For the constitutive equation of clay, an elasto-viscoplastic constitutive model considering structural changes, proposed by Kimoto (2002), Kimoto and Oka (2003), and Kimoto et al. (2004; to appear), was used. The basic theory of viscoplasticity (Perzyna 1963) is the same as that of the elasto-viscoplastic model introduced in **Chapters 2** and **4**. On the other hand, a characterization of the material instability is newly proposed considering the microstructural changes in the geomaterials, and the kinematic hardening rule is not adopted. Structural changes are described as the shrinking of both the overconsolidation boundary surface and the static yield surface with the evolution of viscoplastic strain. In the following, the introduction of the constitutive model will be given.

7.2.1 Overconsolidation Boundary Surface

The overconsolidation boundary introduced in **Section 4.2** is adopted in the model. The overconsolidation boundary surface controls the shape of the plastic potential function (see **Figure 4.2**).

$$f_b = \bar{\eta}^* + M_m^* \ln \frac{\sigma'_m}{\sigma'_{mb}} = 0 \tag{7.1}$$

where $\bar{\eta}^*$ is the relative stress ratio defined as

$$\bar{\eta}^* = \left\{ \left(\eta_{ij}^* - \eta_{ij(0)}^* \right) \left(\eta_{ij}^* - \eta_{ij(0)}^* \right) \right\}^{1/2} \tag{7.2}$$

$$\eta_{ij}^* = \frac{S_{ij}}{\sigma'_m}, \quad S_{ij} = \sigma'_{ij} - \sigma'_m \delta_{ij}, \quad \sigma'_m = \frac{1}{3}\sigma'_{kk} \tag{7.3}$$

in which σ'_{ij} is Terzaghi's effective stress tensor, η_{ij}^* is the stress ratio tensor, S_{ij} is the deviatoric stress tensor, σ'_m is the mean effective stress, δ_{ij} is Kronecker's delta, and subscript $_{(0)}$ indicates the state at the end of consolidation, in other words, the initial state before deformation occurs. M_m^* is the value of $\sqrt{\eta_{ij}^* \eta_{ij}^*}$ at the maximum compression and σ'_{mb} is the parameter which controls the size of the surface.

7.2.2 Structural Changes

Originally, the hardening rule for the overconsolidation boundary surface was defined with respect to the viscoplastic volumetric strain ε_{kk}^{vp} as

$$\sigma'_{mb} = \sigma'_{mbi} \exp\left(\frac{1+e}{\lambda - \kappa} \varepsilon_{kk}^{vp} \right) \tag{7.4}$$

where λ is the compression index, κ is the swelling index, e is the void ratio, and σ'_{mbi} is the initial value of σ'_{mb}, which is defined as the isotropic consolidation yield stress.

In order to describe the degradation of the material caused by structural changes, strain softening is introduced into the hardening parameter with the viscoplastic strain as

$$\sigma'_{ma} = \sigma'_{maf} + (\sigma'_{mai} - \sigma'_{maf}) \exp(-\beta z) \tag{7.5}$$

in which σ'_{mai} and σ'_{maf} are the initial and the final values of σ'_{ma}, and z is an accumulation of the second invariant of viscoplastic strain rate $\dot{\varepsilon}^{vp}_{ij}$.

$$z = \int_0^t \dot{z} dt, \quad \dot{z} = \left(\dot{\varepsilon}^{vp}_{ij}\dot{\varepsilon}^{vp}_{ij}\right)^{\frac{1}{2}} \tag{7.6}$$

Substituting σ'_{ma} into **Equation** (7.4), σ'_{mb} is defined by the hardening rule with respect to the viscoplastic volumetric strain and by the softening rule with respect to structural changes as

$$\sigma'_{mb} = \sigma'_{ma} \exp\left(\frac{1+e}{\lambda-\kappa}\varepsilon^{vp}_{kk}\right) \tag{7.7}$$

in which β is a parameter which denotes the degradation rate of σ'_{ma} in **Equation** (7.5). Since z is equal to 0 at the initial state, the relation of $\sigma'_{ma} = \sigma'_{mai} = \sigma'_{mbi}$ is derived. Hence, two independent parameters, β and σ'_{maf}, are introduced to describe the soil structures. The ratio of σ'_{maf} to σ'_{mai}, namely,

$$n = \sigma'_{maf}/\sigma'_{mai} \tag{7.8}$$

provides the degree for a possible collapse of the structure at the initial state. n satisfies the condition of $0 < n \leq 1$, in which $n = 1$ indicates the soil which loses its structure perfectly. In addition, the ratio of σ'_{ma} to σ'_{mai} is defined by **Equation** (7.5) as

$$N_a = \sigma'_{ma}/\sigma'_{mai} = n + (1-n)\exp(-\beta z). \tag{7.9}$$

When viscoplastic strain does not occur, i.e., $z = 0$, the value of N_a is equal to 1. On the other hand, when the value of z becomes large enough, N_a approaches n, and the softening converges due to structural changes.

7.2.3 Static Yield Function

Adachi and Oka (1982) assumed a Cam-clay type of static yield function to describe the mechanical behavior of clay at its static equilibrium state.

$$f_y = \bar{\eta}^* + \tilde{M}^* \ln \frac{\sigma'_m}{\sigma'^{(s)}_{my}} = 0 \tag{7.10}$$

where the $\sigma'^{(s)}_{my}$ is the static-hardening parameter and $f_y = 0$ represents the static state in which no viscoplastic deformation occurs.

Considering volumetric strain hardening, the hardening rule $\sigma'^{(s)}_{my}$ was originally given as

$$\sigma'^{(s)}_{my} = \sigma'^{(s)}_{myi} \exp\left(\frac{1+e}{\lambda-\kappa}\varepsilon^{vp}_{kk}\right) \tag{7.11}$$

In a similar manner to overconsolidation boundary surface f_b, strain softening is defined in order to express the effect of a structural collapse through changes in $\sigma'^{(s)}_{my}$ with the viscoplastic strain. Adopting **Equation** (7.9) to **Equation** (7.11) yields

$$\sigma'^{(s)}_{my} = \{n + (1-n)\exp(-\beta z)\}\sigma'^{(s)}_{myi} \exp\left(\frac{1+e}{\lambda-\kappa}\varepsilon^{vp}_{kk}\right) \tag{7.12}$$

where $\sigma'^{(s)}_{myi}$ is the initial value of $\sigma'^{(s)}_{my}$. The decrease in $\sigma'^{(s)}_{my}$, defined by **Equation** (7.12), leads to the shrinking of the static yield function according to the structural collapse.

7.2.4 Viscoplastic Potential Function

Viscoplastic potential function f_p is given as

$$f_p = \bar{\eta}^* + \tilde{M}^* \ln \frac{\sigma'_m}{\sigma'_{mp}} = 0 \tag{7.13}$$

where $\tilde{M}^*$ is constant in the NC region, while the value of $\tilde{M}^*$ in the OC region depends on the current stress and σ'_{mc} as

$$\tilde{M}^* = \begin{cases} M^*_m & : \ f_b \geq 0 \\ -\dfrac{\sqrt{\eta^*_{ij}\eta^*_{ij}}}{\ln(\sigma'_m/\sigma'_{mc})} & : \ f_b < 0 \end{cases} \tag{7.14}$$

where σ'_{mc} denotes the mean effective stress at the intersection of the overconsolidation boundary surface and the σ'_m axis as

$$\sigma'_{mc} = \sigma'_{mb} \exp \frac{\sqrt{\eta^*_{ij(0)}\eta^*_{ij(0)}}}{M^*_m} \tag{7.15}$$

In the case of isotropic consolidation, σ'_{mc} equals σ'_{mb}.

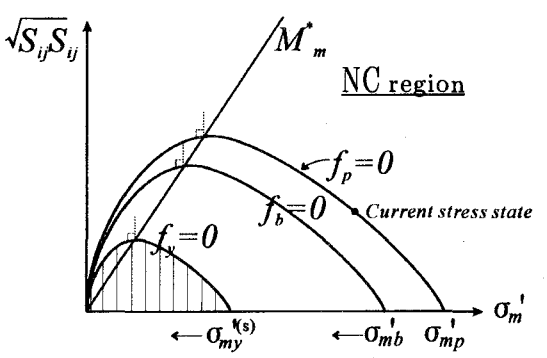

Figure 7.1 OC boundary surface, static yield function, and potential function in the NC region (Kimoto 2002)

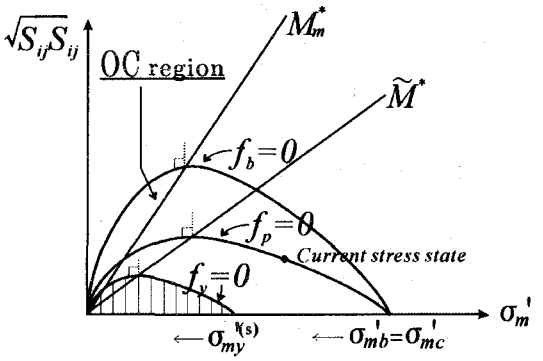

Figure 7.2 OC boundary surface, static yield function, and potential function in the OC region (Kimoto 2002)

Overconsolidation boundary f_b, static yield function f_y, and potential function f_p at $\eta^*_{ij(0)} = 0$ for the NC region and the OC region are demonstrated in the σ'_m-$\sqrt{S_{ij}S_{ij}}$ space in **Figures 7.1** and **7.2**, respectively. σ'_{mb} and $\sigma^{\prime(s)}_{my}$ become small as the accumulation of viscoplastic strain increases. Since the increments in viscoplastic strain for the overstress type of model are determined by the difference between the current stress state and the static state, the shrinkage of the static yield surface due to the degradation of the soil structure increases the viscoplastic strain increments. The static yield function as well as the potential surface are transformed smoothly between the OC and the NC regions, so that calculations can be conducted continuously without interruption.

7.2.5 Viscoplastic Flow Rule

Viscoplastic strain rate tensor $\dot{\varepsilon}_{ij}^{vp}$, based on an overstress type of viscoplasticity theory (Perzyna 1963), is given as

$$\dot{\varepsilon}_{ij}^{vp} = \gamma \langle \Phi_1 (f_y) \rangle \frac{\partial f_p}{\partial \sigma'_{ij}} \tag{7.16}$$

$$< \Phi_1(f_y) >= \begin{cases} \Phi_1(f_y) & ; \quad f_y > 0 \\ 0 & ; \quad f_y \leq 0 \end{cases} \tag{7.17}$$

where Φ_1 indicates the strain rate sensitivity. Based on the experimental data of the strain-rate constant triaxial tests (Adachi and Okano 1974), material function Φ_1 is given as:

$$\begin{aligned} \gamma\Phi_1(f_y) &= C'\sigma'_m \exp\left[m'\left(\bar{\eta}^* + \tilde{M}^* \ln \frac{\sigma'_m}{\sigma'^{(s)}_{my}}\right)\right] \\ &= C\sigma'_m \exp\left[m'\left(\bar{\eta}^* + \tilde{M}^* \ln \frac{\sigma'_m}{\sigma'_{mb}}\right)\right] \end{aligned} \tag{7.18}$$

$$C = C' \exp\left(m'\tilde{M}^* \ln \frac{\sigma'_{mai}}{\sigma'^{(s)}_{myi}}\right) \tag{7.19}$$

in which m' and C are viscoplastic parameters and **Equations** (7.7), (7.9), and (7.12) are used.

Finally the viscoplastic deviatoric strain rate and the viscoplastic volumetric strain rate are obtained as follows:

$$\dot{e}_{ij}^{vp} = C \exp\left[m'\left(\bar{\eta}^* + \tilde{M}^* \ln \frac{\sigma'_m}{\sigma'_{mb}}\right)\right] \frac{\eta^*_{ij} - \eta^*_{ij(0)}}{\bar{\eta}^*} \tag{7.20}$$

$$\dot{\varepsilon}_{kk}^{vp} = C \exp\left[m'\left(\bar{\eta}^* + \tilde{M}^* \ln \frac{\sigma'_m}{\sigma'_{mb}}\right)\right] \left\{\tilde{M}^* - \frac{\eta^*_{mn}(\eta^*_{mn} - \eta^*_{mn})}{\bar{\eta}^*}\right\} \tag{7.21}$$

The additive decomposition of the total strain rate into elastic and viscoplastic parts is assumed, and the elastic strain rate tensor is given by a Hooke's type of isotropic elasticity law.

7.3 Finite Element Analysis of Triaxial Tests for Rectangular Specimens

The finite element formulation used in this chapter is the same as that used in **Chapters 3** and **5**. The governing equations are equilibrium equations for the solid-fluid mixture and a continuity equation for pore fluid. Based on the finite deformation theory, an updated Lagrangian method with the objective Jaumann rate of Cauchy stress is used for the weak form of the rate type of the equilibrium equations. The finite element code is formulated in a three-dimensional setting. The element types used in the three-dimensional analysis are shown in **Figure 7.3**. A twenty-node isoparametric element with a reduced Gaussian (2×2×2) integration for the soil skeleton and an eight-node isoparametric element with a full (2×2×2) integration for pore fluid are used.

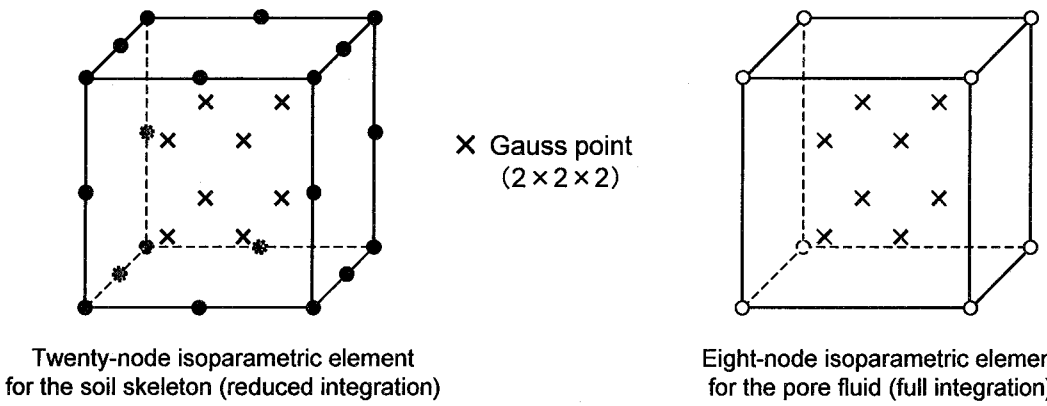

Figure 7.3 Isoparametric elements used in the three-dimensional finite element method

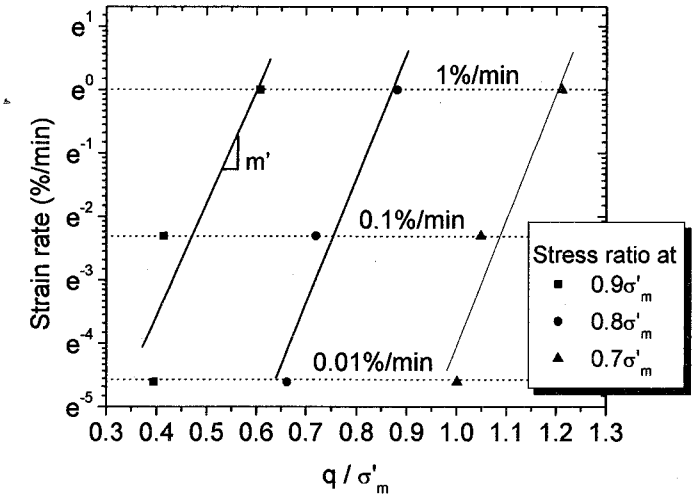

Figure 7.4 Relations between the logarithm of the strain rate and the stress ratio for B_N (Normally consolidated clay, 4 cm×4 cm×8 cm)

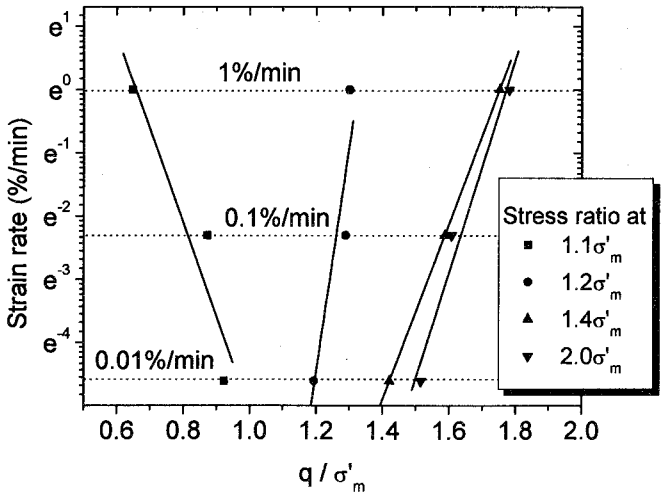

Figure 7.5 Relations between the logarithm of the strain rate and the stress ratio for A_O (Overconsolidated clay, 4 cm×4 cm×12 cm)

7.3.1 Determination of the Material Parameters

Ten material parameters are required by the constitutive model introduced in the last section. They are compression index λ, swelling index κ, initial void ratio e_0, elastic shear modulus G_0, compression yield stress σ'_{mbi}, stress ratio at maximum compression M^*_m, viscoplastic parameter m, viscoplastic parameter C, structural parameter σ'_{maf}, and structural parameter β. All of them are determined by isotropic consolidation tests and more than two undrained triaxial compression tests. Other parameters include coefficient of permeability k and coefficient of earth pressure at rest K_0. The material parameters used in this chapter are listed in **Table 7.1**.

Compression index λ and swelling index κ are given by the slope of the isotropic consolidation and the swelling tests, respectively. We determined λ to be 0.191 and κ to be 0.043 using the isotropic consolidation and the swelling test results for Fukakusa clay by Yamamura (2002).

The initial void ratios, e_0, obtained in each test are listed in **Table 6.2**. In order to simulate the tests accurately, we should use the values obtained in each test, however, we used the average of them since calculating with different void ratios is not appropriate for a comparison of the simulation results. Consequently, the initial void ratios of normally consolidated clay and overconsolidated clay were calculated to be 1.10 and 1.11, respectively.

Elastic shear modulus G_0 is determined by the initial slope of the undrained triaxial compression tests, namely, $G_0 = \Delta q/(3\Delta\varepsilon_{11})$, in which Δq is the increment in deviator stress and $\Delta\varepsilon_{11}$ is the increment in axial strain. In this study, $\Delta\varepsilon_{11}$ was determined to be 0.1%. Elastic shear moduli G_0 are given by normally consolidated clay and overconsolidated clay with each strain rate. Undrained triaxial compression tests on Fukakusa clay by Yamamura (2002) were used for the moduli of the strain rates of 0.1%/min and 0.01%/min, and those of 1.0%/min.

Compression yield stress σ'_{mbi} is assumed to be the pre-consolidation stress. Therefore, that of normally consolidated clay is 200 kPa and that of overconsolidated clay is 300 kPa. The stress ratio at maximum compression M^*_m is defined as the stress ratio whereby maximum compression occurs in the drained compression tests. For clay, however, M^*_m can be equal to the stress ratio at the critical state. Herein, M^*_m is determined from the stress ratio at the residual state in the undrained triaxial compression tests.

Viscoplastic parameters m' and C can be determined from undrained triaxial tests with different strain rates. Adachi and Oka (1982) noted that viscoplastic parameter m' is estimated from the slope of the relation between the stress ratio and the logarithm of the strain rate. In principle, material parameters are determined from elemental tests. In this study, however, undrained triaxial compression tests using cylindrical specimens were conducted only for a strain rate of 1.0%/min. Hence, we applied the test results using rectangular specimens, namely, B (4 cm×4 cm×8 cm) and A (4 cm×4 cm×12 cm) to estimate viscoplastic parameter m', because these shapes are relatively similar to the cylindrical specimens generally used in triaxial compression tests whose diameter is 5 cm and height is 10 cm. **Figure 7.4** shows the relations between the applied strain rates and stress ratio q/σ'_m for normally consolidated clay, in which q is the deviator stress and σ'_m is the mean effective stress. We plotted the stress ratios at $\sigma'_m = 0.9\sigma'_{m0}$, $\sigma'_m = 0.8\sigma'_{m0}$, and $\sigma'_m = 0.7\sigma'_{m0}$, and estimated m' to be 21.7, 23.9, and 24.3, respectively. We used 24.3 as m' since the other two values are so small that the simulation of triaxial tests with

different strain rates would overestimate the strain rate sensitivity. As for the overconsolidated clay, m' is estimated to be -18.1, 43.9, 17.1, and 20.5 from the stress ratios at $\sigma'_m = 1.1\sigma'_{m0}$, $\sigma'_m = 1.2\sigma'_{m0}$, $\sigma'_m = 1.4\sigma'_{m0}$, and $\sigma'_m = 2.0\sigma'_{m0}$ as shown in **Figure 7.5**, respectively. $m' = 20.5$ is used since experience has shown that the others are not appropriate values (e.g., Oka et al. 2002 and Kimoto and Oka 2003). After m' is fixed, viscoplastic parameter C is determined by the peak stress.

Structural parameter σ'_{maf} can be obtained by the deviator stress at the residual stress state, while β, which dominates the decreasing rate of deviator stress, is determined by the curve fitting.

Figures 7.6 and **7.7** show the simulation results of undrained triaxial compression tests for normally consolidated clay and overconsolidated clay, respectively. Note that these simulation results are approximate solutions of the constitutive equation, using the Runge-Kutta method, under the triaxial stress state. In the case of normally consolidated clay, it is seen that the peak stress in the stress-strain relations is different between the test results and the simulations. However, the strain rate sensitivity and the negative dilatancy characteristics of normally consolidated clay are well reproduced. The rate sensitivity and the dilatancy characteristics of overconsolidated clay are also well reproduced, while the axial strain at the peak stress of the simulation is smaller than that of the test results.

The coefficients of permeability for the normally consolidated clay and the overconsolidated clay were obtained by falling head permeability tests in the triaxial cell. The head difference applied by air pressure was 1000 cm for normally consolidated clay and 250 cm for overconsolidated clay. To prevent leakage along the rubber membrane, silicone grease was filled in between the specimen and the membrane.

Table 7.1 Material parameters used in the numerical simulation

Parameter		N.C. clay	O.C. clay
Compression index λ		0.191	0.191
Swelling index κ		0.043	0.043
Initial void ratio e_0		1.10	1.11
Initial elastic shear modulus G_0	0.01%/min	16300 (kPa)	9190 (kPa)
	0.1%/min	17700 (kPa)	9920 (kPa)
	1%/min	23400 (kPa)	13080 (kPa)
Initial mean effective stress σ'_{m0}		200 (kPa)	50 (kPa)
Compression yield stress σ'_{mbi}		200 (kPa)	300 (kPa)
Coefficient of earth pressure at rest K_0[†]		1.0	1.0
Stress ratio at maximum compression M^*_m		1.14	1.14
Viscoplastic parameter m'		24.3	20.5
Viscoplastic parameter C		5.8×10^{-10} (1/s)	2.7×10^{-9} (1/s)
Structural parameter σ'_{maf}		170 (kPa)	270 (kPa)
Structural parameter β		10	5
Coefficient of permeability k[†]		1.63×10^{-9} (m/s)	2.86×10^{-9} (m/s)

[†] K_0 and coefficient of permeability k were used only in finite element analysis.

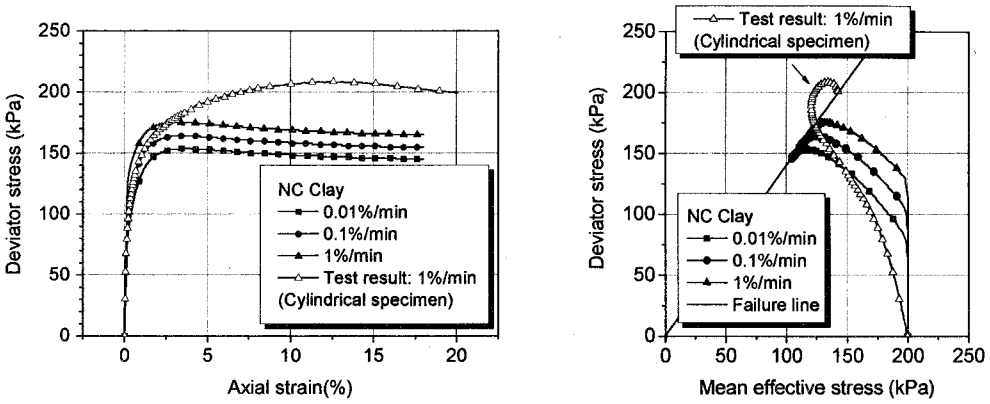

(a) Stress-strain relations (b) Effective stress paths

Figure 7.6 Numerical simulation results of undrained triaxial compression tests for normally consolidated clay

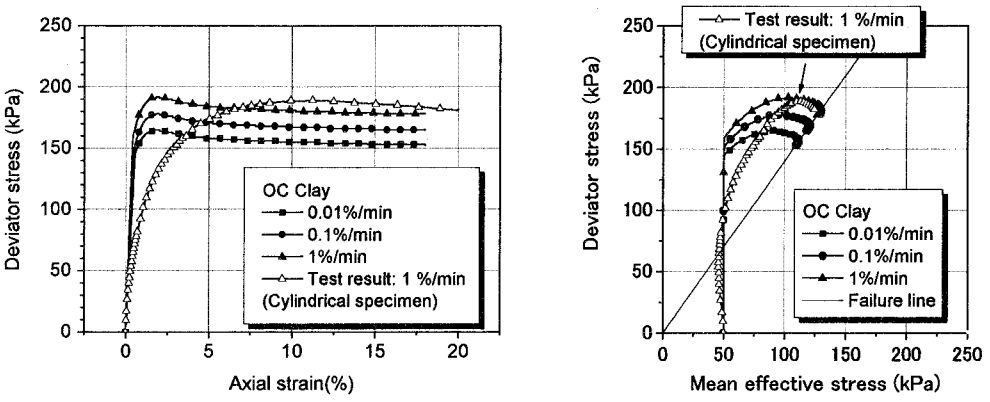

(a) Stress-strain relations (b) Effective stress paths

Figure 7.7 Numerical simulation results of undrained triaxial compression tests for overconsolidated clay

7.3.2 Boundary Conditions

Figure 7.8 shows the boundary conditions for the shape of specimen B, which is set up according to the same boundary conditions as those of the undrained triaxial compression tests with displacement control. All the boundaries are assumed to be impermeable, however, the transport of pore water between each element is allowed. Constant displacements (z-direction) of 0.01%/min, 0.1%/min, and 1%/min are applied to the nodes on the bottom surface. The time increment is determined by the increment of average strain $\Delta\varepsilon = 0.05\%$. As for the top and the bottom surfaces, frictional force occurs between the top and the bottom surfaces and the top cap and the pedestal. Hence, the top and the bottom surfaces deform. We measured the size of the top and the bottom surfaces after the tests listed in **Table 7.2**. 'Before test' indicates the time just after the specimens were trimmed. 'After test' means the time after the specimens were consolidated and sheared under undrained conditions. In all cases, the displacements of the surfaces are rather small, but not negligible. However, it is difficult to measure the friction

coefficient and the maximum static friction force between the soil specimen and the paper filter. Consequently, we assumed that the horizontal (x-direction and y-direction) displacement of the nodes on both the top and the bottom surfaces is constrained. The boundary conditions for the other shaped specimens are the same as those for specimen B. **Figure 7.9** shows the finite element meshes for specimens A, C, and D.

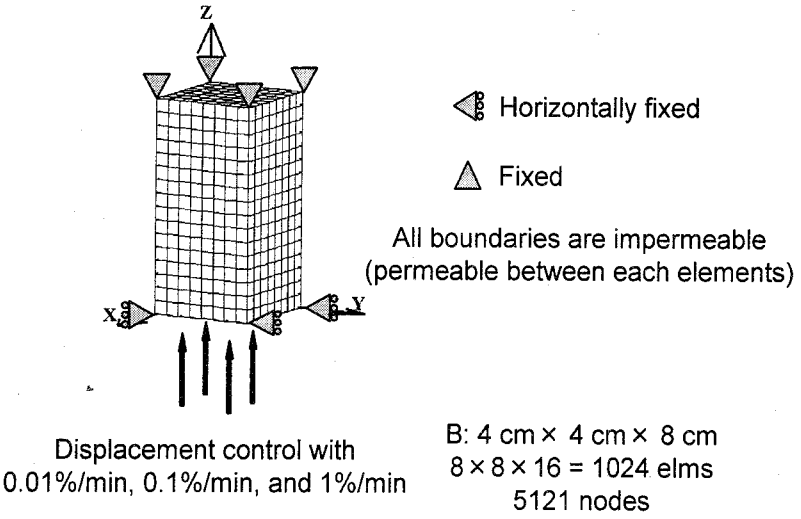

Figure 7.8 Boundary conditions for the three-dimensional finite element analysis

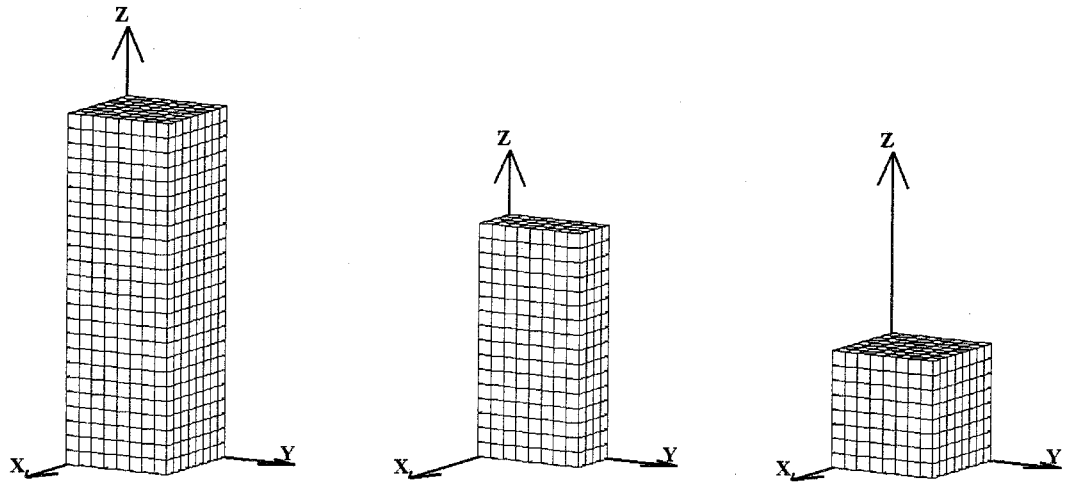

Figure 7.9 Finite element meshes used in the numerical simulations; boundary conditions are the same as those for B (4 cm×4 cm×8 cm)

7.4 Simulation Results

The undrained triaxial compression tests for normally consolidated clay and overconsolidated clay for each size of specimen with different axial strain rates have been simulated. **Figures**

Table 7.2 Sizes of the top and the bottom surfaces measured before and after the tests

Number of specimen	Top surface		Bottom surface	
	Before test	After test	Before test	After test
A_N-1	–	–	–	–
A_N-2	–	–	–	–
A_N-3	–	–	–	–
B_N-1	4.048 × 4.052	4.305 × 4.205	4.009 × 4.013	4.488 × 4.267
B_N-2	4.036 × 4.035	4.176 × 4.163	4.094 × 4.095	4.103 × 4.102
B_N-3	–	–	–	–
C_N-1	3.928 × 1.952	3.921 × 2.232	3.958 × 2.012	3.989 × 2.251
C_N-2	3.968 × 2.097	3.990 × 2.210	3.969 × 2.042	4.021 × 2.291
C_N-3	3.965 × 2.053	4.012 × 2.236	3.990 × 2.103	4.017 × 2.259
D_N-1	–	–	–	–
D_N-2	–	–	–	–
D_N-3	3.860 × 3.903	4.245 × 4.185	3.938 × 3.938	4.217 × 4.199
A_O-1	4.028 × 4.013	4.206 × 4.180	4.092 × 4.121	4.189 × 4.329
A_O-2	–	–	–	–
A_O-3	–	–	–	–
B_O-1	4.002 × 4.001	4.178 × 4.125	4.067 × 4.083	4.341 × 4.244
B_O-2	3.924 × 3.950	4.225 × 4.141	4.039 × 3.990	4.398 × 4.214
B_O-3	–	–	–	–
C_O-1	3.966 × 2.082	3.973 × 2.503	3.958 × 2.106	3.967 × 2.520
C_O-2	3.967 × 2.071	3.978 × 2.413	3.996 × 2.107	4.001 × 2.687
C_O-3	3.958 × 2.029	3.960 × 2.573	3.956 × 2.055	3.996 × 2.450
D_O-1	4.047 × 4.062	4.316 × 4.371	4.052 × 4.116	4.390 × 4.454
D_O-2	–	–	–	–
D_O-3	–	–	–	–

– : not measured, Unit: (cm)

7.10∼**7.17** show the simulation results for normally consolidated clay and overconsolidated clay for each size of specimen, respectively. **Figures 7.10**(a)∼**7.17**(a) show the stress-strain relations with the experimental results, **Figures 7.10**(b)∼**7.17**(b) show the effective stress paths with the experimental results, **Figures 7.10**(c)∼**7.17**(c) show the distributions of shear strain γ, and **Figures 7.10**(d)∼**7.17**(d) indicate the deformed meshes at an axial strain of 20%. In cases where the calculations diverged, the final states are shown.

The deviator stress, the mean effective stress, and the pore water pressure used in the stress-strain curves and the effective stress paths are calculated in the same manner as the experimental data. The deviator stress and the pore water pressure are obtained using the average of those nodal values of the top surface. In order to obtain the distributions of shear strain γ on the surfaces of the specimens, we used a special method, which is the same method as that for experiment introduced in **Section 6.2.3**. **Figure 7.18** displays the procedure for obtaining shear strain γ. After completing the calculations, we picked up the coordinates of the nodes on the xz-surface and the yz-surface. Consequently, we used eight-node isoparametric elements to

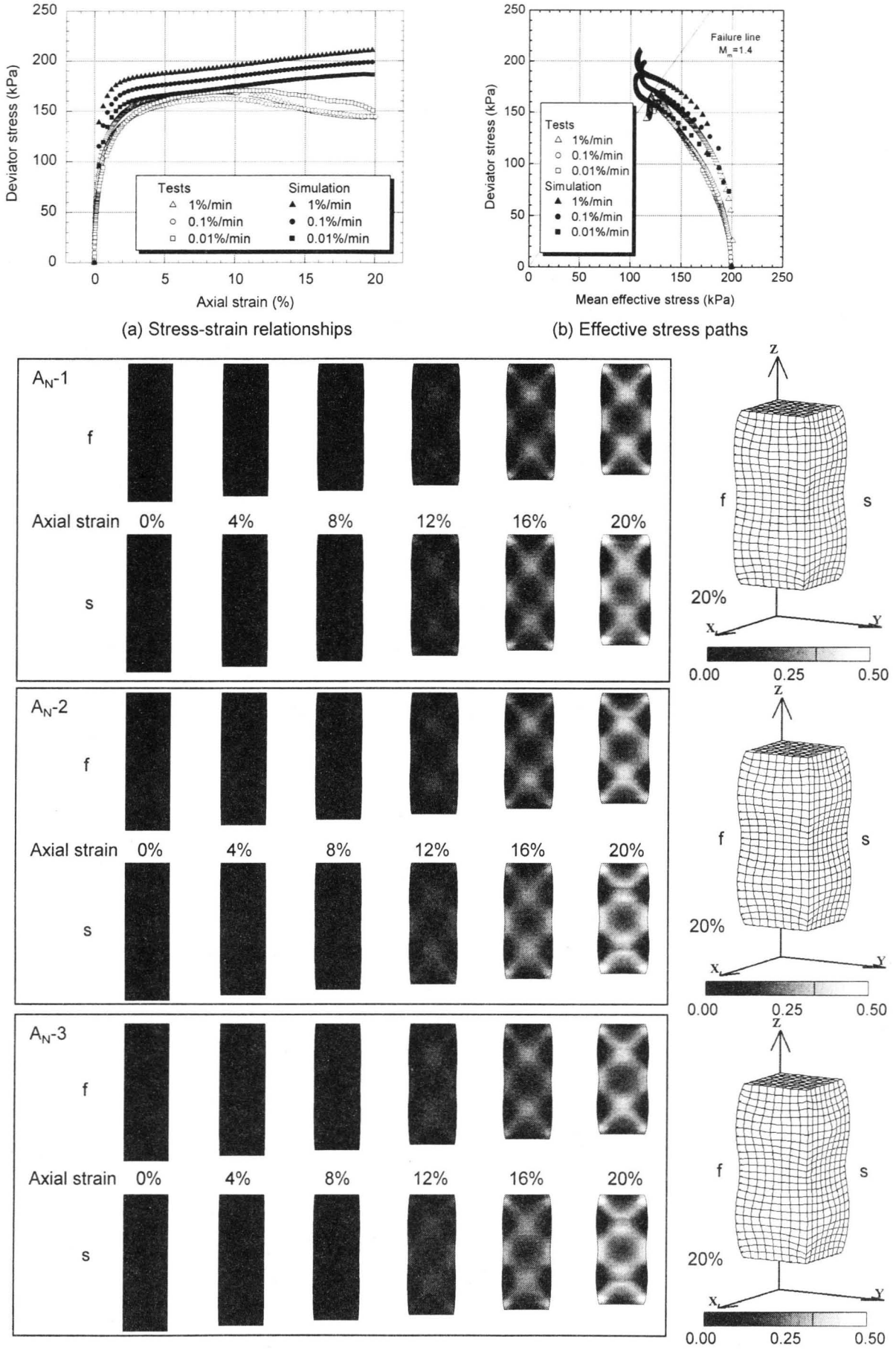

Figure 7.10 Simulation results for the cases of A_N (Normally consolidated clay, 4×4×12 (cm))

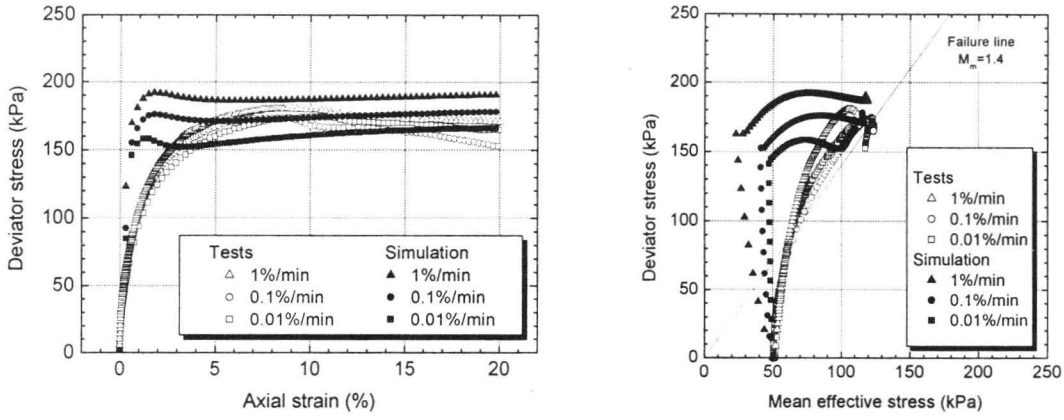

(a) Stress-strain relationships (b) Effective stress paths

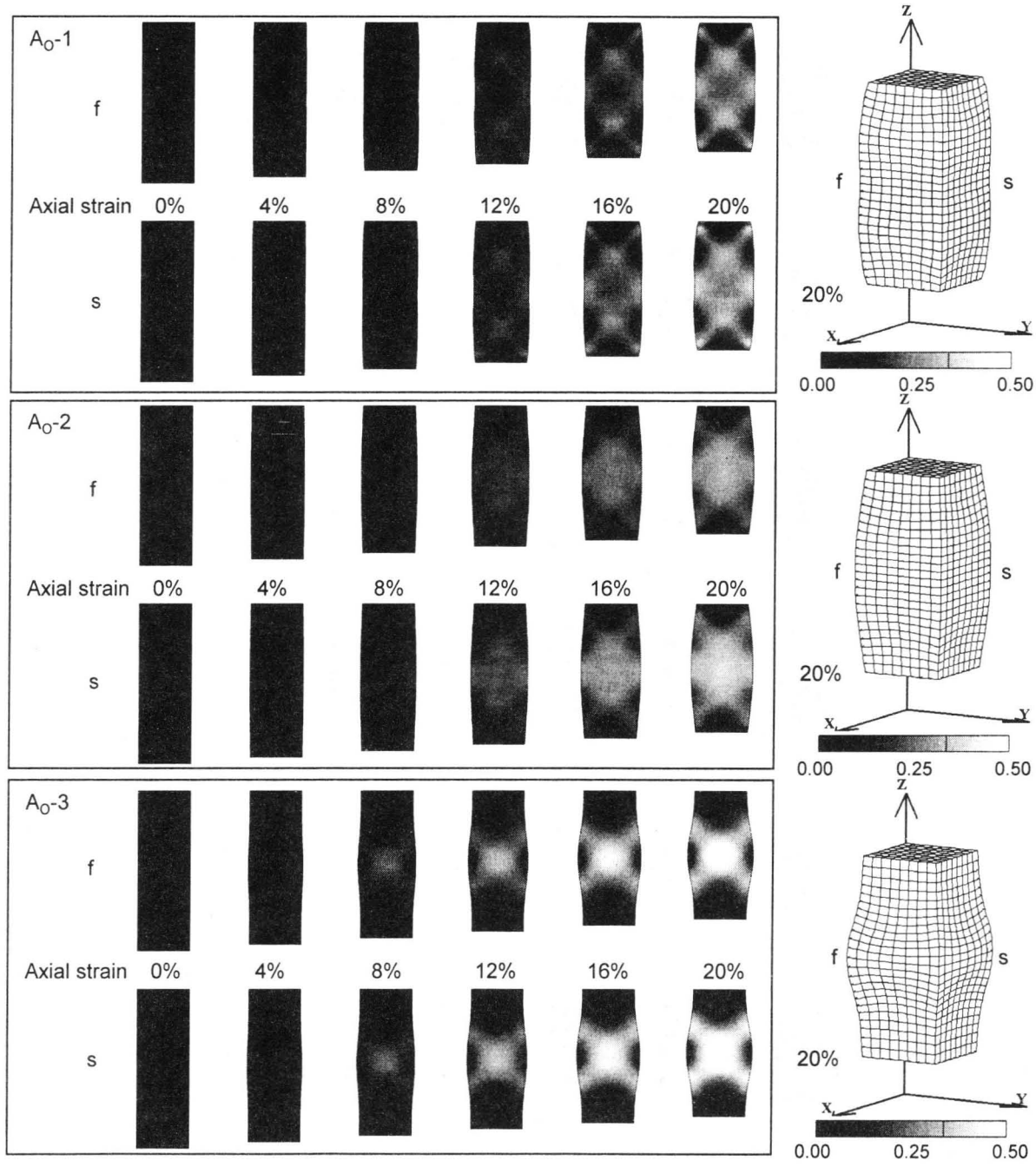

(c) Distribution of shear strain (d) Deformed meshes

Figure 7.11 Simulation results for the cases of A_O (Overconsolidated clay, 4×4×12 (cm))

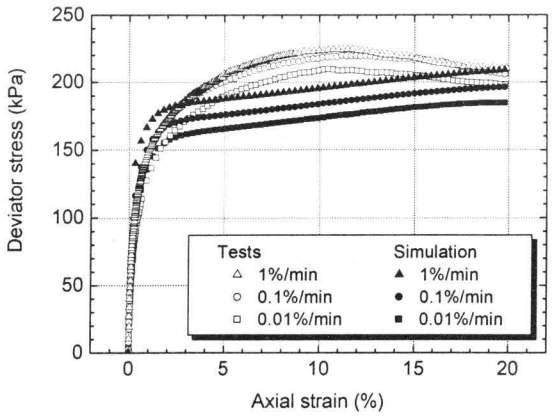

(a) Stress-strain relationships

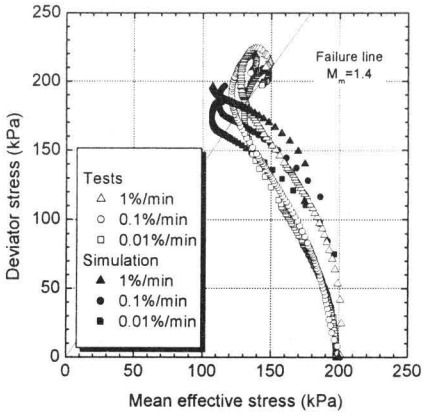

(b) Effective stress paths

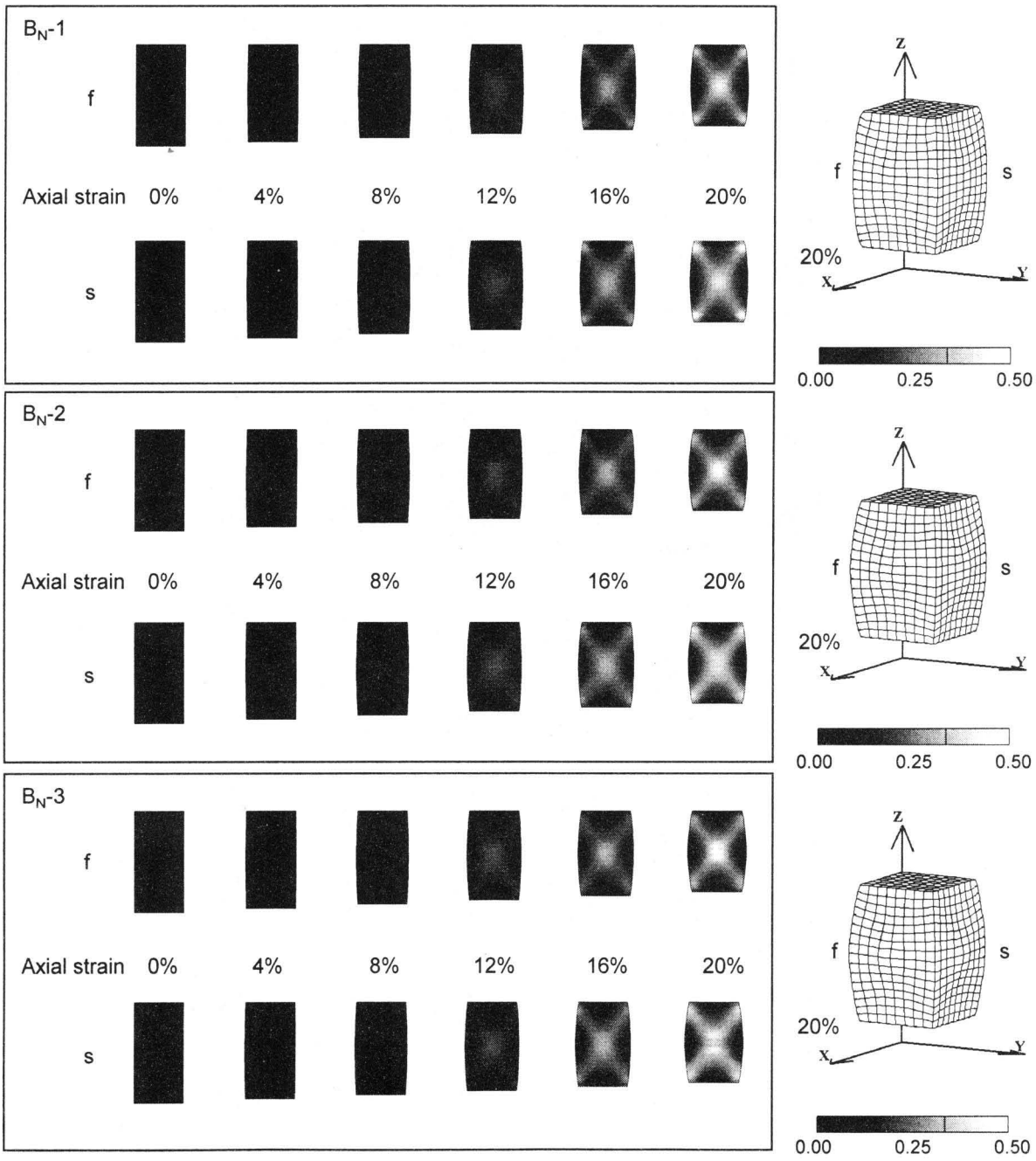

(c) Distribution of shear strain (d) Deformed meshes

Figure 7.12 Simulation results for the cases of B_N (Normally consolidated clay, 4×4×8 (cm))

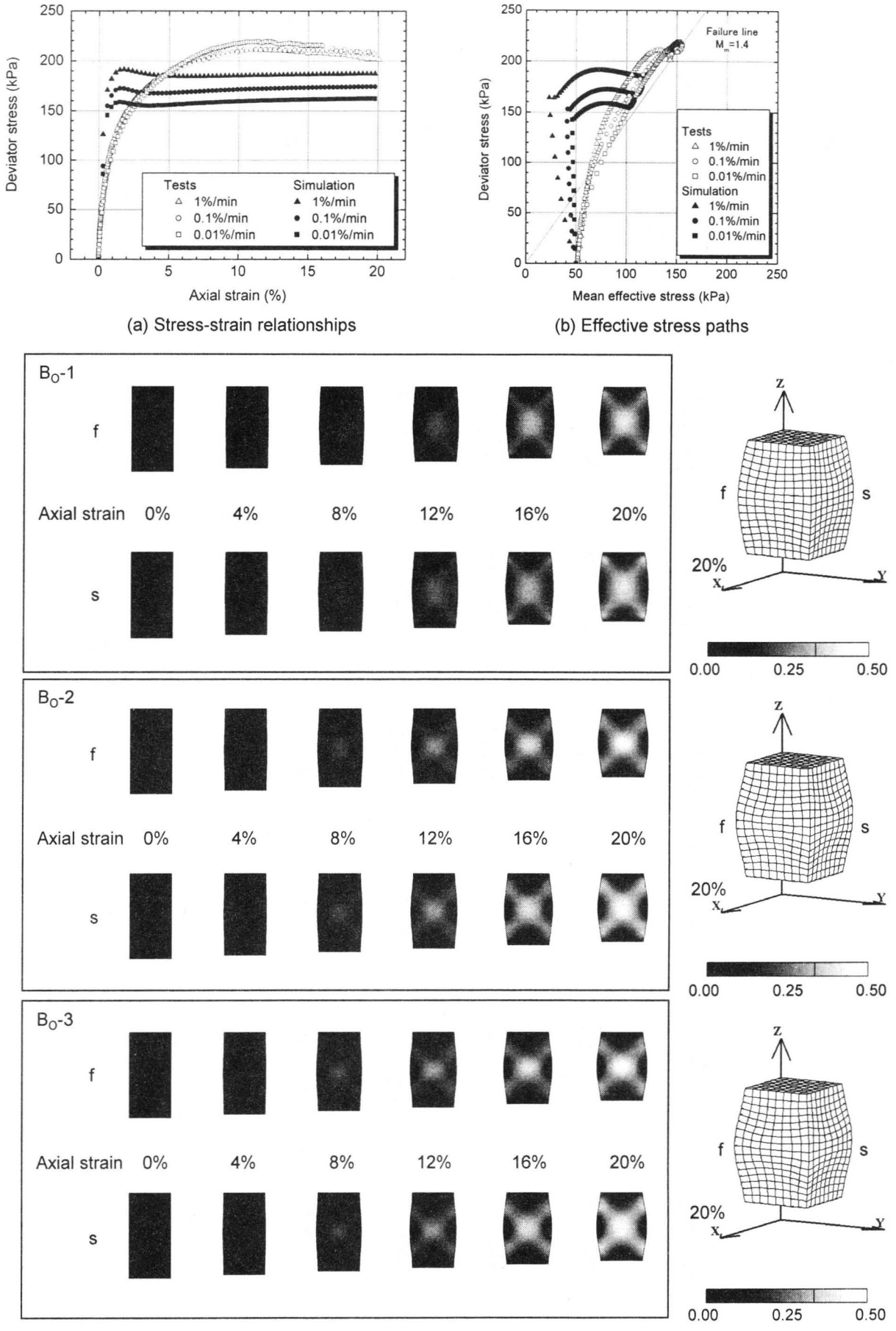

Figure 7.13 Simulation results for the cases of B_O (Overconsolidated clay, 4×4×8 (cm))

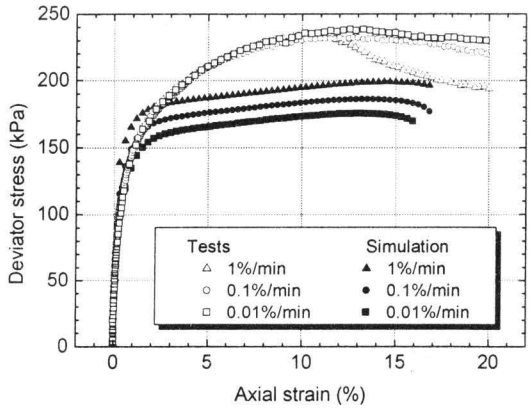

(a) Stress-strain relationships

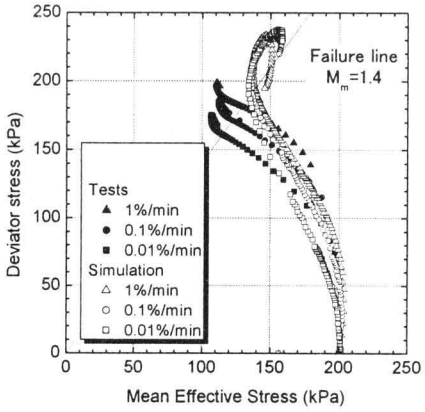

(b) Effective stress paths

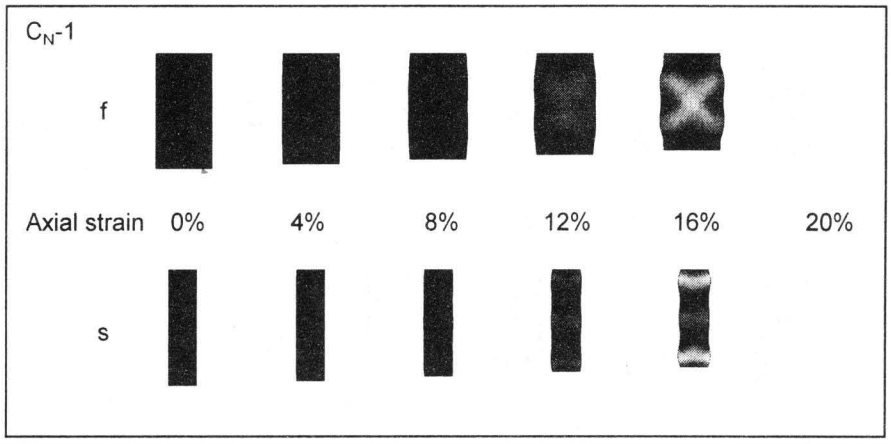

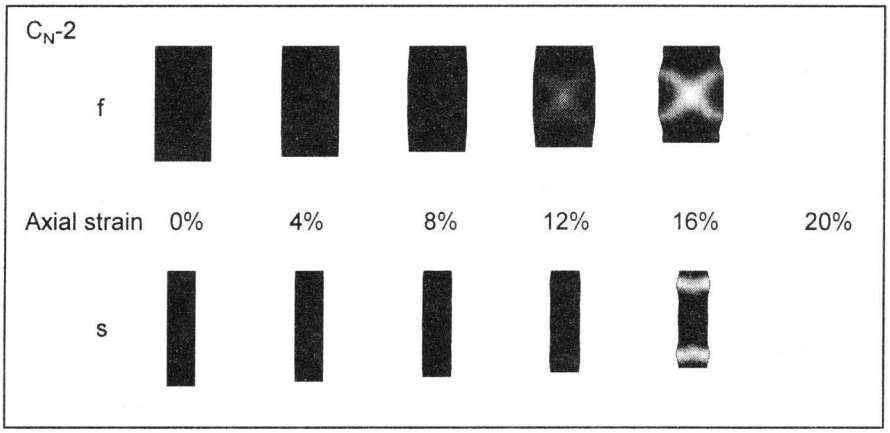

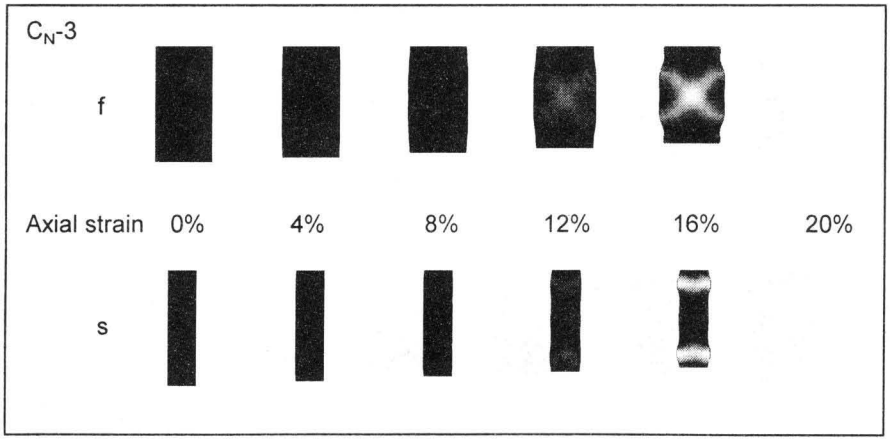

(c) Distribution of shear strain

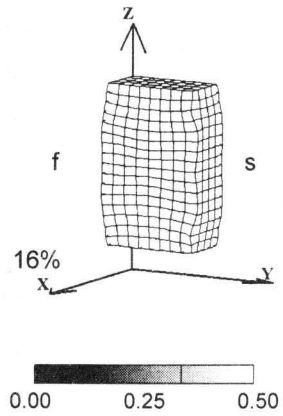

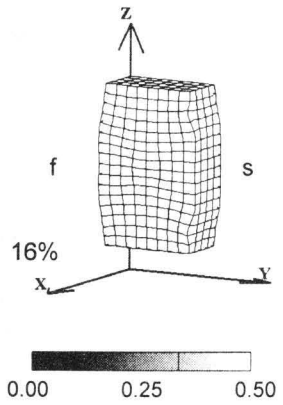

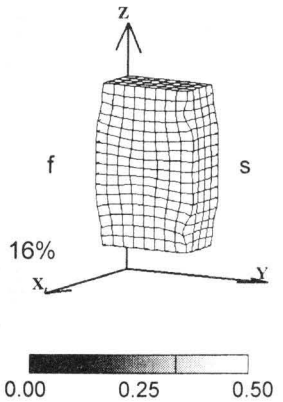

(d) Deformed meshes

Figure 7.14 Simulation results for the cases of C_N (Normally consolidated clay, 4×2×8 (cm))

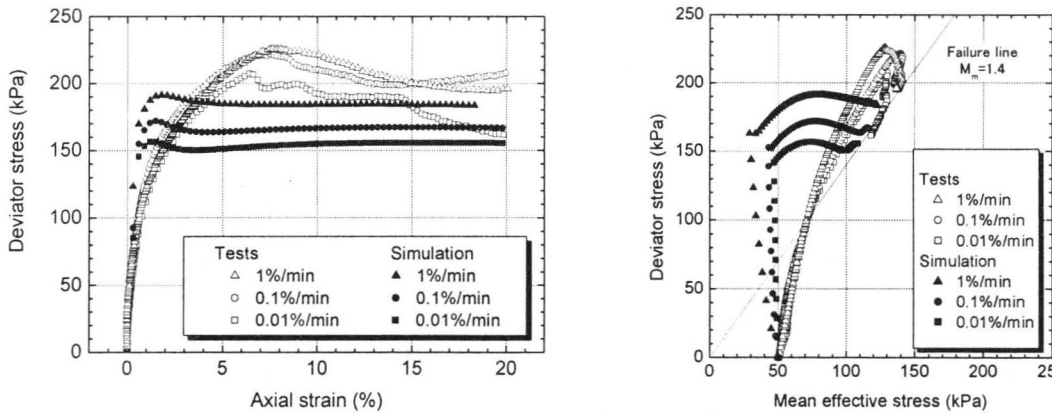

(a) Stress-strain relationships (b) Effective stress paths

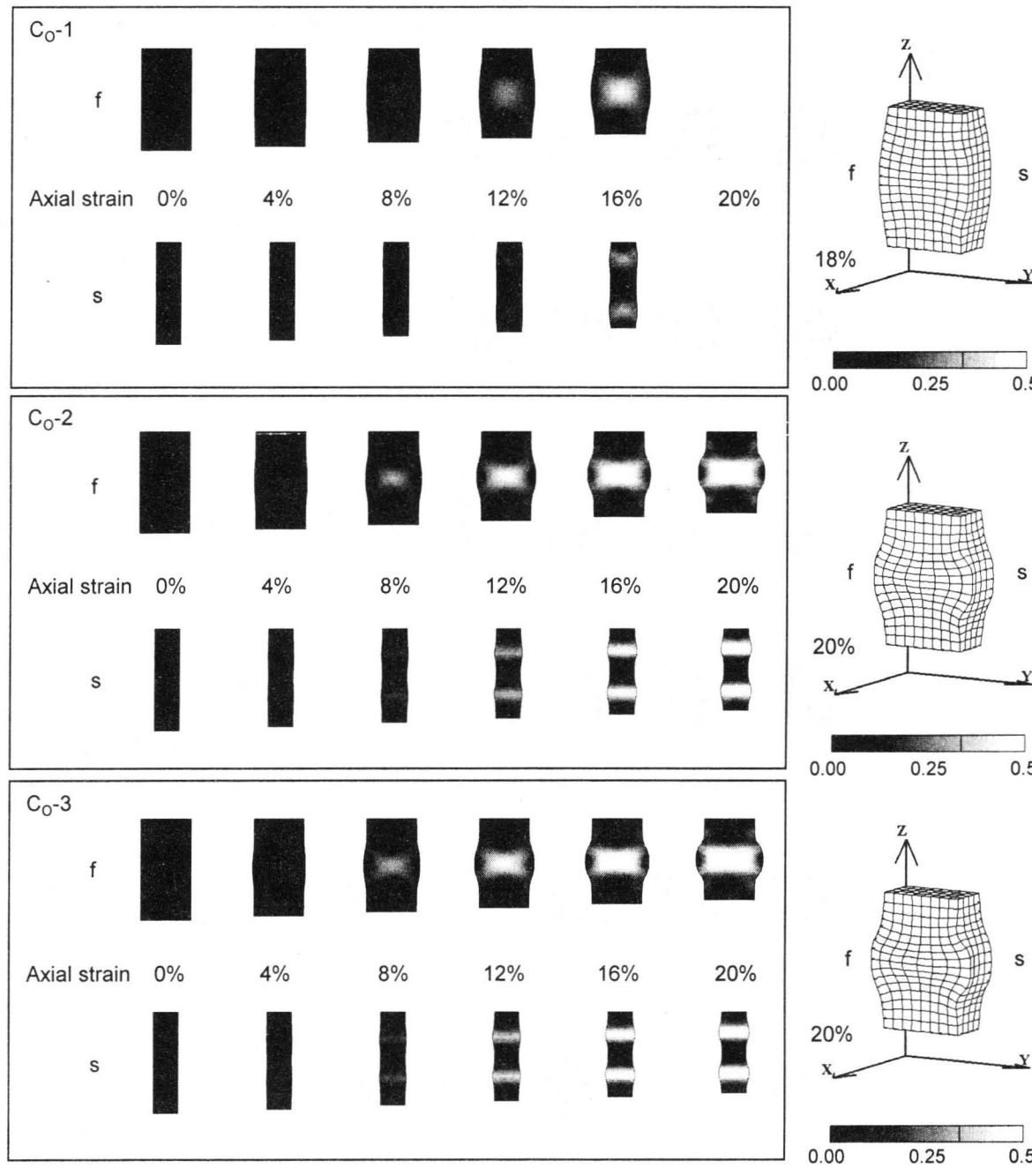

(c) Distribution of shear strain (d) Deformed meshes

Figure 7.15 Simulation results for the cases of C_O (Overconsolidated clay, 4×2×8 (cm))

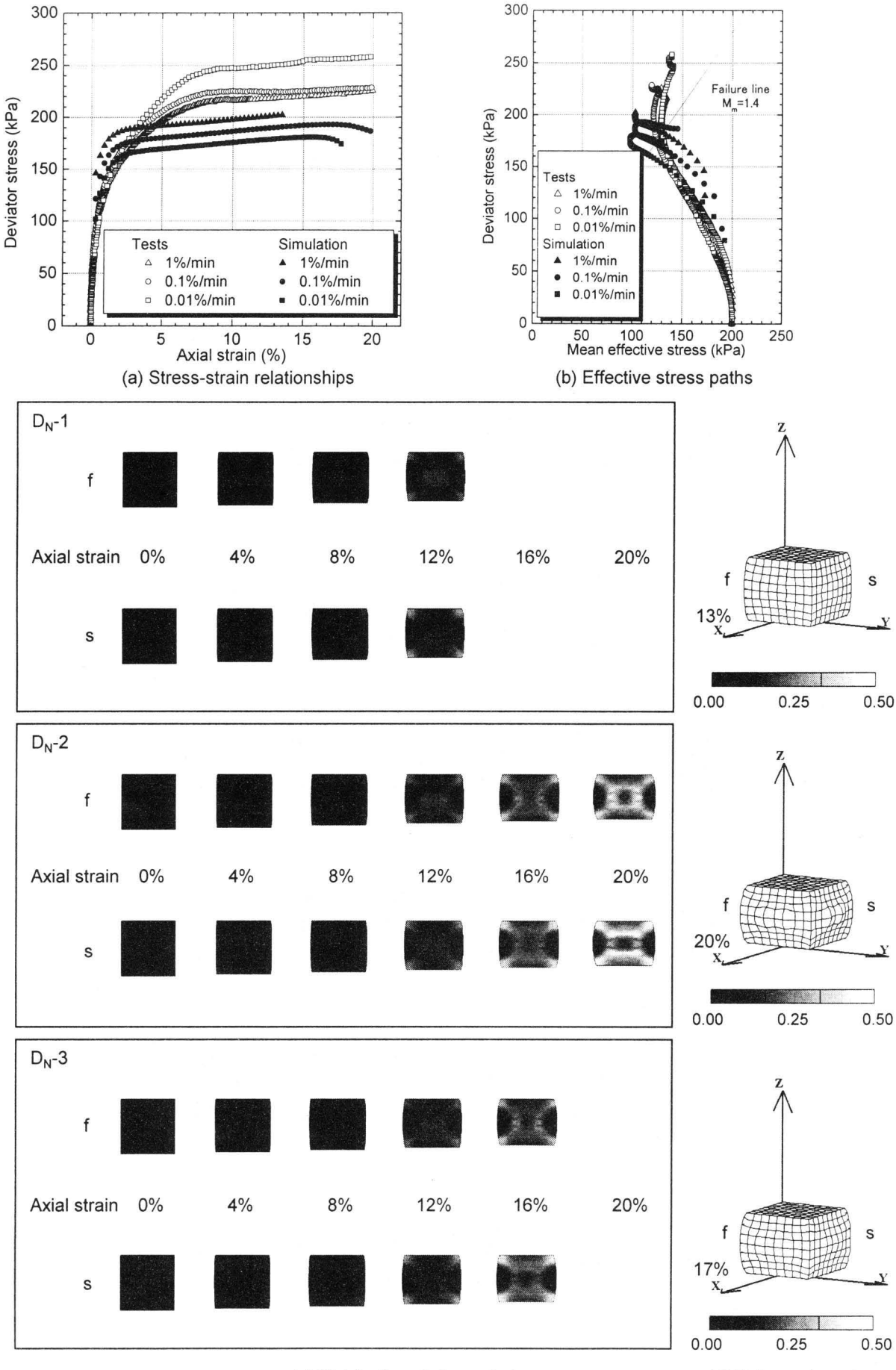

Figure 7.16 Simulation results for the cases of D_N (Normally consolidated clay, 4×4×4 (cm))

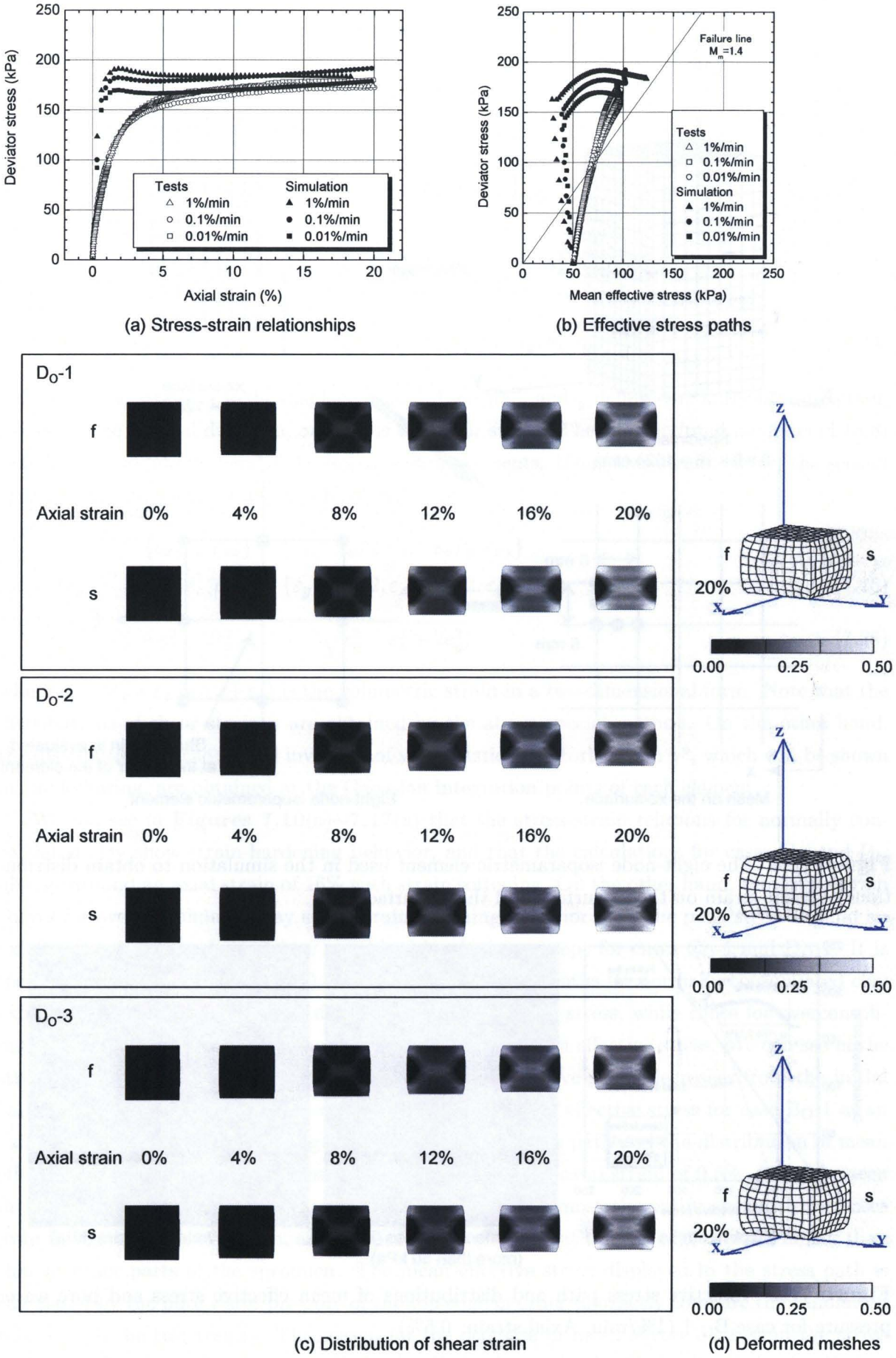

Figure 7.17 Simulation results for the cases of D_O (Overconsolidated clay, 4×4×4 (cm))

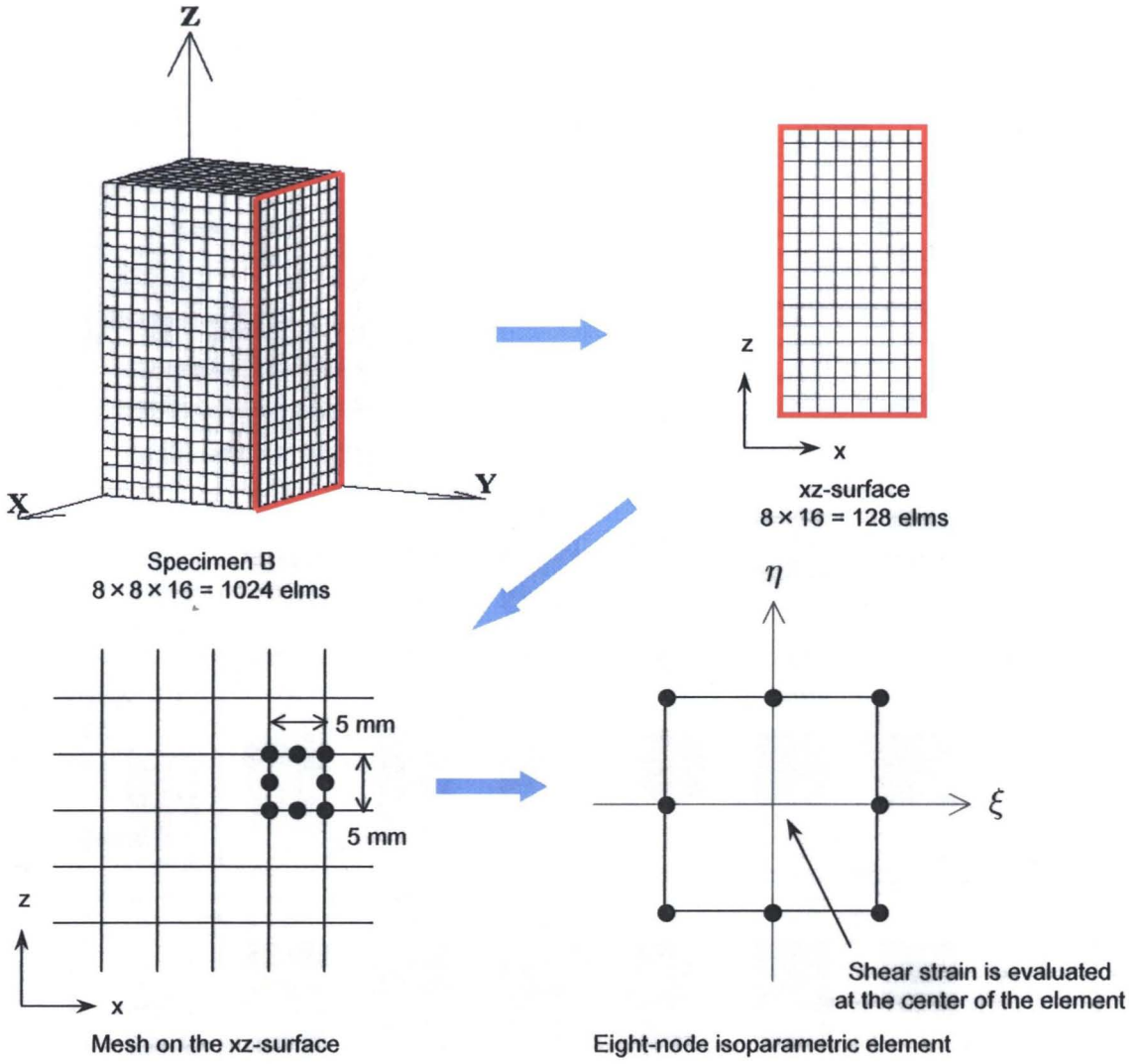

Figure 7.18 The eight-node isoparametric element used in the simulation to obtain distributions of shear strain on the xz-surface and the yz-surface

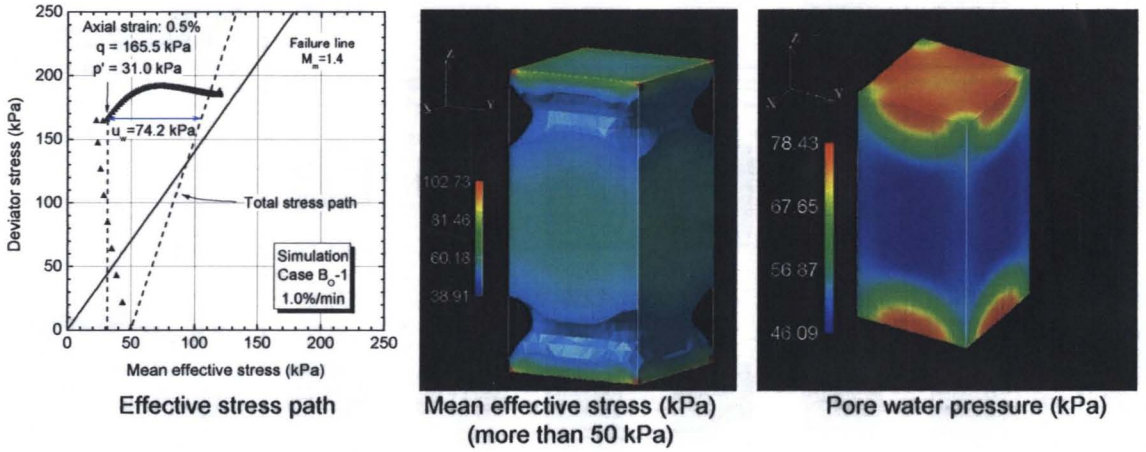

Figure 7.19 Effective stress path and distributions of mean effective stress and pore water pressure for case B_O-1 (1%/min, Axial strain: 0.5%)

calculate strain values γ of the xz-surface and the yz-surface.

$$\{\varepsilon\} = [B]\{u\} \tag{7.22}$$

in which

$$\{\varepsilon\}^{\mathrm{T}} = \{\varepsilon_x, \varepsilon_z, 2\varepsilon_{xz}\} \quad \text{or} \quad \{\varepsilon\}^{\mathrm{T}} = \{\varepsilon_y, \varepsilon_z, 2\varepsilon_{yz}\} \tag{7.23}$$

$$\{u\}^{\mathrm{T}} = \{u_x^1, u_z^1, u_x^2, u_z^2, u_x^3, u_z^3, u_x^4, u_z^4 u_x^5, u_z^5, u_x^6, u_z^6, u_x^7, u_z^7, u_x^8, u_z^8\}$$
or
$$\{u\}^{\mathrm{T}} = \{u_y^1, u_z^1, u_y^2, u_z^2, u_y^3, u_z^3, u_y^4, u_z^4 u_y^5, u_z^5, u_y^6, u_z^6, u_y^7, u_z^7, u_y^8, u_z^8\} \tag{7.24}$$

where ε is the strain, u is the displacement, subscripts $_x$ and $_y$ denote the horizontal direction, $_z$ denotes the vertical direction, and ε_{xy} is the shear strain. The superscripted numbers (1 to 8) indicate the nodal numbers of the isoparametric elements. Using this strain vector, the second invariant of deviatoric strain was calculated.

$$\{e_{xz}\}^{\mathrm{T}} = \{e_x, e_z, e_{xz}\} = \{\varepsilon_x - \varepsilon_v/2, \varepsilon_z - \varepsilon_v/2, \varepsilon_{xz}\}$$
$$\{e_{yz}\}^{\mathrm{T}} = \{e_y, e_z, e_{yz}\} = \{\varepsilon_y - \varepsilon_v/2, \varepsilon_z - \varepsilon_v/2, \varepsilon_{yz}\} \tag{7.25}$$

$$\gamma = \sqrt{e_x^2 + e_z^2 + 2e_{xz}^2}\ , \quad \gamma = \sqrt{e_y^2 + e_z^2 + 2e_{yz}^2} \tag{7.26}$$

where $\varepsilon_v (= \varepsilon_x + \varepsilon_z$ or $\varepsilon_y + \varepsilon_z)$ is the volumetric strain in a two-dimensional form. Note that the distributions of shear strain γ are obtained by the above special method. On the other hand, the distributions of the second invariant of viscoplastic deviatoric strain γ^p, which will be shown in the following, are obtained at the Gaussian integration points of each element.

We can see in **Figures 7.10**(a)~**7.17**(a) that the stress-strain relations for normally consolidated clay show strain-hardening behavior, and that the calculations for cases C_N and D_N diverge around an axial strain of 16% with strain softening. On the other hand, the stress-strain curves for overconsolidated clay show strain-softening behavior after the peak stress around an axial strain of 2%, and then show a gradual hardening, except for cases C_O-1 and D_O-1. It is seen in **Figures 7.10**(b)~**7.17**(b) that the effective stress paths for normally consolidated clay exhibit negative dilatancy, i.e., a decrease in mean effective stress, while those for overconsolidated clay exhibit positive dilatancy, i.e., an increase in mean effective stress. We can see in the stress paths for overconsolidated clay that the mean effective stress decreases from the initial value of 50 kPa in the early stage of loading, e.g., the mean effective stress for case B_O-1 at an axial strain of 0.5% is 31 kPa. **Figure 7.19** shows the stress path and the distribution of mean effective stress and pore water pressure for case B_O-1 at an axial strain of 0.5%. It can be seen in this figure, however, that the mean effective stress of almost the entire specimen increases from the initial value of 50 kPa, and the pore water pressure at the top edge is much higher than that at other parts of the specimen. The mean effective stress displayed in the stress path is calculated by the pore water pressure of the top edge in order to exactly compare the simulation results with the test results. The reason for the decrease in mean effective stress in the stress

paths is that the higher pore water pressure at the top edge leads to an estimation of a lower mean effective stress.

We can see in the deformed meshes shown in **Figures 7.10**(d)~**7.17**(d) that the deformation of the clay specimens depends on the shapes of the specimens, the strain rates, and the dilatancy characteristics. Strain localization and the growing process of shear bands can be seen in the distribution of shear strain in **Figures 7.10**(c)~**7.17**(c). Although homogeneous deformations can be seen until an axial strain of 4% is reached, the strain starts to localize at an axial strain of 8%, and then four or two shear bands appear at an axial strain of 12% and develop with an increased thickness on both surfaces. We can see in all cases that the shear strain at the center of the specimen is larger than that at any other part of the specimen. On the side surfaces of specimen C, shear bands can also be observed.

7.4.1 Strain Localization Pattern

All cases of A_N in **Figure 7.10** show the "X" mode in both the upper part and the bottom part of the specimen. In the experiments shown in **Figure 6.5**, however, cases A_N-1 and A_N-2 show the buckling-like mode. The same tendency can be seen for case A_O-1. It is worth noting, however, that the distribution of shear strain γ of the experiment also shows the "X" mode in both the upper part and the bottom part of the specimen until an axial strain of 8% is reached. As mentioned above in **Section 6.3.1**, bifurcation occurs and leads to the buckling-like mode. It is rather difficult, however, to trace the buckling-like mode because the buckling-like mode may occur due to geometrical imperfections.

It is seen that simulations of specimen B, in **Figures 7.12**(c) and **7.13**(c), effectively represent the strain localization pattern observed in the experiment, the "X" mode shown in **Figures 6.7**(c) and **6.8**(c). Strain starts to localize at an axial strain of 8% due to the fixed conditions of the top and the bottom edges. Shear bands can clearly be seen from the top and the bottom edges at an axial strain of 12%. Finally, the two shear bands form the "X" mode.

The deformations of specimen C, obtained by the finite element simulation, show the "X" mode at the center part of the specimen. In the experiments, we see that specimen C often shows the buckling-like mode. On the other hand, only case C_N-3 does not induce buckling and shows the complicated mode just like the "X" mode shown in **Figure 6.9**. This behavior is well reproduced by the simulation of case C_N-3 in which the "X" mode appears on the front surface and shear bands also appear on the side surface.

The strain localization pattern of specimen D is the "X" mode. It is interesting that we can see two "X"s on both surfaces. Four shear bands appear on both surfaces and form the "X" mode on the left and right sides of the specimen. The simulation results reproduce the "X" mode of D observed in the experiments very well.

Consequently, the various types of "X" mode of the strain localization pattern, due to the fixed conditions at both edges of the specimen, can be seen in all cases. The simulation results can very well reproduce the "X" mode especially for specimens B and D. For specimens A and C, the finite element analysis can very well reproduce the deformation behavior when buckling does not occur, such as in cases C_N-3 and A_O-1. On the other hand, the buckling-like mode due to

geometric instability is not seen in the finite element simulations since geometrical imperfections are not taken into account.

7.4.2 Three-dimensional Shear Bands

We estimated three-dimensional shear bands observed in the experiments in **Section 6.3.2**. In the case of the finite element analysis, however, we can directly see three-dimensional shear bands. **Figures 7.20** and **7.21** depict the distribution of the second invariant of accumulated viscoplastic deviatoric strain γ^p for all cases, namely,

$$\gamma^p = \int d\gamma^p \ , \quad d\gamma^p = \sqrt{de_{ij}^{vp} de_{ij}^{vp}} \tag{7.27}$$

where de_{ij}^{vp} is the deviatoric part of the viscoplastic strain increment tensor. In the distributions, by disregarding smaller values of γ^p, we can see localized strain, i.e., three-dimensional shear bands. Note that γ^p is obtained at the Gaussian integration points of the finite element method and is different from the 'shear strain γ' used in **Figures 7.10**(c)~**7.17**(c).

It is seen that the shear bands of the A_N cases develop from the eight corners of the edges of the specimen. In the upper and the lower parts of the specimen, four shear bands intercross each other from the edges, while the strain localization at the center part of the specimen is more moderate. In the A_O cases, the shear band formation is greatly dependent on the strain rates. The strain localization pattern for case A_O-1 is similar to that for the A_N cases, however, the accumulation of γ^p at the center of the specimen for case A_O-1 is larger than that for the A_N cases.

The shear bands of cases B_N and B_O-1 generate from the eight corners of the edges of the specimen due to the constraint of lateral displacement, and they intersect at the center of the specimen. On the other hand, the shear bands of cases B_O-2 and B_O-3 develop just beneath the corners.

In specimen C, we can see different types of three-dimensional shear bands from the other cases whereby the "X" mode of the shear bands form symmetrically in the x-direction. The accumulation of γ^p at the center of the specimen where the shear bands intersect is higher than for the other parts. In addition, the shear bands can be seen also in the side surface apparently.

The formation of three-dimensional shear bands for specimen D is rather consistent. Shear bands develop at the eight corners and two of them intersect each other and form the "X" mode. Two "X" modes can be seen on one surface and a high accumulation of γ^p is at the center of the specimen.

We cannot see apparent shear bands significantly in any cases, as can be seen in the test results for A_O-2 (**Figure 6.20**). In addition, we can estimate that the three-dimensional shear bands for specimens B and D penetrate the specimens (see **Figure 6.18**). However, the shear bands obtained by the simulations do not penetrate the specimens. **Figure 7.22** depicts the three-dimensional shear bands of case B_N-2 tested and simulated, respectively. In the distributions of shear strain for the test results, the accumulation of shear strain on the front surface is much higher than that on any other and we can see on the side surface that the shear bands penetrate through the specimen. On the other hand, the shear strain of the simulation results

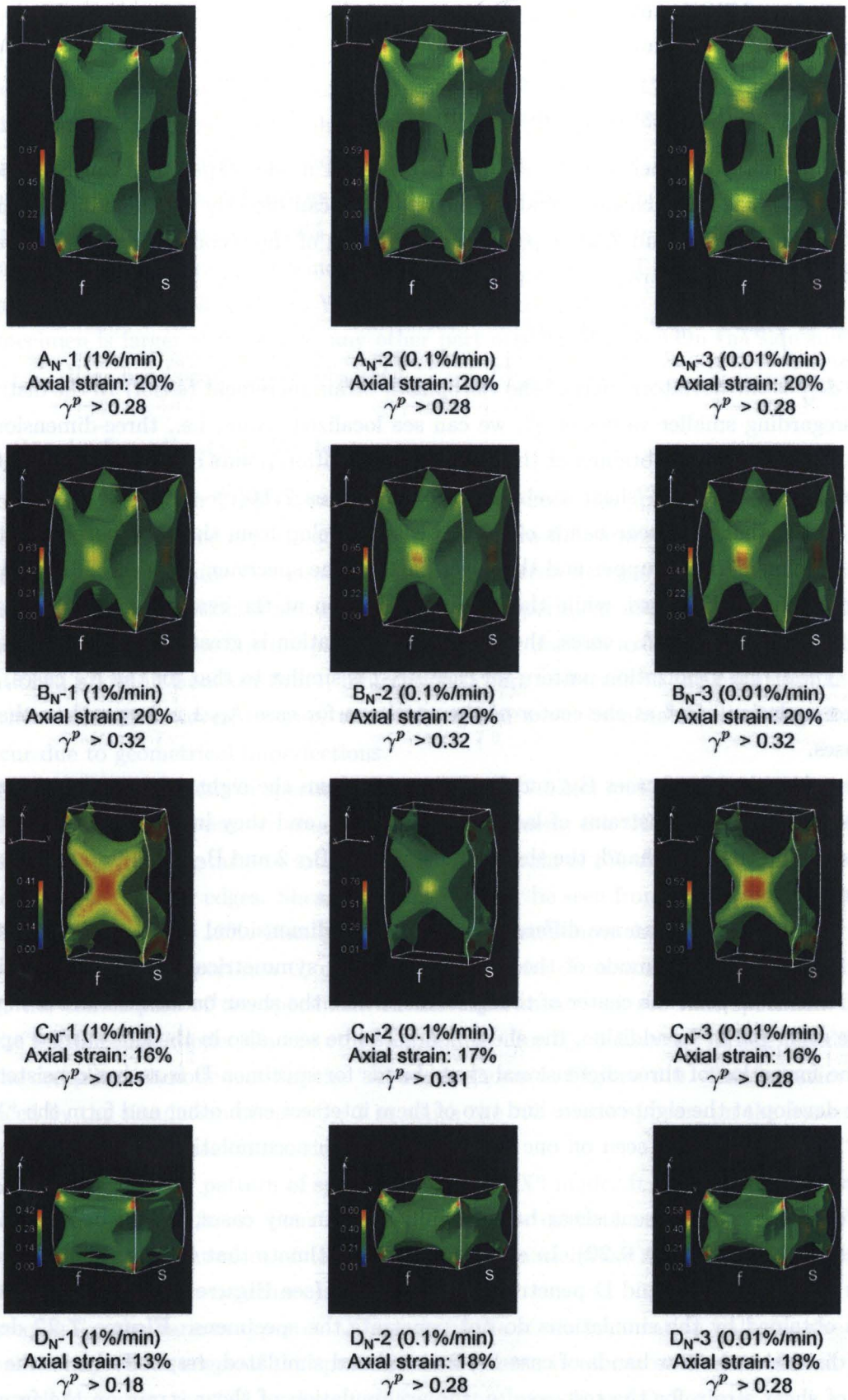

Figure 7.20 Three-dimensional shear bands for the cases of normally consolidated clay (Distribution of the second invariant of viscoplastic deviatoric strain γ^p excluding smaller strain levels)

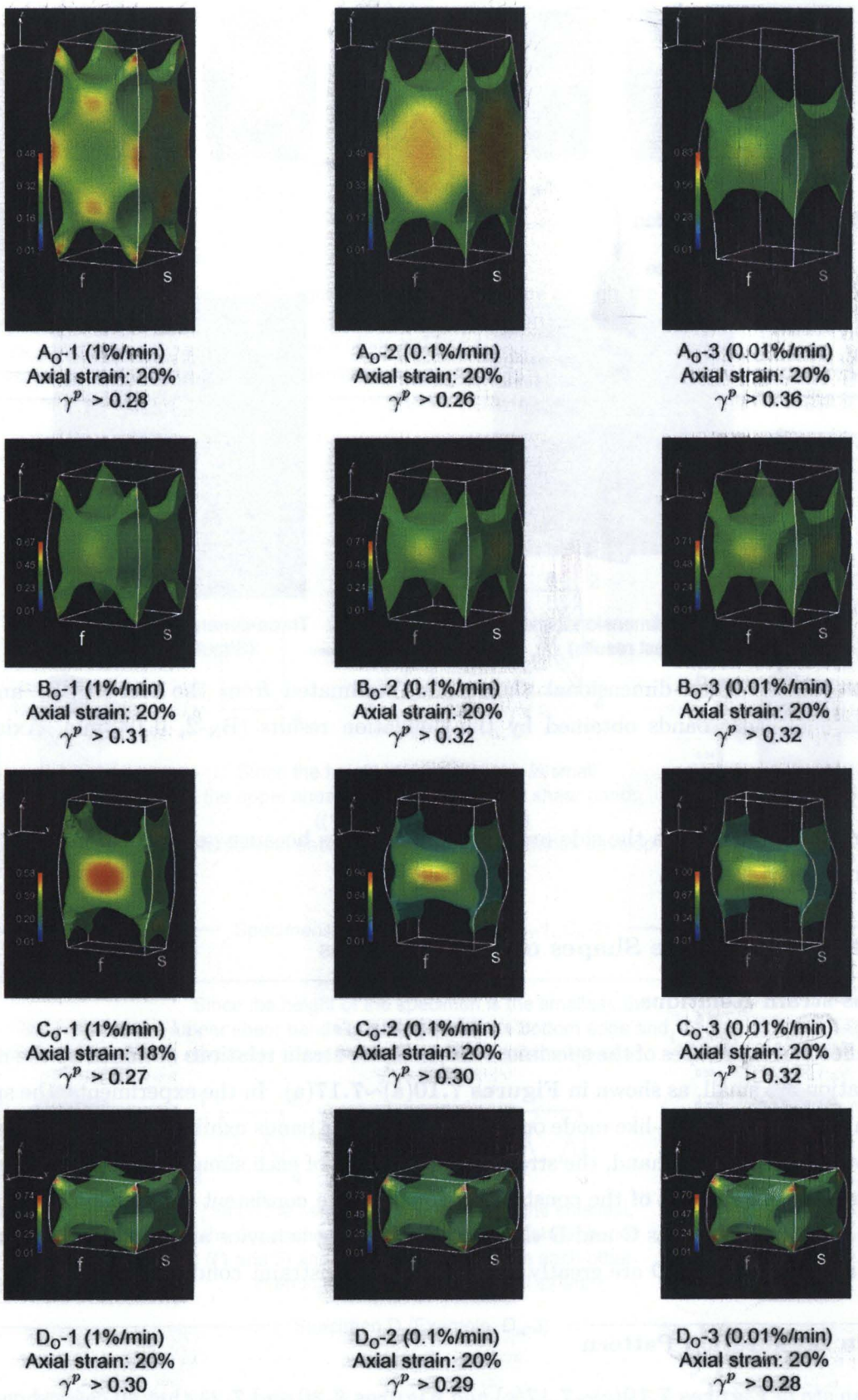

Figure 7.21 Three-dimensional shear bands for the cases of overconsolidated clay (Distribution of the second invariant of viscoplastic deviatoric strain γ^p excluding smaller strain levels)

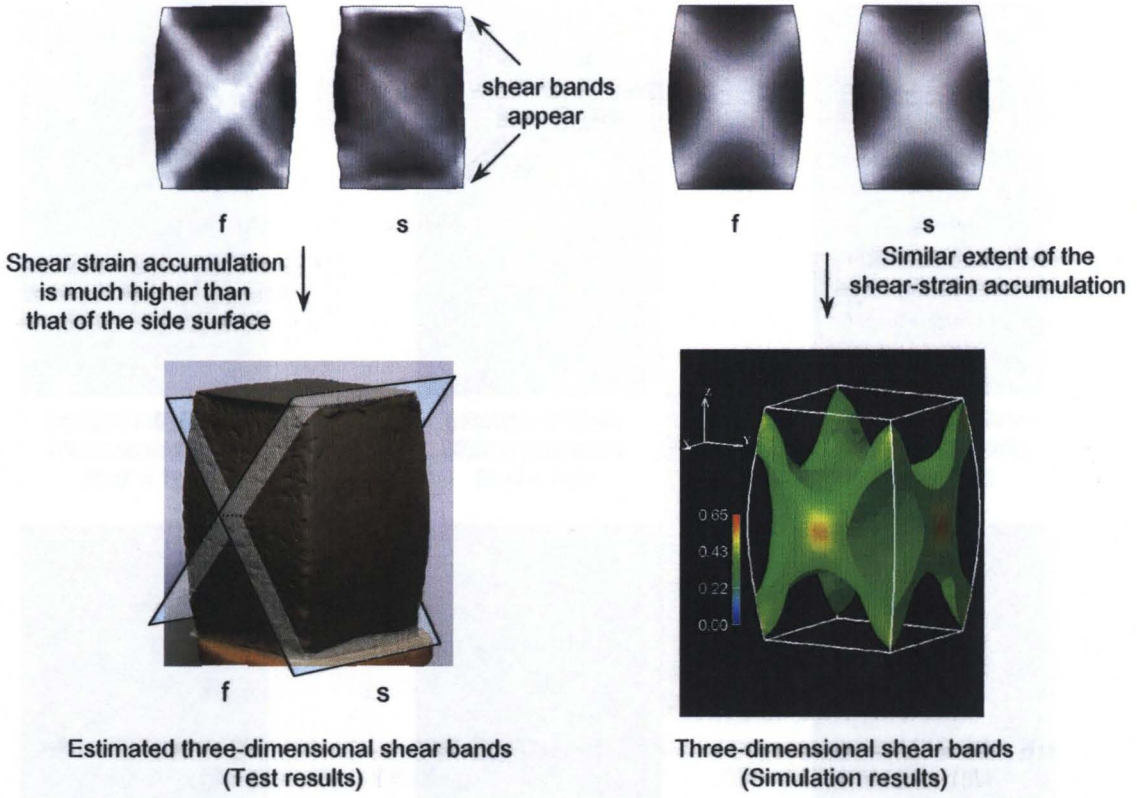

Figure 7.22 Three-dimensional shear bands estimated from the test results and three-dimensional shear bands obtained by the simulation results (B_N-2, 0.1%/min, Axial strain: 20%)

accumulates similarly on the side and the front surfaces because geometrical imperfections are not considered.

7.4.3 Effects of the Shapes of the Specimens

Stress-strain Relations

The effects of the shapes of the specimens on the stress-strain relations obtained by the numerical simulation are small, as shown in **Figures 7.10**(a)∼**7.17**(a). In the experiments, the specimens which show the buckling-like mode or the apparent shear bands exhibit unstable strain-softening behavior. On the other hand, the stress-strain relations of each simulation are similar as long as the material parameters of the constitutive equation are consistent throughout the simulation. Some cases for specimens C and D show strain-softening behavior and the calculations diverge, since specimens C and D are greatly affected by the constraint conditions.

Strain Localization Pattern

We can see in **Figures 7.10**(c)∼**7.17**(c) and **Figures 7.20** and **7.21** that all cases show the "X" mode localization. Shear bands for all cases of the normally consolidated clay and cases A_O-1 and 2, B_O-1, C_O-1, and D_O develop from the corners of the edges of the specimens. **Figure**

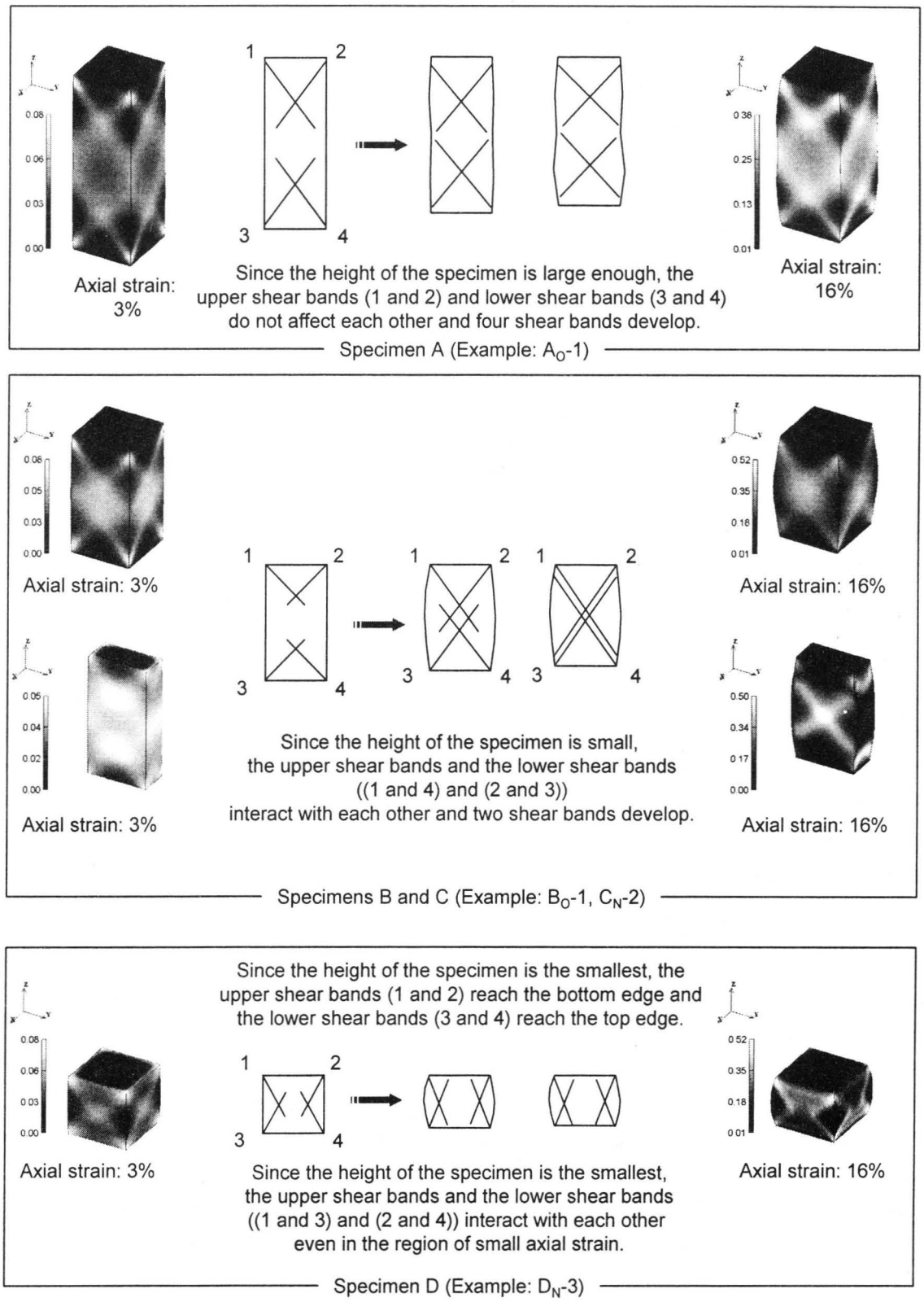

Figure 7.23 Schematic figures of the shear band formation process for each shape of specimen (Color contours are the distribution of γ^p)

7.23 shows the schematic figures of the shear band formation process for each shape of specimen. As shown in the distribution of γ^p at an axial strain of 3%, strain localizes from the corners at small axial strain levels. When the axial strain becomes larger, the generated shear bands develop dependent on the shape of the specimens, as can be seen in the distribution of γ^p at an axial strain of 16%. In the case of specimen A, since the height of the specimen is large enough, shear bands generated in the upper part (1 and 2) and shear bands in the lower part (3 and 4) do not affect each other, and then four shear bands develop. On the other hand, the height of specimen B is smaller than that of specimen A, and the upper shear bands and the lower shear bands interact with each other. Finally, shear bands 1 and 4 and shear bands 2 and 3 develop two apparent shear bands. In the case of specimen D, since the height of the specimen is so small that the upper shear bands and the lower shear bands ((1 and 3) and (2 and 4)) interact with each other even at small axial strain levels. Furthermore, the upper shear bands (1 and 2) reach the bottom edge and the lower shear bands (3 and 4) reach the top edge. These types of behavior are consistent with the formation process of the "X" mode observed in the experiments.

7.4.4 Effects of the Strain Rates

Stress-strain Relations

The rate sensitivity of clay can be seen in **Figures 7.10**(a)~**7.17**(a), except for case D_O-1, although the stress-strain curves obtained by the experiment show the rate sensitivity only at small axial strain levels. This is probably because the stress-strain relations obtained by the experiment are more dependent on strain localization patterns than on the material characteristics, i.e., rate sensitivity. On the other hand, in the case of the numerical simulation, the buckling-like mode or the appearance of apparent shear bands, which induce strain softening, do not occur.

Strain Localization Pattern

Figure 7.24 shows the distributions of shear strain for the simulation of specimen A with different strain rates at an axial strain of 20% and the inclination angles of shear bands compared with the experimental results. In the simulation results displayed in **Figures 7.10**(c)~**7.17**(c), the shear-strain distributions of the front side and of the side surface are similar. Hence, we use mainly those of the front surface in the following discussion.

It is seen that the effects of the strain rates on the simulation of the A_N cases are small. On the other hand, the simulation of the A_O cases is greatly affected by the strain rates. In the case of a higher strain rate, A_O-1, the "X" mode appears in both the upper and the lower parts of the specimen. As the strain rate becomes lower, the strain tends to localize in the center part of the specimen. The simulation can reproduce the tendency of case A_O and the deformation patterns, especially in the case of A_O-1.

Figure 7.25 shows the distribution of γ^p inside the specimen for the A_O cases. We can see that a higher accumulation of viscoplastic strain indicated by a white zone exists in the center

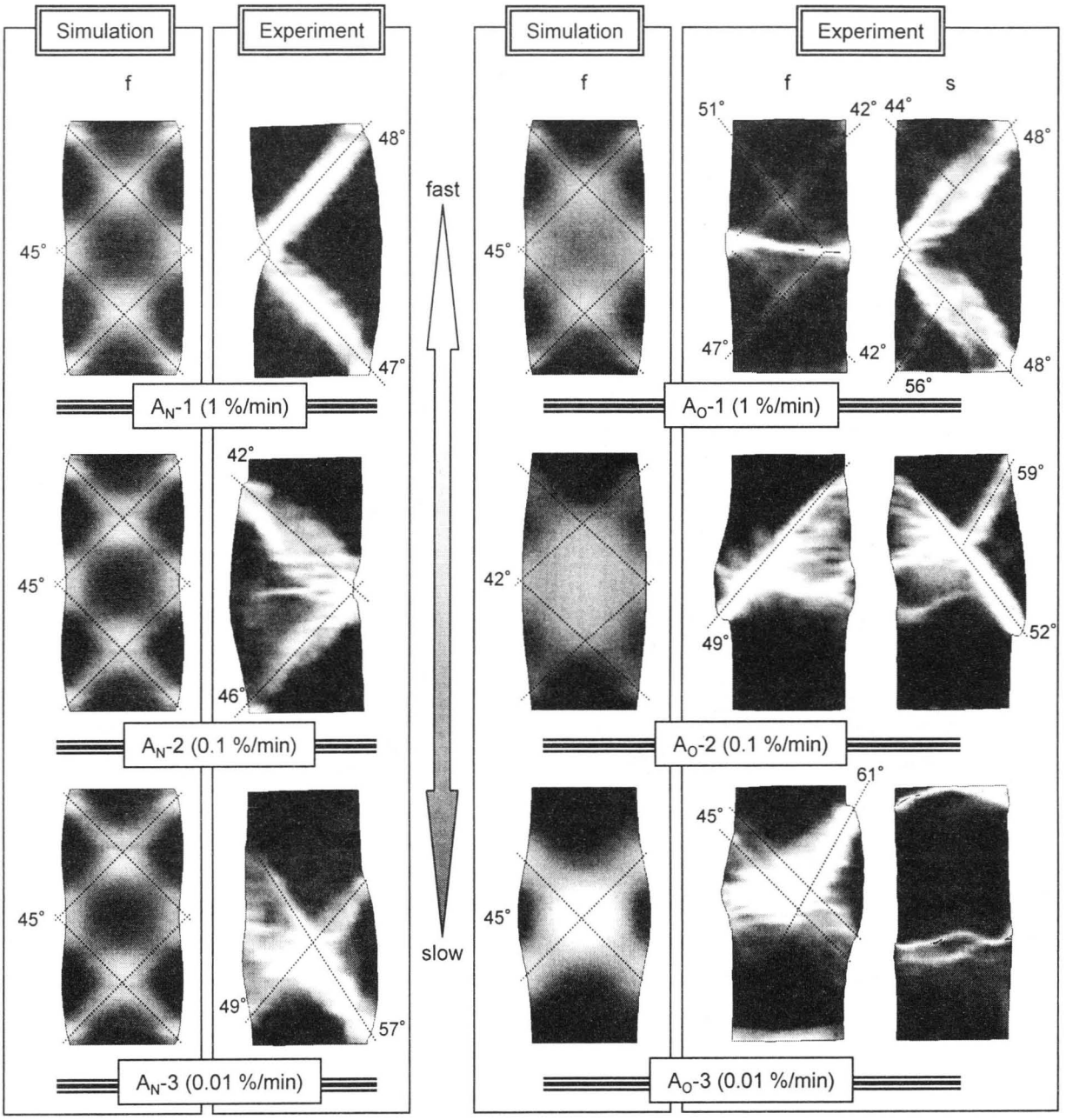

Figure 7.24 Comparison of the distributions of shear strain and the inclination angles of the shear bands for specimen A with different strain rates between the simulation results and the experimental results (Axial strain: 20%)

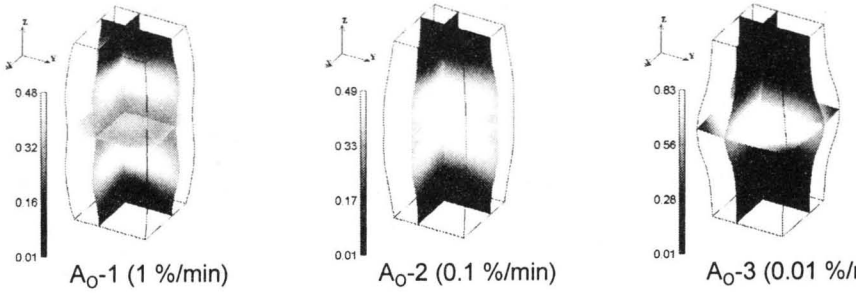

Figure 7.25 Distribution of γ^p inside of the specimen for the A_O cases with different strain rates (Axial strain: 20%)

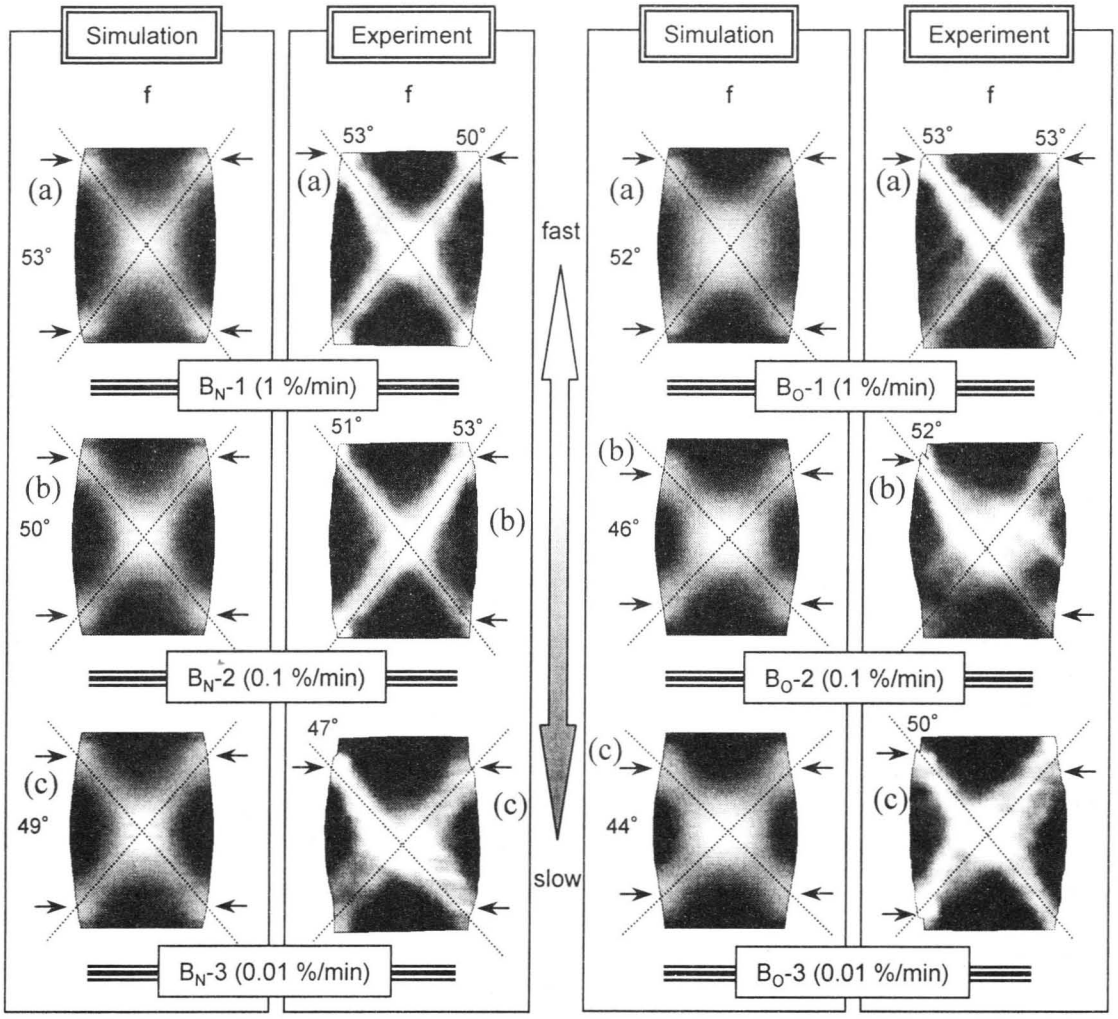

Figure 7.26 Comparison of the distributions of shear strain and the inclination angles of the shear bands for specimen B with different strain rates between the simulation results and the experimental results (Axial strain: 20%, Front surface); (a) shear bands develop from the top edge, (b) and (c) shear bands develop beneath the top edge

of the specimen in the case of A_O-3, while two white zones exist where shear bands from the corners of the top and the bottom edges intercross each other in the case of A_O-1. This tendency can also be seen in **Figure 7.21**. In addition, the accumulation of γ^p in the case of a lower strain rate is larger than that in the case of a higher strain rate due to the strain rate sensitivity. This tendency can be seen not only in A_O, but also in other cases. These results are consistent with the results obtained by the strain localization analysis under plane strain conditions (**Section 5.3.3**).

The shear-strain distributions and the inclination angles of the shear bands of both the simulation and the experiment for specimen B with different strain rates at an axial strain of 20% are shown in **Figure 7.26**. The numerical simulation for specimen B very well reproduces the experimental results with respect not only to the "X" mode, but also to the effects of the strain rates on the strain localization pattern. Shear bands develop from the top and the bottom edges in the case of higher strain rates, while those with lower strain rates develop beneath the

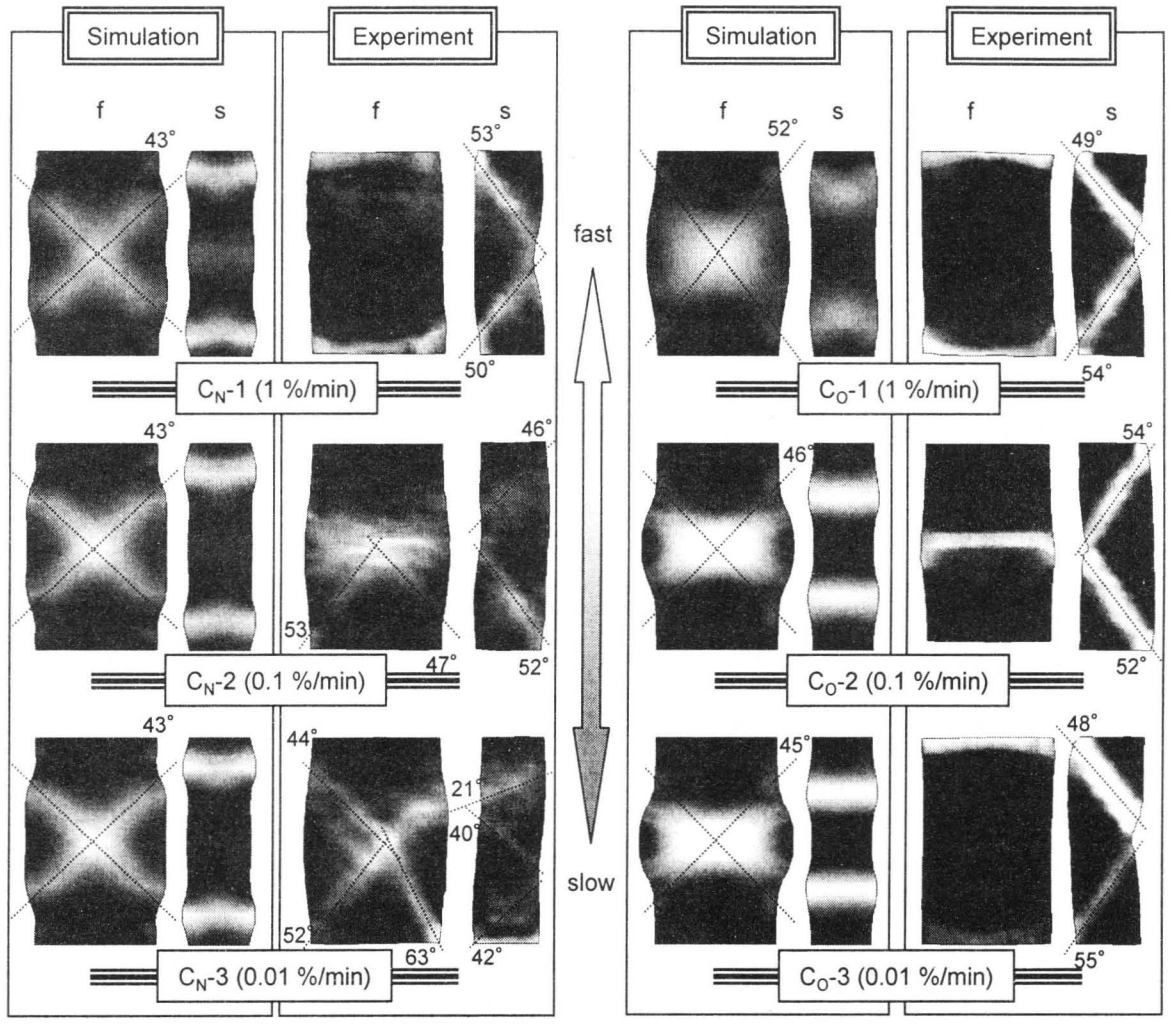

Figure 7.27 Comparison of the distributions of shear strain and the inclination angles of the shear bands for specimen C with different strain rates between the simulation results and the experimental results (Axial strain: 16%)

top and the bottom edges. Due to this tendency, the angles of shear bands become smaller as the strain rate decrease. This result is not consistent with the result obtained in **Section 5.3.3** under plane strain conditions. In addition, the thickness of the shear bands with lower strain rates is larger than that of those with higher strain rates. Note that these types of behavior are more clearly seen in the case of overconsolidated clay, namely, B_O.

In the case of C_N, the effects of the strain rates on the strain localization patterns for the C_N cases are very small, as can be seen in **Figure 7.27**. On the other hand, the effects of C_O are clearly seen in the inclination angles of the shear bands. The angles of shear bands for case C_O-1 are the largest, namely, 52 degrees, while the angles of shear bands for case C_O-3 are the smallest, namely, 45 degrees. This tendency is the same as that of specimen B. It is worth noting that the deformations of C_N-2 and C_N-3 observed in experiments, which are not the buckling-like mode, are well represented by the simulation.

Figure 7.28 displays the distributions of shear strain and the inclination angles of the shear bands of both the simulation and the experiment for specimen D with different strain rates at

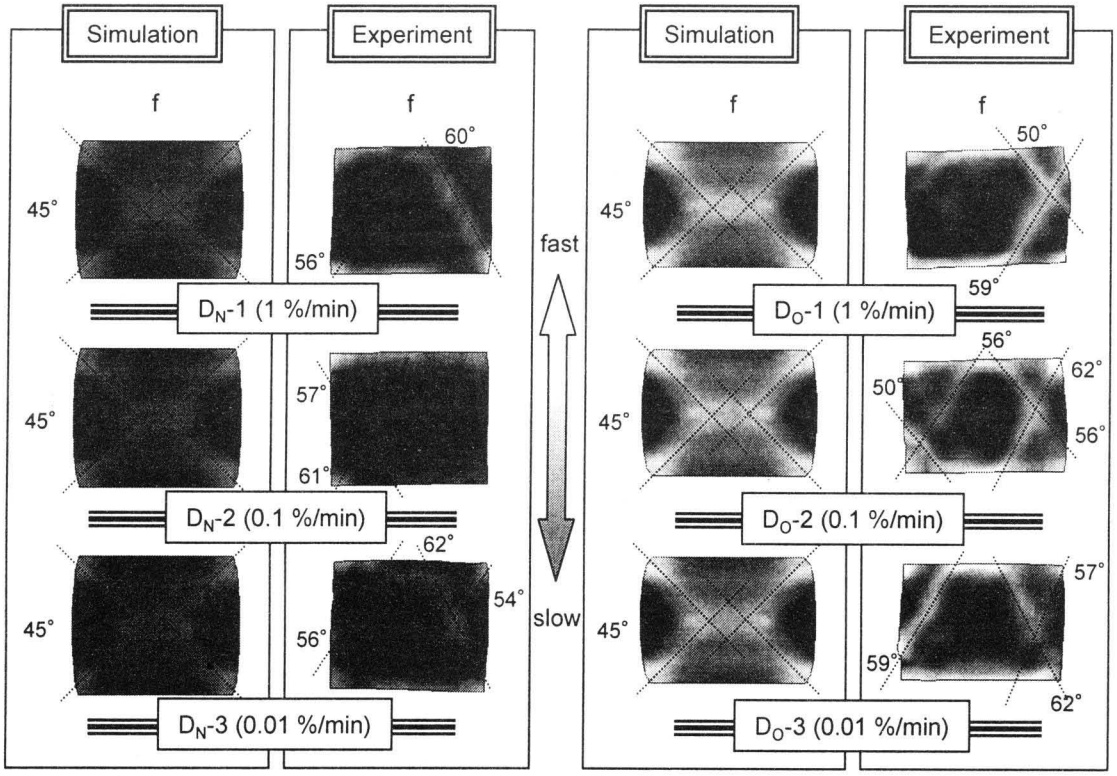

Figure 7.28 Comparison of the distributions of shear strain and the inclination angles of the shear bands for specimen D with different strain rates between the simulation results and the experimental results (Axial strain: 12% for NC clay and 20% for OC clay)

an axial strain of 12% for normally consolidated clay and 20% for overconsolidated clay. We can see in this figure that the effects of the strain rates are not significant. This is probably because the effects of the fixed conditions at the top and the bottom edges on the strain localization pattern of specimen D are much larger than those of the other specimens. The double "X" type of strain localization is well reproduced by the simulation, however, the inclination angles of the shear bands obtained by the simulation are smaller than those observed in the experiment.

On the whole, inclination angles of shear bands observed in the simulations are around 45 degree, which is the preferred orientation of shear band obtained from instability analysis by Oka et al. (1995) under plane strain locally undrained condition using the viscoplastic model presented in **Chapter 2**. On the other hand, those of experiments are rather larger than 45 degrees. It is possible that the migration of pore water and the three-dimensional conditions affected the shear band formation.

7.4.5 Effects of Dilatancy

It is seen in the stress-strain curves shown in **Figures 7.10**(a)∼**7.17**(a) that the axial strain of the peak stress for overconsolidated clay is smaller than that for normally consolidated clay. In addition, we can see in **Figure 7.29** that an accumulation of γ^p at an axial strain of 5% for overconsolidated clay is larger than that for normally consolidated clay, and that the shear bands of overconsolidated clay are more clearly seen than those of normally consolidated clay.

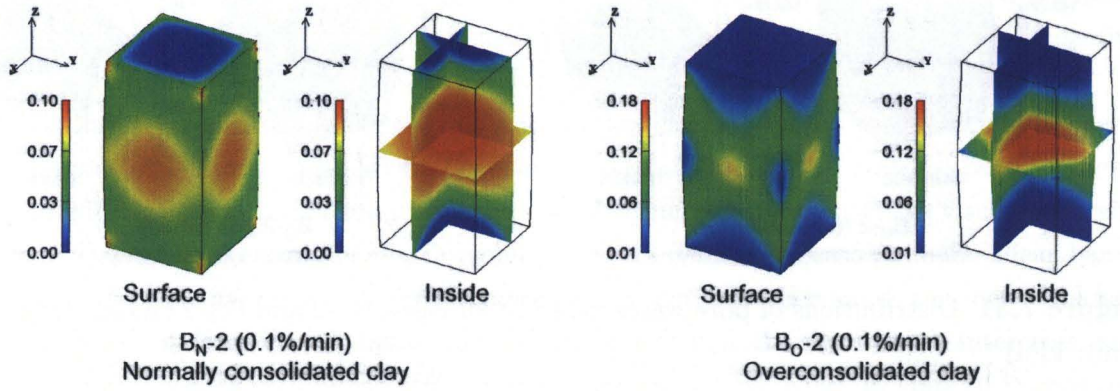

Figure 7.29 Distributions of γ^p for cases B_N-2 and B_O-2 (Axial strain: 5%)

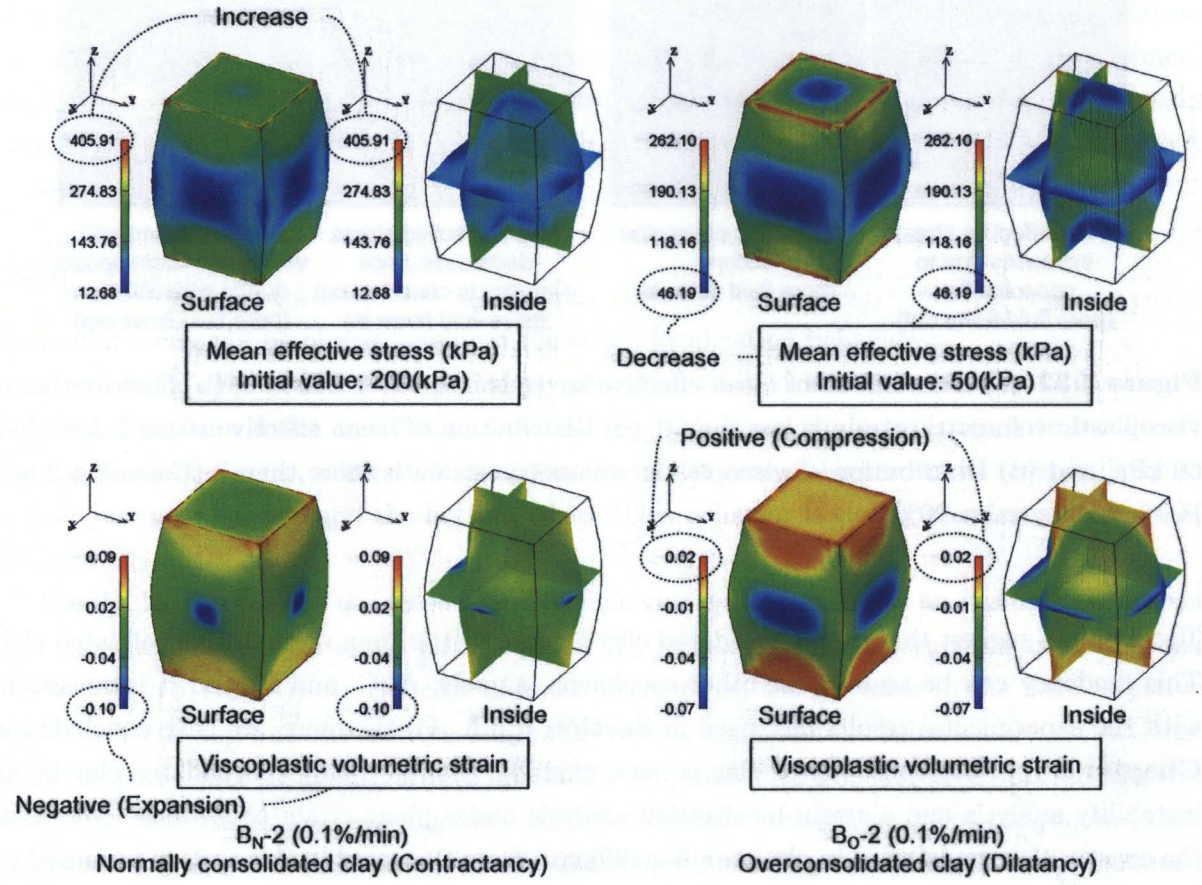

Figure 7.30 Distributions of mean effective stress and accumulated viscoplastic volumetric strain for cases B_N-2 and B_O-2 (Axial strain: 20%)

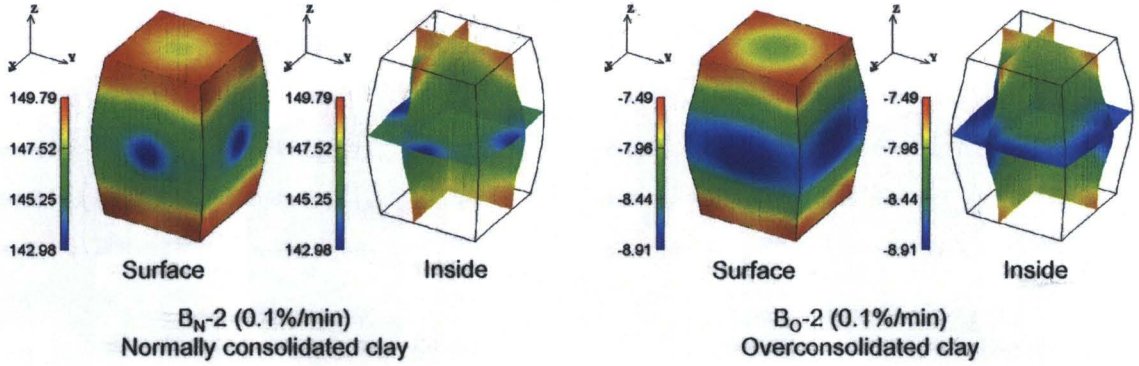

Figure 7.31 Distributions of pore water pressure for cases B_N-2 and B_O-2 (Axial strain: 20%, Unit: kPa)

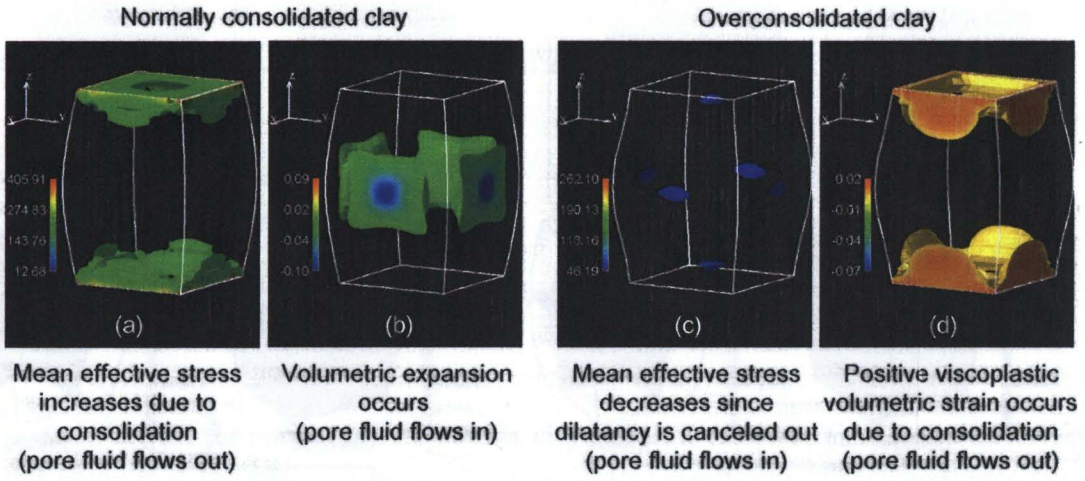

Figure 7.32 (a) Distribution of mean effective stress is more than 200 kPa, (b) Distribution of viscoplastic volumetric strain is less than 0, (c) Distribution of mean effective stress is less than 50 kPa, and (d) Distribution of viscoplastic volumetric strain is more than 0 (Cases B_N-2 and B_O-2, Axial strain: 20%)

These points suggest that overconsolidated clay is more brittle than normally consolidated clay. This tendency can be seen in the other specimens, namely, A, C, and D, and it is consistent with the experimental results discussed in **Section 6.3.5**. Furthermore, we have concluded in **Chapter 5** that overconsolidated clay is more unstable than normally consolidated clay by an instability analysis and a strain localization analysis under plane strain conditions. Note that the constitutive model used in **chapter 5** is different from that used in this section proposed by Kimoto (2002) and Kimoto et al. (2004; to appear). On the other hand, the instability analysis by Kimoto (2002) and Kimoto et al. (2004; to appear), using the same constitutive model in the present simulations, provides that overconsolidated clay is more unstable than normally consolidated clay.

Figure 7.30 shows the distributions of mean effective stress and accumulated viscoplastic volumetric strain for cases B_N-2 and B_O-2. In the case of normally consolidated clay, the mean

effective stress decreases from its initial value of 200 kPa and positive viscoplastic volumetric strain (compression is positive) occurs, namely, negative dilatancy can be seen. In particular, these types of behavior are typically seen inside the shear bands. On the other hand, the mean effective stress of overconsolidated clay increases from its initial value of 50 kPa and negative viscoplastic volumetric strain accumulates due to its positive dilatancy characteristics.

In this way, the typical effects of the dilatancy of clay can be seen in the simulation, however, different types of behavior can also be observed locally. Near the top and the bottom edges, the mean effective stress of normally consolidated clay increases with positive viscoplastic volumetric strain, and negative viscoplastic volumetric strain can be seen where the shear bands intercross each other in spite of the negative dilatancy. On the other hand, the mean effective stress of overconsolidated clay decreases around the point where the shear bands intercross, and viscoplastic compressive volumetric strain accumulates near both edges in spite of its positive dilatancy characteristics. These are closely related to the pore fluid flow. **Figure 7.31** shows the distribution of pore water pressure for cases B_N-2 and B_O-2. We can see in this figure that the distribution of pore water pressure is rather homogeneous. This suggests that the migration of pore fluid can easily occur. Consequently, near the top and the bottom edges, consolidation occurs due to the constraint conditions and pore fluid flows out into the center part of specimen. On the other hand, at the center of each surface where the shear bands intercross, expansion occurs in the case of normally consolidated clay and the effects of dilatancy are canceled out since the pore water flows in (**Figure 7.32**).

7.4.6 Discussion

Particular focus will be placed herein on the strain localization behavior.

It was found that strain rates significantly affect the strain localization patterns, as mentioned before in **Sections 6.3.4** and **7.4.4**. Deformation with lower strain rates tends to localize at the center of specimens, while strain localization in the case of higher strain rates is likely to appear just near the top and the bottom edges. This behavior is clearly seen in cases A_O, B_N, B_O, and C_O.

Firstly, let us consider the reason for this behavior by taking A_O as an example. It is seen that the viscoplastic shear strain for all cases of A_O localizes from the corners at an axial strain of 1% (**Figure 7.33**(a)). In the case of lower strain rates, the increases in the mean effective stress near the top and the bottom edges due to the consolidation behavior are rather large since the pore water easily migrates (**Figures 7.33**(b) and (c)). The increases in mean effective stress due to consolidation and dilatancy enlarge the shear strength near both edges, and then deformation starts to localize at the center of the specimen (**Figure 7.33**(a)) where the mean effective stress is smaller than that near the edges (**Figure 7.33**(c)). On the other hand, in the case of higher strain rates, the increments in mean effective stress due to consolidation are rather small since it is hard for the migration of pore water to occur (**Figures 7.33**(b) and (c)). Thus, the strain localization from each corner develops further and the shear bands form in both the upper and the lower parts of the specimen (**Figure 7.33**(a)) due to small increases in shear strength near both edges (**Figures 7.33**(b) and (c)).

As can be seen in the simulations of cases A_N and C_N, the effects of the strain rates on the strain localization of normally consolidated clay are smaller than those of overconsolidated clay. Since normally consolidated clay is a contractant material, the mean effective stress essentially decreases and the effects of consolidation near the tope and the bottom edges are smaller than for overconsolidated clay. **Figure 7.34** shows the distributions of mean effective stress for the A_N cases with different strain rates at an axial strain of 5%. It can be seen that the red zones (mean effective stress increases from its initial value: 200 kPa) are very small near the top and the bottom edges even in the case of lower strain rates, while the mean effective stress decreases along the shear bands indicated by the blue zones. Hence, the shear strength of normally consolidated clay does not increase and the shear bands easily develop further from each corner (**Figure 7.35**). This is the reason for the difference in the strain rate effects on strain localization between the normally consolidated clay and the overconsolidated clay.

Secondly, the reason why higher strain rates are likely to induce the buckling-like mode will be considered. As shown in **Figure 6.16**, geometric instability induces buckling and the shear bands develop from the point where the buckling occurs to the top and the bottom of the specimen. In the case of higher strain rates, the strain tends to localize in the upper and the lower parts of the specimen (**Figure 7.33**(a)). Consequently, the deformation of higher strain rates goes into the buckling-like mode (**Figure 7.36**(a)). Furthermore, the non-homogeneous distribution of pore water pressure in the case of higher strain rates, e.g., **Figure 7.33**(b), probably enlarges the geometric instability. On the other hand, in the case of lower strain rates, the buckling-like modes do not appear. Deformation with lower strain rates tends to localize in the center part of the specimen due to the effect of consolidation (**Figure 7.36**(b)) even though the aspect ratio of the specimen is large.

Finally, we will discuss geometrical imperfections which may induce the buckling-like mode. The simulation is ideally symmetric, while the experiment is not perfectly symmetric. The lack of homogeneous deformation may be due to geometrical imperfections, e.g., the initial imperfection of specimens and the friction between the porous stone and the specimens. In order to adopt geometrical imperfections into the simulation, frictional boundaries are assumed, as shown in **Figure 7.37**. The coefficient of friction μ_f is 0.1. **Figure 7.38** shows the distributions of γ^p for specimens A and C using the frictional boundaries. We can see in this figure that cases A_N, A_O-1, C_N, and C_O-1 show the buckling-like mode. Two shear bands and the intersection of them can be clearly seen in these cases. Note, however, that asymmetric deformations are induced by the intrinsic imperfections in the numerical calculations. In any event, it is confirmed that the buckling-like mode can only be reproduced if geometrical imperfections are taken into account in some way. In addition, the priori material heterogeneity caused the asymmetric deformation, as shown in **Section 3.8**. It is worth noting that the priori material heterogeneity may also be an important factor in the buckling-like mode. Proper consideration regarding the geometrical imperfections and material heterogeneity will be necessary in the future.

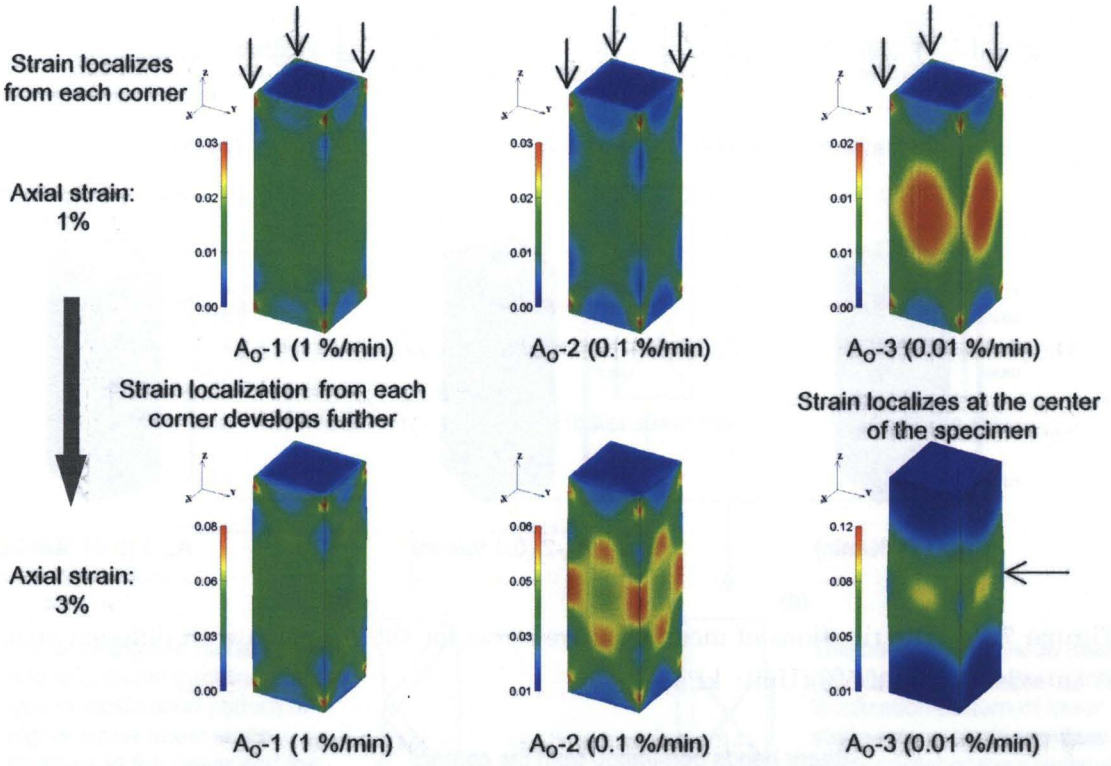

(a) Distribution of γ^p for the A_0 cases with different strain rates

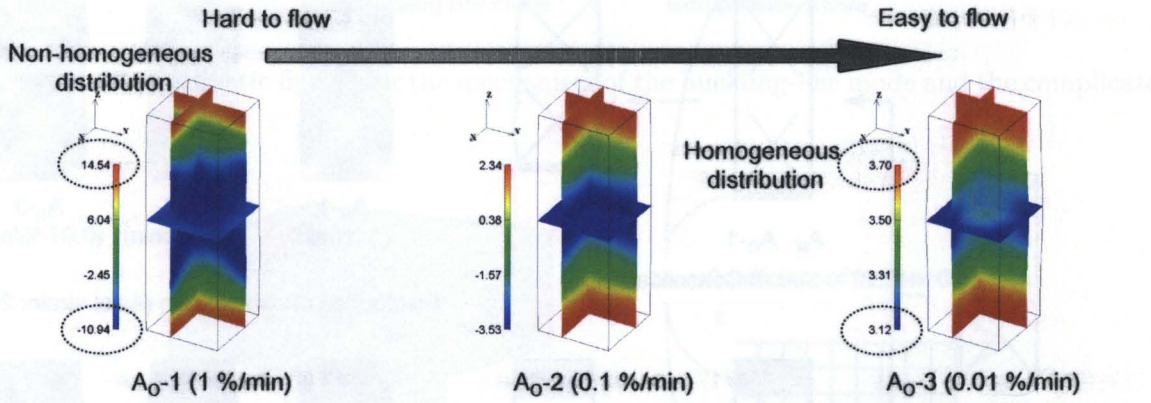

(b) Distribution of pore water pressure for the A_0 cases with different strain rates at an axial strain of 3% (kPa)

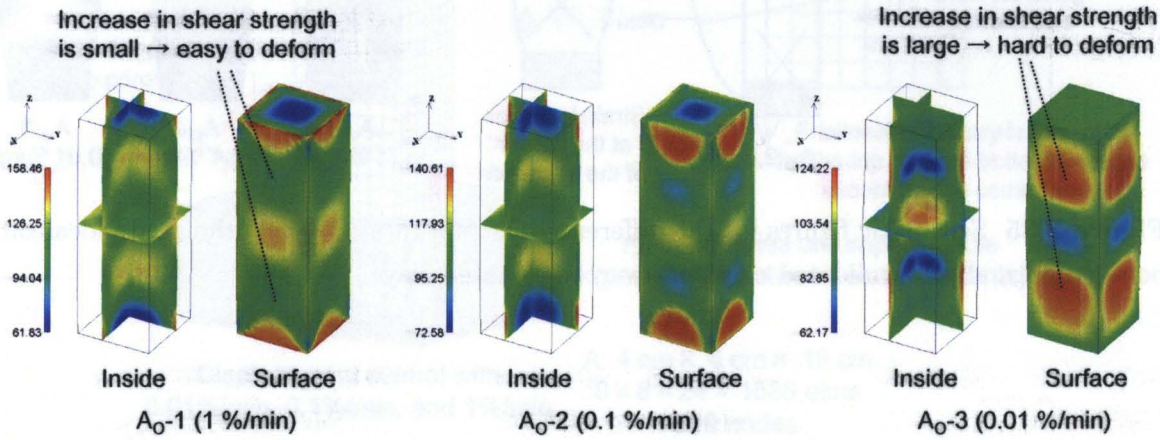

(c) Distribution of mean effective stress for the A_0 cases with different strain rates at an axial strain of 3% (kPa)

Figure 7.33 Mechanism of the effects of the strain rates on the strain localization pattern

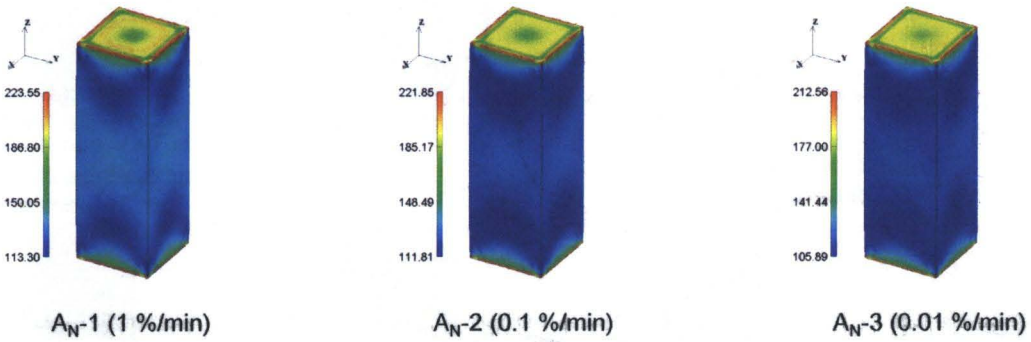

Figure 7.34 Distributions of mean effective stress for the A_N cases with different strain rates at an axial strain of 5% (Unit: kPa)

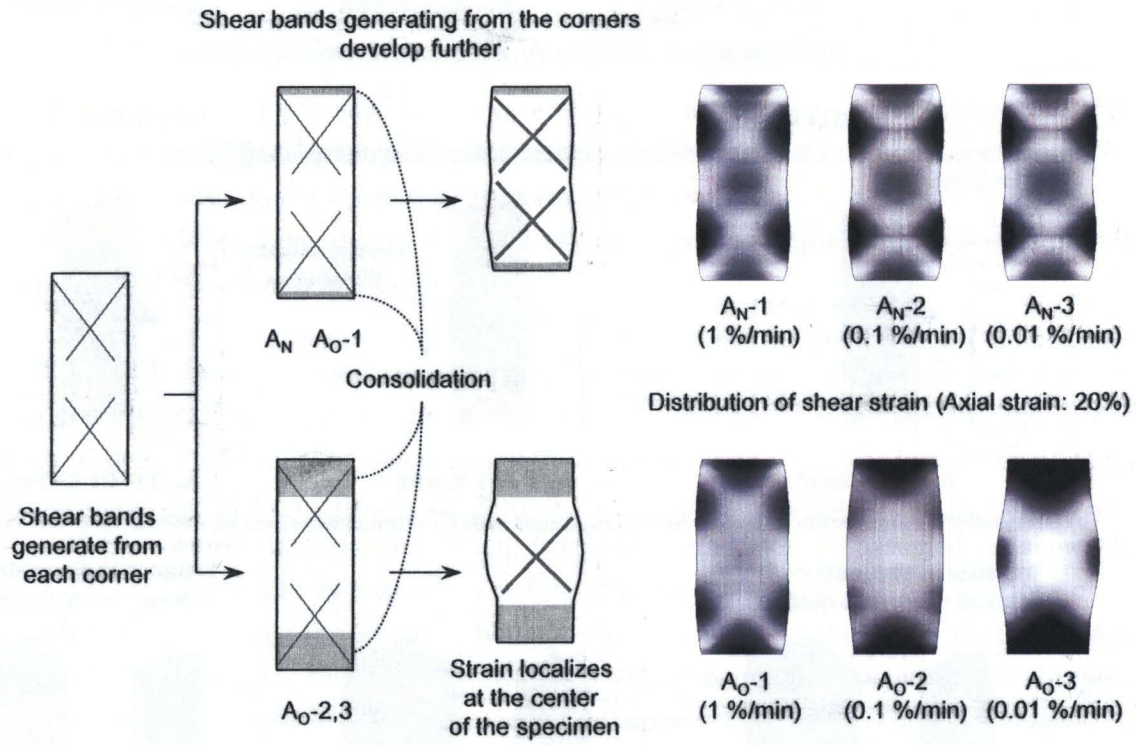

Figure 7.35 Schematic figures for the difference in strain rate effects on the strain localization between normally consolidated clay and overconsolidated clay

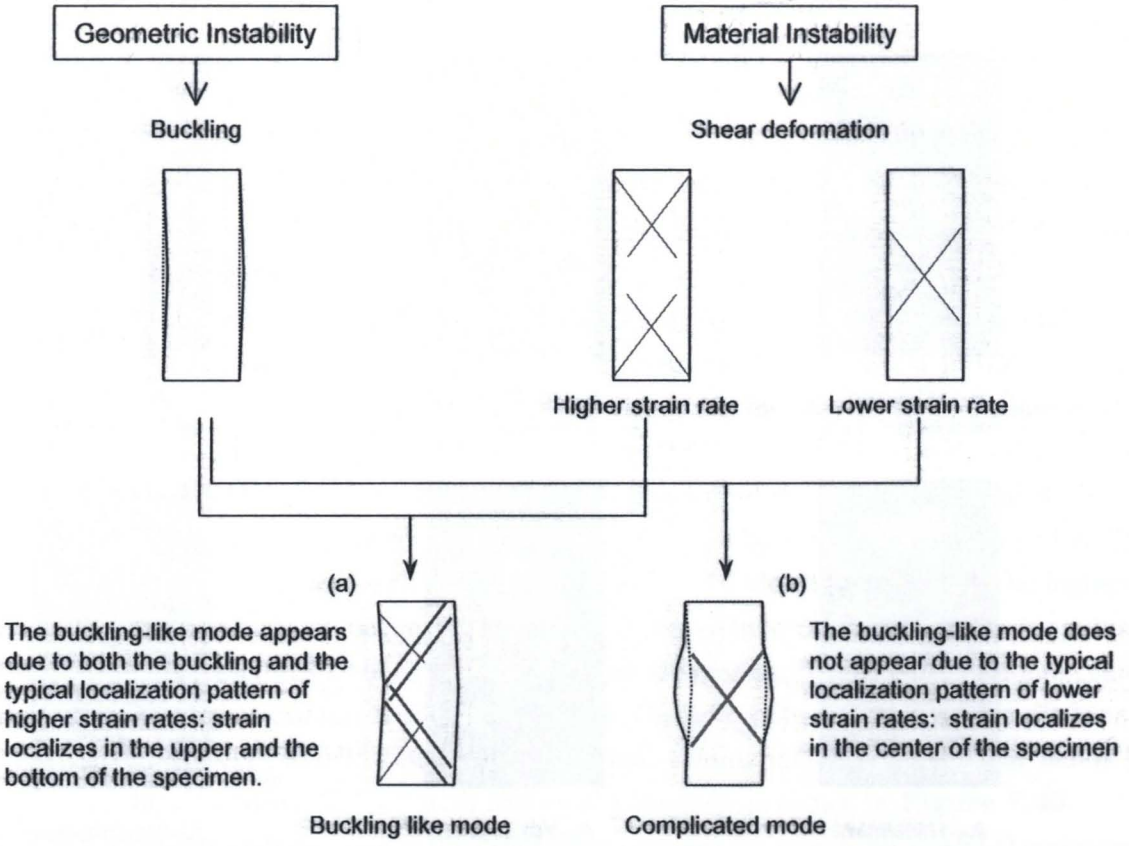

Figure 7.36 Schematic figures for the mechanism of the buckling-like mode and the complicated mode

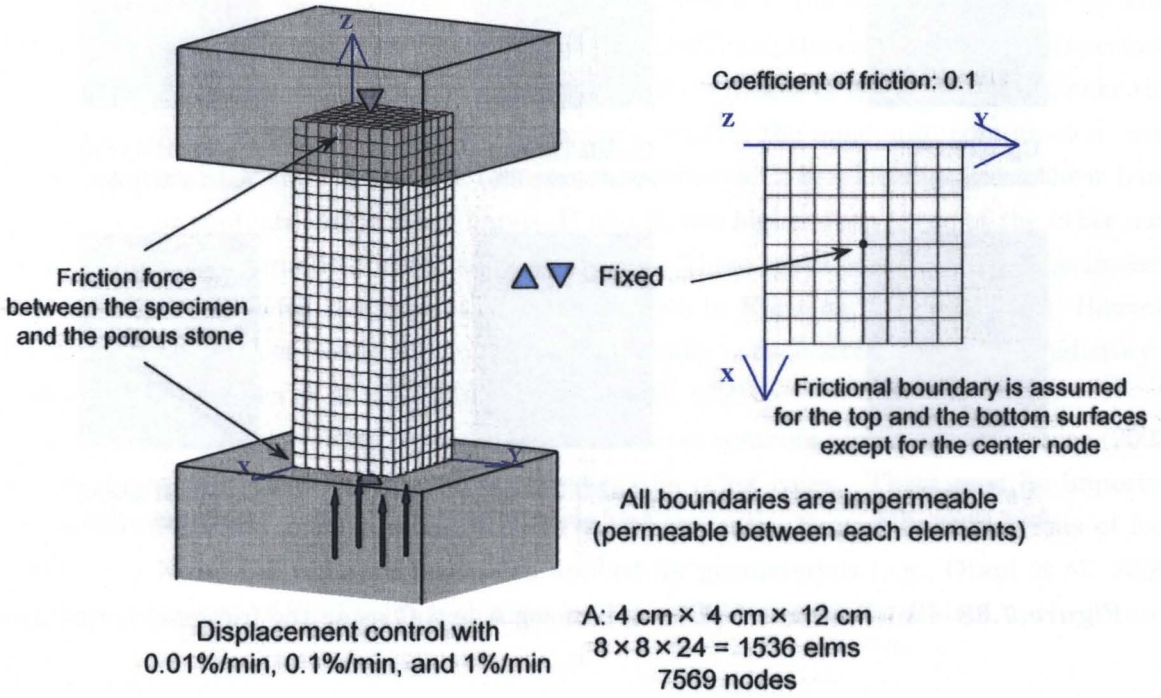

Figure 7.37 Frictional boundary conditions for the three-dimensional finite element analysis (The same boundary conditions are used for specimen C)

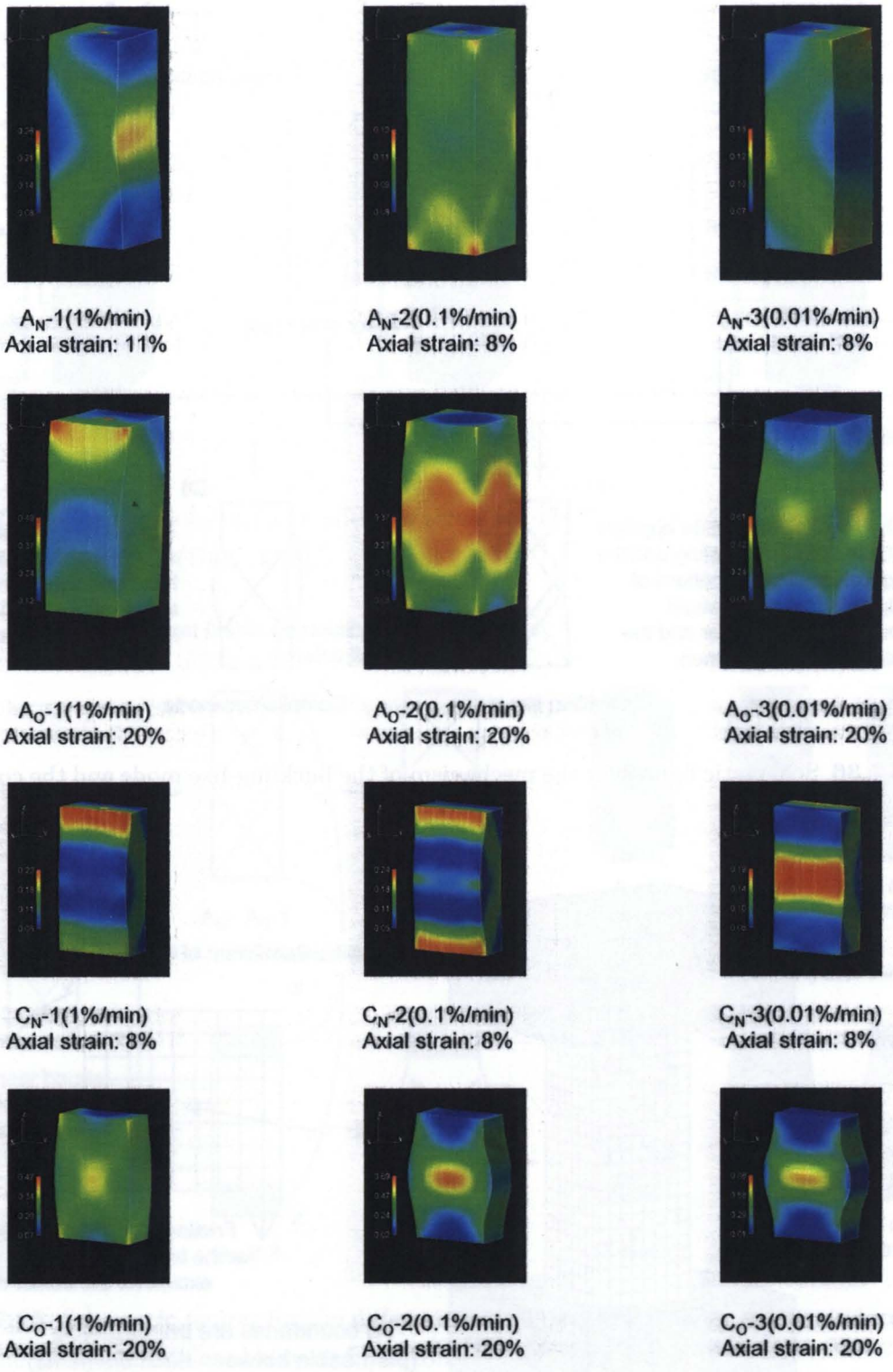

Figure 7.38 Distributions of γ^p for specimens A and C using the frictional boundaries

7.4.7 Local Volume Changes

Figure 7.39 depicts the distributions of total volumetric strain ε_v $(= \varepsilon_{11} + \varepsilon_{22} + \varepsilon_{33})$ for each specimen in the case of simulation with strain rate of 0.1%/min. It is seen in all cases that positive volumetric strain (compression) occurs at the center part of the specimens and near the top and the bottom edges. On the other hand, negative volumetric strain (expansion) occurs near the side surfaces. In the other cases, i.e., simulation with strain rates of 1%/min and 0.01%/min, the same tendency is observed.

Oka et al. (1994) observed in undrained triaxial and plane strain compression tests for normally consolidated clay that water contents along shear bands are lower than those outside shear bands, namely, compression occurs inside shear bands. In the case of drained compression tests by Hicher et al. (1994), normally consolidated clay exhibits compression inside shear bands, while overconsolidated clay (OCR = 10) shows expansion inside shear bands. Shimizu (1982) conducted compression tests for overconsolidated clay (OCR = 8) under the condition that the mean effective stress is constant. In the tests, water contents inside shear bands are the highest, which suggests volume increase occurs inside shear bands. These observations are consistent with the dilatancy characteristics of clay. In the present simulation, it is worth mentioning that expansion inside the shear bands is observed in case C_N-2 in spite of the negative dilatancy characteristic of normally consolidated clay. In addition, volume increase inside shear bands is clearly seen in the simulation of C_N-3 with frictional boundary as shown in **Figure 7.40**.

Figure 7.41 shows distributions of the local water contents for specimens C and D measured after the tests in the present experiment. All of specimens D were divided into seven parts (**Figure 7.41**(a)), and specimens C, which showed the buckling-like mode, were divided into the parts along shear bands and the other parts (**Figure 7.41**(c)). In **Figures 7.41**(b) and (d), w_{local} denotes the water content of each element and w is the water content of the whole specimen. In the case of specimen D, water content of B22, i.e., the center part of the specimen, is lowest, while those of A, C, B1, and B2, i.e., near the surfaces of specimens, are higher than the other parts. This suggests that the center part exhibits the maximum compression, while expansion occurs near the surfaces. In the case of specimens C, in which apparent shear bands appeared, water contents inside shear bands, B and E, are higher than those of the other parts even in the case of normally consolidated clay, C_N-1. These types of behavior of specimens C and D are consistent with the simulation results shown in **Figures 7.39** and **7.40**. However, the local volume changes inside shear bands for normally consolidated clay is contradictory to the observations by Oka et al. (1994) and Hicher et al. (1994).

The other data of the distributions of the local water contents are listed in Ichinose (2003). However, no specific tendency can be observed in the other cases. There may be important problem in the measurement method of local water contents. Recently, observations of local density using X-ray CT scanners have been applied for geomaterials (e.g., Otani et al. 2000). Detail measurements of local volume changes by X-ray CT scanners are desired in the future.

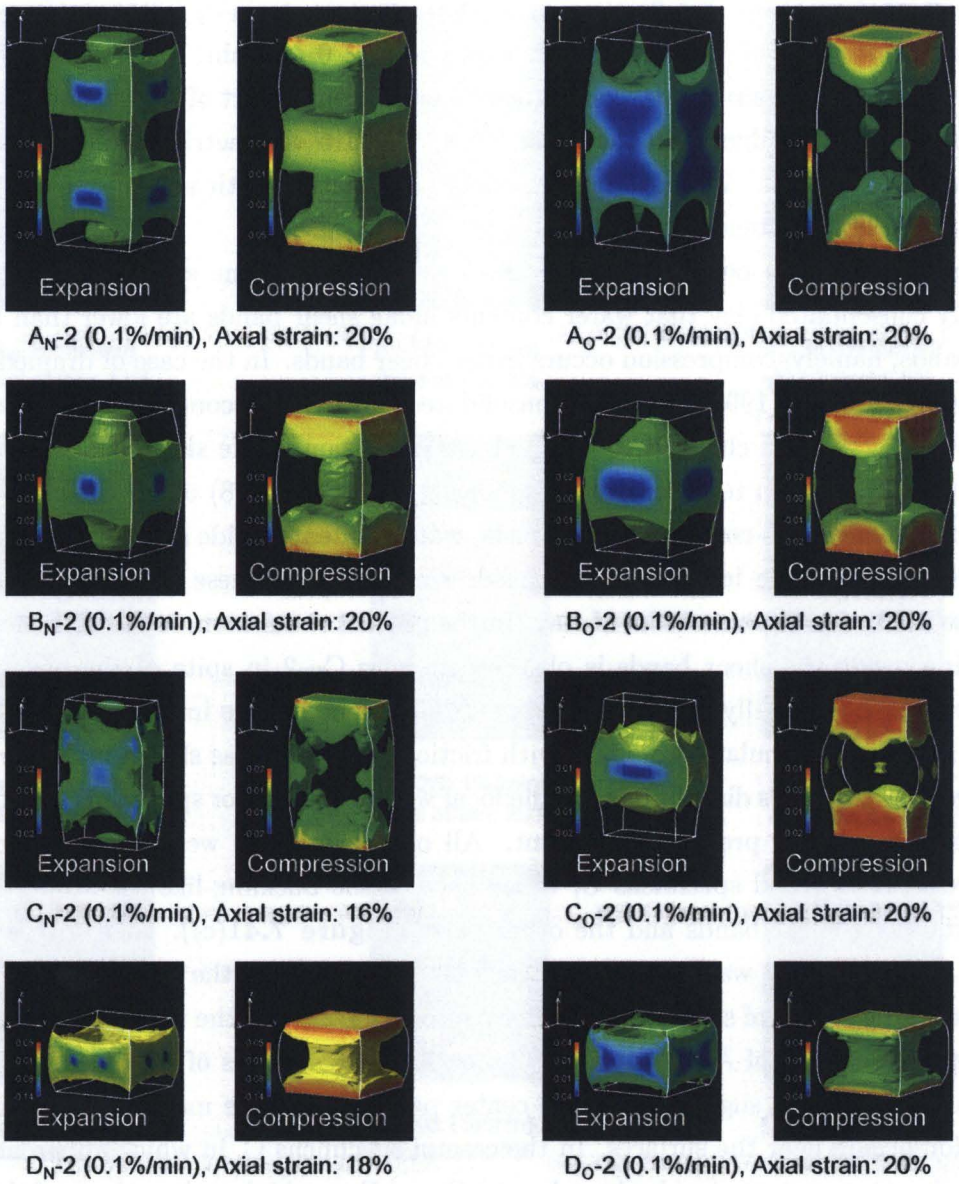

Figure 7.39 Distributions of total volumetric strain (Compression: Positive, Expansion: Negative)

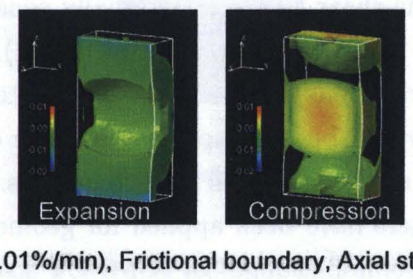

Figure 7.40 Distributions of total volumetric strain in the case of the buckling-like mode (Compression: Positive, Expansion: Negative)

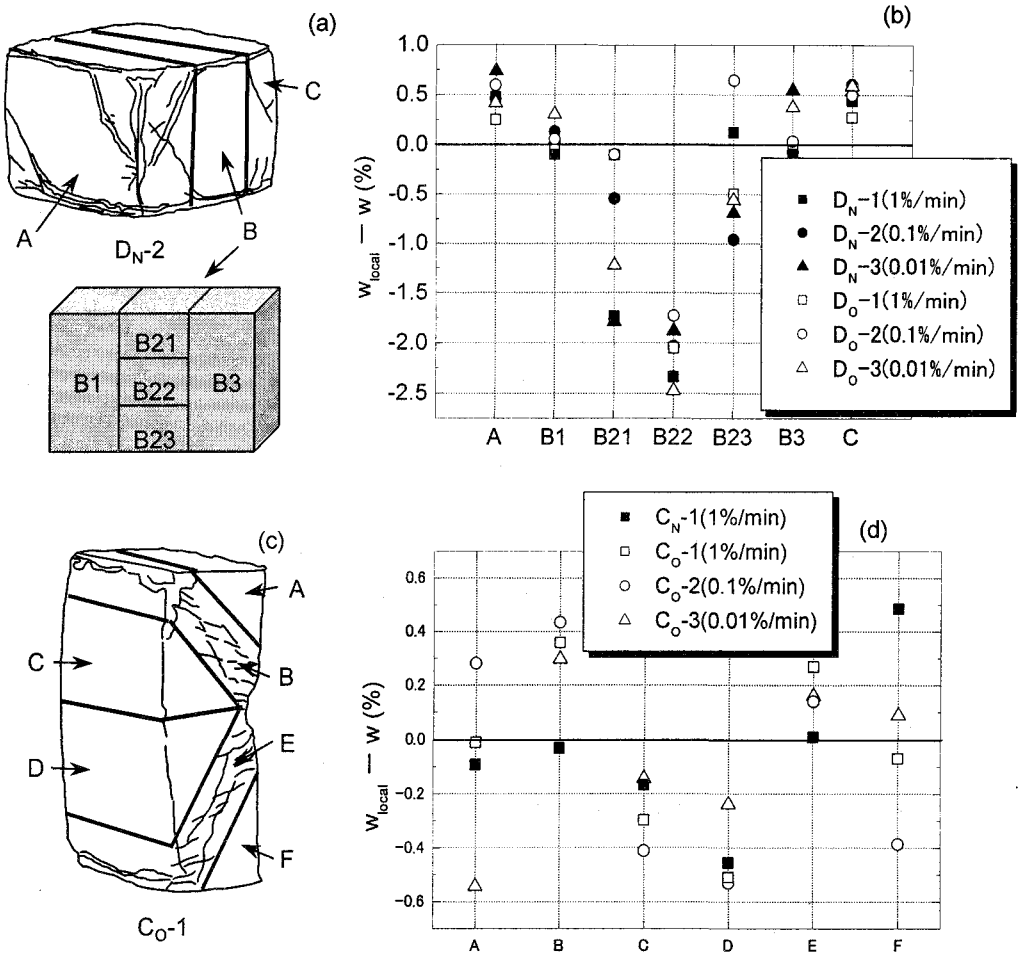

Figure 7.41 Measurements of local water contents for specimens C and D

7.5 Summary

In this chapter, a numerical simulation of undrained triaxial compression tests for normally consolidated clay and overconsolidated clay was conducted by a soil-water coupled finite element analysis based on the finite deformation theory. As for the constitutive equation, an elasto-viscoplastic model for water-saturated clay considering structural changes, proposed by Kimoto (2002), Kimoto and Oka (2003), and Kimoto et al. (2004; to appear) was used. The material parameters used in the simulation were determined by undrained triaxial compression tests and isotropic consolidation tests on Fukakusa clay.

Firstly, we discussed the simulation results. Then, a comparison between the simulation results and the experimental results examined the effects of the shapes of the specimens, the strain rates, and the dilatancy characteristics on the strain localization obtained in the experimental results. The obtained conclusions are summarized as follows:

1. The stress-strain relations and the effective stress paths for all cases well represented the strain rate sensitivity and the dilatancy characteristics. However, the strain-softening behavior corresponding to the formation of shear bands was not observed.

2. It was seen in the distributions of shear strain that the present simulation can well reproduce the timing of the appearance of shear bands and the "X" mode of the strain localization. On the other hand, the buckling-like mode cannot be represented since it may occur due to geometrical imperfections, while the boundary conditions for the simulation are ideally symmetric.

3. The distributions of γ^p gave the three-dimensional shear bands of the simulation results. From those figures, the mechanism of the three-dimensional strain localization was clarified.

4. In all cases of the numerical simulation, shear bands developed from each corner of the specimen. The generated shear bands interacted with each other and were dependent on the shape of the specimen.

5. In the case of specimens A, B, and C, the strain tended to localize in the center of the specimens as the strain rates decreased. The present simulation reproduced this tendency very well.

6. The axial strain at the peak stress of overconsolidated clay was smaller than that of normally consolidated clay, and the shear band formation of overconsolidated clay occurred earlier than that of normally consolidated clay. In other words, overconsolidated clay is more brittle than normally consolidated clay.

7. Normally consolidated clay and overconsolidated clay exhibited contractancy and dilatancy characteristics, respectively. We observed increases in mean effective stress (consolidation) and negative viscoplastic volumetric strain (expansion) even in normally consolidated clay, and decreases in mean effective stress (dilatancy cancel out) and positive viscoplastic volumetric strain (compression) even in overconsolidated clay. These types of behavior resulted from the migration of pore water.

8. The distributions of pore water pressure with higher strain rates were rather non-homogeneous. On the other hand, the distributions with lower strain rates were almost homogeneous. Namely, the migration of pore water occurred more easily in the case of lower strain rates than higher strain rates.

9. Consolidation occurred near the top and the bottom edges of the specimens and the distribution of pore water pressure, which is associated with the amount of pore water flow, caused the difference in strain localization patterns among specimens with different strain rates.

10. The effects of the strain rates on the strain localization patterns for overconsolidated clay were more apparent than those for normally consolidated clay. This tendency is closely related to the consolidation behavior near the both edges.

11. The reason why the buckling-like mode tended to occur in the case of higher strain rates depends on both the effects of the consolidation and the strain localization mode before the buckling-like mode appears.

12. Adopting geometrical imperfections into the simulation by a frictional boundary lead to the buckling-like mode in the cases of specimens A and C. However, it is worth mentioning that the buckling-like mode was induced by intrinsic imperfections in the numerical calculations.

13. Local volume decrease at the center part of the specimen was observed in both the simulation and the measurements for specimens D, while local volume increase near the surfaces of the specimen was seen in both the simulation and the measurements for specimens C.

References

Adachi, T. and Oka, F. (1982), Constitutive equations for normally consolidated clay based on elasto-viscoplasticity, *Soils and Foundations*, **22**, 4, pp. 57-70.

Adachi, T. and Okano, M. (1974), A constitutive equation for normally consolidated clay, *Soils and Foundations*, **14**, 4, pp. 55-73.

Hicher, P.Y., Wahyudi, H. and Tessier, D. (1994), Microstructural analysis of strain localisation in clay, *Computers and Geotechnics*, **16**, pp. 205-222.

Ichinose, T. (2003), Experimental study on strain localization of clay using reconstituted rectangular specimens, Graduation thesis, Kyoto University, Japan, in Japanese.

Kimoto, S. (2002), Constitutive models for geomaterials considering structural changes and anisotropy, Doctoral thesis, Kyoto University, Japan.

Kimoto, S. and Oka, F. (2003), An elasto-viscoplastic model for clay considering destructuralization and prediction of compaction bands, *Proc. Int. Workshop on Prediction and Simulation Methods in Geomechanics*, TC34 of ISSMGE, Athens, Greece, Oka, F., Vardoulakis, I., Murakami, A., and Kodaka, T. eds., pp. 65-68.

Kimoto, S., Oka, F. and Higo, Y. (2004), Strain localization analysis of elasto-viscoplastic soil considering structural degradation, *Computer Methods in Applied Mechanics & Engineering*, to appear.

Oka, F., Yashima, A., Adachi, T., and Aifantis, E.C. (1994), Strain and pore water pressure localization in soft clay, *Proc. Symp. on Material Instability*, Theory and Applications, AMD-Vol. 183, MD-Vol. 50, ASME, Batra, R.C. and Zbib, H.M. eds., pp. 11-18.

Oka, F., Higo, Y. and Kimoto, S. (2002), Effect of dilatancy on the strain localization of water-saturated elasto-viscoplastic soil, *Int. J. Solids and Structures*, **39**, pp. 3625-3647.

Otani, J., Mukunoki, T. and Obara, Y. (2000), Application of X-ray CT method for characterization of failure in soils, *Soils and Foundations*, **40**, 2, pp. 111-118.

Perzyna, P. (1963), The constitutive equations for work-hardening and rate sensitive plastic materials, *Proc. Vibrational Problems*, Warsaw, **4**, 3, pp. 281-290.

Shimizu, M. (1982), Effect of overconsolidation on dilatancy of a cohesive soil, *Soils and Foundations*, **22**, 4, pp. 121-135.

Yamamura, S. (2002), Experimental study on deformation and strength characteristics for reconstituted overconsolidated clay, Master's thesis, Kyoto University, Japan, in Japanese.

Chapter 8

Conclusion and Future Work

8.1 Concluding Remarks

In the present study, the strain localization of clay was investigated through an instability analysis and a finite element analysis using an elasto-viscoplastic constitutive equation. In addition, undrained triaxial compression tests were conducted on rectangular clay specimens and the three-dimensional strain localization behavior was numerically simulated. The conclusions obtained in each chapter are described below.

In **Chapter 2**, a strain gradient-dependent elasto-viscoplastic constitutive model for normally consolidated clay was introduced. The model was derived based on the elasto-viscoplasticity theory proposed by Adachi and Oka (1982) and the gradient plasticity theory proposed by Oka (1995) and Aifantis et al. (1999). We demonstrated that the model can describe such material instability as strain softening and creep failure as well as the time-dependent behavior of clay.

In **Chapter 3**, the effects of permeability and strain gradient parameters on the strain localization of normally consolidated clay were theoretically and numerically studied. A theoretical investigation was conducted with a two-dimensional soil-water coupled instability analysis using a simplified strain gradient-dependent elasto-viscoplastic model. The growth rate of the fluctuation was discussed, and it was determined that materials with higher permeability levels are more unstable than those with lower permeability levels in the case of viscoplastic softening. On the other hand, materials with lower permeability levels are more unstable than those with higher permeability levels in the case of viscoplastic hardening. In addition, it was found that the strain gradient term acts as a stabilizer in the material system. As for the numerical study, a soil-water coupled finite element analysis for normally consolidated clay, based on the finite deformation theory using the strain gradient-dependent elasto-viscoplastic model, was conducted under undrained plane strain conditions. From the numerical investigation, we obtained results consistent with the theoretical ones, namely, the viscoplastic material system with low permeability is less stable in the viscoplastic strain-hardening range, whereas, the material system is less unstable in the large strain, i.e., in the strain-softening range. In addition, it was confirmed

that the accumulated shear strain is less localized when gradient term a_3 is large. It was found that permeability greatly affects the formation of shear bands. The effects of partially drained conditions and inherent heterogeneity on strain localization were also investigated. Under partially drainage conditions, materials with lower strain rates show consolidation. On the other hand, materials with higher strain rates show localized deformation. Material heterogeneity causes strain localization, even though the deformation of homogeneous clay becomes uniform. The initial distribution of material parameters affects the deformation pattern.

In **Chapter 4**, we developed an elasto-viscoplastic model for both normally consolidated clay and overconsolidated clay. The model can be seen as an extension of the elasto-viscoplastic model for normally consolidated clay proposed by Adachi and Oka (1982). In the model, the nonlinear kinematic hardening rule, the overconsolidation boundary surface, and a new definition for the second material function using the stress-history ratio were introduced. The proposed model can very effectively reproduce both positive and negative dilatancy characteristics which are important characteristics of soil.

In **Chapter 5**, firstly, the instability of the model proposed in **Chapter 4** was studied under undrained triaxial creep conditions for simplicity. It was found that the model for normally consolidated clay becomes unstable if the second material function is included. On the other hand, the model for overconsolidated clay was also found to be unstable even if the second material function is not introduced. Secondly, in the strain localization analysis using the finite element analysis with the elasto-viscoplastic model, it was determined that the effect of dilatancy characteristics is very significant in terms of the stress-strain relations and shear band formation. In addition, it was confirmed that permeability and strain rates greatly affect the formation of shear bands, and that the effects of permeability were consistent with the results obtained in **Chapter 3**.

In **Chapter 6**, the strain localization behavior of undrained triaxial compression tests for normally consolidated clay and overconsolidated clay, using various shapes of rectangular specimens with different strain rates, were studied. An image analysis of digital photographs taken during deformation provided the distributions of shear strain. From the image analysis, we observed not only the three-dimensional generation process of shear bands, but also the onset of localization at small strain levels, which would have been invisible if not for the image analysis. It was seen in all cases that strain begins to develop from the top and the bottom edges of the specimens, and that the localized deformations then lead to apparent shear bands. The strain localization patterns were greatly dependent on the shapes of the specimens, the strain rates, and the dilatancy characteristics. We classified the strain localization modes into the "X" mode, the buckling-like mode, and the complicated mode. The "X" mode was seen in specimens B and D, and their stress-strain relations exhibited stable behavior. Specimens A and C often showed the buckling-like mode due to the rather high aspect ratio. It was seen, however, that some of the A and C specimens showed the complicated mode which was identified as being an inter-

mediate mode between the other two modes. Corresponding to the generation of shear bands, strain-softening behavior was observed in the stress-strain relations of the A and C specimens. It was found that the strain rates greatly affect the strain localization patterns, particularly in the A and C specimens. Higher strain rates are likely to induce the buckling-like mode, whereas, lower strain rates lead to the complicated mode. In addition, we estimated the three-dimensional shear bands using the distributions of shear strain.

In **Chapter 7**, the numerical simulation of undrained triaxial compression tests using rectangular clay specimens was conducted with the finite element method in a three-dimensional setting. The constitutive model used in the simulation was the elasto-viscoplastic model for clay considering structural changes proposed by Kimoto (2002). The material parameters of the model were determined by undrained triaxial tests and isotropic consolidation tests on Fukakusa clay. From the simulation, we obtained the distributions of strain, stress, and pore water pressure which are difficult to determine from the experiments. The stress-strain relations and the effective stress paths of all cases well represented the strain rate sensitivity and the dilatancy characteristics. However, the strain-softening behavior corresponding to the formation of shear bands was not observed. The present simulation effectively reproduced the test results in terms of the onset and the development of shear bands. In particular, the "X" mode type of strain localization observed in all of the B and D specimens and some of the A and C specimens has been very well represented. On the other hand, the buckling-like mode was not seen in the simulation results because apparent geometrical imperfections were not taken into account. It was found that the shapes of specimens, the strain rates, and the dilatancy characteristics had a great influence on the strain localization patterns. The effects of the strain rates on the strain localization patterns for specimens A, B, and C were well reproduced by the simulation, especially for the B specimens. Deformations with higher strain rates tend to localize at two parts, i.e., the upper and the lower parts of the specimens, while, deformations with lower strain rates are likely to localize in the center sections of the specimens. From the comparison between the experimental results and the simulation results, we clarified the reasons why the buckling-like mode was often seen in the case of higher strain rates and why the effects of the strain rates on the strain localization pattern were different between the normally consolidated clay and the overconsolidated clay. In addition, it was confirmed that the buckling-like mode can only be simulated if the geometrical imperfections are adopted in an appropriate way. Moreover, we showed the distributions of total volumetric strain, namely, the local volume changes. It was found that compression occurred at the center of the specimens and expansion occurred near the surfaces of the specimens. These types of behavior are consistent with the measurements of local water contents for specimen D. Volume increases inside the shear bands were observed in both the measurements and the simulation for specimen C, in which apparent shear bands appeared.

So far, the instability analysis and the numerical analysis with the finite element method using an elasto-viscoplastic model in this study have clarified some mechanisms of strain local-

ization. In particular, the experimental results and their simulation have given us many findings regarding the shear banding behavior of clay. Through the obtained results, we have confirmed that the finite element analysis method and the elasto-viscoplastic constitutive equation used in this study can very well reproduce the strain localization behavior of both normally consolidated clay and overconsolidated clay under three-dimensional conditions.

8.2 Recommendation for Future Work

Further investigations into strain localization and constitutive equations for clay are required in order to clarify the mechanisms of strain localization. The topics of research which need to be addressed in the future are listed below.

In this study, the role of the strain gradient term was clarified only for normally consolidated clay. However, the constitutive model for clay has been extended to overconsolidated clay. It is necessary, therefore, to investigate the effects of the strain gradients on overconsolidated clay. In addition, the gradient parameters still need to be determined.

Some numerical calculations diverged at rather small axial strain levels; a few elements deformed largely before shear bands appear. It was found that the frictional boundary conditions relaxed the singular behavior. However, in order to calculate in the range of larger axial strain, it is necessary to properly deal with the elements by specific methods, e.g., an adaptive mesh.

In this study, it was confirmed that the present simulation can represent the buckling-like mode only if the geometrical imperfection is taken into account. In addition, it is worth noting that the inherent material heterogeneity caused asymmetric deformations as shown in **Section 3.8**. Namely, it is necessary to introduce the geometrical imperfection and material heterogeneity by proper method.

In the simulation of tests, we have obtained the distributions of total volumetric strain, i.e., local volume changes. In particular, the simulation results were consistent with the measurements of the local water contents for specimens C and D. However, the measurements for other cases were not successful enough to compare with the simulation results. Detail observation of local density by X-ray CT scanners and comparison with the simulation results are desired.

We confirmed that the simulation methods in this study can be very effectively applied to the strain localization behavior of clay under three-dimensional conditions. In the future, analyses of case studies which are related to strain localization, such as slope failure and excavations, are necessary in order to practically verify the proposed method.

References

Adachi, T. and Oka, F. (1982), Constitutive equations for normally consolidated clay based on elasto-viscoplasticity, *Soils and Foundations*, **22**, 4, pp. 57-70.

Aifantis, E.C., Oka, F., Yashima, A. and Adachi, T. (1999), Instability of gradient dependent elasto-viscoplasticity for clay, *Int. J. Numerical and Analytical Methods in Geomechanics*, **23**, pp. 973-994.

Kimoto, S. (2002), Constitutive models for geomaterials considering structural changes and anisotropy, Doctoral thesis, Kyoto University, Japan.

Oka, F. (1995), A gradient-dependent elastic model for granular materials and strain localization, *Continuum Models for Materials with Microstructure*, Mühlhaus, H.-B. ed., John Wiley & Sons, pp. 145-158.

Appendix A

Derivation of $\det[A]$

The matrix form for the governing equations of the instability analysis is given by **Equations** (3.20)~(3.31). In order to obtain $\det[A]$, we have used Mathematica 3.0, namely,

$$\begin{aligned}\det[A] = \frac{1}{6\gamma_w GK\mu^4 q^2\omega^2}(n_1^2+n_2^2)^2\left(\omega+\frac{G''}{\mu}\right)\\ \Big[4\gamma_w\mu^2\omega^3\\ +(4\gamma_w G\mu+6\gamma_w K\mu-6\gamma_w K\mu\mu_k''+4G\mu^2kq^2+6K\mu^2kq^2)\omega^2\\ +(6\gamma_w GK-6\gamma_w GK\mu_k''+4G\mu G''kq^2+12GK\mu kq^2\\ +6K\mu G''kq^2+3K\mu K''kq^2-6GK\mu\mu_k''kq^2)\omega\\ +12GKG''kq^2+3GKK''kq^2-6GKG''\mu_k''kq^2\Big]\end{aligned} \tag{A.1}$$

in which

$$(n_1^2+n_2^2)^2 = 1 \tag{A.2}$$

since $\boldsymbol{n} = (n_1, n_2)$ is the unit vector defined by **Equation** (3.15).

After adopting the condition $\det[A] = 0$, and multiplying and dividing it by $(6\gamma_w GK\mu^4q^2\omega^2)$ and $(4\gamma_w\mu^2)$, respectively, we obtain

$$\left(\omega+\frac{G''}{\mu}\right)\left(\omega^3+\alpha_1\omega^2+\alpha_2\omega+\alpha_3\right) = 0 \tag{A.3}$$

where

$$\alpha_1 = \frac{1}{2\gamma_w\mu}\left[\gamma_w\left\{2G-3K(\mu_k''-1)\right\}+kq^2\mu(2G+3K)\right] \tag{A.4}$$

$$\begin{aligned}\alpha_2 = \frac{1}{4\gamma_w\mu^2}\Big[-6\gamma_w GK(\mu_k''-1)+kq^2\mu\Big\{3K(2G''+K'')\\ +2G(2G''+6K-3K\mu_k'')\Big\}\Big]\end{aligned} \tag{A.5}$$

$$\alpha_3 = \frac{1}{4\gamma_w\mu^2}\left[3GKkq^2\left\{K''-2G''(\mu_k''-2)\right\}\right] \tag{A.6}$$

Material parameters K'' and μ_k'' are defined by **Equations** (3.6) and (3.7), in other words,

$$\mu_k'' = \frac{\mu_k'}{2\mu + \mu_k'} \tag{A.7}$$

$$K'' = \frac{2(\mu K' - \mu_k' G'')}{2\mu + \mu_k'} \tag{A.8}$$

Substituting these into **Equations** (A.4) to (A.6), we obtain the coefficients of the characteristic polynomial, namely,

$$\alpha_1 = \frac{1}{2\gamma_w \mu(2\mu + \mu_k')}\left[2\gamma_w\left\{3K\mu + G(2\mu + \mu_k')\right\} + kq^2\mu(2G + 3K)(2\mu + \mu_k')\right] \tag{A.9}$$

$$\alpha_2 = \frac{1}{2\gamma_w \mu(2\mu + \mu_k')}\Big[6\gamma_w GK + kq^2\Big\{3K\mu(2G'' + K') + G\Big(4\mu(G'' + 3K) + \mu_k'(2G'' + 3K)\Big)\Big\}\Big] \tag{A.10}$$

$$\alpha_3 = \frac{3GKkq^2}{2\gamma_w \mu(2\mu + \mu_k')}(4G'' + K') \tag{A.11}$$

When we use a rigid-viscoplastic model, the following assumptions for elastic shear modulus G and elastic bulk modulus K are applied to make the elastic strain rate negligible:

$$G \to \infty, \quad K \to \infty \tag{A.12}$$

Applying these assumptions, $\det[A]$ is obtained as

$$\det[A] = -\frac{1}{2\gamma_w \mu^4 \omega^2}(n_1^2 + n_2^2)^2\left(\omega + \frac{G''}{\mu}\right) \left[2\left\{\gamma_w(\mu_k'' - 1) + kq^2\mu(\mu_k'' - 2)\right\}\omega + kq^2\left\{2G''(\mu_k'' - 2) - K''\right\}\right] \tag{A.13}$$

By adopting $\det[A] = 0$ and substituting **Equations** (A.7) and (A.8), we obtain

$$\left(\omega + \frac{G''}{\mu}\right)\left[\left\{2\gamma_w + kq^2(4\mu + \mu_k')\right\}\omega + kq^2(4G'' + K')\right] = 0 \tag{A.14}$$

Appendix B

Derivation of Equations (3.54), (3.64), and (3.69)

We will show some derivations of the equations used in the updated Lagrangian finite element formulations based on the lecture notes by Nishimura (2001). In the following, time derivative indicates the material time derivative without specific notations.

Time derivative of Jacobian determinant J

The time derivative of Jacobian determinant J is given as

$$\dot{J} = \dot{\det \boldsymbol{F}} = \frac{\partial(\det \boldsymbol{F})}{\partial F_{ij}} \frac{\partial F_{ij}}{\partial t} \tag{B.1}$$

where $\boldsymbol{F}$ is the deformation gradient tensor and F_{ij} is the components of $\boldsymbol{F}$.

Using the following relations

$$\frac{\partial(\det \boldsymbol{F})}{\partial F_{ij}} = F_{ij}^{cof} \ , \quad F_{ij}^{-1} = \frac{(F_{ij}^{cof})^{\mathrm{T}}}{\det \boldsymbol{F}} \tag{B.2}$$

in which F_{ij}^{cof} is the cofactors of $\boldsymbol{F}$, **Equation** (B.1) yields

$$\dot{J} = (\det \boldsymbol{F}) F_{ji}^{-1} \dot{F}_{ij} = J \,\mathrm{tr}\boldsymbol{L} \tag{B.3}$$

in which $\boldsymbol{L}$ is the velocity gradient tensor defined as: $L_{ij} = \dot{F}_{ik} F_{kj}^{-1}$.

Time derivative of $\boldsymbol{F}^{-\mathrm{T}}$

We consider the time differentiation of the relation of $\boldsymbol{F}^{-1}\boldsymbol{F} = \boldsymbol{I}$ as

$$\dot{\boldsymbol{F}^{-1}}\boldsymbol{F} + \boldsymbol{F}^{-1}\dot{\boldsymbol{F}} = 0 \tag{B.4}$$

$$\dot{\boldsymbol{F}^{-1}} = -\boldsymbol{F}^{-1}\dot{\boldsymbol{F}}\boldsymbol{F}^{-1} \tag{B.5}$$

Therefore, the time derivative of $\boldsymbol{F}^{-\mathrm{T}}$ is obtained as follows:

$$\dot{\boldsymbol{F}^{-\mathrm{T}}} = -\boldsymbol{F}^{-\mathrm{T}}\dot{\boldsymbol{F}}^{\mathrm{T}}\boldsymbol{F}^{-\mathrm{T}} = -\boldsymbol{L}^{\mathrm{T}}\boldsymbol{F}^{-\mathrm{T}} \tag{B.6}$$

Time derivative of the first Piola-Kirchhoff stress tensor

The nominal stress (the first Piola-Kirchhoff stress) tensor $\boldsymbol{\Pi}$ is defined as follows:

$$\boldsymbol{\Pi}^{\mathrm{T}} = J\boldsymbol{T}^{\mathrm{T}}\boldsymbol{F}^{-\mathrm{T}} \tag{B.7}$$

where $\boldsymbol{T}$ is the Cauchy stress, $\boldsymbol{F}$ is the deformation gradient tensor, and J is the Jacobian determinant. Differentiating $\boldsymbol{\Pi}$ with respect to time yields

$$\begin{aligned}\dot{\boldsymbol{\Pi}}^{\mathrm{T}} &= \dot{J}\boldsymbol{T}^{\mathrm{T}}\boldsymbol{F}^{-\mathrm{T}} + J\dot{\boldsymbol{T}}^{\mathrm{T}}\boldsymbol{F}^{-\mathrm{T}} + J\boldsymbol{T}^{\mathrm{T}}\dot{\boldsymbol{F}}^{-\mathrm{T}} \\ &= J(\mathrm{tr}\boldsymbol{L})\boldsymbol{T}^{\mathrm{T}}\boldsymbol{F}^{-\mathrm{T}} + J\dot{\boldsymbol{T}}^{\mathrm{T}}\boldsymbol{F}^{-\mathrm{T}} - J\boldsymbol{T}^{\mathrm{T}}\boldsymbol{L}^{\mathrm{T}}\boldsymbol{F}^{-\mathrm{T}} \\ &= J(\dot{\boldsymbol{T}} + \boldsymbol{T}\mathrm{tr}\boldsymbol{L} - \boldsymbol{T}\boldsymbol{L}^{\mathrm{T}})\boldsymbol{F}^{-\mathrm{T}}\end{aligned} \tag{B.8}$$

in which the symmetry property of the Cauchy stress, namely,

$$\boldsymbol{T}^{\mathrm{T}} = \boldsymbol{T} \tag{B.9}$$

is used.

Relation between the nominal traction rate vector $\dot{\boldsymbol{s}}_t$ and the nominal stress rate tensor $\dot{\boldsymbol{S}}_t$

Yatomi et al. (1989) demonstrated the relation between the nominal traction rate vector $\dot{\boldsymbol{s}}_t$ and the nominal stress rate tensor $\dot{\boldsymbol{S}}_t$.

The total nominal traction rate vector $\dot{\boldsymbol{s}}_t$ is defined by following equation:

$$\dot{\boldsymbol{s}}_t\, ds = \dot{\overline{\boldsymbol{t}\, ds}} = \dot{\overline{\boldsymbol{T}\boldsymbol{n}\, ds}} \tag{B.10}$$

in which Cauchy's stress theorem, **Equation** (3.47), and the symmetry property of the Cauchy stress, **Equation** (B.9), are used, and $\boldsymbol{t}$ is the actual traction vector.

Using Nanson's law, **Equation** (3.51), $\dot{\overline{\boldsymbol{n}\, ds}}$ becomes

$$\begin{aligned}\dot{\overline{\boldsymbol{n}\, ds}} &= \dot{\overline{J\boldsymbol{F}^{-\mathrm{T}}}}\boldsymbol{N}dS_0 \\ &= (\dot{J}\boldsymbol{F}^{-\mathrm{T}} + J\dot{\overline{\boldsymbol{F}^{-\mathrm{T}}}})\boldsymbol{N}dS_0 \\ &= J(\boldsymbol{I}\,\mathrm{tr}\boldsymbol{L} - \boldsymbol{L}^{\mathrm{T}})\boldsymbol{F}^{-\mathrm{T}}\boldsymbol{N}dS_0 \\ &= (\boldsymbol{I}\,\mathrm{tr}\boldsymbol{L} - \boldsymbol{L}^{\mathrm{T}})\boldsymbol{n}\, ds\end{aligned} \tag{B.11}$$

where $\boldsymbol{I}$ is the second order identity tensor.

Substituting **Equation** (B.11) into **Equation** (B.10) yields

$$\begin{aligned}\dot{\boldsymbol{s}}_t\, ds &= \dot{\boldsymbol{T}}\boldsymbol{n}\, ds + \boldsymbol{T}(\boldsymbol{I}\,\mathrm{tr}\boldsymbol{L} - \boldsymbol{L}^{\mathrm{T}})\boldsymbol{n}\, ds \\ &= (\dot{\boldsymbol{T}} + \boldsymbol{T}\,\mathrm{tr}\boldsymbol{L} - \boldsymbol{T}\boldsymbol{L}^{\mathrm{T}})\boldsymbol{n}\, ds\end{aligned} \tag{B.12}$$

The relation between the total nominal traction rate vector $\dot{\boldsymbol{s}}_t$ and the nominal stress rate tensor $\dot{\boldsymbol{S}}_t$ is obtained by using the definition of $\dot{\boldsymbol{S}}_t$, **Equation** (3.57), as follows:

$$\dot{\boldsymbol{s}}_t = \dot{\boldsymbol{S}}_t\boldsymbol{n} \tag{B.13}$$

In addition, another reduction of **Equation** (B.10) can be described as

$$\dot{\boldsymbol{s}}_t\, ds = \dot{\overline{\boldsymbol{t}\, ds}} = \dot{\boldsymbol{t}}\, ds + \boldsymbol{t}\dot{\overline{ds}} \tag{B.14}$$

Let us consider the time derivative of $(ds)^2$ by use of Nanson's law:

$$(ds)^2 = \boldsymbol{n}ds \cdot \boldsymbol{n}ds = J^2 \boldsymbol{F}^{-\mathrm{T}}\boldsymbol{N} \cdot \boldsymbol{F}^{-\mathrm{T}}\boldsymbol{N}(dS_0)^2 \tag{B.15}$$

Thus

$$\begin{aligned} 2ds\,\dot{\overline{ds}} &= 2J\dot{J}\boldsymbol{F}^{-\mathrm{T}}\boldsymbol{N} \cdot \boldsymbol{F}^{-\mathrm{T}}\boldsymbol{N}(dS_0)^2 + 2J^2\dot{\overline{\boldsymbol{F}^{-\mathrm{T}}}}\boldsymbol{N} \cdot \boldsymbol{F}^{-\mathrm{T}}\boldsymbol{N}(dS_0)^2 \\ &= \frac{2\dot{J}}{J}(ds)^2 + 2(-\boldsymbol{L}^{\mathrm{T}}\boldsymbol{F}^{-\mathrm{T}})\boldsymbol{F}^{\mathrm{T}}(\boldsymbol{n}ds \cdot \boldsymbol{n}ds) \\ &= 2(\mathrm{tr}\boldsymbol{L} - \boldsymbol{n} \cdot \boldsymbol{L}^{\mathrm{T}}\boldsymbol{n})(ds)^2 \end{aligned} \tag{B.16}$$

which yields the following relation:

$$\dot{\overline{ds}} = (\mathrm{tr}\boldsymbol{L} - \boldsymbol{n} \cdot \boldsymbol{L}^{\mathrm{T}}\boldsymbol{n})\, ds \tag{B.17}$$

Substituting **Equation** (B.17) into **Equation** (B.14) gives the total nominal stress rate vector $\dot{\boldsymbol{s}}_t$ as

$$\dot{\boldsymbol{s}}_t = \dot{\boldsymbol{t}} + (\mathrm{tr}\boldsymbol{L} - \boldsymbol{n} \cdot \boldsymbol{L}^{\mathrm{T}}\boldsymbol{n})\boldsymbol{t} \tag{B.18}$$

In the present numerical implementation, we assume that the second term of **Equation** (B.18) is negligible on the traction boundary $\partial\mathcal{D}_{\mathrm{t}}$, i.e., the total nominal stress rate vector $\dot{\boldsymbol{s}}_t$ is equal to the actual traction rate vector $\dot{\boldsymbol{t}}$.

References

Nishimura, N. (2001), Lecture notes on Mechanics of Elastic and Inelastic Materials, Lecture presented to Graduate School of Kyoto University, Japan.

Yatomi, C., Yashima, A., Iizuka, A. and Sano, I. (1989), General theory of shear bands formation by a non-coaxial Cam-clay model, *Soils and Foundations*, **29**, 3, pp. 41-53.